

## The Curious Case of Io - Connections Between Interior Structure, Tidal Heating and Volcanism

Steinke, T.

**DOI**

[10.4233/uuid:9e875752-05bc-4dd8-9bdd-77e18cf3c43f](https://doi.org/10.4233/uuid:9e875752-05bc-4dd8-9bdd-77e18cf3c43f)

**Publication date**

2021

**Document Version**

Final published version

**Citation (APA)**

Steinke, T. (2021). *The Curious Case of Io - Connections Between Interior Structure, Tidal Heating and Volcanism*. [Dissertation (TU Delft), Delft University of Technology]. <https://doi.org/10.4233/uuid:9e875752-05bc-4dd8-9bdd-77e18cf3c43f>

**Important note**

To cite this publication, please use the final published version (if applicable). Please check the document version above.

**Copyright**

Other than for strictly personal use, it is not permitted to download, forward or distribute the text or part of it, without the consent of the author(s) and/or copyright holder(s), unless the work is under an open content license such as Creative Commons.

**Takedown policy**

Please contact us and provide details if you believe this document breaches copyrights. We will remove access to the work immediately and investigate your claim.

# **THE CURIOUS CASE OF IO**

CONNECTIONS BETWEEN INTERIOR STRUCTURE,  
TIDAL HEATING AND VOLCANISM



# **THE CURIOUS CASE OF IO**

CONNECTIONS BETWEEN INTERIOR STRUCTURE,  
TIDAL HEATING AND VOLCANISM

## **Proefschrift**

ter verkrijging van de graad van doctor  
aan de Technische Universiteit Delft,  
op gezag van de Rector Magnificus Prof.dr. T.H.J.J. van der Hagen,  
voorzitter van het College voor Promoties,  
in het openbaar te verdedigen op  
maandag 20 december 2021 om 17:30 uur

door

**Teresa STEINKE**

MSc. in Geophysik, MSc. in Geodäsie & Geoinformatik,  
Karlsruher Institut für Technologie, Karlsruhe, Duitsland,  
geboren te Dresden, Duitsland.

Dit proefschrift is goedgekeurd door de promotoren.

Samenstelling promotiecommissie:

Rector Magnificus,	voorzitter
Prof. dr. L.L.A. Vermeersen,	Technische Universiteit Delft, promotor
Prof. dr. I. de Pater,	Technische Universiteit Delft, promotor
Dr. ir. W. van der Wal,	Technische Universiteit Delft, copromotor

*Onafhankelijke leden:*

Prof. dr. T. Spohn,	International Space Science Institute, Zwitserland
Prof. dr. T. Van Hoolst,	Katholieke Universiteit Leuven, België
Prof. dr. B.R. Brandl,	Technische Universiteit Delft
Dr. A.G. Davies,	Jet Propulsion Laboratory, USA
Prof. dr. S. Hickel,	Technische Universiteit Delft, reservelid



The work presented in this dissertation was financially supported by the User Support Programme Space Research, a program of the Netherlands Organization for Scientific Research, under the project number ALW-GO/15-07.

*Keywords:* Io, tidal dissipation, interior, volcanism

*Printed by:* Ipskamp Printing

*Front:* Io. Image Credit: NASA/JPL - Image PIA00494

Copyright © 2021 by T. Steinke

ISBN 978-94-6421-601-1

An electronic version of this dissertation is available at  
<http://repository.tudelft.nl/>.

*... And it was all yellow.*

Coldplay



# CONTENTS

<b>Summary</b>	<b>xi</b>
<b>Samenvatting</b>	<b>xv</b>
<b>1 Introduction</b>	<b>1</b>
1.1 Io in a nutshell . . . . .	2
1.2 Orbital dynamics of the Jupiter system . . . . .	3
1.2.1 Origin and Formation of the Galilean satellites. . . . .	4
1.2.2 Tidal dynamics. . . . .	5
1.2.3 The Laplace resonance and thermal orbital coupling . . . . .	7
1.3 Io's volcanism . . . . .	9
1.3.1 Remote sensing of Io's volcanic activity . . . . .	9
1.3.2 Spatial and temporal characteristics of volcanic activity . . . . .	10
1.3.3 Eruption styles, temperatures and magma composition . . . . .	11
1.4 Io's interior . . . . .	12
1.4.1 Interior structure, physical state and composition . . . . .	13
1.4.2 Tidal heat production . . . . .	16
1.4.3 Heat loss mechanisms . . . . .	18
1.4.4 Io's volcanoes - a window into Io's dynamic interior . . . . .	20
1.5 Research motivation and research questions . . . . .	25
<b>2 Tidally induced lateral variations</b>	<b>29</b>
2.1 Introduction . . . . .	30
2.2 Numerical modelling of volumetric tidal heating . . . . .	32
2.2.1 Periodic tidal forcing. . . . .	32
2.2.2 Finite element approach. . . . .	33
2.2.3 Rheological model and properties of Io's interior structure. . . . .	34
2.3 Thermal modelling . . . . .	37
2.3.1 Steady-state scaling of a volumetric heated convective system. . . . .	38
2.3.2 Lateral heat flow due to convection . . . . .	41
2.3.3 Thermal profile of Io's internally heated mantle . . . . .	42
2.3.4 Magmatic heat transport by melt and iterative procedure . . . . .	44
2.3.5 Lateral thickness variations of the thermal boundary and crust . . . . .	46
2.3.6 Thermal properties of Io models . . . . .	46
2.4 Results . . . . .	47
2.4.1 Tidal dissipation pattern of the finite element model . . . . .	47
2.4.2 Spatial patterns of temperature, magmatic heat output, melt fraction and crustal thickness . . . . .	48
2.4.3 Influence of interior parameters . . . . .	50



2.5	Discussion and conclusion . . . . .	53
2.6	Appendix-A: Correction of mantle temperature distribution . . . . .	56
2.7	Appendix-B: Specifications and benchmark of the finite element model . . . . .	57
2.8	Appendix-C: Variation of Rayleigh-Roberts number. . . . .	58
<b>3</b>	<b>Tidal-heating-rheology feedback in Io's asthenosphere</b>	<b>61</b>
3.1	Introduction . . . . .	62
3.2	Modelling the non-uniform dissipation-rheology feedback. . . . .	64
3.2.1	Reference interior models . . . . .	64
3.2.2	Tidal potential . . . . .	64
3.2.3	Initial tidal dissipation patterns . . . . .	66
3.2.4	Heterogeneous viscosity and shear modulus distribution . . . . .	67
3.2.5	Finite element model . . . . .	70
3.2.6	Feedback. . . . .	71
3.3	Results and Discussion . . . . .	72
3.3.1	Non-uniform distribution of rheological properties . . . . .	73
3.3.2	Squared stress pattern . . . . .	74
3.3.3	Distribution of tidal dissipation . . . . .	76
3.3.4	Feedback. . . . .	81
3.4	Conclusion . . . . .	84
<b>4</b>	<b>Connections between heat transport and volcanic pattern</b>	<b>87</b>
4.1	Introduction . . . . .	88
4.2	Statistical analysis of hot-spot observations. . . . .	90
4.2.1	Selection of volcanic data . . . . .	91
4.2.2	Spherical harmonic analysis of the volcanic density . . . . .	92
4.2.3	Total number of Io's volcanic anomalies . . . . .	93
4.3	Modelling the characteristics of Io's convective layer . . . . .	94
4.3.1	Global presence of magma. . . . .	94
4.3.2	Large-scale anomalies . . . . .	97
4.3.3	Number of small-scale anomalies . . . . .	100
4.4	Results . . . . .	102
4.4.1	Global presence of magma. . . . .	102
4.4.2	Large-scale anomalies . . . . .	103
4.4.3	Number of small-scale anomalies . . . . .	105
4.5	Discussion . . . . .	106
4.6	Conclusion . . . . .	109
4.7	Appendix-A: Alternative observation set . . . . .	110
4.8	Appendix-B: Scaling for the number of volcanoes. . . . .	110
<b>5</b>	<b>Conclusion and Outlook</b>	<b>113</b>
5.1	Answers to research questions . . . . .	113
5.2	Conclusions. . . . .	116
5.3	Recommendations for future work . . . . .	118
5.3.1	Heat transport in a solid-liquid medium . . . . .	118
5.3.2	Tidal dissipation in a solid-liquid medium. . . . .	119

---

5.3.3	Feedback between interior state, heat transport and tidal heat generation . . . . .	119
5.3.4	From global to local scales . . . . .	120
5.4	Outlook . . . . .	120
	<b>References</b>	<b>123</b>
	<b>Acknowledgements</b>	<b>137</b>
	<b>Curriculum Vitae</b>	<b>141</b>
	<b>List of Publications</b>	<b>143</b>



# SUMMARY

Io's spectacular and unique appearance, characterised by its yellowish surface, colorful lava deposits, and black calderas, was first observed by the Voyager I spacecraft in 1979. The reason for this appearance is extensive tidal heating in the moon's interior. Caught in the Laplace resonance with the Galilean moons Ganymede and Europa, Io is the most tidally heated and volcanically active world in the Solar System. It is therefore the best place to study fundamental processes important for the early evolution of terrestrial planets, and the habitability of icy satellites and terrestrial exoplanets subject to tidal heating.

Tidal heating occurs below Io's lithosphere, which is Io's outer elastic layer. However, it is unknown whether a fluid magma ocean or an almost completely solid mantle lies beneath the lithosphere. For this reason, the driving tidal dissipation and heat transport mechanisms are unknown. The physical state of Io's mantle, and the heat production and heat loss mechanisms form a strongly interconnected system: 1) Io's internal temperature and melt distribution are controlled by tidal dissipation and heat loss processes; 2) The total amount and pattern of tidal dissipation depend on the rheological properties of Io's interior; 3) These rheological properties, in turn, depend on the internal temperature and melt distribution. Due to the strong dependence on melt, Io's volcanic activity hints at the dynamics beneath the surface and can therefore be used to improve our understanding of the underlying mechanisms. Aim of this thesis is to improve our understanding of these interconnections (1-3) and to constrain Io's current interior dynamics based on Io's current orbital state and the moon's volcanic activity derived from satellite and Earth-based observations over the last 20 years. Stronger constraints on Io's current interior state will allow to enhance our understanding of terrestrial heat loss processes and interactions between the orbital dynamics of the Jupiter system and Io's interior.

Heat generated in a tidally distorted spherical symmetric interior is radially and laterally non-uniformly distributed. Since the amount of tidal heat generated in Io's interior exceeds the amount of radiogenic heating by several orders of magnitude, the non-uniform heat source represents a unique interior characteristic of Io. In order to investigate the effect of non-uniform tidal heating on Io's interior and surface heat flux, we develop a parameterized thermal model including non-uniform tidal heating, mantle convection, and melt migration. The following interior properties determine how strong the lateral temperature field in the mantle is affected by the heating pattern: In case tidal heating occurs in both the lower mantle and the asthenosphere (layer of the upper mantle with increased melt fraction), the lateral variations are smaller than in a case where heat is mainly produced in the asthenosphere. Mantle convection blurs temperature heterogeneities. The weaker the convective heat transport and the

stronger the magmatic heat transport, the stronger the tidally-induced heterogeneities that remain in the interior. Also, the thinner the convective layer and the higher its viscosity, the weaker the blurring due to convection and the stronger the remaining variations. Depending on these unknown mantle parameters, the resulting peak-to-peak temperature anomaly can vary from less than 1 K up to 190 K. Thus, from a pure modelling perspective it cannot be stated whether Io's mantle is well-mixed and homogeneous or shows significant lateral variations in its melt fraction due to tidal heating.

Earth-based telescope observations with adaptive optics (since the 2000s, ongoing) and satellite-based observations by Galileo (1995–2003) and JUNO (2016-2025) show that the volcanoes are focused at near equatorial areas with two maxima located approximately 30° eastwards of the sub-Jovian point and the anti-Jovian point, respectively. The lack of volcanoes in the polar areas and Io's extreme heat flux in combination with its thick crust favours a magmatic-dominated heat transport within the asthenosphere, which is rheologically separated from the lower mantle. For these interior characteristics the thermal model above shows significant tidally-induced heterogeneities. As analytical models can only compute tidal dissipation patterns for spherical symmetric rheological structures, we develop a numerical model based on finite elements in order to include the arising tidally-induced heterogeneities. The results of the finite element model show that the distribution of the generated tidal heat is different for models with laterally varying rheological profiles compared to a model with homogeneous layers. Regions with above average melt fractions show a regional increase in tidal heating, and vice versa for regions with melt fractions below the average. In addition, the spatial variation of the time delay of the visco-elastic response of the asthenosphere induces an asymmetry of the tidal dissipation pattern with respect to the prime meridian. Next, we investigate the feedback between interior properties and tidal heating: We use the resulting tidal dissipation pattern to derive a new rheological profile and then use this new profile to compute a new dissipation pattern with our finite element model. Continuously repeating these two steps, we find that the asymmetry increases until an equilibrium between the melt-dependent rheological structure and the tidal heating pattern is achieved. The two locations of maximum tidal dissipation are shifted 15° eastward compared to the points of maximum dissipation for the homogeneously layered visco-elastic interior model. Whereas in previous studies the offset in Io's observed volcanic activity field could only be explained by tidal dissipation in a fluid magma ocean, our finding suggests that the offset could also be caused by a feedback mechanism between non-uniform tidal heating and rheological properties in Io's visco-elastic asthenosphere.

Io's observed volcanic activity can also be useful to constrain heat transport processes in the interior. For that, three different spatial characteristics of Io's volcanic pattern are identified: i) The presence of global volcanism, which is assumed to constrain the mantle temperature; ii) the presence of long-wavelength variations in Io's volcanic activity, which is assumed to constrain the strength of the lateral heat transport; and iii) the average distance between two neighbouring volcanic systems, which is assumed to constrain the spatial characteristics of the convection pattern in Io's mantle. For our analysis we allow for vertically separated convective systems in Io's mantle and assume

that only the character of the upper convective system, here referred to as upper mantle, is linked to the volcanism at the surface. Using a scaling-based analysis we find that a partially convective and partially magmatic heat transport in Io's upper mantle can produce the observed (i) global and (ii) long-wavelength characteristics of Io's observed volcanic pattern. Provided also that (iii) the spatial density of Io's volcanoes is controlled by sub-lithospheric anomalies caused by convective flow, we find that 80% or more of Io's internal heat is transported by magmatic advection and that Io's upper mantle needs to be thicker than 50 km.

The research accomplished in this dissertation improves the consistency of models for Io's interior by considering the interior as one coupled system including many interconnected mechanisms. We could show that taking into account mantle heterogeneities arising due to mantle convection and tidal heating leads to different results and conclusions. The biggest advances to previous research mark the findings that 1) a combination of magmatic heat transport and solid-state convection in Io's mantle can explain the global, large- and small-scale characteristics of Io's volcanic field; and that 2) incorporating tidally-induced variations of the asthenosphere produces an offset in the tidal dissipation pattern. These findings suggest that a visco-elastic asthenosphere with low to medium melt fraction (up to 25%) and a combination of magmatic and convective heat transport can explain available Io observations, such as the high-temperature eruptions, the eastward offsets of the peaks in volcanic activity, and the induced magnetic field by a fluid component in the interior. In addition to Io-related improvements, the models developed in this thesis can be applied to terrestrial planets remote in time and space.

To further advance our understanding of Io's interior, the dissipation and heat transport models developed in this thesis need to incorporate interactions between solid and liquid phases. This requires the investigation of mechanisms on short temporal (10 years to days) and small spatial (one kilometer to 100 kilometers) scales. The correlation between anomalies in a convective mantle and Io's volcanoes, suggested in this thesis, needs to be verified with 2D and 3D models including chemical aspects. These regional models can then be verified with the various eruption styles of Io's volcanoes observed by the Galileo mission, ranging from silent events to powerful outbursts. Furthermore, the feedback mechanism in the spatial domain between non-uniform tidal heating and rheological properties needs to be studied for an extended parameter space. Despite many possibilities for modelling advances, observations of tidal deformation, libration amplitudes, passive radar sounding, and the induced magnetic field are likely indispensable to conclude whether a global magma ocean or a visco-elastic partially molten asthenosphere is present beneath Io's crust. Finally, a verification of suggested interior mechanisms and model parameters by an Io-dedicated mission would lead to a more precise evaluation of habitable environments and their preconditions for icy and Earth-like worlds in the Solar System and beyond.



# SAMENVATTING

Het spectaculaire en unieke uiterlijk van Io, gekenmerkt door zijn geelachtige oppervlak, kleurrijke lavaafzettingen en zwarte caldera's, is voor het eerst waargenomen door Voyager I in 1979. De reden voor dit unieke uiterlijk is de omvangrijke opwarming binnen in de maan, veroorzaakt door de getijden. Gevangen in een Laplace baanresonantie met de Galileïsche manen Ganymedes en Europa, is Io de maan met de grootste getijdenverhitting. Ook is Io het meest vulkanisch actieve lichaam in ons zonnestelsel. Om deze reden is Io de uitgelezen plek om de fundamentele processen te bestuderen die belangrijk zijn voor 1) de vroege evolutie van aardachtige planeten en 2) de leefbaarheid van ijsmanen en aardse exoplaneten onderworpen aan getijdenverhitting.

Getijdenverhitting vindt plaats onder de korst van Io. Het is echter onbekend of er een vloeibare magmaoceaan of een bijna geheel vaste mantel onder de korst aanwezig is. Hierdoor is het nog onduidelijk wat de mechanismes zijn van de getijdenverhitting en het hittetransport in deze maan. De kenmerken op het oppervlak geven samen met de vulkanische activiteit van Io aanwijzingen voor de dynamiek onder het oppervlak en deze waarnemingen kunnen daarom gebruikt worden om onze kennis van de mechanismes te verbeteren. De fysieke staat van de mantel van Io, hitteproductie in het binnenste van de maan, en het mechanisme om hitte te verliezen zijn sterk met elkaar verbonden op de volgende manier: 1) De temperatuur in het binnenste van Io wordt samen met de verdeling van smelt en de vulkanische activiteit bepaald door de getijdenverhitting en het hitteverlies; 2) De totale hoeveelheid en het patroon van getijdenverhitting hangt af van de rheologische eigenschappen in het binnenste van Io; 3) Deze rheologische eigenschappen hangen op hun beurt weer af van de temperatuur en de smelt.

Het doel van dit proefschrift is om deze onderlinge verbindingen beter te leren begrijpen en om de huidige dynamiek in het binnenste van Io te verklaren aan de hand van de omloopbanen en de vulkanische activiteit, beiden afkomstig van satelliet-waarnemingen en waarnemingen op aarde van de laatste 20 jaar. Het verklaren van het gedrag binnenin Io maakt het mogelijk om de onderlinge verbindingen tussen de baandynamica van het Jupitersysteem met Io en het warmteverlies van aardachtige planeten in hun vroege evolutie beter te leren begrijpen.

Getijdendissipatie in het binnenste van een sferisch symmetrische bol is in radiële en laterale richting niet uniform verdeeld. Aangezien er aanzienlijk (enkele orders van grootte) meer warmte gegenereerd wordt door getijden in Io dan door radiogene processen, zorgt de getijdenverhitting als warmtebron voor een uniek kenmerk van Io. Om het effect te onderzoeken van een niet-uniforme getijdenverhitting op het binnenste van Io en zijn warmtestroomdichtheid aan het oppervlak, ontwikkelen we een



geparametriseerd thermisch model met daarin een niet-uniforme getijdenverhitting, mantel convectie en smeltmigratie. De volgende eigenschappen bepalen hoe sterk het verhittingspatroon de laterale temperatuur in de mantel en de vulkanische activiteit aan het oppervlak beïnvloedt: in het geval dat getijdenverhitting aanwezig is in zowel het onderste als het bovenste deel van de mantel zijn de laterale verschillen kleiner dan wanneer de hitte voornamelijk gegenereerd wordt in de asthenosfeer. Mantelconvectie vervaagt de heterogeniteit in de temperatuur. Naarmate het convectieve warmtetransport zwakker wordt en het magmatische warmtetransport sterker wordt, wordt de heterogeniteit, veroorzaakt door de getijden in het binnenste, sterker. Daarnaast zorgt ook een dunnere convectielaag en een hogere viscositeit voor minder vervaging door convectie en worden de resulterende variaties ook sterker. Afhankelijk van deze onbekende parameters in de mantel kunnen de piek-tot-piek variaties in de temperatuur-anomalie variëren van minder dan 1K tot wel 190K. Door middel van modelleren alleen kan dus niet vastgesteld worden of Io's mantel goed gemengd en homogeen is of dat de getijdenverhitting zorgt voor significante laterale variaties in de hoeveelheid smelt.

Telescoopobservaties op aarde met aangepaste optica (voortdurend sinds de jaren 2000) en op satelliet gebaseerde observaties door de Galileomissie (1995-2003) en JUNO (2016-2025) laten allemaal zien dat de vulkanen geconcentreerd zijn in gebieden rond de evenaar, met twee maxima ongeveer 30 graden ten oosten van het sub-Joviaanse punt en het anti-Joviaanse punt, respectievelijk. De afwezigheid van vulkanen in poolgebieden en de extreme warmteafgifte van Io zorgen er samen met een dikke korst voor dat de modellen een voorkeur hebben voor een warmtetransport dat voornamelijk magmatisch is en zich bevindt in een rheologisch gescheiden bovenmantel (de asthenosfeer). Voor de kenmerken in het binnenste laat het thermische model significante afwijkingen zien ten opzichte van een sferisch symmetrische rheologische structuur. Omdat analytische modellen alleen de patronen van getijdendissipatie voor een sferisch symmetrische rheologische structuur kunnen berekenen, ontwikkelen we een numeriek model dat gebaseerd is op eindige elementen, zodat we de heterogeniteit door getijden mee kunnen nemen in de berekening.

Resultaten van het eindig elementen model laten zien dat de verdeling van de gegenereerde getijdenwarmte verschillend is voor modellen met laterale variaties in de rheologische parameters in vergelijking tot een model waarin de parameters in de lagen homogeen verdeeld zijn. Regio's met gemiddeld een grotere hoeveelheid smelt laten een regionale toename zien in getijdenverhitting, en het omgekeerde geldt in regio's met een gemiddeld lagere hoeveelheid smelt. Daarnaast zorgt ook de ruimtelijke variatie van de vertraging in de visco-elastische respons van de asthenosfeer voor een asymmetrie in het patroon van getijdenverhitting, ten opzichte van de nulmeridiaan. Hierna onderzoeken we de feedback tussen eigenschappen binnenin Io en de getijdenverhitting: we gebruiken de resulterende verdeling van de gegenereerde getijdenwarmte om een nieuwe rheologische structuur af te leiden. Vervolgens gebruiken we deze nieuwe rheologische structuur om een nieuw dissipatiepatroon te berekenen met het eindig elementen model. Door deze twee stappen te herhalen vinden we dat de

asymmetrie toeneemt totdat er een evenwicht gevonden is tussen de smeltafhankelijke rheologische structuur en het patroon in de getijdenwarmte. De twee locaties met maximale getijdendissipatie liggen 15 graden ten oosten van de sub-Joviaanse en anti-Joviaanse punten. In tegenstelling tot vorige studies waarin de offset in de vulkanische activiteit op Io alleen kan worden uitgelegd door getijdendissipatie in een vloeibare magma oceaan, suggereert onze bevinding dat de offset ook verklaard kan worden door een feedbackmechanisme tussen niet-uniforme getijdenverhitting en de rheologische eigenschappen in de visco-elastische asthenosfeer van Io.

De geobserveerde vulkanische activiteit van Io kan ook worden gebruikt om processen van warmtetransport in het binnenste van de maan te onderzoeken. Hiervoor gebruiken we drie verschillende eigenschappen van het ruimtelijke patroon van Io's vulkanen: (i) de aanwezigheid van vulkanen op een wereldwijde schaal, waardoor we meer kunnen zeggen over de temperatuur in de mantel; (ii) de aanwezigheid van langgolelige variaties in de vulkanische activiteit op Io, waaruit we de kracht van het laterale warmtetransport kunnen afleiden; (iii) de gemiddelde afstand tussen twee naburige vulkanische systemen, waarmee de ruimtelijke kenmerken van het convectiepatroon in Io's mantel bepaald kunnen worden. Gebruikmakende van een op schaaufactoren gebaseerde analyse vinden we dat een deels convectief en deels magmatisch warmtetransport in de bovenmantel van Io zowel (i) het geobserveerde globale patroon als (ii) de langgolelige kenmerken van Io's vulkanische activiteit kan reproduceren. Indien (iii) de ruimtelijke dichtheid van Io's vulkanen bepaald wordt door de sub-lithosferische anomalieën veroorzaakt door convectieve stromen, vinden we dat 80% of meer van de interne hitte van Io getransporteerd wordt door magmatische processen en dat de bovenmantel van Io dikker moet zijn dan 50 km.

Het onderzoek in dit proefschrift zorgt voor een hogere mate van consistentie tussen de modellen voor Io door het binnenste te beschouwen als een gekoppeld systeem met meerdere met elkaar verbonden mechanismen. We kunnen laten zien dat het meenemen van mantelheterogeniteit, ontstaan door mantelconvectie en getijdenverhitting, leidt tot andere resultaten en conclusies. De grootste vooruitgang ten opzichte van eerder onderzoek is geboekt door de resultaten waarin 1) een combinatie van magmatisch en convectief warmtetransport in de mantel van Io de wereldwijde, langgolelige en kortgolelige eigenschappen van Io's vulkanen kan verklaren; en dat 2) het meenemen van variaties in de asthenosfeer, veroorzaakt door getijden, zorgt voor een offset in het patroon van getijdendissipatie. Deze bevindingen suggereren dat een visco-elastische asthenosfeer met een lage tot gemiddelde hoeveelheid smelt (maximaal 25%) samen met een combinatie van magmatisch en convectief warmtetransport een verklaring kan zijn voor de beschikbare observaties op Io, zoals de uitbarstingen op hoge temperaturen, de offsets in oostelijke richting van de pieken in de vulkanische activiteit en de Galileo-observaties van het geïnduceerde magneetveld op Io. Bovenop deze Io-gerelateerde verbeteringen kunnen de modellen die ontwikkeld zijn in dit proefschrift ook toegepast worden op aardse planeten die ver van ons af staan.

Om het binnenste van Io nog beter te begrijpen zouden de dissipatie en warmte-

transportmodellen ontwikkeld in dit proefschrift de interacties tussen vaste en vloeibare fases mee moeten nemen. Dit vergt een onderzoek van de mechanismen op een kleine tijd (maximaal 10 jaar tot enkele dagen) en ruimteschaal (1 kilometer tot 100 kilometers). De correlatie van anomalieën in een convectieve mantel met Io's vulkanen, zoals gesuggereerd in dit proefschrift, kan geverifieerd worden met behulp van 2D en 3D modellen die chemische aspecten meenemen. Deze regionale modellen kunnen vervolgens weer geverifieerd worden met de verschillende vormen van vulkanisme op Io, van zwakke evenementen tot krachtige uitbarstingen, zoals geobserveerd is door de Galileomissie. Verder kan het ruimtelijke patroon in het feedbackmechanisme tussen niet-uniforme getijdenverhitting en rheologische eigenschappen bestudeerd worden door meer parameters te beschouwen. Ondanks de vele mogelijkheden voor vernieuwingen in het model, zijn observaties van de getijdenvervorming, de libratieamplitude, de passieve radarsondewaarnemingen en het geïnduceerde magnetische veld vermoedelijk onmisbaar om te concluderen of een globale magma oceaan of een visco-elastische deels gesmolten asthenosfeer aanwezig is onder de korst. Als laatste kunnen de gesuggereerde mechanismes en gevonden parameterwaardes geverifieerd worden door een specifieke missie voor Io, waardoor we de leefbaarheid van gebieden en de voorwaarden voor het ontstaan van ijs- en aardachtige werelden in het zonnestelsel en daarbuiten nog beter kunnen evalueren.

# 1

## INTRODUCTION

The remarkable diversity of celestial bodies and fundamental physical processes in the Solar System is a major driver of planetary exploration and research. Jupiter's moon Io, with its bright yellowish surface, marks an outstanding example, representing a far end of this diversity spectrum. Io's specific characteristics show impressively how a fundamental and prevalent physical process, which is the transfer of mechanical energy into thermal energy, can shape the interior and surface characteristics of a celestial body.

The first discovery of Io along with the other three Galilean moons, Europa, Ganymede and Callisto, by Galileo Galilei, in 1610, marks the beginning of a new epoch. The discovery that other planets are surrounded by orbiting satellites contributed to the reversal of the idea of an Earth-centered universe and allowed a new perception of Earth as one world of many in the Universe. About 370 years later, the detection of active volcanoes on Io by Voyager I ([Morabito et al., 1979](#)), as predicted by Stanton J. Peale, Patrick Cassen and Ray T. Reynolds ([Peale et al., 1979](#)), delivered the proof of concept that energy stored in the movement of the celestial bodies can be transformed into internal energy and that this process can be so powerful to melt the interior and cause active volcanism at the surface. This additional heat source could potentially allow life to exist on worlds located far away from their host stars (e.g. [Dobos et al., 2017](#); [Jackson et al., 2008](#)) and therefore changed our view of habitable environments ([Huang, 1959](#)). Today, further observations of the Galileo mission (1995 - 2003) and more continuous telescope observations from Earth, have greatly advanced our understanding of Io as an active body. Io became an archetype of a tidally heated exo-world hosting extreme volcanism. In addition, the moon can provide insight in the history of Earth and our neighbouring planets. Io's effective, by magma driven, heat loss mechanisms are thought to have been crucial in the early evolutionary stages of Earth, the Moon, Venus, and Mars. However, the understanding of how tidal heating, melting, and heat transport interact is lacking. The aim of this thesis is to provide a better knowledge of Io's unique interior state and dynamics using interior modelling and observations of Io's volcanic activity. A better understanding of these dynamic processes would allow to improve

interior models of other celestial bodies, distant in space and time.

The aim of this first chapter is to introduce and motivate the research presented in the subsequent chapters of this thesis. The focus will be on Io's heating mechanism, Io's current volcanic activity, and Io's interior state. Section 1.1 will provide a brief introduction to Io, the starring character of the thesis. This is followed by introducing Io's surrounding environment, i.e. the Galilean satellite system, which provides the necessary conditions for Io's extensive volcanism (Section 1.2). Section 1.3 gives an overview of the past and ongoing remote observations of Io's volcanoes, which serve as the base for the interior modelling advances presented in this thesis. Section 1.4 reviews previous advances in modelling work of Io's interior state and dynamics, motivating the main research question of this thesis, which is introduced in Section 1.5. This main research motivation is split into various specific scientific questions, which are answered in Chapters 2, 3 and 4.

## 1.1. IO IN A NUTSHELL

Io is the innermost of the four Galilean satellites orbiting the planet Jupiter, but contrary to the other Galilean moons, Io's surface is rocky and has a bright yellowish appearance. Its size and mass (Table 1.1) are comparable to Earth's moon. However, in contrast to the Moon, Io is still geologically active. With hundreds of active volcanoes covering its surface, and eruptions more powerful than on Earth (e.g. *Davies et al., 2018*), Io is claimed to be the most active world in the Solar System. Io's eruptions are so large that they can be detected remotely from Earth, allowing for long-term observations of Io's activity (*de Pater et al., 2016; de Pater et al., 2017; Veeder et al., 1994*).

Io has been visited by the Voyager missions (1979) and the Galileo mission (1995-2002). These missions provided high resolution images of Io's surface and other observations, which can be used as constraints on Io's interior. Io's surface is covered by sulfur and sulfur dioxide frost (yellow and white appearance), black lava calderas, steep mountains and other colorful volcanic deposits (Figure 1.1). Observations of Io's gravity field reveal that the interior is differentiated into a core, mantle, and crust (*Anderson et al., 2001; Schubert et al., 1981; Sohl et al., 2002*). The state of Io's upper mantle is highly debated in the literature (Section 1.4.1). It has been suggested by models and observations that Io maintains a magma ocean beneath its solid crust, i.e. a completely or primarily fluid layer of molten rock (e.g. *Khurana et al., 2011; McEwen et al., 1998*). However, these observations are not conclusive. Other models and observations suggest a mainly solid mantle with a small melt fraction (e.g. *Moore, 2001; Roth et al., 2017; Spencer et al., 2020a*).

The source of heat that drives Io's volcanism and determines Io's interior state is strong tidal dissipation, also referred to as tidal heating (e.g. *Moore, 2003; Peale et al., 1979; Ross and Schubert, 1985; Schubert et al., 1981; Segatz et al., 1988*). Radiogenic heat, ohmic dissipation and accretional heating have been excluded as major contributions to Io's current thermal state (see *Schubert et al., 1981*, and references therein). Tidal dissipation is a mechanism that transforms kinetic energy into heat due to friction

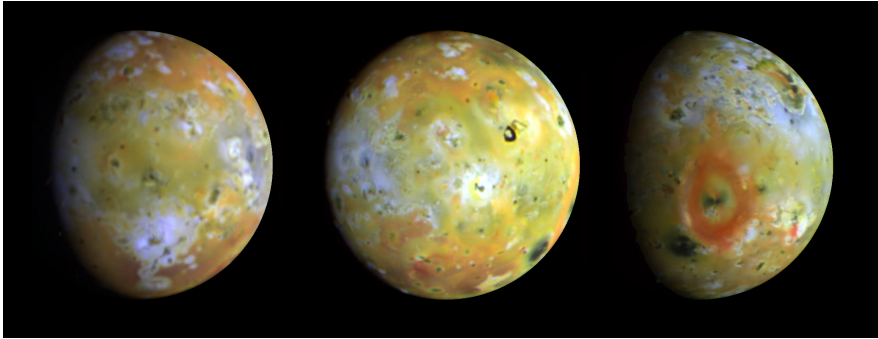


Figure 1.1: Three views of Io's surface as seen by the NASA's Galileo spacecraft camera. On the far left: Io's leading hemisphere with several bright areas. Central: Io's sub-Jovian hemisphere with Loki Patera (black spot in the northern hemisphere). On the far right: Trailing hemisphere with the volcano Pele (southern hemisphere). Red areas are associated with very recent volcanic plume deposits. Courtesy of NASA/JPL - PIA00292.

arising in the interior. This friction arises because the body is stretched and squeezed by a periodically changing gravitational pull of Jupiter caused by the comparatively high eccentricity of Io's orbit given the short orbital period of approximately 1.77 Earth days. As many other moons in the Solar System, Io is tidally locked. This means that, while Io orbits its host planet, the same hemisphere is always facing towards Jupiter. Tidal dissipation will play a key role in this thesis and is therefore explained in detail in Section 1.2.2.

Io possesses a thin atmosphere fed by sulphur dioxide and volcanic ejecta (*Kumar, 1980; Lellouch et al., 2007*). However, strong interactions of Io's primary atmosphere with ionized particles caught in Jupiter's magnetosphere lead to a constant loss of atoms and molecules into space (*Saur et al., 1999; Wilson et al., 2002*). The periodic collapses of Io's atmosphere, each time Io enters the shadow of Jupiter (*Tsang et al., 2016*), indicates that a part of Io's atmosphere is controlled by sublimation of  $\text{SO}_2$  frost given direct sun-light. It is very unlikely that Io hosts life. Given the low atmospheric pressure, water at the surface cannot exist. Furthermore, since Io's atmosphere and surface are depleted from any significant gaseous and fluid medium, heat, which is mainly focused at volcanoes, cannot be transported effectively. That way, temporally stable temperature conditions, important for life, cannot be found on Io's surface.

## 1.2. ORBITAL DYNAMICS OF THE JUPITER SYSTEM

With its four Galilean moons, Io, Europa, Ganymede, and Callisto (Figure 1.2), as well as many other smaller orbiting objects, the Jupiter system can be seen as a miniature planetary system. The evolution of this miniature planetary system is closely connected to Io's formation and evolution and current conditions. Io is the most dense of the four Galilean moons, and, in contrast to Europa, Ganymede, and Callisto, it lacks an icy cover. Europa is the smallest of the four satellites, it is covered by an icy shell and includes a

Table 1.1: Properties of Io taken from (1) Geophysical and geodetic parameters of Io taken from (1) *Anderson et al. (2001)*, (2) *Yoder (1979)*, and (3) *Lainey et al. (2009)*.

Parameter	Notation	Value	Unit
Mass <sup>(1)</sup>	$M_{Io}$	$8.9319 \cdot 10^{22}$	kg
Mean density <sup>(1)</sup>	$\rho_{Io}$	3527.8	$\text{kg m}^{-3}$
Mean radius <sup>(1)</sup>	$R_{Io}$	1821.6	km
Orbital radius	$a_{orbit}$	$421.6 \cdot 10^3$	km
Eccentricity <sup>(2)</sup>	$e_{orbit}$	0.0041	-
Orbital period	$P_{orbit}$	1.769138	days
Rotation period	$2\pi/\omega$	1.769138	days
Surface gravity	$g_{Io}$	1.796	$\text{m s}^{-2}$
Normalized moment of inertia <sup>(1)</sup>	$C_{Io}/(M_{Io}R_{Io}^2)$	0.37685	-
Internal energy dissipation <sup>(3)</sup>	$k_2/Q$	0.015	-

subsurface ocean. Ganymede is the largest in size, highly differentiated, and possesses a thick ice and water layer. Callisto is the outermost satellite, and compared to the other three moons, hardly differentiated. Orbital interactions between the Galilean satellites provide the conditions responsible for Io's current volcanic activity.

### 1.2.1. ORIGIN AND FORMATION OF THE GALILEAN SATELLITES

The four Galilean moons, Io, Europa, Ganymede, and Callisto are believed to not be captured objects, but to have formed within the circumplanetary disk that also formed Jupiter (*Canup and Ward, 2002; Lunine and Stevenson, 1982; Mosqueira et al., 2010*). With its orbit far out and its old inactive surface, Callisto has been argued to have accreted slower than the inner three Galilean satellites (*Oberg et al., 2020*). With increasing distance from Jupiter, the Galilean satellites show an increase in ice fraction and a decrease in their bulk density. Three processes have been suggested to explain this correlation:

1. Models by *Lunine and Stevenson (1982)* assume that the satellites accreted at different distances from the centre of the disk and that their current composition reflects the composition of the region of the disk in which the satellites formed. A decrease in temperature with increasing distance from the centre leads to a compositional gradient of the proto-Jovian disk. A central element of this hypothesis is the ice-stability line. In regions closer in, temperatures are too high to allow for the presence of ice. The presence of large amounts of ice and the fact that the satellitesimals did not fall into Jupiter suggest that the satellites must have been formed in a circumplanetary disk with a continuous inflow of gas and solids from the proto-planetary disk that formed the Solar System (*Canup and Ward, 2002*).
2. Due to high surface temperatures during accretion, the Galilean satellites likely were covered by a water envelope, a kind of proto-atmosphere. Powered by the accretion energy, parts of the water-envelope heated up, expanded, and escaped to space. It is suggested that this hydrodynamic escape occurred while the satellites were still accreting (*Bierson and Nimmo, 2020; Kuramoto and Matsui, 1994*).

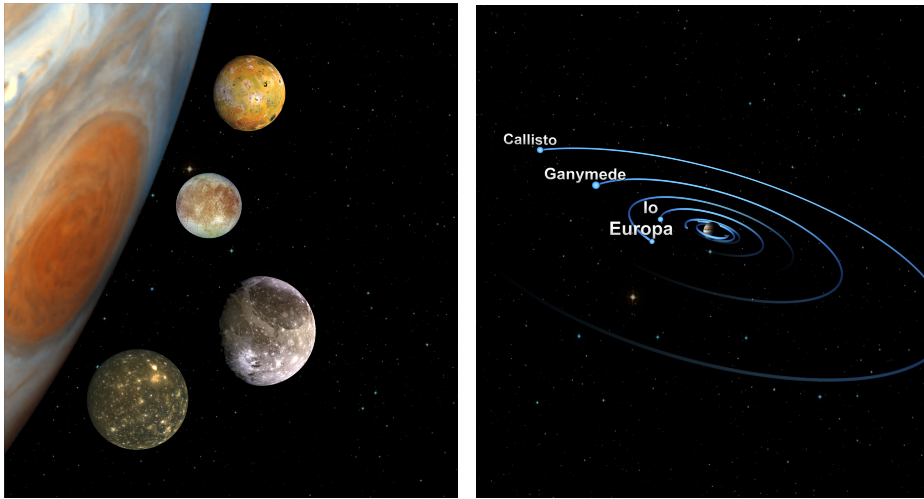


Figure 1.2: a) Family portrait shows a collage of Jupiter and its four Galilean satellites in scale. In the top, Io, and below the three icy moons, Europa, Ganymede and Callisto. Courtesy of NASA/JPL - Image PIA00600. b) Orbit of the four satellites around Jupiter in scale. Courtesy of NASA.

3. Tidal heating provides energy to heat up the interior once the accretion has been completed. In case Io was primordial ice-rich but remained in an orbital resonance over long time scales causing strong and continuous tidal heating, this tidal heating could have contributed to a loss of erupting material and volatiles (e.g. [Canup and Ward, 2009](#)). The conversion of tidal heat into water vapor and the loss of this vapor to space are only loosely constrained processes. Generous estimations of mass loss processes caused by tidal heating show that tidal dissipation alone would have not provided enough energy to explain the increasing ice fraction with increasing distance from Jupiter ([Bierston and Steinbrügge, 2021](#)).

Since these processes do not exclude each other, they could have all jointly contributed to the ice-depleted characteristics of Io. Furthermore, this supports the hypothesis that ice-free moons may also exist in other Solar Systems and that, given an extra Solar System perspective, the rocky surface of a moon around a gas giant is not a unique characteristic of Io. This motivates to further investigate the tidal dynamics of the Galilean System, further determining Io's tidally heated nature and volcanic activity.

### 1.2.2. TIDAL DYNAMICS

Tidal forces are differential forces across a body with extended mass distribution, which orbits an external mass. When a body orbits an external mass, at the centre of its mass the gravitational force and centrifugal force are in equilibrium. However, locations away from the centre of mass of the body experience differential forces (see [Murray and Dermott, 1999](#), as a review). Tide-raising potentials occur in both, the central body (primary body) and the orbiting body (secondary body) of smaller mass and can therefore be found in all bodies of the Solar System. The potentials increase proportionally with



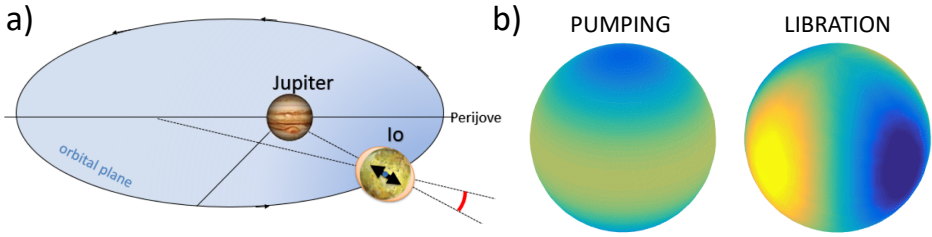


Figure 1.3: a) Orbital constellation in a two-body problem - b) The two types of periodic tidal potential patterns raised on Io: 1) The pumping tide is caused by the changing distance between primary and secondary object; 2) The libration tide, rotating around the body, is caused by differences between the rotation rate and the orbital rate due to Io's eccentric orbit.

distance from the centre of mass. Temporal changes arise due to the rotation of the body, deviations of its orbit from a perfectly circular orbit, and the gravitational effects of other external masses. The tidal potential does affect the solid body, and, if present, the oceans and the atmosphere.

In this section, only the orbital dynamics and tidal interactions in a two-body system are considered. As will become clear in Section 1.2.3 additional gravitational interactions in a multi-body system lead to changes in the tidal dynamics (see review in [Murray and Dermott, 1999](#)) and can have a crucial influence on the orbital and thermal state of the bodies, such as is the case for Io in the Galilean system ([Yoder and Peale, 1981](#)). Furthermore, we only focus on the tides raised in the secondary body, which is in this case Io, in synchronous rotation around its primary body, i.e. Jupiter (Figure 1.3a).

If we neglect any minor orbital deviations, such as the obliquity and inclination ([Bills, 2005](#)), physical librations ([Van Hoolst et al., 2013](#)) and tides raised by the other Galilean satellites ([Hay et al., 2020](#)), Io's tidal potential only contains spherical degree components of degree 2 and can be divided into a constant part and a periodic part (Equation 5 in [Van Hoolst et al., 2013](#)). For the Io-Jupiter system, the main contribution of the periodic tide-raising potential is due to the eccentricity of Io's orbit. The distance between satellite and planet and therefore the gravitational force vary periodically. This is the pumping tide (Figure 1.3b1). In addition, the meridian, facing Jupiter in Perijove, does not continuously face Jupiter throughout the orbit (Figure 1.3a). This is causing a libration tide, rotating around Io, while Io orbits Jupiter (Figure 1.3b2). The amplitudes of these variations are approximately ten times stronger than the amplitudes of the tidal potential on Earth raised by the Moon.

As Io is not completely rigid, the body responds to these differential forces by deformations of the interior and surface, which also affects the gravity field (see review on visco-elastic relaxation by [Sabadini et al., 2016](#)). In addition to the flattening due to Io's own rotation, the constant contribution of the tidal force leads to an additional flattening and elongation of Io's static shape. The periodic perturbation with a period of

Io's orbital period leads to periodic surface deformations, changes in the stress field, and changes in the gravity field. The non-rigid response of the interior is anelastic and not perfectly instantaneous. This causes two effects in the tidal response of a visco-elastic body ([Kaula, 1964](#)):

1. The visco-elastic response of the body lags behind the initial perturbing force. This means that the tidal bulge raised by the external mass does not exactly point towards the perturbing mass.
2. Kinetic energy is dissipated into heat. This process is called tidal dissipation. Hereby, mechanical energy stored in the motion and rotation of the planetary bodies is transferred into internal energy. Tidal dissipation is a fundamental process governing the dynamics of planetary systems, controlling the evolution of gaseous, rocky, and icy worlds.

Both effects are, in a non-trivial manner, related (see [Kaula, 1964](#); [Segatz et al., 1988](#)). The strength of the viscous response, its time delay, and how much and where in the body orbital energy is transferred into thermal energy, depend on the perturbing frequency, the spherical harmonic components of the tidal potential, and the eigenfrequencies of the body. The latter are a function of the body's size and stratification of rheologic properties, and the rheology model ([Sabadini et al., 2016](#)). The body's rheologic properties are the density, the viscosity, the Poisson ratio, and the shear modulus. The physical description between the body's rheologic properties, strain and arising stress is the rheology model. The Maxwell rheology is the simplest and most common rheology model for geophysical applications, which can be schematically represented by an elastic spring element and a viscous dashpot element in series. The distributions and values of the rheologic properties within Io's interior are approximated based on geodetic parameters and the knowledge of the rheological behavior of rocks on Earth. However, these rheologic properties remain the least constrained parameters quantifying the tidal response ([Segatz et al., 1988](#); [Spohn, 1997](#)).

Tidal dissipation in a planetary body also influences the orbital dynamics of a planetary system, since the kinetic energy of the system is removed. The torques caused by the phase lag decrease the rotation rate of both the primary and the secondary body. This tidal de-spinning leads eventually to a 1:1 spin-orbit resonance ([Murray and Dermott, 1999](#)), where the primary and secondary body are facing each other with the same side. If the mass of the secondary is significantly smaller, this state is reached quicker by the secondary than the primary, as for example in the Earth-Moon system and the Galilean system. Furthermore, in a two-body problem, dissipation dampens the eccentricity of the orbit. Both effects eventually decrease the amount of dissipated energy. Orbital resonances, however, can counteract this damping and lead to complex systems coupling the interior with the orbital dynamics ([Fischer and Spohn, 1990](#); [Greenberg, 1981](#); [Hussmann and Spohn, 2004](#); [Ojakangas and Stevenson, 1986](#); [Yoder and Peale, 1981](#)).

### 1.2.3. THE LAPLACE RESONANCE AND THERMAL ORBITAL COUPLING

A special characteristic of the Jupiter system is its orbital dynamics. Io, Europa and Ganymede are in an orbital resonance, a configuration known as the Laplace resonance

(*Murray and Dermott, 1999; Peale, 1976*). While Io orbits Jupiter twice, Europa orbits Jupiter once. In addition, Europa is in a 2:1 resonance with Ganymede, orbiting Jupiter twice, while Ganymede orbits Jupiter once. In a two body system (only considering Io and Jupiter) dissipation in Io would decrease the eccentricity of Io's orbit to almost zero (*Murray and Dermott, 1999; Yoder, 1979; Yoder and Peale, 1981*) and dissipation in Jupiter would continuously push Io outwards. In the Laplace resonance, however, Io's eccentricity is forced. The balance between dissipation in Jupiter, tidal dissipation in Io increased by the gravitational influence of Europa, and angular transfer between Io and Europa keep Io in a relatively stable orbital constellation and allows for consistently strong tidal dissipation in Io's interior that leads to Io's ongoing volcanic activity (*Peale et al., 1979; Yoder, 1979*)

Currently, it is unclear whether the Laplace resonance remains stable over billions of years, or whether the satellites periodically move in and out of the resonance, leading to periodically repeated strong tidal heating events. Dissipation in Jupiter's interior reduces the mean motion of Io, while dissipation in Io's interior acts to increase the mean motion while reducing the eccentricity of Io's orbit (*Murray and Dermott, 1999; Ojakangas and Stevenson, 1986*). The change of Io's dissipation rate with time and the dissipation rate and mechanism of Jupiter are highly uncertain, however important in order to predict the evolution of the Laplace resonance. The tidal dissipation rate, i.e. the amount of kinetic energy that is transferred to heat per orbit, couples the orbital evolution of the system to the thermal evolution of the bodies. A complex coupled process evolves, which is referred to as thermal-orbital-evolution. In case more tidal heat is produced than can be transported to the surface, oscillations around the Laplace resonance (*Fischer and Spohn, 1990; Greenberg, 1981; Hussmann and Spohn, 2004; Ojakangas and Stevenson, 1986*) are introduced. For a thorough review on coupled thermal and orbital evolution models see *Spohn (1997)*. Recent models by *Rovira-Navarro et al. (2021)*, which use an advanced rheology model and include magmatic heat transport processes, show that an equilibrium between tidal heating and heat transport can exist. In this case, orbital oscillations driven by Io's thermal inertia, do not exist. Although the good agreement between Io's current heat output constrained by Earth-based observations (*Veeder et al., 1994*) and the observed rate of change of Io's mean motion (*Lainey et al., 2009*) are consistent with the assumption that Io is in thermal equilibrium, it does not necessarily prove this assumption: First, in case complex orbital oscillations are present, the rate of change of Io's mean motion does not necessarily allow for a derivation of Io's current dissipation rate and secondly, even small deviations between dissipation rate and heat loss rate could sum up. Observations of Io's active volcanoes are only available for a bit more than 40 years and also the analysis of Io's young geologic surface features only allows for a look back in time of a maximum of  $10^5$  years (*McEwen et al., 2004*). This is much shorter than the periods of a few million years to one billion years, commonly suggested for thermal-orbital oscillations (*Fischer and Spohn, 1990; Hussmann and Spohn, 2004; Yoder and Peale, 1981*). Therefore it will be challenging to distinguish between the different evolution models. However, a detailed knowledge about Io's interior structure would allow to set stronger constraints on Io's long-term interior evolution and orbital evolution.

### 1.3. IO'S VOLCANISM

Due to a lack of observation, the characteristics of Io remained unknown until the late 20<sup>th</sup> century. Just as the Earth's moon, which is similar in size, Io was expected to be covered by ancient craters. However, images by Voyager I revealed that Io is covered by a young volcanic terrain instead. In addition, active volcanic plumes were discovered by the Voyager I and Voyager II spacecrafts (*Morabito et al., 1979; Smith et al., 1979b*). Measuring Io's intrinsic luminosity with infrared radiometry over a course of ten years (*Veeder et al., 1994*) determined Io's heat flow to be  $2.5 \text{ W m}^{-2}$ . More detailed observations, taken by the Galileo mission between 1995 and 2002 proved that Io is the most volcanically active body of our Solar System, and the only place in the outer Solar System where active silicate volcanism can be observed. An extensive review of these observations and the findings can be found in *Davies (2007)* and *Lopes and Williams (2005)*. Plume deposits, paterae (caldera-like depressions), lava fields, and lava bands define Io's surface appearance. Detected eruption styles include explosive powerful events (*Davies et al., 2018*), steady but less powerful hotspots (*de Kleer and de Pater, 2016*), overturning lava lakes (*de Kleer et al., 2017*), channelized flows (*McEwen et al., 2000*), and transient volcanic activity (*de Kleer et al., 2019; Roth et al., 2020*). Monitoring Io's volcanos with high resolution cameras and telescope arrays over long time spans is motivated by three research objectives: 1) The continuous and powerful manner of Io's volcanism provides possibilities to learn about the former and present volcanism on Earth and other planets and well as related near-surface processes; 2) monitoring Io's activity and the correlated atmospheric interaction with Jupiter's magnetic field allows to draw conclusions about mass loss events, Io's atmosphere, and Jupiter's harsh environment; 3) treating Io's volcanoes as an observable feature and symptom of the vigorous magma-driven dynamics in the moon's interior, the volcanoes provide insights into Io's interior state. The characteristics of Io's volcanic activity resulting from satellite and Earth-based observations will be presented here. With focus on objective 3) special attention is given here to the spatial distribution of the volcanic activity pattern, the eruption temperatures and the derivation of eruption styles and magma compositions. A thorough discussion of implications of these characteristics on Io's interior state and dynamics will follow in Section 1.4.4.

#### 1.3.1. REMOTE SENSING OF IO'S VOLCANIC ACTIVITY

Volcanic activity and volcanic features can be observed remotely. In particular spectroscopy from millimeter wavelengths to the far-infrared. Remote sensing at infrared wavelengths is a very valuable method to quantify the thermal emission of Io's volcanoes. The temperature of a volcanic event can be derived by fitting combinations of multi-spectral observations of one eruption event to the Planck curve for black body radiation (*Davies, 2007*). To achieve accurate temperature estimates, it is advantageous to observe at wavelengths close to peaks in the Planck curve. For high-temperatures lava this is between  $1.5 \mu\text{m}$  and  $2 \mu\text{m}$ . Observations in the visual wavelengths ( $0.38\text{-}0.75 \mu\text{m}$ ) provide a higher spatial resolution, which enables the analysis of geologic features on Io's surface, such as surface changes between images taken on different Io flybys. These type of analyses allow for approximations of the amount of the erupted material and, to some extent, the determination of the surface composition. Complementary to spectroscopy in the infrared and visual wavelengths, observations in the millimeter wavelengths allow

for the detection of gases in Io's atmosphere that can be attributed to volcanic activity (*de Pater et al., 2020*).

#### SATELLITE-BASED OBSERVATIONS

Flybys by Voyager I and II (1979-1980) (*Morabito et al., 1979; Smith et al., 1979b*), and the Galileo mission (1995 - 2002) (*Davies, 2001, 2007; Lopes and Williams, 2005*) provided high-resolution data at visible, near- and far- infrared wavelengths. These observations allowed for the first detection of surface changes due to eruptions (*Geissler et al., 2004*). The Galileo mission, dedicated to observe the Galilean satellites, carried multiple imaging sensors. The two thermal imaging sensors, the Near Infrared Mapping Spectrometer (NIMS) operating at frequencies between  $0.7\mu\text{m}$  and  $5.2\mu\text{m}$  and a spatial resolution up to  $0.5\text{ km/pixel}$  (*Carlson et al., 1992*) and the Photo-Polarimeter Radiometer (PPR) (*Russell et al., 1992*) for low temperature regions, mapped Io's thermal emission. In addition to the thermal imaging sensors, the Solid State Imaging experiment (SSI) measured the spectral surface properties in the visual wavelengths (*McEwen et al., 1998*). Also other missions not dedicated to observe Io's volcanism, such as JUNO and New Horizon, provided additional observations of Io's (*Mura et al., 2019; Tsang et al., 2014*). To this date, no dedicated Io mission has flown.

#### EARTH-BASED OBSERVATIONS

Ground-based telescope observations and observations from Earth's orbit provide an additional way to observe Io's volcanic activity. In contrast to the snapshots in time provided by satellites, Earth-based telescope observations provide a more continuous possibility to monitor Io's volcanoes. Since the detection of eruption stages and the decay of the thermal signal of events are important parameters to define the eruption style (*Davies, 2007*), the characterisation of Io's volcanic activity requires daily to weekly observations. Technical improvements, such as large optical interferometers and adaptive optics techniques, provide resolution of up to  $30\text{ km}$ . Telescopes on Earth, such as Keck 2 (since 2001) and Gemini North (since 2013), allow for multi-wavelength observations using different filters (*de Kleer and de Pater, 2016; de Pater et al., 2014, 2016*). Large arrays such as the Atacama large (sub)millimeter array (ALMA) provide valuable millimeter-wavelengths measurements, valuable to characterise atmospheric gases such as  $\text{SO}_2$ ,  $\text{SO}$  and  $\text{KCl}$ , and Io's (sub-)surface properties (*de Pater et al., 2020*).

### 1.3.2. SPATIAL AND TEMPORAL CHARACTERISTICS OF VOLCANIC ACTIVITY

The characteristic manner of how volcanoes on planetary objects are distributed can give valuable insights into the interior of the body. On Earth, most of the volcanoes can be found at the plate boundaries. On Io, the volcanic distribution may hint on regional variations or upwelling patterns in the mantle. Using large-scale variations of the volcanic density and the statistical spreading behaviour between neighbouring volcanoes to constrain Io's interior marks a central part of this thesis. Io's active volcanoes and geological volcanic features detected by satellite-based, Earth-ground-based, and Earth-orbit-based observations are presented in Figure 1.4. Io's most active regions can be found at mid-latitudes,  $30^\circ$  eastward of the sub-Jovian and anti-Jovian points (*Cantrall et al., 2018; Davies et al., 2015; de Kleer and de Pater, 2016; Hamilton et al.,*

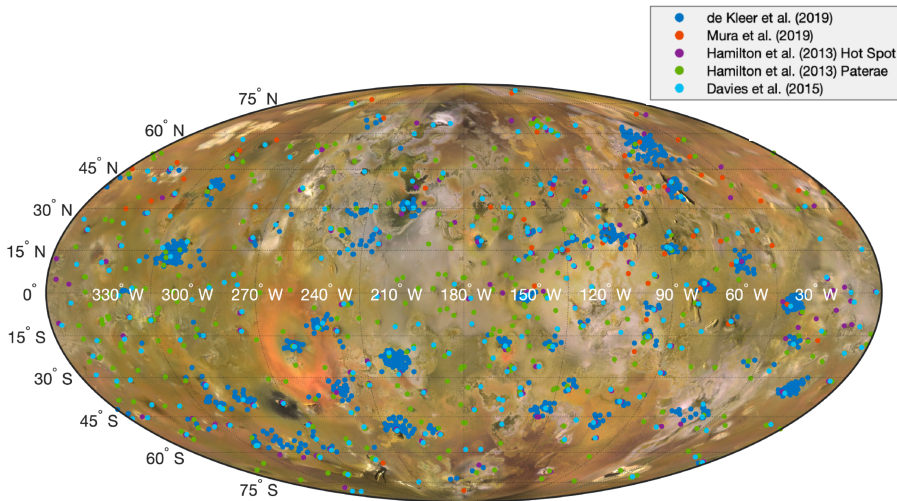


Figure 1.4: 1982 volcanic centers and events together with mosaic of Io's surface (*Williams et al., 2011a*). Data set includes satellite-based, Earth-ground-based and Earth-orbit-based observation from *Davies et al. (2015)*, *Hamilton et al. (2013)*, *Mura et al. (2019)*, *de Kleer et al. (2019)*. Multiple detections of the same volcanic centre were not removed. Graph generated by Duncun van Sliedregt (*van Sliedregt, 2020*).

2013; *Kirchoff et al., 2011*). This can be seen in both the spatial density of the volcanoes as well as in their intensities as shown in *Davies et al. (2015)*. On global scales volcanoes and mountains are anti-correlated *Kirchoff et al. (2011)*. However, many mountains can be associated to Io's caldera-like structures on local scales of a few kilometres (*McEwen et al., 2000*). Analysing the spreading characteristics of Io's volcanoes using a nearest-neighbour analysis shows that Io's hot-spots are evenly and not randomly spread (*Hamilton et al., 2013*), meaning that the mean distance between two volcanoes is statistically larger than for a random distribution.

About half of Io's total thermal emission can be associated to volcanic activity (*Veeder et al., 2015*). The most powerful persistent active volcano is Loki Patera. Recently, its contribution to Io's total thermal emission has been approximated to be 9% (*Veeder et al., 2012*). Loki Patera has been active for many decades and shows a periodicity in its eruption frequency (*de Kleer et al., 2019a; de Pater et al., 2017*). It remains an open question how Loki Patera retains this activity.

How these observed characteristics on various spatial and temporal scales can be used in combination with geodynamic models to get insight into the interior and challenges related to this approach are discussed in Section 1.4.4.

### 1.3.3. ERUPTION STYLES, TEMPERATURES AND MAGMA COMPOSITION

Erupted lava contains a lot of useful information about Io's interior state such as the extent of the differentiation of the mantle and ongoing recycling processes. It therefore

provides a valuable input for geodynamic models. Correlations between four characteristics, known from remote sensing on Earth, enables conclusions on the erupted lava despite incomplete spectral signatures (e.g. [Davies, 1996](#); [Davies et al., 2001](#)). Following [Davies et al. \(2010\)](#) and [Keszthelyi et al. \(2007\)](#), the four parameters are 1) the magma composition; 2) the eruption temperature; 3) the magma viscosity; and 4) the eruption style. Given a similar rocky composition known from terrestrial planets, magma low in silica and high in Ca, Fe, and Mg correlates with a high eruption temperature, a low viscosity, and an effusive eruption style. In contrast, magma with a high silica content correlates with low temperatures and a high viscosity. The reason for this is the difference in the liquidus temperature. On top of this relation, volatiles, which dissolve in silicate melts under sufficient pressure and reduce the bulk density of the magma, play a major role in determining the eruption style. On Io, S and SO<sub>2</sub> are the dominating volatiles and the driving forces of Io's explosive volcanic activity (e.g. [Smith et al., 1979a](#)).

The high eruption temperatures (> 1473 K) measured by the Galileo mission for roughly a dozen events suggest that the most powerful Io eruptions are driven by ultramafic magma (low in silicate, high in Ca Fe Mg) ([Keszthelyi et al., 2007](#); [McEwen et al., 1998](#)). This would indicate a deep origin of the magma, i.e. the deep mantle, or an upper mantle with low differentiation and an effective recycling between crust and upper mantle. However, as only the temperature and not the composition of the lava can be determined, these extreme temperatures could also indicate that Io's mantle has a high degree of melting or that intense viscous heating happens during the magma ascent ([Keszthelyi et al., 2007](#)). In addition to the detection of these extreme temperatures, also low and medium temperature eruptions and transient volcanoes have been detected ([Davies, 2007](#); [Veeder et al., 2012](#)). Part of the silicate magma does not rise directly from the mantle to the surface, but forms intrusions in the crust. In case this magma intersects with sulphurous material, subsequently buried by eruptions, the melting temperature of the material is reduced allowing for powerful eruptions ([Leone et al., 2011](#)). It remains unknown whether the diversity in Io's volcanoes is caused by a diversity of shallow crustal processes or anomalies in the mantle. How these observations and the remaining unknowns influence the advances in modelling Io's interior is further discussed in Section [1.4.4](#).

## 1.4. IO'S INTERIOR

To unravel Io's interior it is important to obtain a consistent description that is in agreement with all available observations as well as various chemical and physical laws dictating the heat transport, heat production, and phase state. Besides the observation of Io's volcanoes discussed in the previous section, geophysical and geodetic observations as well as the application of physical and chemical principles provide constraints on the interior. Here Io's global interior structure is discussed based on various observations. This is followed by presenting the physical principles of the most dominant drivers of Io's interior dynamics: 1) tidal heat production and 2) heat loss. Provided the aim of this thesis, special focus is given to discuss and evaluate current research using various scales of Io's volcanic activity to learn more about the physics of tidal heating and heat loss, and how both processes are coupled with each other.

### 1.4.1. INTERIOR STRUCTURE, PHYSICAL STATE AND COMPOSITION

Besides the observation of Io's volcanoes, geodetic observations such as the gravity field, the magnetic field, and the determination of the moon's long-wavelength shape and topography allow valuable conclusions on Io's interior.

While a spacecraft flies by Io, gravitational deflections, which lead to a subtle change in the trajectory of the spacecraft, can be measured from Earth and allow to constrain Io's gravity field. The values obtained for Io's gravity field (*Anderson et al., 2001*) and the topography from limb observation (*Thomas et al., 1998*) are consistent with Io being in hydrostatic equilibrium. Under the assumption that Io's static gravitation field represents the satellite's tidal and rotational equilibrium, Io's radial density distribution can be derived. These gravity observations indicate that Io is a differentiated body, which possesses an iron-core, a mantle, and a silicate crust (Figure 1.5). Based on these geodetic constraints and complemented with observations of the magnetic field and knowledge derived from Earth's interior the following conclusions on Io's global structure, physical state and composition can be made. Special focus is placed on Io's mantle layer. It is the layer where the bulk of tidal heat production takes place, and therefore the layer that determines Io's interior dynamics, surface processes, exosphere and the orbital dynamics of the Galilean system.

#### CORE

The size and mass fraction of the core depend on the core composition. Possible radii and mass fractions range from 650–950 km and 10–20%, respectively (*Sohl et al., 2002*). It is commonly argued that Io's core is molten (*Schubert et al., 2004; Spohn, 1997; Wienbruch and Spohn, 1995*). *Wienbruch and Spohn (1995)* find that a dynamo action in Io's core is unlikely, unless strong orbital oscillations causing variations in the tidal heating rate are present.

#### MANTLE

Io has a silicate mantle. The thermal state of the mantle, its sub-layer structure, and the amount and distribution of melt in this layer are of great importance to understand the dynamics of Io's volcanic systems and Io's tidal heating mechanism. However, in particular, the state of the mantle layer is highly debated (Section 1.4.1). The outstanding question is whether Io's mantle is mostly fluid or mostly solid, and how both states are interconnected.

Five types of mantle structures are presented in Figure 1.5 and further described below; two models based on a visco-elastic, mainly solid mantle; one model comprises the transition between solid mantle and magma ocean; and two types of magma ocean models. The models are sorted according to the amount of molten material in the mantle. Note that the transition between these five models should be considered as smooth.

**Homogeneous mantle:** Io's mantle is one homogeneous, visco-elastic layer, which is mostly solid with zero to very low melt fraction. This model has first been suggested by *Segatz et al. (1988)* and is motivated by the mantle composition and structure of other



terrestrial bodies. Given this interior structure, tidal heat is produced at the core-mantle boundary and transported upwards by solid state convection and magmatic advection. A non-uniform dissipation pattern in the mantle arises, with maxima at the poles.

**Asthenosphere:** Io's mantle has two layers: 1) a visco-elastic low-viscosity upper layer with a low melt fraction, and 2) a deeper mantle with even less or no melt. The upper layer is referred to as asthenosphere. For this model it is assumed that the fluid pores in the partially molten asthenosphere are not connected and the layer still has a resistance to shear forces (non-zero shear modulus). This model was first proposed by [Segatz et al. \(1988\)](#). Active downwellings in a internal heated convective asthenosphere (e.g. [Parmentier and Sotin, 2000](#)) could provide sufficient mixing and crustal recycling, required to explain Io's ultramafic lava composition ([McEwen et al., 1998](#)). Tidal heat production is mostly focused in the asthenosphere and transported upwards by magmatic advection. A non-uniform dissipation pattern in the asthenosphere evolves, with maxima at the sub-Jovian and anti-Jovian points.

**Mantle with decompaction layers:** Models coupling magmatic segregation, compaction and heat piping by [Spencer et al. \(2020a\)](#) show that a thin high-melt-fraction region between mantle and crust may arise as a consequence of lateral compression hindering magma to migrate upwards. These thin layers could explain magnetic field measurements of the Galileo spacecraft that suggest high-melt-fraction region ([Khurana et al., 2011](#)), without requiring a global magma ocean.

**Mushy magma ocean:** The upper part of the mantle is partially molten such that interconnected melt pockets arise, similar to a sponge. Below the mushy magma ocean the melt fraction decreases due to increasing pressure. In contrast to the visco-elastic dissipation models ([Bierson and Nimmo, 2016](#); [Segatz et al., 1988](#)), the dynamics of a fluid, such as inertia and rotational effects ([Tyler, 2009](#); [Tyler et al., 2015](#)), are included. The evolving dissipation pattern is focused at the equator and mid latitudes. It is not certain whether an eastward offset with respect to the sub-Jovian and anti-Jovian points, as for a fluid magma ocean ([Tyler et al., 2015](#)) is present. However, the fluid mobility of the mushy magma ocean likely vanishes the lateral differences in the heating. This model was first suggested by [Ross and Schubert \(1985\)](#) and was further supported by Galileo magnetic field measurements ([Khurana et al., 2011](#)) and the high eruption temperatures (> 1800 K). These high eruption temperature, indicating high mantle temperatures ([Davies et al., 2001](#)) and ultramafic (magnesium-rich) lava, are difficult to be explained by a differentiated mostly solid mantle. Vigorous convection of the mushy medium, however, would lead to a sufficient mixing and recycling of the crust ([Keszthelyi et al., 1999](#)). However, other observations and theoretical models contradict with the magma ocean hypothesis and suggest a mostly solid mantle: The analysis of Io's aurora shows that observed auroral oscillations are inconsistent with magma ocean models ([Roth et al., 2017](#)). Re-analysing Galileo magnetometer data, [Blöcker et al. \(2018\)](#) suggest that plasma interactions with an asymmetric atmosphere could cause the induction-like signal in the magnetometer measurements. Also, the high eruption temperatures observed by Galileo, supporting the magma ocean hypothesis, have been

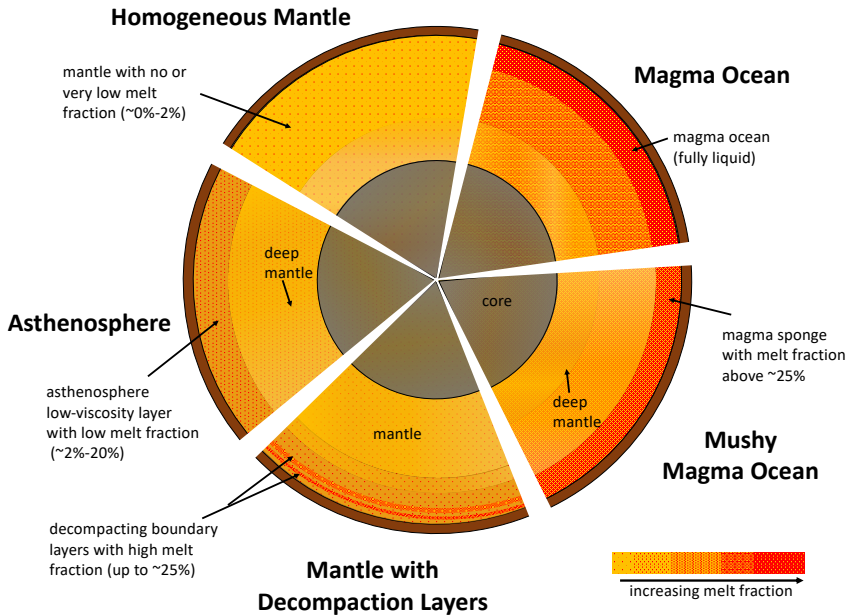


Figure 1.5: The five suggested mantle structures.

corrected downwards (*Keszthelyi and McEwen, 1997*). The corrected temperatures remain high, but uncertainties in the composition allow for both a magma ocean or a mantle with some amount of melt.

**Fluid magma ocean:** The upper mantle is fully molten. The remaining solid material is disconnected and fully supported by fluid magma. Heat is transported by turbulent convection in the magma ocean. This model is motivated by the same observations as the mushy magma ocean. Note, however, that several studies rejected a fully molten magma ocean, as it would lose heat rapidly (*Ojakangas and Stevenson, 1986*). The dissipation pattern is asymmetric with respect to the sub-Jovian and anti-Jovian meridians (*Tyler et al., 2015*). The vigorous liquid-state convection likely vanishes any laterally non-uniform tidal heating pattern, such that the locations of volcanoes are controlled by lithospheric weaknesses, which permit the advection of melt.

#### CRUST/LITHOSPHERE

Io's mantle is covered by an elastic outer layer composed primarily of a thick stack of solidified silicate lava. On Earth we distinguish between the crust, as a chemically distinct layer from the mantle, and the lithosphere, as a rheological distinct layer from the easily deformable asthenosphere. As a consequence of this the Earth's crust comprises the upper part of the lithosphere. Given the large uncertainties in the extent of differentiation and crustal recycling in Io's mantle, the differences between the depths of the lithosphere-asthenosphere boundary and the crust-mantle boundary are uncertain and

are therefore commonly, apart from their physical definition, treated as identical for Io. Values for the lithospheric thickness can be approximated. A strong lithosphere is required to support the observed large mountains of more than 10 km (*Carr et al., 1979*). *Carr et al. (1998)* suggest a lower limit of 30 km. Heat pipes transport the bulk of Io's heat flux through Io's conductive crust to the surface (*O'Reilly and Davies, 1981*). Magmatic intrusions, which do not make it to the surface, play an important role in the thermal heat budget of Io's lithosphere (*Spencer et al., 2020a*). Io's surface is constantly resurfaced. Estimates range from 0.02 cm per year to 14 cm per year (*Phillips et al., 2000*). The continuously buried and downward transported material causes thermal stresses in the crust, which could explain Io's large and steep volcanoes (*Kirchoff and McKinnon, 2009; Kirchoff et al., 2020*).

#### 1.4.2. TIDAL HEAT PRODUCTION

With hardly any observational clues, *Peale et al. (1979)* predicted that Io possesses active volcanism that is driven by an internal heating process referred to as tidal heating. While the theoretical existence of tidal friction was known before, the power of this mechanism and its importance for Io had not been anticipated before. This publication marks a prime example where theoretical considerations led to the correct prediction of an observation. Voyager I, approaching Io just after this paper was published, detected eight active volcanic eruptions in only one flyby (*Soderblom, 1980*). Io delivered the proof that tidal dissipation can be a driving mechanism for the interior structure and evolution of planetary bodies.

Friction is an irreversible process by which kinetic energy is converted into heat. It is the sum of microscopic events, i.e. irreversible interactions on atomic scales, given a distortion of the body. Frictional mechanisms are diverse and depend on the characteristics of the distorted medium, such as its physical state, grain size, melt fraction, properties between boundaries, and the frequency of the perturbing force. Friction can be found within visco-elastic materials, between solid-solid, solid-fluid or fluid-fluid boundaries (e.g., *Karato, 2008; Liao et al., 2020; Nosonovsky, 2007; Sagan and Dermott, 1982; Tabor, 1992; Tyler, 2009*).

We speak of tidal dissipation or tidal heating when this friction is a consequence of the periodic tidal distortion of a planetary body described in Section 1.2.2. In a macroscopic view, tidal dissipation shows in the temporal response behaviour of planetary bodies. A visco-elastic body responds to the tidal potential with a time delay. This delay depends on the amount of tidal dissipation. Observing the response of a planetary body from the outside it cannot be seen where and how individual frictional processes happen within the body. The distribution of tidal dissipation within the body is not homogeneous and depends on the rheological structure and the frictional properties of the layers and layer boundaries

Tidal heating is an important heat source for many moons of the outer Solar System. In the case of Io, the heating due to tidal dissipation (approximately  $10^{14}$ W) is three orders of magnitude higher than the heat generated by the current decay of radioac-

tive elements (approximately  $10^{11}$ W) (*Bierson and Steinbrügge, 2021*). What kind of frictional mechanisms are dominating in Io's interior is strongly linked to Io's unknown interior state, discussed in Section 1.4.1. In particular, the unknown state of Io's mantle, ranging from a homogeneous solid mantle to a fluid magma ocean, makes conclusions on the dominating tidal dissipation process impossible. This dilemma marks one of the main motivations of this thesis. The two main dissipation mechanisms suggested for Io, their relation to the mantle models in Section 1.4.1, and their implications on the spatial distribution of tidal heat production in Io's interior are discussed below. A discussion on what Io's volcanic distribution can tell us about the ongoing tidal heating processes can be found in Section 1.4.4.

#### DISSIPATION WITHIN A VISCO-ELASTIC SOLID LAYER

Dissipation within a visco-elastic solid material occurs due to irreversible failures in the rock matrix. Rheology models (Section 1.2.2), which link deformation and stress, build the basis to calculate the amount and distribution of tidal dissipation. The same interior parameters and rheology models as for the calculation of tidal deformations, introduced in Section 1.2.2, are required. Spherically symmetric visco-elastic models, originally developed to calculate the large-scale deformation of the Earth (*Sabadini et al., 2016*), have been further developed to be suitable to compute the amount and distribution of Io's tidal dissipation (*Bierson and Nimmo, 2016; Fischer and Spohn, 1990; Hussmann and Spohn, 2004; Renaud and Henning, 2018; Ross and Schubert, 1986; Ross et al., 1990; Segatz et al., 1988*). Linear rheology models for geophysical applications, such as the commonly used Maxwell rheology for an incompressible material, assume that the tidal dissipation is proportional to the squared stress field (*Beuthe, 2013; Hanyk et al., 2005*). However, it has been shown by laboratory experiments that the visco-elastic behaviour of rock samples at typical tidal frequency does not follow the Maxwell rheology (*Castillo-Rogez et al., 2011; Jackson, 1993*). That is why more elaborate rheology models, such as the Burgers model or the Andrade model have been proposed. These models incorporate a transient time dependent creep behaviour leading to a more realistic frequency-dependent response of the material (*Castillo-Rogez et al., 2011; Efroimsky, 2012*). Applications to Io show that higher viscosities than for the Maxwell rheology model can be used to satisfy Io's expected amount of tidal dissipation (*Bierson and Nimmo, 2016; Renaud and Henning, 2018*). The spatial distribution of tidal dissipation is, however, not expected to change (*Beuthe, 2013*).

In the asthenosphere model (Figure 1.5) the bulk of Io's tidally generated heat is produced in the low-viscosity layer beneath Io's elastic crust (*Segatz et al., 1988*). We refer to this as asthenosphere heating. The low resistance of this layer, compared to the lithosphere and lower mantle, leads to strong lateral deformations in the centre of the asthenosphere throughout the orbit. The arising shear stresses cause dissipation. In case Io's mantle is homogeneous, tidal dissipation is located at the core-mantle boundary (e.g. *Beuthe, 2013; Segatz et al., 1988*). We refer to this as mantle heating. How the total amount of Io's tidal dissipation is partitioned between these two layers depends on the rheologic properties of the layers and is not known. Both models, however, have a different longitudinal and latitudinal distribution pattern of the heat (*Beuthe, 2013; Hamilton et al., 2013; Segatz et al., 1988*): In the homogeneous mantle

the heat production is focused at the poles. In case Io possesses an asthenosphere, the heat production is focused at the equatorial regions. Depending on the heat loss mechanisms the heating pattern could remain visible at the surface, in terms of Io's variation of heat output through volcanic eruptions and transient background heat output, as described in Section 1.4.4.

#### DISSIPATION WITHIN A FLUID LAYER

While tidal dissipation within a solid interior is recognized as a crucial mechanism for Io, tidal dissipation within a potential magma ocean has been resuggested only recently (Tyler *et al.*, 2015). For this mechanism to be applicable to Io, melt pockets need to be interconnected, such that melt can form a continuous fluid, i.e. a global magma ocean. In a fluid medium, dissipation occurs when the momentum of internal waves is damped through turbulence and solid-fluid interactions, i.e. bottom drag or laminar flow of magma through a permeable medium. In such two-phase regimes, where both solid and liquid phases are present and interconnect, either just as a solid-fluid boundary on top and at the bottom of an ocean or as a porous medium, the viscous dissipation depends on the viscosity of the fluid, the velocity of the tidally directed flow, and the boundary layer friction. The fact that the degree of melting in Io's asthenosphere is not constrained and also the phenomenological friction parameter is only loosely constrained parameter, makes an accurate approximation of the amount of dissipated heat in the ocean impossible. Resonances lead to a strong increase in tidal dissipation for certain frequencies. Their location depends on the ocean thicknesses and viscosity of the ocean. This characteristic also allows for significant fluid tides in Io excited by Europa's gravitational forcing (Hay *et al.*, 2020). The effect of lateral variations and the coupling between visco-elastic deformations and fluid flow through pores in a highly porous medium has only received quantitative treatment for Enceladus (Liao *et al.*, 2020), but not for Io. The potential impact of modelling advances in this direction are discussed as future research in Chapter 5.

Tidal dissipation in a global magma ocean of Io produces a significantly different tidal dissipation pattern than tidal dissipation in a solid medium discussed before (Tyler *et al.*, 2015). The major additional effect is an eastward longitudinal offset of the maxima at the sub-Jovian, and anti-Jovian points. This offset is also present in the observed volcanic intensity and density patterns (Hamilton *et al.*, 2013; Kirchoff *et al.*, 2011), and could therefore be considered as the favoured spherical symmetric end-member model. However, due to the strong fluid motion, the magma ocean would be well-mixed and the presence of a detectable surface pattern remaining from the heating pattern is unlikely.

#### 1.4.3. HEAT LOSS MECHANISMS

Io's approximated surface heat flow of  $2.3 \text{ Wm}^{-1}$  (Veeder *et al.*, 1994, 2012) is more than 100 times larger than the heat flux of Earth's moon (Langseth *et al.*, 1976) and therefore requires an effective heat loss mechanism. It remains an open question whether the observed surface heat flux is in balance with the produced tidal heating generated in Io's mantle. On the macroscopic scale, three main internal heat loss mechanisms are suggested to be present in Io's interior: Conduction, convection, and advection of melt

through a solid matrix. These mechanisms are introduced below. These processes exist simultaneously but the contribution of each mechanism to the total heat transport varies in each layer and is loosely constrained. The knowledge of the strength of each heat loss mechanism is key to determine Io's internal dynamics.

#### CONDUCTION

Conduction is a fundamental process of heat transfer. In an atomic view, conduction in a solid is the transfer of kinetic energy between molecules and atoms, without transport of material (e.g. *Turcotte and Schubert, 2002*). The ability of the material to transfer heat in this way is controlled by the thermal conductivity. Conduction is most prominent in the lithosphere of planetary bodies. Conduction is very inefficient, compared to the heat transport processes introduced below. Given the heat flux of Io a purely conductive body can neither explain Io's deep interior state, nor Io's thick crust (*O'Reilly and Davies, 1981*). Therefore other heat transport mechanisms invoking the transport of material are required to explain Io's interior state.

#### CONVECTION

Convection is the transfer of heat due to the movement of material. It is driven by small density variations in a gravity field. These variations arise from thermal or chemical heterogeneities. Solid-state convection is the most dominant heat transport mechanism in Earth's mantle (*Schubert et al., 2001*). The geometry, heating mode, and properties of the convective medium define the vigor of the convection and the typical wavelength of a convection cell (*Schubert et al., 2001*). Convection has been suggested as the dominant heat loss process for Io's mantle (e.g. *Hussmann and Spohn, 2004; Ojakangas and Stevenson, 1986; Tackley et al., 2001*). Sophisticated Io-specific convection models, which include specific boundary conditions for the upper lid and a boundary between deep mantle and upper low-viscosity zone, have been applied (*Monnereau and Dubuffet, 2002; Shahnas et al., 2013; Tackley et al., 2001*). These studies show that for different conditions and mantle properties the spatial characteristics of the evolving convection planforms vary. Based on the hypothesis that the heat output pattern at Io's surface and the spatial density of convection instabilities in the mantle correlate, constraints on the Io's mantle could be placed. *Tackley (2001)* and *Tackley et al. (2001)* investigated the effect of three dimensional tidal heating and found that depending on the vigour of convection lateral temperature variation can remain. However, one common problem of both the parameterized solid-state convection scalings and the numerical approaches is that the models require a very low viscosity to be efficient enough to transport Io's observed heat output. This suggests either a vigorously convecting magma ocean or a heat transport by melt migration. As no other objects in the Solar System are known to have these characteristics, this requires Io-tailored heat loss models (*Stevenson, 2003*).

#### MAGMATIC HEAT TRANSPORT

Melt migration and heat piping are heat transport mechanisms where a fluid rises through a solid matrix. Requirements for a magmatic heat transport are, first of all, the presence of melt and a pressure gradient or density contrast (buoyancy). The geometry of the melt pockets, grain size, and the distribution and amount of magma are crucial factors that influence the efficiency of the heat transport. Different conditions

and drivers for the advection of melt apply depending on whether the process occurs in the mantle or in the crust. Different terms can be found in the literature. In the following, the term melt advection and magmatic heat transport is used to describe the upward-focused motion of melt, regardless of the location and the physical process. Heat piping is the advection of melt through the crust in connection with volcanism (e.g. *Moore and Webb, 2013; O'Reilly and Davies, 1981; Spencer et al., 2020a*). In contrast to that, the term melt migration is used, when referring to the advection of melt through diffuse pores in the mantle. Both processes describe mainly the vertical rising of melt. Magmatic segregation and melt segregation describe the process of melt production and melt focusing in the mantle. The amount of melt and heat loss are therefore strongly coupled to mantle conditions, such as the temperature, pressure, and composition, which, in turn, are dependent on the heat loss mechanism (*Keszthelyi and McEwen, 1997; Keszthelyi et al., 1999; McEwen et al., 1998; Spencer et al., 2020b*).

Even though magmatic heat loss is not a dominating heat transport process in other planetary bodies in the Solar System, it is particularly important for Io, given the moon's large heat flux and small pressure gradient. Both of these characteristics provide conditions for the likely presence of melt in the mantle, even reaching to high depths. Heat-pipe mechanism through the crust was first proposed by *O'Reilly and Davies (1981)* and motivated by the discrepancy that a thick crust, required to support Io's large mountains would lead to too high mantle temperatures if the crust would be purely conductive. In the mantle *Moore (2001)* proposes melt advection through a porous medium, based on Darcy's law. His results show that already low melt fractions are sufficient to transport Io's current heat through the mantle.

Heat loss in a partially magmatic and partially convective mantle has not been quantified. Parameterisations only exist for sub-solidus convection (*Schubert et al., 2001*). Convection in a partially molten mantle has been treated in a simplified manner. The effect of molten material on convective dynamics and total heat transport as well as the effect of convection given a magma-dominated regime have been neglected (*Moore, 2001; Tackley, 2001; Tackley et al., 2001*). Furthermore, how heat is transported laterally, i.e. how melt is focused at a volcanic system, such as Loki Patera, is a not well-understood process, however required to explain Io's volcanic characteristics.

#### 1.4.4. IO'S VOLCANOES - A WINDOW INTO IO'S DYNAMIC INTERIOR

The characteristics of Io's volcanoes, such as their eruption style, geological characteristics, as well as their spatial distribution and temporal behaviour, provide valuable insights into the moon's interior. Since Io is a very active body, investigating Io's tidal heating, heat loss, interior state, or surface volcanism independent from each other, rather than as a coupled system, can lead to incomplete or incorrect conclusions (Figure 1.6). Io's interior processes, such as non-uniform tidal heating and vigorous up- and downwellings induce small and large-scale variations on the interior. For this reason, it is important to look at different spatial scales in Io's volcanic activity pattern, in order to get the most complete picture of Io's interior.

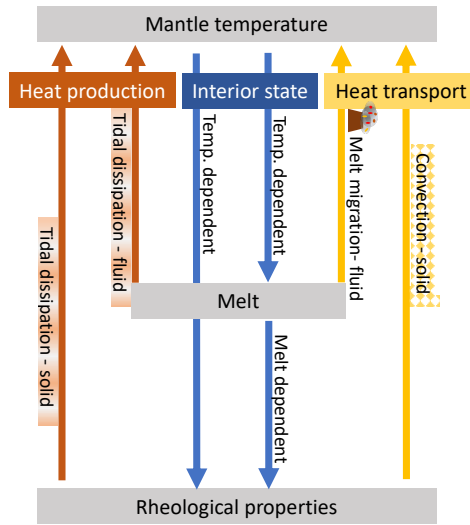


Figure 1.6: Io's mantle system with the interacting mechanisms: tidal heating, internal state and heat transport. These mechanisms couple the temperature, the melt fraction, and the rheological properties of Io's mantle. Simply stated, the melt migration provides the link to observable surface volcanism. Interactions affect reservoirs on a global scale. Additionally, small- and large-scale variations, which are stimulated by convection and tidal heating, propagate through the entire system and affect the other mechanisms and reservoirs.

A planetary body, such as Io, can be understood as a low-pass filter in the spatial and time domain. The further away an observation is taken from a point within the body, the less high-frequency features of that point can be received. Since high temporal and spatial frequency characteristics from Io's deep interior can only be perceived at the surface in a strongly damped manner, local and short-term anomalies detected at the surface are more likely to be associated with shallow processes. To derive properties of Io's deep interior, we can make use of global and long-term surface properties.

The combination of the localised behaviour of Io's volcanic activity in time and space and the fact that our observations of Io's volcanoes are limited in space and time make the derivation of global or large-scale parameters challenging and not free of uncertainties: 1) The available 30 years of Io observation can be considered as a snapshot, given that geological processes are slow. We may therefore witness a volcanic distribution that does not represent the average distribution of the recent geological epoch. 2) We do not have a perfect observation set. Io's surface has been covered with different resolutions. In particular observations of the poles are missing. These uncertainties need to be taken into account when conclusions on the interior based on volcanic observations are made.

In the following the most important interconnections between interior processes and Io's volcanism as well as interactions of interior processes with each other are reviewed. In doing so, constraints and open questions that build the basis of the



modelling work presented in the following Chapters are presented. As special focus of this dissertation is placed on processes in Io's mantle, shallow crustal processes are only discussed briefly.

#### CONSTRAINTS OF IO'S GLOBAL HEAT FLUX ON THE THERMAL STATE OF IO'S INTERIOR

The thermal state of a planetary body is determined by the structure and dynamics of the interior. At the same time, the thermal budget determines the interior structure and dynamics of internal processes (Figure 1.6). Io's widely spread volcanic activity gives insight into Io's global thermal state. It indicates that temperatures below the crust need to be above the solidus temperature, such that magma, which is the driver of Io's volcanoes, can be present.

The question whether Io is in thermal equilibrium, or in other words whether Io's heat production is the same as Io's heat output, is one of the most crucial and central questions to unravel Io's interior dynamics. The good agreement between Io's observed thermal output (*Davies et al.*, 2015; *Veeder et al.*, 1994, 2012, 2015) and the dissipation rate, derived from astrometric observations of changes in the orbital periods of the Galilean satellites (*Lainey et al.*, 2009), supports the hypothesis of a current thermal equilibrium (see further discussion in Section 1.2). Models based on Maxwell rheology and solid-state convection could not find an interior structure that can explain the equilibrium between tidal heating and heat transport (*Moore*, 2003). Coupling these thermal models with orbital dynamics through the transfer of mechanical energy into internal heat, *Ojakangas and Stevenson* (1986), *Fischer and Spohn* (1990) and *Hussmann and Spohn* (2004) suggest thermal-orbital oscillations around an instable thermal state due to the thermal inertia of the system. However, models developed in this dissertation assume that Io is in thermal equilibrium as suggested by *Lainey et al.* (2009). *Rovira-Navarro et al.* (2021) could show that by using an Andrade rheology and melt advection in the mantle in addition to mantle convection (*Moore*, 2001; *Spencer et al.*, 2020a; *Stevenson*, 2003), a thermal equilibrium is possible at Io's current heat flux rate. In this dissertation, special focus is placed on the latter model addition (Chapter 2 and Chapter 4).

#### CONSTRAINTS OF THE HIGH ERUPTION TEMPERATURES ON THE HEAT TRANSPORT AND DEGREE OF DIFFERENTIATION IN IO'S MANTLE

In addition to the investigation of Io's global heat flow, volcanism provides the perfect opportunity to sample the composition of material originating from Io's interior. As explained in Section 1.3.3, high-temperature melts, detected for some of Io's hotspots, indicate an ultramafic composition of the erupted material. But also hotspots with significant lower temperatures were detected, which indicate for mafic material and elements that lower the melting temperature, such as sulphur (*McEwen et al.*, 2000). Besides the composition, also information on the degree of differentiation of Io's mantle and crust and the heat transport can be inferred from this information. The eruption characteristic and temperatures are therefore important observations to help to answer two fundamental questions of this dissertation: Which kind of heat transport in Io's mantle is capable to transport Io's heat to the surface? Does Io's mantle possess compositional and rheological sub-layers?

Ultramafic volcanism is inconsistent with a highly differentiated mantle. Volcanism on a differentiated Io would be dominated by relatively low temperature and silicate-rich melts (*Keszthelyi and McEwen, 1997*). Besides the degree of differentiation, this places constraints on the heat transport. *Moore (2001)* shows that low to medium melt fractions (5%-20%) in Io's mantle are sufficient to transport Io's tidally produced heat to the crust. However, this upward migration of molten mantle material drives the differentiation of Io's mantle. Heat transport by uprising magma chemically extracts elements with low melting temperature, leaving elements with high melting temperature behind. This process is called magmatic differentiation. Three options are suggested that prevent strong differentiation of Io's mantle: 1) Re-mixing by convection can counteract differentiation in a mantle dominated by a magmatic heat transport. Active downwellings in an strongly heated mantle is capable to drag parts of the lower crust into the mantle (e.g. *Schools and Montesi, 2019*). 2) *Spencer et al. (2020b)* developed a magmatic differentiation model that allows for a deep source of Io's magma to explain the observed high-temperature melts. 3) *Keszthelyi et al. (1999)* suggest a mushy or fully fluid magma ocean. In these regimes, vigorous convection is able to mix back crustal material into the upper fluid-dominated mantle. For this dissertation, we treat option 1) as the preferred explanation, however, the other two options are not disregarded.

#### CONSTRAINTS OF IO'S VOLCANIC HEATING PATTERN ON DISSIPATION PROCESSES IN IO'S MANTLE

Io's volcanic centers and hot spots show a long-wavelength pattern (see Section 1.3.2). This pattern is expected to reflect the tidal heating distribution in Io's interior (Figure 1.6). As explained in Section 1.4.2, different tidal heating mechanisms, i.e. visco-elastic versus fluid, in different layers, i.e. asthenosphere versus mantle, result in different patterns at the surface. The correlation between these resulting non-uniform tidal dissipation patterns and Io's non-uniform volcanic activity at the surface has been investigated for example by *Segatz et al. (1988)*, *Bierson and Nimmo (2016)*, *Hamilton et al. (2013)*, and *Tyler et al. (2015)*. In addition, also Io's figure could hint to Io's non-uniform heating pattern in the interior. (*Ross et al., 1990*). The central questions that these studies try to answer is: Where in the mantle is tidal heat produced? What kind of tidal mechanisms drive the heating in the interior? These are also central questions in this thesis. For a comparison between Io's observed heat flux and tidal dissipation models see *de Pater et al. (2021)*.

Standard tidal heating models (end-members) only show a poor correlation with the observed large-scale variations in Io's volcanic activity. This makes it impossible to answer the two questions above with certainty. The higher volcanic heat output at mid-latitudes and equatorial areas compared to polar areas (*Davies et al., 2015*) favours asthenosphere or fluid ocean heating. However, asthenosphere heating cannot explain the observed 30° eastward shift with respect to the sub-Jovian and anti-Jovian points, and fluid ocean heating cannot explain the large number of vigorous volcanoes at mid-latitudes.

The detection of the spatially non-uniform volcanic heat flow and significant long-

wavelength variations in the spatial density of Io's volcanic features (Section 1.3) implies that interactions between tidal dissipation, heat loss, and temperature dependent-rheology does not only influence the global properties, but also break the spherical symmetry of Io's interior. To this date, only semi-analytical tidal dissipation models have been used, which are only valid for spherically symmetric bodies and cannot incorporate any lateral variations of rheological properties. Spatial variations in the mantle temperature arise self-consistently in case the lateral non-uniform tidal heating cannot be removed by lateral flow of mantle convection (Tackley, 2001; Tackley et al., 2001). As a consequence, the visco-elastic properties of the asthenosphere, i.e. the viscosity and the shear modulus, which depend strongly on the melt fraction and temperature, vary laterally. A spatially varying heat flux and temperature in the mantle may also lead to variations of the thickness of individual layers (Spencer et al., 2021; Tyler et al., 2015). Whether locations with a stronger heating result in a thicker or thinner lithosphere depends on whether magmatic intrusions form at a constant rate in the lithosphere or at a rate proportional to the heat flux through volcanic conduits (Spencer et al., 2021). In addition to large-scale variations of Io's interior due to tidal dissipation, also small scale features arise due to the heat transport. These features can be cold downwelling and warm upwelling with higher and lower viscosity than the surrounding mantle, thin decompaction layers with high melt fraction (Spencer et al., 2020a), magma chambers and magma-filled heat pipes. The effects of small-scale features arising from convection and large-scale features arising from non-uniform heating on the resulting tidal dissipation have been studied for Earth-like exoplanets (Běhounková et al., 2010, 2011) and icy moons (Běhounková et al., 2010; Beuthe, 2019; Han and Showman, 2010) but not for Io's asthenosphere with strong lateral deformations. To what extent such anomalies in the upper mantle and crust contribute to the amount of tidally produced heat or change its distribution is therefore unknown.

The disagreement between observations and dissipation patterns resulting from semi-analytical spherical symmetric models while neglecting the presence of features originating in a self-consistent manner from tidal dissipation and heat transport motivates the need for advanced tidal heating models. This thesis aims at developing a numerical model that is based on a finite element approach such that each discrete location in Io's interior (Figure 1.7) can be given a different specific property. Thus, deviations from the traditional spherical symmetric body can be accommodated to obtain a more realistic description of Io's complex interior and tackle the questions raised above.

#### CONSTRAINTS OF LOCAL AND RAPID VOLCANIC PROCESSES IN IO'S CRUST

Looking at features of scales between tens of kilometres and a few 100 kilometres allows to investigate more shallower processes. The many different types of observed eruption styles on Io (Section 1.3.3) suggest that miscellaneous processes near the crust are present. Even though crustal processes are given less attention throughout this dissertation, the understanding of localised behaviour of volcanoes is also important in order to understand Io as a global system. This is because Io's hotspots and paterae, covering approximately 1.2% of Io's surface, contribute approximately 50% to Io's total heat output (Veeder et al., 2012). Therefore, local volcanic processes contribute significantly to

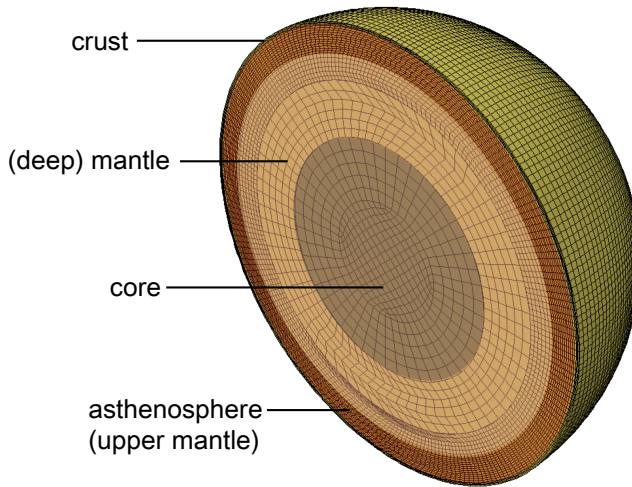


Figure 1.7: Finite element mesh for Io's interior. Each element can be given a different property. This way, the effect of the lateral rheological structure or local anomalies on the spatial distribution of tidal dissipation can be modelled.

Io's thermal state. Models of Io's crust, in turn, require better constraints on processes in the mantle, such as how Io's volcanic systems are fed with magma, to better explain the statistical behaviour between neighbouring volcanic features ([Hamilton et al., 2013](#); [Kirchoff and McKinnon, 2009](#); [Kirchoff et al., 2020](#)) and the quasi-periodic behaviour of frequently active volcanoes ([de Kleer et al., 2019a](#)).

## 1.5. RESEARCH MOTIVATION AND RESEARCH QUESTIONS

The layer responsible for Io's volcanic activity is the moon's silicate mantle. However, the state and structure of Io's mantle and what kind of tidal heating and heat loss processes drive Io's dynamics are highly debated. As demonstrated in the previous sections, a better understanding of tidal dissipation and heat loss, and a better knowledge of the physical state of Io's mantle go hand in hand. On the one hand, tidal dissipation and heat loss mechanisms are determined by the state and structure of Io's interior, on the other hand, they determine the state and structure. In addition, the relation of these interior processes to Io's volcanic activity at the surface is not understood. We do not know at which depth tidal heat is generated, which kind of tidal heating mechanism is dominating, how Io's interior is capable to lose the tidally generated heat, and in what way tidal dissipation and heat loss are interacting with each other. All these questions cannot be studied separately. Using the full potential of a volcanic pattern as an observable feature of Io's interior dynamics requires consideration of not only global one-dimensional processes, but also of large- and small-scale characteristics of the interior mechanisms (Section 1.4.4). In doing so, it is crucial to also consider possible interactions between arising regional or local anomalies on other interior processes in a consistent manner. The most prominent and unique dilemma for Io's tidally-heated

interior is that the assumption of a homogeneously layered body immediately breaks this assumption, given by the fact that tidal dissipation within a homogeneously layered body is not uniformly distributed in the interior.

A better understanding of the interactions between mechanisms in the mantle and their relation to Io's volcanoes would lead to significant advances in modelling the thermal evolution of tidally heated exo-planets and other terrestrial and icy bodies in the Solar System. Improving these models would therefore lead to a more precise evaluation of habitable environments, and the pre-conditions and evolution paths leading to habitable conditions in the Solar System and beyond.

*The goal of this thesis is to improve the understanding of the interconnection between Io's volcanic activity and the thermal state and dynamics of the moon's mantle.*

To reach this goal in a structured way, the goal is split in a number of research questions (RS), which are addressed in the following chapters.

First, the effect of the non-uniform tidal heating on Io's interior and surface heat flux needs to be analysed. This builds the basis for the following research projects. We phrase the following questions:

RS 1: *What mantle properties and processes influence the strength of the lateral variations induced by non-uniform tidal heating?*

RS 2: *To what extent does the non-uniform heating influence the lateral temperature distribution in the mantle and the volcanic heat output at the surface?*

These questions form the basis of Chapter 2. In order to answer these two questions we calculate the distribution of tidal dissipation using a finite element model. Following that, we relate the resulting heat production pattern to the interior temperature and melt distribution by using a steady-state scaling law, which incorporates mantle convection and melt migration.

Once these questions are answered, in a second step, it needs to be investigated how the long-wavelength variation in Io's rheological structure influences the tidal heating pattern. Chapter 3 deals with the following questions:

RS 3: *What is the influence of the tidally-induced lateral variations in the rheological properties on the tidal heating pattern?*

RS 4: *How does such a tidal-dissipation-rheology feedback influence Io's volcanic pattern?*

To answer these questions we use the finite element model developed in Chapter 2 and incorporate lateral variation of the rheological properties in the asthenosphere, that remain from the tidal dissipation pattern obtained from a homogeneously layered interior structure. Based on the updated dissipation pattern, this procedure is repeated

such that the evolution of the continuous feedback can be evaluated.

Last, the focus is set on Io's heat loss mechanism and its relation to the various spatial scales of Io's observed volcanic distribution. We assume that the heat transport model in the mantle needs to be consistent with the volcanic pattern at the surface. This requires 1) mantle temperatures consistent with the global presence of melt; 2) a lateral heat flow by convection that does not erase the large-scale variations in the volcanic density pattern; and 3) a convection pattern in the mantle that is in agreement with Io's mean spatial volcanic density. Based on these requirements the two following questions shall be addressed in Chapter 4:

RS 5: *Can the small and large-scale characteristics of Io's volcanic activity pattern be explained by a partially convective and partially magmatic heat transport?*

RS 6: *What constraints do the characteristics of the volcanic activity pattern place on Io's upper mantle?*

We use the scaling-law developed in Chapter 2 as well as an additional scaling law providing the spatial density of downwellings in Io's upper mantle.

Chapter 2 has been published in the peer-reviewed Icarus Journal and Chapter 4 has been published in the peer-reviewed Journal of Geophysical Research - Planets. Therefore, Chapter 3 is also structured as a paper, for consistency. To improve the readability of this thesis, references to above mentioned publications have been changed to references to the respective chapters of this dissertation. Furthermore, minor changes, such as the denotation of model variables for the sake of consistency, and minor clarifications to the text have been applied. While the single chapters are concluded individually in their respective conclusion sections, the answer to the research questions above are collected in the final chapter of this thesis, Chapter 5. In addition, Chapter 5 provides recommendations for further work and an outlook to future Io observations.



# 2

## TIDALLY INDUCED LATERAL VARIATIONS OF IO'S INTERIOR

**T. STEINKE , H. HU, D. HÖNING, W. VAN DER WAL,  
B. VERMEERSEN**

*Satellite and recent Earth-based observations of Io's surface reveal a specific spatial pattern of persisting hotspots and sudden high-intensity events. Io's major heat producing mechanism is tidal dissipation, which is thought to be non-uniformly distributed within Io's mantle and asthenosphere. The question arises to what extent Io's non-homogeneous heat production can cause long-wavelength variations in the interior and volcanic activity at the surface. We investigate dissipation patterns resulting from two different initially spherical symmetric visco-elastic rheological structures, which are consistent with geodetic observations. The spatial distributions of the time-averaged tidal heat production are computed by a finite element model. Whereas for the first rheological structure heat is produced only in the upper viscous layer (asthenosphere-heating model), the second rheological structure results in a more evenly distributed dissipation pattern (mixed-heating model) with tidal heating occurring in the deep mantle and the asthenosphere. To relate the heat production to the interior temperature and melt distribution, we use steady-state scaling laws of mantle convection and a simple melt migration model. The resulting long-wavelength thermal heterogeneities strongly depend on the initial tidal dissipation pattern, the thickness of the convective layer, the mantle viscosity, and the ratio between magmatic and convective heat transport. While for the asthenosphere-heating model a strong lateral temperature signal with up to 190 K peak-to-peak difference can remain, convection within a thick convective layer, as for the mixed-heating model, can reduce the lateral temperature variation to less than 1 K, if the mantle viscosity is sufficiently low.*

This chapter is published in Icarus [Steinke et al. \(2020a\)](#).



*Models with a dominating magma heat transport preserve the long-wavelength pattern of tidal dissipation much better and are favoured, because they are better to explain Io's thick crust. The approach presented here can also be applied to investigate the effect of an arbitrary interior heating pattern on Io's volcanic activity pattern.*

## 2

## 2.1. INTRODUCTION

Unlike any of the other satellites in the Solar System that we know Io shows signs of active silicate volcanism (Carr, 1986; McEwen *et al.*, 1998). In contrast to terrestrial planets with recent or active silicate volcanism, Io's present heat output is not due to remnant cooling, but due to extreme and non-uniform tidal heating (Beuthe, 2013; Ross *et al.*, 1990; Segatz *et al.*, 1988). Because of this uniqueness within the Solar System, Io serves as a potential archetype of rocky exoplanets and exomoons undergoing extreme tidal heating. Understanding Io's recent cooling processes could provide insight into the early evolution of the terrestrial planets, when they were still hotter and possibly had a similar heat flux as Io has today.

Io's observed volcanic activity is an important link to help understanding the satellite's interior processes. The non-uniform volcanic pattern is commonly associated with a radial heat flux originating from Io's non-uniform long-wavelength heat production pattern (Davies *et al.*, 2015; Hamilton *et al.*, 2013; Ross *et al.*, 1990). However, the complex interplay of Io's internal heat transport mechanism and physical properties makes the assumption of a purely radial heat flow questionable.

The distinct heat production distribution depends in an intricate way on the tidal perturbation and rheology of Io's interior (Beuthe, 2013). Several studies based on the physics of solid visco-elastic material have been conducted (Bierson and Nimmo, 2016; Ross *et al.*, 1990; Segatz *et al.*, 1988) to predict a heat dissipation distribution. Tyler *et al.* (2015) suggested a dynamic modelling approach by assuming that Io's asthenosphere is a global fluid layer. Both solid and fluid types of models match the strong degree two component that can be found in Io's inferred heat flux maps and Io's global volcanic distribution (Davies *et al.*, 2015; Hamilton *et al.*, 2013). However, whereas the solid model is not able to predict the observed longitudinal shift of the maxima in the volcanic concentration, the fluid model is not in agreement with the strong volcanic activity at medium latitudes.

Io's interior heat production, heat distribution, and heat transport mechanisms are significantly different from other terrestrial bodies. Io's produced heat is partially transported by convection (Moore *et al.*, 2007). However, due to the extreme heat in Io's interior and low pressures, Io's mantle contains high portions of melt (Khurana *et al.*, 2011). Volcanic channels arise allowing the transport of molten material and heat to the surface, cooling Io's interior more effectively (Bierson and Nimmo, 2016; Elder, 2015; Moore, 2001). Furthermore, dissipative heat forms the most significant part of Io's heat budget as opposed to remnant cooling from the core (Lainey *et al.*, 2009; Peale *et al.*, 1979). Because of the heterogeneous nature of the tidal dissipation pattern, Io's heat is not distributed uniformly in radial and in lateral directions. This leads to a convection

system, which cannot be described by scaling laws based on adiabatic temperature profiles and one-dimensional mantle structures as proposed for Mars, Venus and Mercury (*Schubert et al., 2001*).

Planetary evolution models (e.g. *Schubert et al., 2001*; *Spohn, 1991*) show that the amount of heat in the interior determines the interior structure of celestial bodies due to the temperature-dependence of the melt fraction and the mantle viscosity. The question arises if a strong non-homogeneous internal heat production, such as for Io, has a lateral varying effect on the interior structure. In this case, Io's interior structure would have a three-dimensional distribution of interior properties, and thus, a possibly different evolving dissipation pattern than derived from radially symmetric structures (*Bierson and Nimmo, 2016*; *Hamilton et al., 2013*; *Ross et al., 1990*; *Segatz et al., 1988*).

The effect of tidal heating on the interior structure of celestial bodies due to the temperature-dependency of the viscosity has been explored for icy satellites of the outer planetary systems (*Běhounková et al., 2010*; *Han and Showman, 2010*; *Ojakangas and Stevenson, 1989*; *Roberts and Nimmo, 2008*; *Tobie et al., 2005*). Terrestrial bodies, however, have been given less attention because of the minor role of tidal dissipation for the terrestrial planets of the Solar System. *Běhounková et al. (2010)* and *Běhounková et al. (2011)* investigated the feedback between the heterogeneous rheological structure resulting from mantle convection and the rheology-dependent tidal dissipation in a three-dimensional numerical model for Earth-like exoplanets. However, because their investigations are based on different orbital and interior properties their conclusions cannot be applied to Io. Studies focusing on Io have been conducted by *Tackley (2001)*, *Tackley et al. (2001)* and *Bierson and Nimmo (2016)*. The first two studies investigate the effect of the three-dimensional heating pattern on the temperature structure and lateral heat flux pattern for a purely convective asthenosphere and mantle. This approach possibly underestimates the effect of tidally induced heating on the heat flux pattern, as it neglects advection of melt. This heat removal mechanism transports heat more quickly and maintains a more radial direction. In contrast, *Bierson and Nimmo (2016)* derived a three-dimensional melt distribution based on the assumption that the lateral varying produced heat is exclusively transported by magma through a solid porous matrix. This approach, however, possibly overestimates the tidal-dissipation induced signal on the surface heat flux pattern, as lateral flow due to mantle convection is neglected. We suggest that a combination of solid-state convection and magmatic heat transport would improve the estimations of tidally induced variations of Io's surface heat flux and volcanic activity pattern.

In this paper we aim to explore whether Io's heterogeneous heating causes lateral variations of the internal structure or whether the assumption of a well-mixed radially symmetric mantle is justified. To achieve that we combine heterogeneous tidal heat dissipation with a coupled system of mantle convection and advection of melt. Further, we link our modelling results to observables, such as Io's surface pattern of volcanic features (e.g. *Davies et al., 2015*; *de Kleer and de Pater, 2016*; *Kirchoff et al., 2011*; *Veeder et al., 2015*). We focus on first-order effects of the tidal dissipation pattern on the

interior. To model Io's convective mantle we use a steady-state scaling law and ignore small-scale anomalies triggered by mantle convection as they are difficult to predict. Thus, our resulting long-wavelength patterns can be seen as a statistically averaged solution.

2

Since our main aim is to explore the relation between the tidal dissipation patterns and the tidal-dissipation-induced lateral variations we do not explore the full range of possible dissipation patterns. Instead, we investigate two end-members of possible tidal dissipation pattern based on [Ross et al. \(1990\)](#). We choose to compute the tidal dissipation with a numerical finite element (FE) model that can deal with three-dimensional variations of the viscosity. In contrast to semi-analytical methods based on a one-dimensional approach ([Jara-Orué and Vermeersen, 2011](#); [Sabadini et al., 2016](#)), this allows to calculate the effect of the tidally induced lateral viscosity variations on the tidal dissipation itself in future work.

The FE model and the thermal modelling of Io's interior are introduced in [Section 2.2](#) and [Section 2.3](#), respectively. In [Section 2.4](#) we present the resulting lateral maximum temperature and melt distributions for our interior models for a range of model variables. In [Section 2.5](#) we discuss the influence of the model assumptions on the obtained results and the implications of our results on the interpretation of Io's volcanic surface features.

## 2.2. NUMERICAL MODELLING OF VOLUMETRIC TIDAL HEATING

In this section the three components of the numerical model for the volumetric tidal heating are introduced and discussed: 1) the periodic tidal forcing, 2) the solution of the equation of motion, here implemented in a finite element (FE) model, and 3) the rheological model and the choice of the interior properties.

### 2.2.1. PERIODIC TIDAL FORCING

Io's eccentric orbit causes periodic variations of the distance between Io and Jupiter, and also causes differences between the rotation velocity and orbital velocity of the satellite. The potential due to the 1:1 spin-orbit resonance at a point is given as a function of the time  $t$ , and the spherical coordinates of the point, the radial distance from the centre of Io  $r$ , and the longitude  $\phi$  and co-latitude  $\theta$  ([Kaula, 1964](#)):

$$V_p(t, r, \theta, \phi) = \omega^2 r^2 e \left( \frac{3}{2} P_{2,0}(\cos\theta) \cos(\omega t) - \frac{3}{4} P_{2,2}(\cos\theta) \cos(2\phi) \cos(\omega t) - P_{2,2}(\cos\theta) \sin(2\phi) \sin(\omega t) \right), \quad (2.1)$$

where  $\omega = 2\pi/P_{orbit}$  is the mean motion with  $P_{orbit}$  the orbital period of Io, and  $e$  the eccentricity of Io's orbit.  $P_{2,0}(\cos\theta)$  and  $P_{2,2}(\cos\theta)$  are the degree two associated Legendre polynomials of order zero and two, respectively. The inclination of Io's rotation axis and physical librations are unknown but expected to be small (e.g. [Yoder and Peale, 1981](#)). Thus, their effects on the dissipation pattern ([Beuthe, 2013](#); [Frouard and Efroimsky, 2017](#)) are neglected. Furthermore, we assume that Io is fully relaxed under every

Table 2.1: Geophysical and geodetic parameters of Io taken from (1) *Anderson et al. (2001)*, (2) *Lissauer and De Pater (2013)*, and (3) *Lainey et al. (2009)*.

Parameter	Notation	Value	Unit
Mean density <sup>(1)</sup>	$\rho$	3527.8	$\text{kg m}^{-3}$
Mean radius <sup>(1)</sup>	$R$	1821.6	km
Eccentricity <sup>(2)</sup>	$e$	0.0041	-
Normalized moment of inertia <sup>(1)</sup>	$C/MR^2$	0.37685	-
Orbital period <sup>(2)</sup>	$P_{orbit}$	1.769138	days
Imaginary part of Love number <sup>(3)</sup>	$\text{Im}(k_2)$	0.015	-

static force and neglect the effect of any static bulge of the body on the periodic tidal response. The geophysical and geodetic parameters used to describe the strength and the period of the tidal forcing for Io are presented in Table 2.1.

### 2.2.2. FINITE ELEMENT APPROACH

We solve the equation of motion using a finite element model (ABAQUS version 6.14) and follow the method of *Wu (2004)* to account for self-gravitation in an iterative way. The FE model was developed by *Hu et al. (2017)* to calculate the change of the moment of inertia tensor for non-spherical symmetric bodies. For this study, the model is used to calculate the effect of periodic tidal forces (Equation 2.1) on Io's interior.

The FE model solves for the deformation field  $u$  for each time step, following the conservation of mass

$$\nabla \cdot u = 0, \quad (2.2)$$

and the conservation of momentum

$$\nabla \cdot \sigma + f = 0 \quad (2.3)$$

where  $f$  is the body force applied as a surface load at boundaries between the layers of different densities.  $\sigma$  is the incremental stress field tensor, including both: the isotropic part of the stress field, controlling the volumetric changes, and the deviatoric part of the stress field, related to any shape changes. The restoring force of isostasy at each boundary of radial change in density is applied following *Wu (2004)*. Any forces due to inertia are neglected. The effect of compressibility is also not included. To include self-gravitation the additional potential due to deformation needs to be included in the body force. The total force that is applied to each boundary at a density jump with a density difference of  $\delta\rho$  is consequently described as

$$f = -\delta\rho(\nabla V_p + \nabla\Lambda), \quad (2.4)$$

where  $V_p$  is the external tidal potential given in Equation 2.1 and  $\Lambda$  is the potential of the perturbation of the gravity field. The latter perturbation arises due to the mass redistribution, which is a consequence of the tidal deformation field  $u$ . In each iteration step,  $\Lambda$  is re-computed numerically using the deformation field  $u$ . The newly calculated load  $f$  is applied until the deformation  $u$  and stress field  $\sigma$  for each time step  $t$  have

converged. The number of required iterations depends on the specific problem and is therefore addressed in Section 2.4. The type of elements used in the finite element model is important for the stress calculation. Whereas for the deformation and self-gravitation linear elements (8 nodes) deliver sufficient accuracy, the calculation of stresses requires quadratic elements (20 nodes) to account for the non-cubic shape of the elements. However, solving the stress field in the finite element model with quadratic instead of linear elements is a computationally expensive procedure. Therefore, we only apply a quadratic mesh in the final iteration of the self-gravitation iteration.

As the time scale for solid-state convection, modelled in Section 2.3, is assumed to be much larger than one orbital period, the volumetric tidal heat production is averaged over one orbital period to result in an average three-dimensional tidal dissipation pattern. The average volumetric heat dissipation  $h_{node}$  is calculated for each integration point following [Hanyk et al. \(2005\)](#)

$$h_{node} = \frac{1}{P_{orbit}} \int_{\tau}^{\tau+P_{orbit}} \frac{\sigma_D : \sigma_D}{2\eta_{diss}} dt, \quad (2.5)$$

where  $\sigma_D : \sigma_D$  denotes an inner matrix product of the deviatoric stress tensor  $\sigma_D$ ,  $\eta_{diss}$  is the viscosity of the visco-elastic mantle at the corresponding integration point, and  $\tau$  is the time required for the visco-elastic model to adjust to the steady state. Note that since we only use the deviatoric stress field for the calculation of the volumetric dissipation  $h_{node}$ , the transformation of the isotropic stress tensor given by [Wu \(2004\)](#) has no effect. The values of the heat dissipation  $h_{node}$  are interpolated to an equiangular grid to facilitate spherical harmonic expansion later. The resulting spatial varying internal heating functions  $H(r, \phi, \theta)$  are used in Section 2.3 to calculate the effect of the tidal heat production on Io's interior.

### 2.2.3. RHEOLOGICAL MODEL AND PROPERTIES OF IO'S INTERIOR STRUCTURE

We choose to simulate the visco-elastic behaviour of Io's interior with the Maxwell rheology. The Maxwell rheology is a very good approximation of the material behaviour for low-frequency loading (e.g. [Sabadini et al., 2016](#)), and has been applied to Io in previous studies ([Husmann and Spohn, 2004](#); [Ross et al., 1990](#); [Segatz et al., 1988](#)). However, laboratory and geodetic observations show that the Maxwell rheology underestimates the frictional dissipation of a visco-elastic material for perturbations shorter than the Maxwell time of a material ([Castillo-Rogez et al., 2011](#); [Efroimsky, 2012](#), and references therein). This is the case for realistic rock properties of Io's interior and Io's short tidal perturbation period of about 42 hours. For this reason more advanced rheology models, such as the Andrade rheology, have been used for Io by several authors ([Bierson and Nimmo, 2016](#); [Makarov and Efroimsky, 2014](#); [Renaud and Henning, 2018](#)). They obtain mantle viscosities that can produce Io's estimated total dissipation  $\dot{E}_{total}$  ([Lainey et al., 2009](#)) and still allow a solid-state convection.

As suggested by [Tobie et al. \(2005\)](#) and [Běhounková et al. \(2010\)](#) we deal with the discrepancy between the viscosity required for the Maxwell rheology and the mantle

viscosity by treating the visco-elastic rheology separated from the mantle viscosity associated with solid-state convection. In contrast to the magnitude of the produced heat in each layer, the spatial pattern does not depend on the used viscosity (*Beuthe, 2013*). Consequently, small differences in the resulting heat flux pattern arise when Andrade rheology instead of Maxwell rheology is used, which, however, do not affect our final conclusions. In the following, we use the term Maxwell viscosity  $\eta_{diss}$  valid for Io's dominating forcing period  $P_{orbit}$  when referring to the viscosity used to calculate the dissipation due to internal friction in a visco-elastic medium. In contrast, we use the term mantle viscosity  $\eta_{con}$  for the viscosity that controls the convection of Io's mantle and asthenosphere.

The spatial distribution of heat production is strongly coupled to the rheology properties of the body's interior, i.e. the shear modulus  $\mu$ , the Maxwell viscosity  $\eta_{diss}$ , and the density distribution  $\rho$ . Unfortunately, these parameters cannot be uniquely constrained for Io. A full exploration of possible dissipation patterns is not within the scope of this paper and can be done more efficiently using theoretical considerations such as provided by *Beuthe (2013)*. We instead investigate tidal dissipation patterns resulting from two different interior structure models. The properties of the two models are chosen such that the corresponding initial dissipation patterns result in maximal spatial variations for one model and minimal spatial variations for the other model. Thus, the two models are considered as end-members. Both models have a spherical symmetric structure, as no three-dimensional variations of the interior are known a priori. The structure is composed of a liquid core, a visco-elastic mantle that is divided into a deep high-viscosity layer and a shallow low-viscosity melt containing layer, i.e. the asthenosphere, and a fully elastic crust. In contrast to *Segatz et al. (1988)* both of our models contain an asthenosphere since observations of Io's interaction with Jupiter's magnetic field suggest a melt containing layer (*Khurana et al., 2011*). The parameters are selected such that they match with Io's observed mean density, mean radius, the polar moment of inertia provided in Table 2.1 and Io's average surface heat flux of  $2.24 \pm 0.45 \text{ W m}^{-2}$  assuming a thermal equilibrium (*Lainey et al., 2009*). We select an asthenosphere thickness of 200 km for both models as a compromise between estimates for the thickness of the partially molten layer of several hundreds of kilometres (*Bierson and Nimmo, 2016*) and estimates of 30 km-50 km (*Ross et al., 1990; Segatz et al., 1988*). For our FE models we set the crustal thickness to 30 km in agreement with *Turtle et al. (2007)* who suggest a range between 10 km and 50 km. The crustal rheology is based on values by *Segatz et al. (1988)*. For the core we take the density of a Fe-FeS eutectic, which is an approximation of the minimal core density (*Anderson et al., 2001*).

To account for the unknown composition of the deep mantle we investigate a potential interior model of Io with all the heat produced in the asthenosphere based on *Segatz et al. (1988)*, which we term ModelA. We neglect any heat contribution from the deep mantle for ModelA (asthenosphere-heating scheme). Thus, the heat production in the asthenosphere  $\dot{E}_{ast}$  is equal to Io's total heat production  $\dot{E}_{total}$  but shows large regional variations. For ModelB both the asthenosphere and the deep mantle contribute to Io's total heat production. We choose a fraction of 40% asthenosphere-heating

Table 2.2: Common parameters of the rheology and thermal modelling for Model A and Model B following (1) *Anderson et al.* (2001), (2) *Turtle et al.* (2007), (3) *Segatz et al.* (1988), (4) *Roberts* (1967), and (5) *Tackley* (2001).

Rheology parameter	Notation	Value	Unit
Core density <sup>(1)</sup>	$\rho_c$	5150	$\text{kg m}^{-3}$
Core-Mantle Boundary	$R_{cmb}$	965	km
Mantle/Crust density	$\rho_m$	3244	$\text{kg m}^{-3}$
Crustal thickness <sup>(2)</sup>	$d_{diss,crust}$	30	km
Crustal shear modulus <sup>(3)</sup>	$\mu_{crust}$	$6.5 \cdot 10^{10}$	Pa
Crustal Maxwell viscosity <sup>(3)</sup>	$\eta_{diss,crust}$	$10^{23}$	Pa s
Asthenosphere thickness	$d_{ast}$	200	km
Thermal parameter	Variable	Value	Unit
Mantle thermal conductivity	$k_m$	3	$\text{W m}^{-1} \text{K}^{-1}$
Lid thermal conductivity	$k_{lid}$	3	$\text{W m}^{-1} \text{K}^{-1}$
Grav. acceleration for convection	$g$	1.7	$\text{m s}^{-2}$
Surface temperature	$T_s$	100	K
Thermal diffusivity	$\kappa$	$10^{-6}$	$\text{m}^2 \text{s}^{-1}$
Thermal expansivity	$a_m$	$2 \cdot 10^{-5}$	$\text{K}^{-1}$
Critical Rayleigh number <sup>(4)</sup>	$Ra_{H,crit}$	2772	-
Activation energy	$E_a$	$3 \cdot 10^5$	$\text{J mol}^{-1}$
Gas constant	$R_{gas}$	8.314	$\text{J K}^{-1} \text{mol}^{-1}$
Blurring coefficient <sup>(5)</sup>	$C$	4.413	-
Blurring exponent <sup>(5)</sup>	$\beta$	0.2448	-
Reference mantle viscosity	$\eta_{con}$	$10^{12} - 10^{18}$	Pa s
Heat flux fraction	$\bar{f}_{cc}$	5 – 95	%

and 60% mantle-heating which, leads to a minimisation of regional differences in the spatial heat production pattern at the surface (*Ross et al.*, 1990). The viscosity of the asthenosphere and deep mantle of Model A and B are adjusted in a way to produce the desired heating distribution between the deep mantle and the asthenosphere and Io's total heat production rate  $\dot{E}_{total}$ . All common parameters defining the rheological structures of Model A and Model B are presented in Table 2.2. Model A and B specific parameters are presented in Table 2.3. We calculate the total heat production rate using the macroscopic approach (e.g. *Beuthe*, 2013), which is given as a function of the imaginary part of the complex Love number  $\tilde{k}_2$ :

$$\dot{E}_{total} = -\text{Im}(\tilde{k}_2) \frac{(\omega R)^5}{G} \frac{21}{2} e^2, \quad (2.6)$$

with  $G$  being the gravitational constant equal to  $6.674 \cdot 10^{-11} \text{ m}^3 \text{ kg}^{-1} \text{ s}^{-2}$ .  $\tilde{k}_2$  is given in Table 2.1 and is obtained by the rheological structures of Model A and Model B using a semi-analytical approach based on normal mode theory (*Jara-Orue and Vermeersen*, 2011; *Sabadini et al.*, 2016). This semi-analytical method requires much less computational costs as it is based on a one-dimensional description of the interior structure, whereas our FE model is three dimensional.

Table 2.3: Individual parameters of the rheology and thermal modelling for Model A and Model B.

Rheology Parameter	Notation	Model A	Model B	Unit
Deep mantle shear modulus	$\mu_m$	$6 \cdot 10^{10}$	$2 \cdot 10^9$	Pa
Deep mantle Maxwell viscosity	$\eta_{diss,m}$	$10^{20}$	$8 \cdot 10^{14}$	Pa s
Asthenosphere shear modulus	$\mu_{ast}$	$7.8 \cdot 10^5$	$9 \cdot 10^7$	Pa
Asthenosphere Maxwell viscosity	$\eta_{diss,ast}$	$10^{11}$	$3.5 \cdot 10^{12}$	Pa s
Mantle heat production ratio	$\dot{E}_m / \dot{E}_{total}$	0	60	%
Asthenosphere heat production ratio	$\dot{E}_{ast} / \dot{E}_{total}$	100	40	%
Thermal Parameter	Variable	Model A	Model B	Unit
Thickness of convective layer	$d$	200	826.6	km
Radius bottom of convective layer	$R_{con}$	1591.6	965	km
Geometry factor	$a_f$	0.8925	0.6096	-

## 2.3. THERMAL MODELLING

Heat generated by dissipation within Io's interior is transported by thermal diffusion, melt migration, and solid-state convection (e.g. [Elder, 2015](#); [Moore, 2001](#); [Tackley, 2001](#)). Our aim is to obtain the temperature distribution in the upper layers of the mantle resulting from the spatial pattern of the tidal dissipation taking into account all heat transport mechanisms. The difficulty is that the intensities of the convective, conductive, and magmatic heat transport strongly depend on each other. In the following, we outline our approach to address this problem in order to find a statistically averaged regional solution. For that we make use of scaling laws, which are typically used to analyse the thermal state and evolution of planets and satellites (e.g. [Hussmann and Spohn, 2004](#); [Schubert, 1979](#); [Spohn, 1991](#); [Tosi et al., 2017](#)). Doing so reduces the large number of model parameters. All major steps are presented in [Figure 2.1](#).

In the first step the three-dimensional volumetric dissipation is projected to Io's surface. The resulting heat production per unit area is then smoothed to account for lateral convective flow. We will refer to this procedure as blurring, as introduced by [Tackley \(2001\)](#). Next, we split the obtained total heat flux  $Q(\theta, \phi)$  into a magmatic and a convective-conductive contribution

$$Q(\theta, \phi) = Q_{cc}(\theta, \phi) + Q_{mag}(\theta, \phi), \quad (2.7)$$

where  $Q_{mag}(\theta, \phi)$  is the pattern of the magmatic heat flux and  $Q_{cc}(\theta, \phi)$  is the pattern of the convective-conductive heat flux. We treat the fraction

$$\bar{f}_{cc} = \frac{\bar{Q}_{cc}}{Q}, \quad (2.8)$$

between the globally average convective-conductive heat flux  $\bar{Q}_{cc}$  and the globally average total heat flux  $Q$  as a variable. We name this ratio the heat flux fraction. Note that  $Q_{mag}(\theta, \phi)$  is related but not equivalent to the observed hot spot heat flow as Io's background heat flow is also fed by intrusive magma ([Stevenson and McNamara, 1988](#)). To compute the distribution of the maximum mantle temperature and melt fraction



for each longitude  $\phi$  and co-latitude  $\theta$  we use an analytically derived scaling law from [Vilella and Kaminski \(2017\)](#) to approximate the radial temperature field due to mantle convection. The magmatic heat output  $Q'_{mag}(\theta, \phi)$  per unit area is approximated based on the melt fraction and the heat flux fraction  $\bar{f}_{cc}$ . In the last step, the spatially varying convective-conductive heat flux  $Q_{cc}(\theta, \phi)$  is updated keeping  $\bar{f}_{cc}$  and the globally average total heat flux  $\bar{Q}$  constant (Equation 2.7). The last steps are repeated several times (see Figure 2.1) until  $Q_{cc}(\theta, \phi)$  converges and an equilibrium mantle temperature, melt fraction and magmatic heat output are found.

In the following we give a general description of a volumetric heated system (Section 2.3.1) before we describe the different steps of the above introduced model procedure: the blurring of Io's produced heat (Section 2.3.2), the approximation of the mantle temperature (Section 2.3.3), and the inclusion of the laterally varying magmatic heat transport and the iteration scheme (Section 2.3.4).

### 2.3.1. STEADY-STATE SCALING OF A VOLUMETRIC HEATED CONVECTIVE SYSTEM

Io is intensively heated from within the mantle. Its heat flux is more than 100 times larger than the heat flux of Earth's moon ([Langseth et al., 1976](#)), therefore radioactive decay and remnant heat play a minor role for Io's heat budget. For this study, it is therefore assumed that the net heat flux from the core to the mantle is zero ([Tackley et al., 2001](#); [Wienbruch and Spohn, 1995](#)). We assume that Io's mantle is incompressible, convective, and separated from the surface by a stagnant lid ([Moore, 2003](#)). Furthermore, we assume that the heat production rate is close to the heat loss of the system as suggested for Io by [Lainey et al. \(2009\)](#). Scaling laws for internally heated Cartesian systems in a thermal steady state have been investigated numerically ([Parmentier and Sotin, 2000](#); [Parmentier et al., 1994](#); [Vilella and Kaminski, 2017](#)) and by laboratory experiments ([Limare et al., 2015](#)). Both types of experiments show that in a volumetric heated system active down-welling with passive up-welling occurs. This leads to a sub-adiabatic geotherm as schematically shown in Figure 2.2. Thus, the maximum temperature within the convective system can be found at the bottom of the thermal boundary layer, which is a thin layer below the stagnant lid. The thermal boundary is still a part of the convective layer, according to the used scaling law, although its temperature profile is conductive. We assume that the heat transport by magma is proportional to the maximum melt fraction. Consequently, knowledge of the slope of the adiabat is not required. However, the used scaling law for mantle convection does not account for the presence of melt, thus it is implicitly assumed that melt and heat are removed immediately, without interfering with the mantle convection. To estimate the maximum temperature specific parameters of the convective system, such as the temperature increase across the convective layer and the strength of convection, the Rayleigh-Roberts number is required. This will be briefly introduced here. In a purely internally heated system the temperature jump across the convective layer  $\Delta T_H$  can be non-dimensionalized using a volumetric heat production scale ([Schubert et al., 2001](#))

$$\Delta T_H = a_f \frac{Hd^2}{k_m}, \quad (2.9)$$

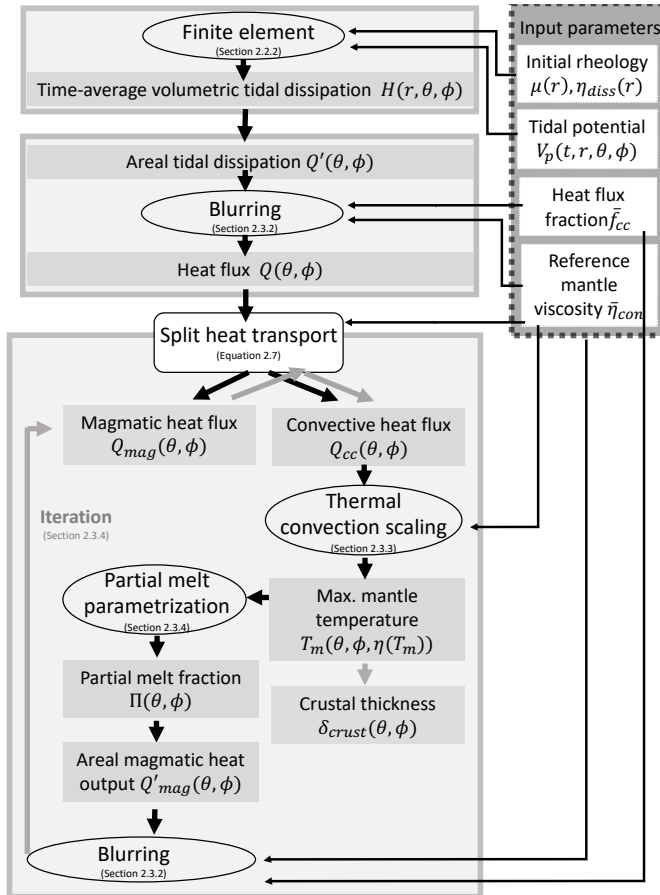


Figure 2.1: Flow chart of all modelling steps. Big grey boxes give the three main model steps. The finite element model is described in Section 2.2, the blurring, the steady-state scaling, and the partial melt parametrization and the iteration of the local heat flux fluctuation  $Q_{cc}(\theta, \phi)$  are presented in Section 2.3. The dashed box on the right represents the main input parameters, oval boxes give modelling sub-procedures and rectangular boxes display intermediate and final model outputs.

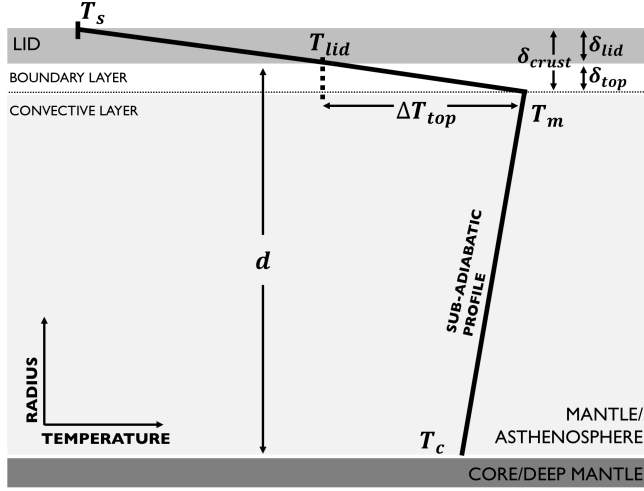


Figure 2.2: Schematic temperature profile of Io. The geotherm is plotted in a Cartesian system of the radius and temperature. In the modelling we correct for the spherical geometry.

where  $H$  is the volumetric heat production,  $d$  the thickness of the convective layer and  $k_m$  is the thermal conductivity. The factor

$$a_f = \frac{1}{3} \left[ 1 + \frac{R_{con}}{R_{con} + d} + \left( \frac{R_{con}}{R_{con} + d} \right)^2 \right] \quad (2.10)$$

is the correction due to the spherical geometry ([Deschamps et al., 2012](#)), where  $R_{con}$  is the radial distance from the centre of Io to the bottom of the convective layer.

To estimate the lateral heat flow and to approximate the geotherm throughout the convective layer we need to know the Rayleigh-Roberts number ([Roberts, 1967](#)). The Rayleigh-Roberts number ([Roberts, 1967](#)) is a variant of the Rayleigh number describing the ratio between convection driving and convection inhibiting forces ([Schubert et al., 2001](#)) for a volumetric heated system and is given by

$$Ra_H = \frac{a_f \rho_m g \alpha H d^5}{k_m \eta_{con} \kappa}, \quad (2.11)$$

where  $\rho_m$  is the reference mantle density,  $\kappa$  is the thermal diffusivity,  $\eta_{con}$  the mantle convection viscosity,  $\alpha$  the thermal expansion coefficient, and  $g$  the acceleration of gravity. Since we only consider direct effects of the tidal dissipation pattern on the temperature distribution, we assume that these mantle properties do not change with depth throughout the convective system. The influence of a radially non-homogeneous heating on the temperature profile of a convective system has been investigated for a two-layered spherically symmetric heating pattern ([Vilella and Kaminski, 2017](#)). However, to our knowledge no scaling laws are available that can deal with complex radially varying

heating distributions, as for Io. That is why we merge the three dimensional volumetric heating patterns  $H(r, \theta, \phi)$  obtained in Section 2.2 into a two-dimensional pattern

$$Q'(\theta, \phi) = \int_{R_{con}}^{R_{con}+d} H(r, \theta, \phi) dr, \quad (2.12)$$

where  $d$  is the thickness of the simultaneously internally heated and convective layer. Note that  $Q'(\theta, \phi)$  obtained from Equation 2.12 is not Io's actual heat flux  $Q(\theta, \phi)$ .  $Q'(\theta, \phi)$  is the pattern of the heat production per unit area, or, in other words, a projection of the produced three-dimensional volumetric heat production onto Io's surface. In the following the blurring model, which estimates the actual heat flux pattern  $Q(\theta, \phi)$  taking into account lateral flow due to convection, is explained.

### 2.3.2. LATERAL HEAT FLOW DUE TO CONVECTION

The heat flow in a convective medium is not only in radial direction but also in lateral direction. This convective heat flow in lateral direction results in a lateral smoothing of the spatial varying heating pattern. Blurring can be described as a weakening of higher degrees of the computed power spectrum of the dissipation pattern, thus it acts as a low-pass filter. The heat production per unit area is decomposed into spherical harmonics:

$$Q'(\theta, \phi) = \bar{Q}' + \sum_{n=1}^{n_{max}} \sum_{m=0}^n \bar{P}_{nm}(\cos\theta) (C_{nm} \cos m\phi + S_{nm} \sin m\phi). \quad (2.13)$$

$\bar{P}_{nm}$  is the fully normalized associated Legendre function of degree  $n$  and order  $m$  and  $\bar{Q}'$  the mean global heat flux. The actual total heat flux function is derived by

$$Q(\theta, \phi) = \bar{Q} + \sum_{n=1}^{n_{max}} B(n) \sum_{m=0}^n \bar{P}_{nm}(\cos\theta) (C_{nm} \cos m\phi + S_{nm} \sin m\phi), \quad (2.14)$$

with

$$\bar{Q}' = \bar{Q}. \quad (2.15)$$

The blurring is achieved through a filter  $B(n)$ , i.e. the blurring factor, which is given by

$$B(n) = C \bar{Ra}_H^{-\beta} \frac{R\pi}{nd}. \quad (2.16)$$

According to [Tackley \(2001\)](#),  $C$  is a constant and  $\beta$  is equal to 1/4 for the analytically investigated homogeneous case. However, for a boundary-focused heating profile (e.g. Figure 1 in [Tackley et al., 2001](#)), characteristic for Io's asthenosphere,  $\beta$  changes its value as shown numerically by [Tackley \(2001\)](#). The effectiveness of the blurring is approximated using the globally averaged Rayleigh-Roberts number  $\bar{Ra}_H$

$$\bar{Ra}_H = \frac{a_f \rho_m g \alpha \bar{f}_{cc} \bar{Q} d^4}{k_m \bar{\eta}_{con} \kappa}, \quad (2.17)$$

which is derived from Equation 2.11, but here given as a function of the globally averaged convective-conductive heat flux  $\bar{f}_{cc} \bar{Q}$  and the reference mantle viscosity  $\bar{\eta}_{con}$ . Because

we do not consider any radial fluctuation of the blurring strength, we replace the volumetric heat  $H$  with  $Q/d$ . To fulfil the conservation of energy, the globally averaged heat flux ( $n = 0$ ) needs to remain the same (see Equation 2.15). Consequently,  $B(n = 0)$  is set equal to 1. As none of the higher degree signals should be increased by the blurring,  $B(n > 0)$  is forced to be 1 if resulting in a value larger than 1. From Equation 2.13 and Equation 2.16 it becomes obvious that a large Rayleigh-Roberts number  $\overline{Ra}_H$  as well as a large convective layer thickness  $d$  cause strong blurring of the tidal dissipation signal.

Also the magmatic heat output driven by melt  $Q'_{mag}(\theta, \phi)$ , calculated in Section 2.3.4, needs to be blurred in order to approximate the amount of heat  $Q_{mag}(\theta, \phi)$  neighbouring regions can feed a magma reservoir due to convective motion. This allows the surface heat output by melt  $Q'_{mag}(\theta, \phi)$  to regionally exceed the tidal heat production  $Q'(\theta, \phi)$  directly produced below a specific area, which is usually the case for magmatic systems.

### 2.3.3. THERMAL PROFILE OF IO'S INTERNALLY HEATED MANTLE

Next, we compute the maximum mantle temperature at the bottom of the thermal boundary layer and corresponding properties of Io's thermal profile using the parameters determined in Section 2.3.1. For that, only the convective-conductive part of the heat flux  $Q_{cc}(\theta, \phi)$  (Equation 2.8) is considered. In contrast to the approximation of the blurring where we considered a global average Rayleigh-Roberts number (Equation 2.17) because of the global filtering approach (Equation 2.14), the Rayleigh-Roberts number  $Ra_H(\theta, \phi)$  is treated as a spatial-dependent property of the interior here.

The relation between the convective-conductive heat flux and magmatic heat flux changes locally, since we assume that the intensity of the magmatic heat flux depends on the amount of melt. The melt distribution is initially unknown, as it depends on the initially unknown local mantle temperature and initially unknown distribution of  $Q_{cc,final}(\theta, \phi)$ . That is why we take the global average convective-conductive heat flux  $Q_{cc,i=1} = \overline{f}_{cc}Q(\theta, \phi)$  as an a-priori value in the first iteration step  $i = 1$ . Each further iteration step  $Q_{cc,i}(\theta, \phi)$  is updated (see Figure 2.1), until the final distribution of the heat flux variation  $Q_{cc,final}(\theta, \phi)$  is found. Thereby, the local heat flux fraction  $f_{cc,i}(\theta, \phi)$  between the local heat flux  $Q(\theta, \phi)$  and the convective-conductive heat flux  $Q_{cc,i}(\theta, \phi)$  is allowed to change. However, we force the globally averaged convective-conductive heat flux  $\overline{Q}_{cc}$  and consequently the heat flux fraction  $\overline{f}_{cc}$  given in Equation 2.8 to remain constant for each iteration step.

We substitute  $H/d$  with the convective-conductive heat flux  $Q_{cc,i}(\theta, \phi)$  in Equation 2.11 and Equation 2.9. The Rayleigh-Roberts number distribution for each iteration step  $i$  is therefore given by

$$Ra_{H,i}(\theta, \phi) = \frac{a_f \rho_m g \alpha Q_{cc,i}(\theta, \phi) d^4}{k_m \eta_{con}(\theta, \phi) \kappa}, \quad (2.18)$$

and the distribution of the a-priori temperature jump across the convective layer is given by

$$\Delta T_{H,i}(\theta, \phi) = a_f \frac{Q_{cc,i}(\theta, \phi) d}{k_m}. \quad (2.19)$$

We use the scaling law introduced by *Vilella and Kaminski (2017)* to approximate the temperature at the top of up-streaming vents just below the thermal boundary layer, i.e. the maximum mantle temperature (see Figure 1 in *Vilella and Kaminski, 2017*). We follow their approach for two reasons: 1) The scaling is based on an analytical description allowing to consider a wide range of the Rayleigh-Roberts numbers. 2) Other scaling laws for volumetric heating schemes (e.g. *Parmentier et al., 1994*) investigate the mean mantle temperature. Using these kind of scaling laws, we would underestimate the melt fraction. As described in *Vilella and Kaminski (2017)* this maximum mantle temperature arising in hot up-streams is not omnipresent in a convective mantle. Thus, applying the resulting temperature and corresponding melt fraction globally, would result in an over-estimation of the presence of melt. However, the fraction between hot up-streams and cold down-streams is implicitly included in the variable  $\bar{f}_{cc}$ , which we use for the estimation of the heat flux transported by melt in Section 2.3.4. As the variable  $\bar{f}_{cc}$  comprises a large set of poorly known parameters it is investigated for a wide range of possible values. Thus, an explicit knowledge of the surface fraction is not required, as long as we assume that the up-streams are uniformly distributed. A schematic temperature profile with all the important parameters introduced in the following is shown in Figure 2.2.

The maximum temperature jump  $\Delta T_{top,i}(\theta, \phi)$  across the thermal boundary layer is determined by

$$\Delta T_{top,i}(\theta, \phi) = \frac{1}{2} \Delta T_{H,i}(\theta, \phi) \left( \frac{Ra_{H,crit}}{Ra_{H,i}(\theta, \phi)} \right)^{1/4}, \quad (2.20)$$

following *Vilella and Kaminski (2017)*. In contrast to Equation 18 in *Vilella and Kaminski (2017)* the spherical symmetric correction factor  $a_f$  is not included in Equation 2.20, as the correction is already included in  $\Delta T_{H,i}$  (Equation 2.19). The critical Rayleigh-Roberts number  $Ra_{H,crit}$  provides a threshold value that determines whether the system is convective or conductive. The maximum mantle temperature at the corresponding latitude and longitude is a function of the maximum temperature jump across the thermal boundary layer  $\Delta T_{top,i}$  and can be approximated by (*Grasset and Parmentier, 1998; Tosi et al., 2017*)

$$T_{m,i}(\theta, \phi) = \sqrt{\Delta T_{top,i}(\theta, \phi) \frac{E_a}{2.9 R_{gas}}}, \quad (2.21)$$

with the activation energy  $E_a$  and the gas constant  $R_{gas}$ .

Substituting Equation 2.18 and 2.19 into Equation 2.21 and further simplification results in a new expression for the maximum mantle temperature

$$T_{m,i}(\theta, \phi) = \gamma_0 \left( a_f Q_{cc,i}(\theta, \phi) \right)^{\frac{3}{8}} \eta_{con}(\theta, \phi)^{\frac{1}{8}}, \quad (2.22)$$

with

$$\gamma_0 = \sqrt{\frac{E_a}{5.8R_{gas}}} \left( \frac{\kappa Ra_{H,crit}}{\rho_m g \alpha k^3} \right)^{\frac{1}{8}}. \quad (2.23)$$

From Equation 2.22 it can be seen that the maximum mantle temperature increases with increasing viscosity and increasing magmatic heat output.

Note that  $\eta_{con}(\theta, \phi)$  is not constant as it depends on the mantle temperature distribution  $T_m(\theta, \phi)$ . Despite this being a minor effect, we developed a procedure correcting for it using the Lambert relation. We describe the full procedure in 2.6.

#### 2.3.4. MAGMATIC HEAT TRANSPORT BY MELT AND ITERATIVE PROCEDURE

We assume that the amount of heat transported by magma in a certain region depends on the local melt fraction. To calculate the latter, we follow *Katz et al. (2003)* considering an anhydrous solidus of a peridotitic lherzolite, which can be found in the Earth's mantle. The parametrization for the melt fraction is a function of pressure and temperature and serves as a good approximation of the ultra-mafic material, which is present at some of Io's volcanoes (*Davies et al., 2010*). Note, however, that sulphur is an abundant material on Io's surface and plays an important role in Io's volcanic activity. The melting temperature reducing effect of sulphur is not included in this study, since the presence and influence of sulphur in Io's deep layers are not well known.

The melt fraction is given as a fractional distance between solidus and liquidus (*Hirschmann, 2000*)

$$\Pi_i(\theta, \phi) = \frac{T_{m,i}(\theta, \phi) - T_{sol}(P)}{T_{liq}(P) - T_{sol}(P)}, \quad (2.24)$$

where  $T_{sol}(P)$  and  $T_{liq}(P)$  are polynomial functions of the pressure  $P$  (Table 2, Equation 4 and 5 in *Katz et al., 2003*). Note that the above version of the melt parametrization results in small but increasing inaccuracies with increasing melt fractions. Furthermore, we ignore any spatial variation of the crustal thickness (Equation 2.31) as well as the thickness of the thermal boundary layer, and approximate the maximum melt fraction at the depth of the initial crustal thickness of the rheological model (Section 2.2). From Equation 2.24 we calculate the globally averaged maximum melt fraction  $\bar{\Pi}_i$  in up-rising plumes.

Parameters that determine how much melt is transported per surface fraction are difficult to predict for Io. We assume that the melt transport efficiency is proportional to the melt fraction just below the thermal boundary layer, and that the melt-containing up-streams are not omnipresent but equally distributed. Thus, we determine the global heat transport efficiency

$$\bar{\varphi}_{melt,i} = \frac{\bar{Q}_{mag}}{\bar{\Pi}_i}, \quad (2.25)$$

using the average global magmatic heat flux  $\bar{Q}_{mag} = (1 - \bar{f}_{cc})\bar{Q}$  and the globally averaged melt fraction  $\bar{\Pi}_i$ . Note again, that  $\bar{Q}$  is an observational constraint and the variable

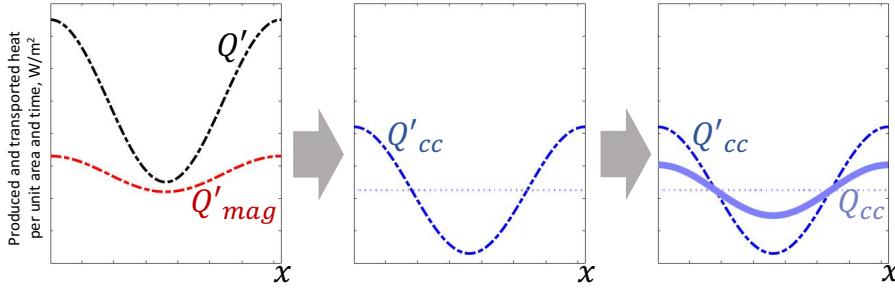


Figure 2.3: Schematic graph of a heat production and heat transport profile along an arbitrary profile  $x$  (one wavelength only). Out of the total produced heat per unit area and unit time  $Q'$  (black dashed line) and the magmatic heat output  $Q'_{mag}$  (red dashed line) we derive the amount of remaining heat that needs to be transported by mantle convection. We get  $Q'_{cc} = Q' - Q'_{mag}$  (blue dashed line). For  $Q'_{cc}$  the lateral flow due to convection is not considered. Therefore,  $Q'_{cc}$  is blurred to account for lateral flow and we get  $Q_{cc}$  (blue solid line). Regions with  $Q'_{cc} > Q_{cc}$  have a negative lateral net heat flow. Regions with  $Q'_{cc} < Q_{cc}$  have a positive lateral net heat flow. The average convective heat flow  $\bar{Q}_{cc}$  (thin dotted blue line) remains the same for  $Q'_{cc}$  and  $Q_{cc}$ .

$\bar{f}_{cc}$  is constant throughout the iterations. The factor  $\bar{\varphi}_{melt,i}$  determines a heat flux per melt fraction. It combines several heat pipe parameters, such as the fraction of hot upstreams within a certain area, the latent heat, the buoyancy or corresponding velocity and the density of melt as used by [Moore \(2001\)](#), [Elder \(2015\)](#) and [Bierson and Nimmo \(2016\)](#). Next, we solve for the magmatic heat output per unit area

$$Q'_{mag,i}(\theta, \phi) = \bar{\varphi}_{melt,i} \Pi_i(\theta, \phi). \quad (2.26)$$

$Q'_{mag,i}(\theta, \phi)$  is considered as a negative heat source per unit area, i.e. the opposite sign as the produced heat  $Q'(\theta, \phi)$ . We apply the blurring filter (Equation 2.16) resulting in  $Q_{mag,i}(\theta, \phi)$  and obtain the new convective-conductive heat flux:

$$Q_{cc,i+1}(\theta, \phi) = Q(\theta, \phi) - Q_{mag,i}(\theta, \phi). \quad (2.27)$$

Due to the linear behaviour of the blurring filter it is also possible to derive  $Q_{cc,i+1}(\theta, \phi)$  given in Equation 2.27 in a different way (Figure 2.3).

We enter the result of Equation 2.27 into Equation 2.22 and recalculate Equations 2.22-2.26 until convergence is found. This way an equilibrium between convective-conductive and magmatic heat flux for each co-latitude and longitude is found for a specific set of input parameters. The obtained equilibrium considers the initial heat production, the convective manner of the asthenosphere and mantle, the temperature-dependence of melt occurrence, and heat transport by melt. Once convergence is found ( $Q_{cc,i-1} \approx Q_{cc,i} = Q_{cc,final}$ ) we obtain the posteriori lateral pattern of  $T_m(\theta, \phi)$ ,  $Q'_{mag}(\theta, \phi)$ ,  $Q_{cc}(\theta, \phi)$  and the lateral varying melt distribution  $\Pi(\theta, \phi)$  (see Figure 2.1).



### 2.3.5. LATERAL THICKNESS VARIATIONS OF THE THERMAL BOUNDARY AND CRUST

In the last step, we check whether our thermal models result in crustal thicknesses in agreement with the rheological structure given in Section 2.2.3. For that, the final heat flux distribution  $Q_{cc}(\theta, \phi)$  and the final maximum mantle temperature  $T_m(\theta, \phi)$  are taken into account.

The thickness of the boundary layer is calculated according to *Vilella and Kaminiski (2017)*:

$$\delta_{top}(\theta, \phi)/d = \left( \frac{Ra_{H,crit}}{Ra_H(\theta, \phi)} \right)^{1/4}. \quad (2.28)$$

From Equation 2.21 we get the maximum temperature below the lid

$$T_{lid}(\theta, \phi) = T_m(\theta, \phi) - \Delta T_{top}(\theta, \phi). \quad (2.29)$$

We calculate the thickness of the conductive stagnant lid

$$\delta_{lid}(\theta, \phi) = k_{lid} \frac{T_{lid}(\theta, \phi) - T_s}{Q_{cc,i}(\theta, \phi)}, \quad (2.30)$$

where  $k_{lid}$  is the thermal conductivity of the stagnant lid and  $T_s$  is the surface temperature. Both parameters are assumed to be spatially uniform. We neglect any heat production in the conductive lid. Further, we assume that the conductive heat flux in the stagnant lid is equal to the convective heat flux in the mantle. Finally, we obtain the conductive crustal thickness (Figure 2.2), adding the thickness of the thermal boundary layer and the thickness of the stagnant lid:

$$\delta_{crust}(\theta, \phi) = \delta_{lid}(\theta, \phi) + \delta_{top}(\theta, \phi). \quad (2.31)$$

Note the minor discrepancy between the thermal and the visco-elastic model. For the thermal model the thermal boundary layer belongs to the heated asthenosphere, however, its visco-elastic characteristics are more in agreement with the crust. However, this discrepancy has no effect on our results and conclusions because the evolving thickness of the thermal boundary layer is very small for most of the investigated mantle viscosities.

### 2.3.6. THERMAL PROPERTIES OF IO MODELS

In this section we discuss the thermal properties of the two end-member cases that have already been introduced in Section 2.2. For Model A, we allow only the asthenosphere to be convective because all of the tidal heating will occur in the asthenosphere (defined in Table 2.3). We treat the asthenosphere-deep mantle boundary as a non-permeable layer, allowing no exchange of material and neglect the heat flux from the core and the deep mantle. A fully convective mantle including the deep mantle and the asthenosphere is assumed for Model B. As presented in Table 2.3 both the deep mantle and the asthenosphere are heated by tides and therefore need to lose heat efficiently. Accordingly, the thickness of the convective layer  $d$  and the geometrical correction for the spherical

geometry  $a_f$  for Model B are different from Model A.

For simplicity, we assume that the mantle properties such as the viscosity  $\eta_{con}$ , the density  $\rho_m$ , the thermal expansivity  $\alpha$ , the conductivity  $k_m$  and the diffusivity  $\kappa$  (all given in Table 2.2) are constant throughout the convective system. We also consider the mantle viscosity  $\eta_{con}$  for Model B to be radially constant, but we use different Maxwell viscosities  $\eta_{dis}$  for the deep mantle and the asthenosphere (Table 2.3). For the stagnant lid, which is assumed to be present for Io (Moore, 2003), the critical Rayleigh-Roberts number is 2772 (Roberts, 1967). The respective proportionality constants  $C$  and  $\beta$  quantifying the strength of the blurring are taken for a boundary-focused heating profile from Tackley (2001) (both given in Table 2.2). The average gravitational acceleration  $g$  is calculated at the top of the convective system based on the density profile given in Section 2.2. The surface temperature  $T_s$  is set to 100 K as done in Moore (2003) and the thermal conductivity of the lid  $k_{lid}$  is the same as for the mantle.

## 2.4. RESULTS

In this section we present the volumetric heat distribution of our benchmarked finite element models. Further, we follow Section 2.3.3 and 2.3.4 and present the spatial temperature, melt, and heat flux patterns for selected sets of interior parameters. This is followed by a parameter study, investigating the strength of the tidally-induced effect on Io's interior for a wide range of parameters.

### 2.4.1. TIDAL DISSIPATION PATTERN OF THE FINITE ELEMENT MODEL

We set up the numerical model as described in Section 2.2. All model specific adjustments and a benchmark showing that the accuracies of the numerical results are sufficient for further use can be found in 2.7. The resulting spatial patterns of heat production  $H(r, \phi, \theta)$  for both models, averaged over one orbit are given in Figure 2.4.

For Model A, strong heating is present at the lid-asthenosphere-boundary and at the asthenosphere-deep-mantle-boundary. This is because strong lateral deformation is present within the viscous asthenosphere causing friction at the boundaries. These deformations are smaller towards high latitudes. In the polar cut, large variations between the polar areas at 90° N and 90° S and the equatorial areas are seen. The rheological structure chosen for Model B results in a more evenly distributed volumetric heat production.

The differences between Model A and Model B become also obvious in the two-dimensional pattern of the heat production per unit area  $Q'(\phi, \theta)$  (Figure 2.5) obtained after the radial integration of the produced heat. Both rheological structures have a similar average heat flux (Table 2.5) but result in different dissipation patterns. For Model A 30° North and South of the sub-Jovian point the maximum areal heat production is approximately  $3.6 \text{ W m}^{-2}$  and no tidal heat is produced at the poles. For Model B the heat generation is more evenly distributed. The patterns in Figure 2.5a and Figure 2.5b are qualitatively compatible to Figure 2b and Figure 3c in Ross *et al.* (1990) for which

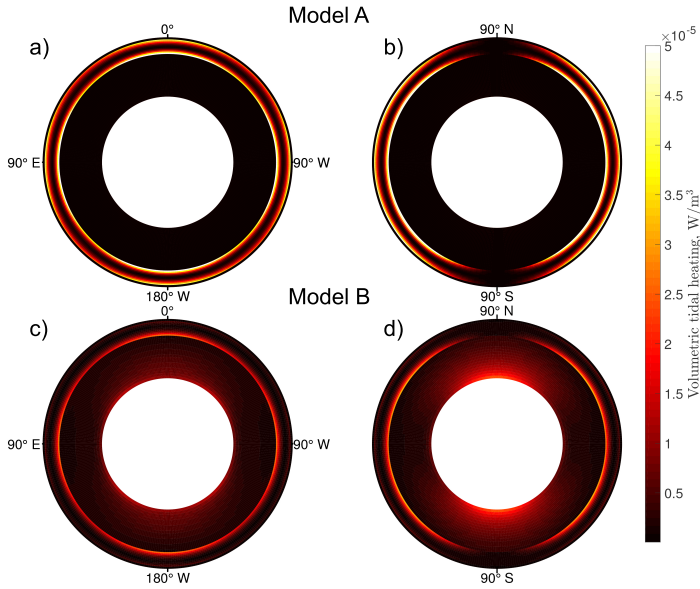


Figure 2.4: Volumetric dissipation in Io's mantle and asthenosphere Model A and Model B. a) and c) cross-sections along Io's equator plane for Model A and Model B, respectively. b) and d) cross-sections along the plane of the North and South pole, and Io's sub-Jovian point.

slightly different rheological structures were used.

#### 2.4.2. SPATIAL PATTERNS OF TEMPERATURE, MAGMATIC HEAT OUTPUT, MELT FRACTION AND CRUSTAL THICKNESS

In this section we calculate the temperature, magmatic heat flux, melt fraction and crustal thickness for a set of main input parameters, which are the heat flux fraction  $\bar{f}_{cc}$  and the reference mantle viscosity  $\bar{\eta}_{con}$ . The sets only produce one out of many possible outcomes for Model A and Model B and are chosen in a way that the input values are realistic to describe Io's interior and on the other hand result in model outputs close to our initial rheological model. For the filter we chose  $n_{max} = 10$  (Equation 2.14). This is sufficient to describe the modelled tidal dissipation pattern, which, apart from minor numeric-induced artefacts, only contains components of  $n \leq 4$  (Beuthe, 2013). Next, we iterate Equations 2.22-2.26. We only consider solutions that fulfil the convergence criteria of  $Q_{cc,i-1} - Q_{cc,i} < 10^{-3} \text{ W m}^{-2}$  for each single co-latitude and longitude within 400 iterations. However, for most of the models this is achieved in 20-30 iterations. Testing for different starting values and step sizes indicates that the obtained results are stable.

The two different sets of reference mantle viscosity and heat flux fraction and major resulting interior properties are presented in Table 2.4. For Model A and Model B the chosen parameter sets result in a globally averaged maximum mantle temperature  $\bar{T}_m$

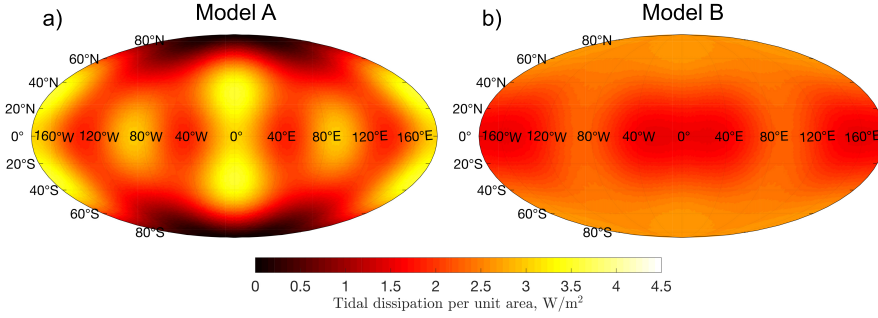


Figure 2.5: Produced heat per unit area projected onto Io's surface (Mollweide projection) for Model A (a) and Model B (b).

Table 2.4: Parameter sets of  $\bar{f}_{cc}$  and  $\bar{\eta}_{con}$  for Model A and Model B, which result in similar globally averaged maximum mantle temperature  $\bar{T}_m$ .

Model	$\bar{f}_{cc}$	$\bar{\eta}_{con}$	$\bar{\delta}_{crust}$	$\bar{T}_m$	$\max(T_m) - \min(T_m)$
A	0.18	$4.6 \cdot 10^{14}$ Pa s	12.7 km	1514.0 K	98.1 K
B	0.0815	$1.34 \cdot 10^{16}$ Pa s	29.4 km	1514.5 K	18.9 K

close to 1513 K. This temperature corresponds to the solidus temperature at a depth of 230 km (Section 2.3.4) implying a 200 km thick partially molten layer. However, only for Model B we achieve an average crustal thickness of approximately 30 km as provided in the initial rheological model (Table 2.2). Because of the difference in the thickness of the convective layer  $d$  no solution can be found for Model A for the chosen parameter set of Model B and vice versa. This will be discussed in more detail in Section 2.4.3.

We visualize the spatial distribution of the maximum mantle temperature  $T_m(\theta, \phi)$ , the magmatic heat output  $Q_{mag}(\theta, \phi)$ , the distribution of the melt fraction  $\Pi(\theta, \phi)$  and the crustal thickness  $\delta_{crust}$  for both model specific parameter sets of Model A and B in Figure 2.6. The mantle temperature patterns of Model A and Model B (Figure 2.6a and 2.6b) follow the pattern of the areal heat production (Figure 2.5). However, all degree 4 components are significantly suppressed due to the lateral convection as simulated by the blurring filter. Note again that the presented temperature distribution gives maximal possible values of the mantle temperature at the bottom of the thermal boundary layer and is only valid in case a hot up-streaming plume is present below this location. In addition, temperature buffering near the solidus due to latent heat is not included (as e.g. discussed in Ross *et al.*, 1990). The resulting melt fractions also represent maximum values (Figure 2.6e and 2.6f). The average melt fractions are consequently much lower.

The magmatic heat output is assumed to be proportional to the volcanic activity level. Consequently, the resulting magmatic heat output maps can be used to indicate the expected eruption intensity and frequency for Io. For Model B the volcanic activity due to any tidally induced lateral varying thermal differences fluctuates about 7%

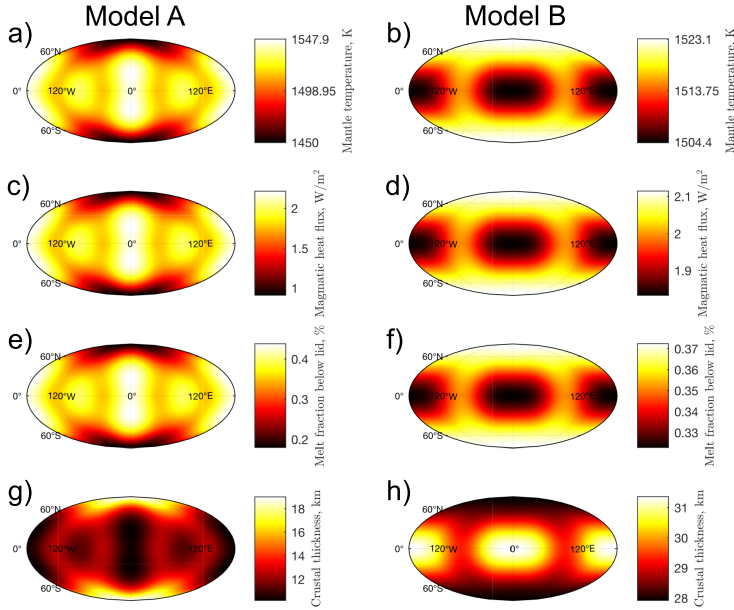


Figure 2.6: Spatial pattern of maximum mantle temperature (a and b), magmatic heat output (c and d), melt fraction (e and f), and crustal thickness (g and h) for Model A and Model B, respectively.

around its average value. This fluctuation might be too small to be detected through long-term observations of Io's volcanic activity pattern. For the chosen parameter set of Model A a fluctuation of around 37% can be expected. The crustal thickness maps (Figure 2.6g and 2.6h) show converted patterns of the temperature distribution. Note that processes such as volcanic re-surfacing, near-surface intrusions, and the change in effectiveness of melt advection with changing crustal thickness are neglected (*O'Reilly and Davies, 1981; Stevenson and McNamara, 1988*).

### 2.4.3. INFLUENCE OF INTERIOR PARAMETERS

In the following, we derive the average maximum mantle temperature  $\bar{T}_m$ , the maximum temperature variation (peak-to-peak), the maximum difference of the normalized magmatic heat output  $(\max(Q'_{mag}) - \min(Q'_{mag})) / \bar{Q}_{mag}$ , and the average crustal thickness for a wide range of  $\bar{\eta}_{con}$  and  $\bar{f}_{cc}$  according to Table 2.2. We use the normalized value here for the magmatic heat output, as  $\bar{Q}_{mag}$  changes with  $\bar{f}_{cc}$ . By normalizing the peak-to-peak values with  $\bar{Q}_{mag}$ , the relative differences in the strength of the magmatic heat output, and hence the relative difference of the volcanic activity level, become comparable. The results for Model A and Model B are presented in Figure 2.7a-h. The Rayleigh-Roberts number, which quantifies the vigor of the convective flow and thus the strength of the blurring (Equation 2.16), is presented in 2.8.

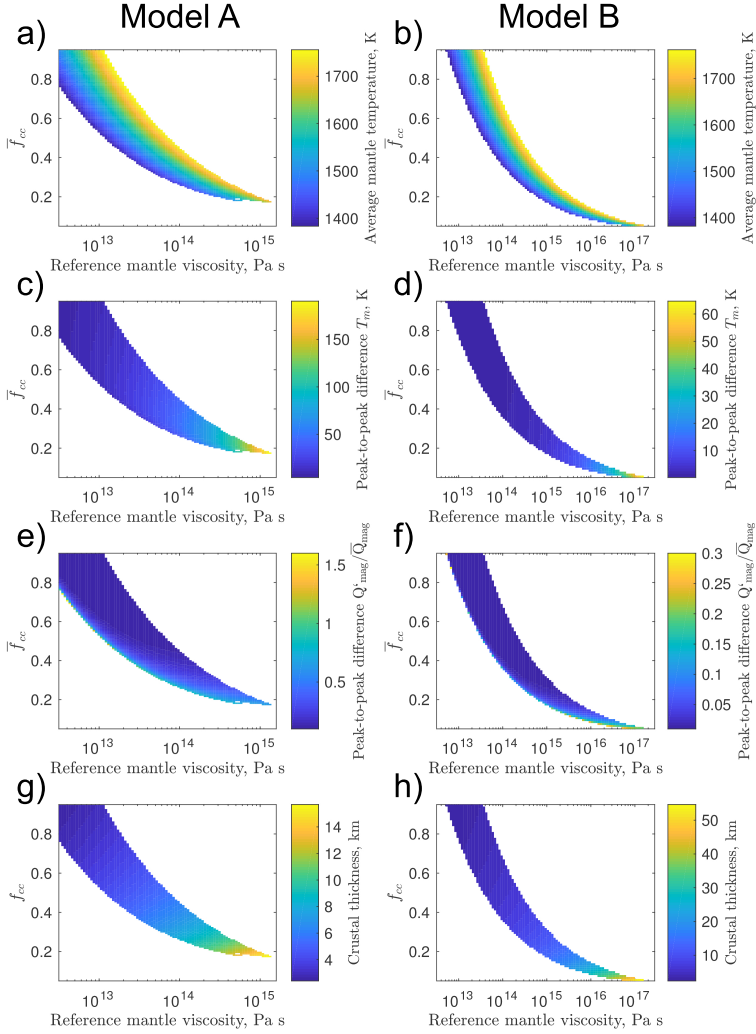


Figure 2.7: The figure shows average maximum mantle temperature (a and b), peak-to-peak temperature difference (c and d), normalized peak-to-peak magmatic heat output per unit area (e and f), and average crustal thickness (g-h) for Model A and Model B as a function of the mantle viscosity  $\bar{\eta}_{con}$  and  $\bar{f}_{cc}$ .  $\bar{f}_{cc}$  quantifies the dominant heat transport mechanism, with small values representing models with a magma-dominating heat transport, and values close to 1 representing models with a convection-dominating heat transport. Note the different scales for the reference viscosities.

Although we test all combinations of  $\bar{f}_{cc}$  and  $\bar{\eta}_{con}$ , solutions can only be found for the coloured regions. A reason for this is that the maximum mantle temperatures need to be between the solidus and liquidus. In case no melt is present no heat can be transported by melt. Thus, no solution can be found for  $\bar{f}_{cc} < 1$ . Furthermore, melt fractions larger than 1 at any location are not allowed. Due to these boundary conditions valid solutions are found to be in parabolic-shaped regions running from high  $\bar{f}_{cc}$  and low  $\bar{\eta}_{con}$  values to low  $\bar{f}_{cc}$  and high  $\bar{\eta}_{con}$  values. Within these regions the highest average maximum temperatures are obtained for high  $\bar{f}_{cc}$  values and high reference viscosities  $\bar{\eta}_{con}$  (Sub-figures a and b of Figure 2.7). A high viscosity suppresses vigorous mantle convection leading to higher mantle temperatures. A mantle in thermal equilibrium with a high fraction of magmatic heat transport (low  $\bar{f}_{cc}$  value) would be cooler than a mantle with the same reference mantle viscosity but a low fraction of magmatic heat transport (high  $\bar{f}_{cc}$  value).

In contrast to Model B, we cannot find solutions for any parameter sets with  $\bar{f}_{cc} < 0.17$  for Model A. This can be explained as follows: For parameter sets resulting in a low average maximum mantle temperature but large temperature differences, the temperature does not remain above the solidus for each location. Consequently, only some regions sustain melt. However, in the case where we force the model to yield a high fraction of global magmatic heat output (low  $\bar{f}_{cc}$  value), the regions that sustain a mantle temperature above the solidus need to maintain a high magmatic heat output per unit area  $Q'_{mag(\theta,\phi)}$ . This magmatic heat output per unit area  $Q'_{mag(\theta,\phi)}$  can be theoretically larger than the heat  $Q'(\theta,\phi)$  produced directly underneath this location, but only up to the extent to which convection is able to provide the remaining heat from the neighbouring regions. Viewed analytically,  $Q_{cc,i}(\theta,\phi)$  needs to be positive (Equation 2.27) in order for Equation 2.22 to result in a non-imaginary value and allow for convergence. This implies that for a very strong initial dissipation pattern with very high fluctuations and a thin convective layer, such as for Model A, a low mantle viscosity and a convective-conductive heat flux fraction larger than 0.17 are necessary.

Not all of the successfully converged parameter sets (Figure 2.7) necessarily result in realistic interior models. Parameter sets resulting in high average mantle temperatures causing an average melt fractions above 40% are inconsistent with model assumptions: 1) The melt fraction computation based on *Katz et al. (2003)* is only valid for low melt fractions. 2) The melt transport model is based on the assumptions that melt flows through pores in a solid matrix, which is only valid for melt fractions below 30% (*Moore, 2001*). However, the obtained melt fractions estimates give maximum values and occur only locally. Hot up-streams are not omnipresent and Io's sub-adiabatic geotherm and increasing pressures prevent melt production for deeper layers. Thus, even we do not favour these sets, we decide not to eliminate them from our results. Also parameter sets resulting in a average crustal thickness below 8 km are not favoured (Figure 2.7g), but are included in the graphs for the sake of completeness.

Io's melt fraction obtained from observations is still under discussion (*Khurana et al., 2011; Roth et al., 2017*) and cannot be used to constrain the parameter space. Note

that the parameter  $\gamma_0$  (Equation 2.23) contains a collection of parameters determining the mantle convection. Some of these parameters, such as the activation energy  $E$ , the thermal conductivity  $k_m$ , and the critical Rayleigh-Roberts number are not exactly known. For a smaller  $\gamma_0$  the parabolic line of Figure 2.7 would be shifted to larger viscosities. Thus, the reference viscosity would need to be larger to reach the comparable average maximum mantle temperatures and peak-to-peak differences. The opposite is the case for a larger  $\gamma_0$ .

The maximum temperature fluctuations (peak-to-peak) for ModelA shown in Figure 2.7c are more than one order of magnitude larger than for sets with the same reference mantle viscosities of ModelB. For ModelA peak-to-peak maximum mantle temperature differences between 5 K ( $\bar{f}_{cc} = 0.95$  and  $\bar{\eta}_{con}=10^{12}$  Pa s) and 190 K ( $\bar{f}_{cc} = 0.17$  and  $\bar{\eta}_{con}=1.3 \cdot 10^{15}$  Pa s) are achieved. Differences less than 1 K ( $\bar{f}_{cc} = 0.95$  and  $\bar{\eta}_{con}=10^{12}$  Pa s) up to 65 K ( $\bar{f}_{cc} = 0.05$  and  $\bar{\eta}_{con}=1.4 \cdot 10^{17}$  Pa s) are found for Model B.

The average crustal thickness, shown in Figure 2.7g and Figure 2.7h, is affected by the dominating heat transport mechanism. It decreases with decreasing  $\bar{\eta}_{con}$  and increasing  $\bar{f}_{cc}$ . For ModelB we find a crustal thickness that is equal to the starting assumption of 30 km for  $\bar{f}_{cc}$  in the range 0.075-0.09. Due to the lack of convergence for specific parameter sets, discussed above, we cannot obtain a crustal thickness of 30 km for Model A. However, reasonable values within the lower range of the observational constraints for Io's crustal thickness are achieved. Large spatial fluctuations of the magmatic heat output as shown in Figure 2.7e and Figure 2.7f arise for low average maximum mantle temperatures and low global heat flux values. Although solutions can be found for low global heat flux values for ModelB, peak-to-peak variations remain small (around 15% around the average value). Accurate and long-term observations of Io's active volcanic features will be necessary to detect this signal. For ModelA a 91% fluctuation in volcanic activity around the average value is obtained, which is more easily detectable.

## 2.5. DISCUSSION AND CONCLUSION

Io's exceptional position within the celestial bodies of the Solar System makes it a unique laboratory to investigate hot terrestrial bodies that undergo intense heat loss. In this study, we introduce a model that couples Io's non-uniform tidal dissipation with Io's main heat transport mechanisms, i.e. mantle convection and melt advection, to investigate the spatial effect of the heterogeneous heat production on Io's interior structure and surface heat flux. We investigate two spherically symmetric end-member models. For ModelA only the asthenosphere is tidally heated and convective. For Model B, both Io's deep mantle and asthenosphere are tidally heated and convective. We compute the dissipation patterns using a finite element model based on Maxwell rheology and benchmark our results with semi-analytical models. For the thermal modelling, we combine 1) lateral convective flow simulated by reducing high-frequency signals (*Tackley, 2001*), 2) mantle convection for a volumetric heated regime using a steady-state scaling law by *Vilella and Kaminski (2017)* to compute the temperature



within uprising plumes just below the thermal boundary layer, and 3) magmatic heat transport depending on the local melt fraction following *Katz et al. (2003)*. The laterally varying heat transport mechanisms are iteratively adjusted until an equilibrium state of magmatic heat output and convective-conductive heat flux for each angular position is found.

One of the essential additions to former models is the coupling of convective and conductive heat transport with magmatic heat transport. This has been done previously by *Elder (2015)* for a one-dimensional heating structure using a different model approach, but is here incorporated for a three-dimensional heating pattern. In contrast to *Moore (2001)* and *Bierson and Nimmo (2016)*, we assume that melt does not occur due to the necessity of heat transport but due to the temperature and pressure conditions favouring the occurrence of melt. Thus, we allow for a spatially varying mantle temperature pattern and a spatially varying depth of Io's melt containing layer. In addition, we include the spatially varying magmatic heat flux in the calculation of the temperature distribution.

The incorporation of melt migration allows for a wide range of mantle viscosities to result in realistic mantle temperatures. For Model A we acquire higher mantle viscosities for Io's asthenosphere than those obtained by *Tackley (2001)* and *Tackley et al. (2001)* for a purely convective heat transport. Thus, if Io sustains a large fraction of magmatic heat transport, no global magma ocean (*Tyler et al., 2015*) is required to explain Io's high heat output. Furthermore, the inclusion of magmatic heat transport also preserves the long-wavelength pattern of tidal dissipation. This is due to two reasons. First, the time scales of rising magma are much shorter than the convective time scales of solid material. Therefore, heat transport by magma facilitates a more radial heat flow direction than convection. Second, the addition of magmatic heat transport allows for a higher solid mantle viscosity due to the additional heat transport mechanism cooling the mantle. This allows Io's asthenosphere and mantle to sustain a thermal steady state with a less vigorous convection and less lateral smoothing of the initial tidal dissipation pattern. Further, the modelling approach is suitable to get a crustal thickness range in agreement with the literature (*Turtle et al., 2007*).

The results reveal that tidal dissipation within Io's interior can cause significant lateral variations in Io's interior structure. The strength of the tidally induced signal on Io's interior structure and surface depends to a large extent on the spatial variations of the initial tidal dissipation pattern  $H(r, \theta, \phi)$ . The variations are damped by a large thickness  $d$  of the convective system, a low reference convective mantle viscosity  $\bar{\eta}_{con}$ , and a high heat flux fraction  $\bar{f}_{cc}$ , i.e. a convection-dominating heat transport mechanism. Consequently, the two models result in very different peak-to-peak mantle temperature differences. For Model A differences between 5 K up to 190 K are achieved depending on the viscosity and dominating heat transport mechanism. Temperature differences of less than 1 K and up to 65 K are found for Model B. Sets within the lower range of the  $\bar{f}_{cc}$  fraction, corresponding to sets with significant peak-to-peak temperature differences, are favoured, since parameter sets with a high heat flux fraction  $\bar{f}_{cc} > 0.4$  obtain very thin crustal thicknesses not in agreement with the observations. A better knowledge

of  $\bar{f}_{cc}$  is necessary to constrain Io's mantle viscosity and average mantle temperature (Figure 2.7). Unfortunately, it is not possible to derive  $\bar{f}_{cc}$  from Io's observed volcanic heat flow (Davies *et al.*, 2015; de Kleer and de Pater, 2016; Veeder *et al.*, 2015) and Io's poorly constrained continuous background heat flow. This is because the observed background heat flow could also arise from near-surface magmatic intrusions and former volcanic events (Stevenson and McNamara, 1988).

Investigating the modelled peak-to-peak difference of the magmatic heat output, which could serve as a prediction of the spatial volcanic activity variations, we find that the largest fluctuation amplitudes result from models that obtain an average maximum mantle temperature just above the solidus: For Model A a fluctuation of 91% around the average volcanic activity is possible, which should be detectable in a long time-series of observations. The maximum possible fluctuation for Model B (15%) would be difficult to detect. Current observations show Io's volcanic centre to be 30°-60° away from the sub- and anti-Jovian point (Hamilton *et al.*, 2013). All of our resulting magmatic heat output patterns corresponding to a relative measure of the volcanic activity are symmetric towards Io's 0° W/E longitudinal plane independent of the varied parameters. Thus, based on our modelling approach it is not possible to favour one of the investigated end-member models for Io's interior.

The most crucial components of the modelling are the blurring of the produced heat and the separate, angle-wise estimation of the maximum mantle temperature using the scaling law of Vilella and Kaminski (2017) designed for a global convective system. A comparison between the scaling law of Vilella and Kaminski (2017) and three-dimensional, numerical modelling results by Laneuville *et al.* (2013) show that a large-scale anomaly, i.e. a differently heated hemisphere of the moon, maintains its individual steady-state solution obtained by the scaling law. This supports the validity of our model approach as we analyse only large-scale patterns comparable to the investigated anomaly. In addition to that, any lateral variations of the produced heat are already softened by the applied blurring (Section 2.3.2) before we apply the scaling law to approximate the temperature field. Furthermore, we assume that the used scaling law for a melt-free convective system is not affected by magma and that for any radial profile the heat transported by melt is proportional to the heat produced by tidal dissipation.

We only investigate large-scale patterns that are caused directly by tidal heating. The actual signature on Io's observable volcanic distribution is also influenced by structural and compositional inhomogeneities of Io's interior and crust. In particular mantle convection, featuring up-streams and down-streams, is a source of small-scale temperature heterogeneities. In a convecting medium up-streams occur more likely above areas with high temperatures or increased heating. However, our approach does not consider that Io's heating pattern (Figure 2.4) may therefore facilitate certain convection schemes of up- and down-streaming patterns as suggested by Ross *et al.* (1990) and Tyler *et al.* (2015).

Any tidally induced feedbacks (secondary effects) of short- and long-wavelength

patterns of the rheology on the heating pattern and convection scheme are not included in the model. For example, the lateral differences in the melt fraction and lid thickness (Figure 2.6) eventually result in a different dissipation pattern than retrieved from our initial spherically symmetric rheological models. *Běhounková et al. (2010)* and *Han and Showman (2010)* investigated this feedback and found that the tidal perturbation in a medium with temperature anomalies produces a heating pattern with small-scale features. In particular the strong boundary-focused manner of the asthenosphere-heating (Figure 2.4) would be suppressed. In addition, areas within the asthenosphere containing both solid and fluid material could be subject to a local and strong dissipative mechanism as suggested by e.g. *Keszthelyi et al. (2007)* and *Tyler et al. (2015)*, thereby further increasing local heat production anomalies.

Despite the model uncertainties discussed above we conclude that tidal dissipation has a quantifiable effect on Io's lateral long-wavelength structure. Four interior properties determine whether the heating pattern becomes visible on Io's surface: The initial heating pattern itself, the heat transport mechanism, and the thickness and viscosity of the upper convective layer. Our results indicate that the assumption of a well-mixed interior is violated for a large number of model variables. That is why three-dimensional modelling approaches are necessary both for the computation of Io's tidal dissipation pattern and for the computation of Io's thermal heat transport. Our model based on finite elements can further be used for an extended investigation of Io's volcanic activity pattern resulting from any arbitrary or tidally induced three-dimensional rheological structure, or for investigating tidally heated exoplanets and exomoons.

## 2.6. APPENDIX-A: CORRECTION OF MANTLE TEMPERATURE DISTRIBUTION

Before we are able to estimate the melt fraction we need to correct the mantle temperature distribution for the temperature dependence of the mantle viscosity. To find the corrected distribution of the maximum temperature at the bottom of the thermal boundary layer we include a laterally varying mantle viscosity distribution. The mantle viscosity distribution  $\eta_{con}(\theta, \phi)$  is a function of the maximum mantle temperature  $T_{m,i}(\theta, \phi)$  and the initially given reference mantle viscosity  $\bar{\eta}_{con}$ . It is given by

$$\eta_{con}(\theta, \phi) = \eta_0 \exp\left(\frac{E_a}{R_{gas} T_{m,i}(\theta, \phi)}\right), \quad (2.32)$$

where

$$\eta_0 = \bar{\eta}_{con} \exp\left(-\frac{E_a}{R_{gas} \bar{T}_{m,i}}\right), \quad (2.33)$$

and  $\bar{T}_{m,i}$  is the global average of  $T_{m,i}(\theta, \phi)$ . We assume that the mean temperature of the whole mantle is not significantly smaller than the maximum temperature  $T_{m,i}$  and follows the same variations with longitude and co-latitude. Next, we substitute Equation 2.33 and 2.32 into Equation 2.22 and obtain

$$T_{m,i}(\theta, \phi) = b_1 \exp\left(\frac{b_2(\theta, \phi)}{T_{m,i}(\theta, \phi)}\right), \quad (2.34)$$

with

$$b_1 = \frac{E_a}{8R_{gas}}, \quad (2.35)$$

and

$$b_2(\theta, \phi) = \gamma_0 \left( a_f Q_{cc,i}(\theta, \phi) \right)^{\frac{3}{8}} \eta_0^{\frac{1}{8}}. \quad (2.36)$$

Equation 2.34 can be solved using the Lambert relation  $\mathcal{W}_0$ . The Lambert relation describes a set of functions providing solutions to equations where the variables are found in both the exponent and the base. We obtain our final equation for the maximum mantle temperature

$$T_{m,i}(\theta, \phi) = \frac{b_1}{\mathcal{W}_0\left(\frac{b_1}{b_2}\right)}. \quad (2.37)$$

## 2.7. APPENDIX-B: SPECIFICATIONS AND BENCHMARK OF THE FINITE ELEMENT MODEL

To ensure that the numerical finite element models work adequately, we compare the total dissipated energy rates with the results obtained by the semi-analytical approach (Jara-Oru  and Vermeersen, 2011; Sabadini et al., 2016). To get the total dissipated energy for the FE model we average over one orbital period (Equation 2.5) and interpolate all nodes of the same sub-layer to an equiangular grid and integrate radially with the midpoint Riemann sum taking the spherical geometry into account. The values for the total heat production for the semi-analytical approach and FE of Model A and Model B are given in Table 2.5.

To capture the entire dissipated power in Io's asthenosphere, a dense grid in radial direction is required. For Model A the asthenosphere is divided into 11 sub-layers to be able to capture the boundary focussed dissipation and the mantle is divided in 7 sub-layers. In Model B the asthenosphere and the mantle are divided in 8 and 10 sub-layers, respectively. The lateral mesh size for each layer in the mantle and crust is set to 2  at Io's surface and 4  for the core. The mesh for Model B is shown in Figure 2.8. Seven iterations are required for the models to converge to their final solution including the effect of self-gravitation (Section 2.2.2). A time sampling of 12 steps per one Io orbit is deemed sufficient, as the resulting total heat production rate  $\dot{E}_{total}$  does not change significantly for a higher sampling rate. The effects of initializing the model are shown to be negligible after the first orbital cycle for the interior models used here. Due to Io's short tidal period of less than two days the deformation amplitude as well as the stress amplitudes are controlled by the elastic response of the body. The eigenmodes of both visco-elastic models, Model A and Model B, are either of small strength or have periods that are much longer than the forcing period. Hence, we set  $\tau = P_{orbit}$  for computing the dissipation with Equation 2.5.

The final relative residuals (Table 2.5) between the semi-analytical model and the numerical model are below 4%. Large parts of this error are expected to occur at the asthenosphere boundaries. 1) Numerical inaccuracies in the stress calculation

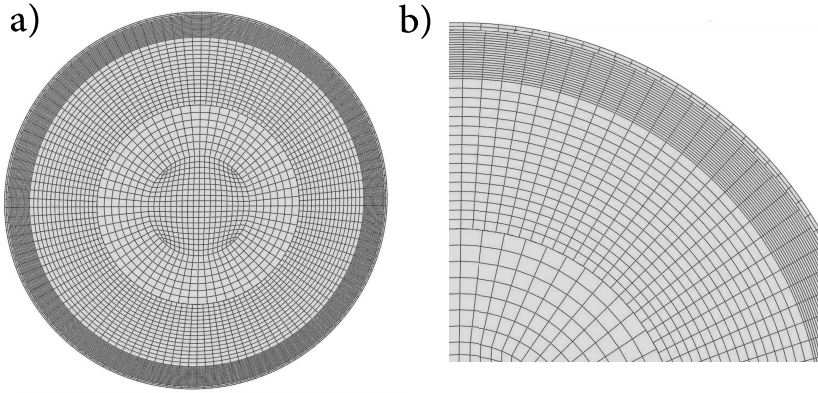


Figure 2.8: Mesh of Model B a) equatorial cut , b) close-up view of mesh for the asthenosphere, mantle, and crust.

Table 2.5: Total heat dissipation  $\dot{E}$  and total average heat flux  $\bar{Q}$  for Model A and Model B resulting from the finite element method. The relative errors are calculated with respect to the given reference values given in the literature (*Lainey et al., 2009*).

Value	Reference	Model A	Model B
$\dot{E}$	$9.33 \cdot 10^{13} \text{ W}$	$9.02 \cdot 10^{13} \text{ W}$	$9.07 \cdot 10^{13} \text{ W}$
$\bar{Q}$	$2.24 \text{ W m}^{-2}$	$2.15 \text{ W m}^{-2}$	$2.16 \text{ W m}^{-2}$
relative error	-	3.4%	2.8%

may arise due to large lateral displacements within the asthenosphere. 2) The radial discretization of the finite element model is crucial because the heating function varies over several orders of magnitudes towards the boundaries of the asthenosphere as described by *Beuthe (2013)* and *Tackley (2001)*. However, the estimation of Io's total heat production rate is afflicted with inaccuracies (*Lainey et al., 2009*) and several other aspects of modelling such as Io's unknown heterogeneous rheology introduce much larger uncertainties. Thus, the accuracy of the results is deemed to be sufficient to be used for our further calculations.

## 2.8. APPENDIX-C: VARIATION OF RAYLEIGH-ROBERTS NUMBER

In Figure 2.9 we present the variation of the average Rayleigh-Roberts number as a function of the heat flux fraction  $f_{cc}$  and the reference mantle viscosity  $\bar{\eta}_{con}$ . It can be seen that the Rayleigh-Roberts number varies over more than several order of magnitude for Model A and B.

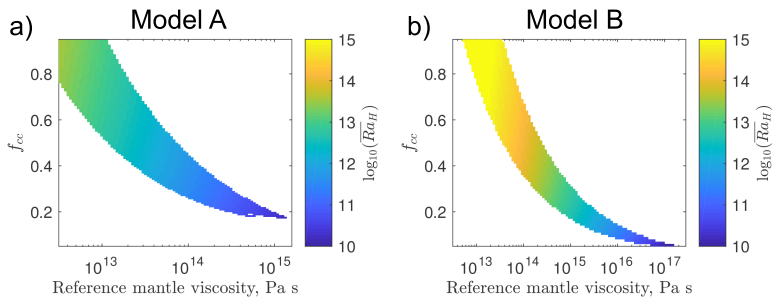


Figure 2.9: Globally averaged Rayleigh-Roberts number as a function of the heat flux fraction  $\bar{f}_{cc}$  and the reference mantle viscosity  $\bar{\eta}_{con}$  for Model A and Model B.



# 3

## THE TIDAL-HEATING-RHEOLOGY FEEDBACK IN IO'S ASTHENOSPHERE

**T. STEINKE, M. ROVIRA NAVARRO, W. VAN DER WAL,  
B. VERMEERSEN**

*Recent models coupling Io's non-uniform tidal dissipation with Io's main heat transport mechanisms (Chapter 2) indicate that non-uniform tidal dissipation within Io's interior likely causes significant regional variations of Io's interior melt distribution. The consequences are lateral variations in Io's viscosity and shear modulus. Conversely, these properties control the amount and distribution of tidal dissipation. This motivates the investigation of the feedback arising between Io's heterogeneous tidal heating pattern and its rheologic structure. In this study, we focus on Io's asthenosphere and assume that the bulk of Io's heat is produced in this layer. We explore to what extent Io's heterogeneous tidal heat production in the asthenosphere is affected by tidally induced regional rheologic variations and under which conditions a continuous feedback between tidal heating and the rheologic structure of Io's asthenosphere leads to a new equilibrium heat flux pattern. Our results show that lateral variations in the rheological parameters lead to a regional change in the amount of tidal dissipation. For melt fractions below 20% the dissipated heat increases with increasing melt fraction and decreases with decreasing melt fraction. In addition, the lateral variations cause spatial variations of the time delay in the visco-elastic response of the material, which, in turn, induces an asymmetry of the tidal dissipation pattern with respect to the prime meridian. In order to investigate the continuous feedback between non-uniform tidal dissipation and rheologic properties we repeatedly re-calculate the tidal dissipation using an updated pattern of the rheological parameters*



based on the previous dissipation patterns. We obtain an equilibrium tidal heating pattern, which is shifted with respect to the prime meridian. For a model with moderate values for the lateral heat transport and melt sensitivity the corresponding equilibrium melt fraction pattern peaks  $15^\circ$  eastward of the sub-Jovian and anti-Jovian points. Our findings suggest that the eastward offset in Io's observed volcanic activity field could be caused by the here investigated feedback mechanism between non-uniform tidal dissipation and melt-dependent visco-elastic rheologic properties in Io's asthenosphere.

## 3

### 3.1. INTRODUCTION

Undergoing extreme tidal dissipation, Io serves as an archetype of rocky exoplanets and exomoons that underwent run-away heating and remain in a state of extreme heating. Thus, understanding tidal dissipation processes in Io's interior and their interaction with the interior properties provides insights into the origin and evolutionary path of tidally heated planetary bodies.

Io's tidal dissipation pattern depends on both the tidal potential field caused by Jupiter and on Io's unknown interior properties. At the same time, the dissipated heat influences Io's interior. Besides the influence on Io's global structure (e.g. [Bierson and Nimmo, 2016](#); [Hussmann and Spohn, 2004](#)), the heterogeneous characteristics of the tidal heat production pattern also influences Io's melt distribution and mantle viscosity laterally (Chapter 2). Studies investigating the spatial distribution of tidal dissipation based on a solid visco-elastic rheology have only accounted for spherically symmetric interior structures ([Beuthe, 2013](#); [Bierson and Nimmo, 2016](#); [Ross et al., 1990](#); [Segatz et al., 1988](#)) thereby not taking into account a potential three-dimensional distribution of interior properties originating from non-uniform tidal heating. The arising feedback between tidal dissipation and rheological parameters could possibly lead to a heterogeneous three-dimensional temperature field and distribution of partial melt, and different dissipation pattern compared to the anticipated end-member models based on a spherical symmetric interior. Based on the assumption that Io's volcanic pattern at the surface mirrors the tidal dissipation pattern in the interior ([Hamilton et al., 2013](#); [Segatz et al., 1988](#); [Tyler et al., 2015](#)), the distribution of Io's observed volcanic features and hotspots allows to draw conclusions on the interior. Currently, the  $30^\circ$  offset in eastward directions of the peaks in the volcanic activity pattern with respect to the sub-Jovian and anti-Jovian points ([Hamilton et al., 2013](#); [Kirchoff et al., 2011](#)) favours tidal dissipation in a magma ocean ([Tyler et al., 2015](#)). Dissipation in a mostly solid mantle with no lateral variations leads to dissipation patterns symmetric towards the prime meridian and cannot explain the observed asymmetry. However, changes in the tidal heating patterns, evolving due to tidally-induced variations in the mantle, could potentially require a reconsideration of previous conclusions on Io's interior and could even place new constraints on the moon's internal state.

The feedback between tidal dissipation and temperature-dependent visco-elastic properties has been explored for small-scale convection features in Earth-like silicate mantles and icy layers by [Han and Showman \(2010\)](#), [Běhounková et al. \(2010\)](#) and [Běhounková et al. \(2011\)](#). Their results show that tidal dissipation in hot upwellings

is typically enhanced. For tidally heated Earth-like interior structures, large-scale variations of the mantle temperature originating from heterogeneous tidal heating almost vanish completely (*Běhounková et al., 2010*). However, Io's interior has specific characteristics that suggest that the arising temperature heterogeneities originating from tidal heating as well as the effects of these arising heterogeneities on the rheologic properties are likely stronger than for the models investigated above:

1. The majority of Io's total heat is likely produced within Io's thin asthenosphere. As the amount of lateral heat transport scales with the thickness of the heated layer (*Tackley, 2001*), this induces stronger long-wavelength heterogeneities of the interior than for planetary bodies with tidal heating near the core-mantle boundary and solid-state convection in the whole mantle as considered by *Běhounková et al. (2010)*. Furthermore, Io's high heat flow is likely driven by advection of melt (*Elder, 2015; Spencer et al., 2020a*). Advection of melt is a rapid process. The proportion between heat transport in radial direction and heat transport in lateral direction is larger for melt advection than for mantle convection. Accordingly, it allows for stronger thermal heterogeneities in the interior to remain from non-uniform tidal heating compared to a fully convective mantle. As shown in Chapter 2, peak-to-peak temperature differences in Io's asthenosphere due to tidal heating are strongly enhanced for magma-dominated heat transport.
2. Due to the extreme heat in Io's interior and low pressures, Io's mantle contains high portions of melt (*Khurana et al., 2011*). Changes in the melt fraction have a more significant influence on the viscosity and shear modulus than temperature variations without any phase changes (*Berckhemer et al., 1982a*). Therefore, already small variations in the melt fraction cause significant differences in the rheological properties of the material.
3. Tides induce strong displacements in Io's asthenosphere. (*Beuthe, 2013; Tackley, 2001*). These lateral deformations in combination with a laterally varying viscoelastic response of the laterally varying asthenosphere induce non-linear effects, which do not exist for a homogeneous asthenosphere.
4. The large-scale variations (degree 2) of Io's observed volcanic activity field are statistically significant (*Kirchoff et al., 2011*) and unlikely caused by a random distribution. This indicates lateral heterogeneities in Io's interior (*Hamilton et al., 2013*, and Chapter 4).

In this paper we aim at investigating the feedback between tidal dissipation and melt-dependent, and therefore heating-dependent, rheologic properties of Io's asthenosphere. We assume that the bulk of Io's tidal dissipation is generated in the asthenosphere by viscoelastic friction. In the Sections 3.2.1-3.2.3, we introduce the rheological structures of the laterally homogeneous starting models as well as the tidal potential and initial tidal dissipation patterns. The relation between the produced heating pattern and the change in melt fraction, based on a simplified form of the thermal model presented in Chapter 2, is introduced in Section 3.2.4. With our finite element model

(Section 3.2.5), which can incorporate lateral changes in the viscosity and shear modulus, we compute the new tidal dissipation pattern. By recurrently using the newly computed rheological properties, we investigate the feedback (Section 3.2.6) between tidal heating and asthenosphere rheology. In Section 3.3 we compare the resulting stress and heating patterns with the initial patterns that originate from radial symmetric structures. Furthermore, we present the dissipation patterns arising for a continuous feedback between tidal dissipation and rheology properties. Finally, we discuss possible indications of Io's spatial distribution of volcanic features on the interior (Section 3.4).

### 3.2. MODELLING THE NON-UNIFORM DISSIPATION-RHEOLOGY FEEDBACK

To investigate the feedback, the initial tidal dissipation pattern, which depends on the interior structure and the tidal forcing, needs to be determined. For this we use the initial tidal dissipation patterns resulting from spherically symmetric layered interior structures. In order to complete the feedback two additional components need to be considered: 1) the transition from a tidal heating pattern into a lateral varying interior structure; and 2) the calculation of the new dissipation pattern based on the updated rheology structure requires a finite element model that can deal with a three-dimensional rheologic distribution.

#### 3.2.1. REFERENCE INTERIOR MODELS

We assume that Io is composed of a fluid core, a visco-elastic mantle and an elastic crust. The mantle is divided into a high-viscosity lower mantle layer and a low-viscosity upper layer, which we refer to as asthenosphere. We assume a linear Maxwell rheology, which is characterised by the viscosity  $\eta$  and the shear modulus  $\mu$ . Note that the reference viscosity used for the visco-elastic model should be considered as an effective viscosity (e.g. *Běhounková et al., 2010*), which is only valid for Io's perturbing potential with a period of 1.77 days. The viscosity used to describe the properties of steady-state convection on longer time scales is treated independently from the visco-elastic model. Possible effects of more complex rheology models, such as the suggested Andrade rheology (*Renaud and Henning, 2018*), on our results are discussed in Section 3.3.3.

Our standard interior model has an asthenospheric thickness of 200 km. The model is the same as Model A in Chapter 2. The rheologic parameters are chosen such that the model fulfills the total dissipated power that is constrained by thermal observations as well as by orbital changes (*Lainey et al., 2009; Veeder et al., 2012*). Furthermore, for this model, the bulk (> 99%) of Io's dissipated power is produced in the asthenosphere. Model parameters are presented in Table 3.1.

#### 3.2.2. TIDAL POTENTIAL

Io orbits Jupiter in a 1:1 spin-orbit resonance with an eccentricity  $e$  of 0.04 and an orbital period of approximately 1.77 Earth days. The difference between the rotation around its own axis velocity and the orbital velocity of Io and the periodic variations of the distance between Io and Jupiter cause periodic tides. The tidal potential for a specific location on

Table 3.1: Model parameters following (1) *Anderson et al. (2001)*, (2) *Turtle et al. (2007)*, (3) *Segatz et al. (1988)*, (4) *Lainey et al. (2009)*, (5) *Bierson and Nimmo (2016)*, and (6) *Mei et al. (2002)*.

Rheology parameter	Notation	Value	Unit
Core density <sup>(1)</sup>	$\rho_c$	5150	kg m <sup>-3</sup>
Mantle/Crust density	$\rho_m$	3244	kg m <sup>-3</sup>
Core-Mantle Boundary	$R_{cmb}$	965	km
Deep mantle shear modulus	$\mu_m$	$6 \cdot 10^{10}$	Pa
Deep mantle viscosity	$\eta_{diss,m}$	$10^{20}$	Pa s
Asthenosphere thickness	$d_{ast}$	200	km
Asthenosphere shear modulus	$\mu_{ast}$	$7.8 \cdot 10^5$	Pa
Asthenosphere viscosity	$\eta_{diss,ast}$	$10^{11}$	Pa s
Crustal thickness <sup>(2)</sup>	$d_{diss,crust}$	30	km
Crustal shear modulus <sup>(3)</sup>	$\mu_{crust}$	$6.5 \cdot 10^{10}$	Pa
Crustal viscosity <sup>(3)</sup>	$\eta_{diss,crust}$	$10^{23}$	Pa s
Radius Io <sup>(1)</sup>	$R_{Io}$	1821.6	km
Orbital parameter	Notation	Value	Unit
Orbital period	$P_{orbit}$	1.769138	days
Eccentricity	$e_{Io}$	0.04	-
Feedback parameter	Notation	Value	Unit
Mean heat flux <sup>(4)</sup>	$\bar{Q}$	2.3	W m <sup>-2</sup>
Mean melt fraction	$\bar{\Phi}$	0.1	-
Melt factor shear modulus <sup>(5)</sup>	$B_\mu$	67/15	-
Melt factor viscosity <sup>(6)</sup>	$B_\eta$	20	-
c-factor	$c$	0.01 and 0.02	W <sup>-1</sup> m <sup>2</sup>

Io can be described as a function of the radial distance  $r$ , the longitude  $\phi$ , the co-latitude  $\theta$ , and the time vector  $t$  (*Van Hoolst et al., 2013*):

$$V_p(t, r, \theta, \phi) = \omega^2 r^2 e_{Io} \left( \frac{3}{2} P_{2,0}(\cos\theta) \cos(\omega t) - \frac{3}{4} P_{2,2}(\cos\theta) \cos(2\phi) \cos(\omega t) - P_{2,2}(\cos\theta) \sin(2\phi) \sin(\omega t) \right). \quad (3.1)$$

with the origin of the coordinate system at the centre of mass of the body and the mean motion

$$\omega = 2\pi / P_{orbit} \quad (3.2)$$

where  $P_{orbit}$  is the orbital period of Io, and  $P_{2,0}(\cos\theta)$  and  $P_{2,2}(\cos\theta)$  are the degree two associated Legendre polynomials of order zero and two, respectively. The inclination of Io's rotation axis and physical librations are unknown but expected to be small (*Yoder and Peale, 1981*) and therefore their effects on the dissipation pattern are neglected.

### 3.2.3. INITIAL TIDAL DISSIPATION PATTERNS

The spatial characteristics of the tidal dissipation pattern for a homogeneous asthenosphere and the tidal potential as given in Section 3.2.2 can be described analytically (*Beuthe, 2013*). Even though the obtained solutions would be, apart from numerical errors, the same, we here use the analytical solution as the starting patterns since it can be easily assessed and is quite accurate compared to numerical or semi-analytical solutions for the four-layer interior structure.

Analytical derivations show that the tidal dissipation pattern of Io's asthenosphere is dominated by a certain pattern ( $\Psi_B$  in Equation 36 in *Beuthe (2013)*), which is the sum of three contributions

$$\Psi_B(\theta, \phi) = \Psi_0 + 0.5\Psi_2(\theta, \phi) - \frac{2}{3}\Psi_4(\theta, \phi) \quad (3.3)$$

with the constant

$$\Psi_0 = \frac{21}{5}, \quad (3.4)$$

the degree 2 components

$$\Psi_2(\theta, \phi) = 0.5 \left( -\frac{33}{7} P_{20}(\cos\theta) + \frac{9}{14} P_{22}(\cos\theta) \cos(2\phi) \right), \quad (3.5)$$

and the degree 4 components

$$\Psi_4(\theta, \phi) = \frac{387}{140} P_{40}(\cos\theta) - \frac{27}{140} P_{42}(\cos\theta) \cos(2\phi) - \frac{3}{160} P_{44}(\cos\theta) \cos(4\phi). \quad (3.6)$$

Other patterns, such as the  $\Psi_A$  and  $\Psi_C$ , introduced in *Beuthe (2013)*, only make a minor contribution to the dissipation pattern in Io's asthenosphere and are therefore

neglected. While only the strength of the above described pattern  $\Psi_B$  changes with depth, not the pattern itself, the projection of the produced dissipation to Io's surface can also be described by  $\Psi_B$ , while the amplitudes are normalized by Io's mean heat flux  $\bar{Q}_{prod}$ .

Based on the dissipation pattern contributions (Equation 3.4-3.6) arising for a homogeneous asthenosphere we investigate three patterns in order to account for observations of Io's volcanic activity field and a different strength of the lateral heat transport in the asthenosphere: Pattern D2-0 only contains degree 2 components, thereby mimicking a strong blurring of higher degrees by convection (Tackley et al., 2001):

$$Q_{prod,D2-0}(\theta, \phi) = \frac{\Psi_0 + \Psi_2(\theta, \phi)}{\Psi_0} \bar{Q}_{prod} \quad (3.7)$$

Pattern D2-30 is similar to Pattern D2-0, but shifted eastwards by  $30^\circ$ . The choice of this parameter is motivated by the observation that the center of the strongest volcanic activity is shifted by  $30^\circ$  (Hamilton et al., 2013; Kirchoff et al., 2011). Pattern D4 has the full contribution, degree 2 and degree 4. Given Io's mean heat flux  $\bar{Q}_{prod}$  (Table 3.1), we derive the tidal heating pattern:

$$Q_{prod,D4}(\theta, \phi) = \frac{\Psi_B}{\Psi_0} \bar{Q}_{prod} \quad (3.8)$$

The three dissipation patterns are displayed in Figure 3.1.

### 3.2.4. HETEROGENEOUS VISCOSITY AND SHEAR MODULUS DISTRIBUTION

The melt fraction has a significant influence on the rheological properties of Io's interior. The presence of melt weakens the mantle and lowers the viscosity. Also the temperature has an effect on the rheological properties, but if no phase change is present, the effect of melt is much larger (Berckheimer et al., 1982b). For this study the pure temperature-dependency is therefore neglected. We restrict our investigations on the effects in Io's asthenosphere and only to lateral variations in the viscosity and shear modulus for the visco-elastic tidal response arising due to lateral variations in the melt fraction (Chapter 2). Changes of the thickness of the asthenosphere in longitude and latitude caused by non-uniform heating (Spencer et al., 2021, and Chapter 2) are not investigated here. This is because it is not yet certain whether locations with more heating and higher magmatic heat advection result in a thicker or thinner lithosphere as discussed by Spencer et al. (2021). Also additional radial variations, arising due to the pressure-dependence of the melt fraction (Bierson and Nimmo, 2016), radial variations of the tidal dissipation in the asthenosphere (Beuthe, 2013; Tackley et al., 2001), and small-scale anomalies caused by mantle convection are neglected.

We base the calculation of the strength of the tidally-induced structural heterogeneities on the thermal model presented in Chapter 2. In Section 2.3, we derive a full model that converts the tidal heating pattern  $Q_{prod}(\theta, \phi)$  as a function of longitude and latitude into a melt distribution pattern  $\Phi(\theta, \phi)$ . Various parameters determine the mean conditions and the amplitude of the arising heterogeneities: the fraction between

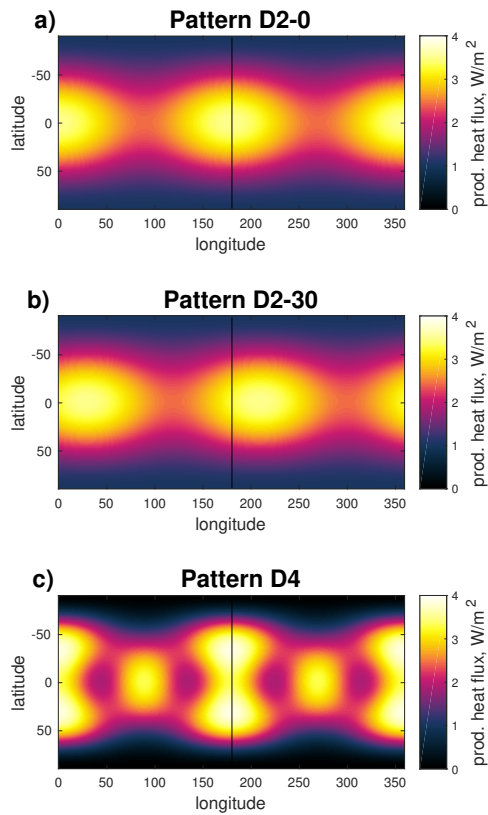


Figure 3.1: The three tidal dissipation pattern used as starting heterogeneous patterns in Section 3.3. Pattern D2-0 only contains degree 2 components; Pattern D2-30 is a 30° shifted version of Pattern D2-0. Pattern D4 includes degree 2 and 4 components with no eastward shift.

magmatic and convective heat transport; the viscosity and thickness of the asthenosphere; and the initial dissipation pattern. However, for this study we aim to reduce the amount of unknown parameters of the thermal model presented in Chapter 2: Two parameters are sufficient to mimic the outcome of the thermal model with a highly reduced computation effort: 1) a variable that determines the strength of the variations around a mean melt fraction. For that we assume, based on our result presented in Chapter 2, that the variation of the tidally produced heat flux and the anomalies in the melt fraction distribution in Io's asthenosphere are proportional to each other; 2) a variable that determines the mean melt fraction, which is strongly connected to the mean mantle temperature.

The starting tidal heating patterns are given in Section 3.2.1. We introduce the proportionality factor  $c$ , quantifying the ratio between the anomaly in the produced heat and the anomaly in the melt fraction distribution in Io's asthenosphere:

$$\delta\Phi(\theta, \phi) = c\delta Q_{prod}(\theta, \phi), \quad (3.9)$$

where the anomaly of the heat production is defined as

$$\delta Q_{prod}(\theta, \phi) = Q_{prod}(\theta, \phi) - \bar{Q}_{prod}, \quad (3.10)$$

and the anomaly of the melt fraction is defined as

$$\delta\Phi(\theta, \phi) = \Phi(\theta, \phi) - \bar{\Phi} \quad (3.11)$$

with  $\bar{\Phi}$  being the mean melt fraction of the asthenosphere. The  $c$ -factor indicates the strength of the blurring of the tidal dissipation distribution by lateral flow, with small values of  $c$  representing a stronger blurring than large values of  $c$ . It combines various parameters such as the viscosity and thickness of the convective layer, the fraction between convective and magmatic heat transport, and the solidus and liquidus temperature of the system. The variation of the  $c$ -factor scales almost linearly with the peak-to-peak variations computed by a thermal model shown in Figure 2.7c) and d). The  $c$ -factor can be roughly approximated by dividing the peak-to-peak temperature variations  $\Delta T_m$  of Figure 2.7 by the factor  $(350\text{K} \cdot \Delta Q_{prod})$ , where the 350 K comes from the difference between solidus and liquidus temperature (Hirschmann, 2000) and  $\Delta Q_{prod}$  describes the peak-to-peak amplitude of  $\delta Q_{prod}(\theta, \phi)$  (Figure 2.5). This results in possible values for  $c$  between 0.13 and values approaching zero. However, in contrast to the thermal model of Chapter 2, the introduced parameterisation (Equation 3.9), does not include the wavelength-dependent weakening of the tidal dissipation pattern (Equation 2.14) and small non-linear effects on the mantle temperature pattern (Equation 2.22) arising with increasing peak-to-peak temperature variations and larger melt fractions. In order to keep the difference between the used constant- $c$  approach and the thermal model of Chapter 2 small, we only consider mean mantle temperatures close to the solidus temperature of the system and therefore a relatively small mean melt fraction  $\bar{\Phi}$ . For this study, we take the values 0.01 and 0.02 for  $c$ . These are rather small values, given the full possible range of  $c$  approximated above. This is due to two reasons: 1) In contrast to the thermal model presented in Chapter 2, we do not consider that the



interior is fully adjusted to the lateral varying tidal dissipation pattern; 2) for small mean melt fraction  $\bar{\Phi}$ , as here assumed, the maximum possible variations and therefore the  $c$ -factor are smaller than the above indicated range between 0 and 0.13. For  $\bar{\Phi} = 0.1$  an approximate maximum of  $c = 0.06$  is possible following the results of Chapter 2 and the above given formula for the approximation of the  $c$ -factor.

We define the models such that the mean melt fractions between the reference model with homogeneous asthenosphere and the models with heterogeneous asthenosphere do not change. The lateral viscosity distribution is calculated using the melt distribution  $\delta\Phi(\theta, \phi)$  resulting from Equation 3.9 with

$$\eta(\theta, \phi) = \eta_{ast, \bar{\Phi}} \exp(-B_\eta(\delta\Phi(\theta, \phi))) \quad (3.12)$$

following Moore (2003). Note that  $\eta_{ast, \bar{\Phi}}$  is not the viscosity for a melt free asthenosphere, but the specific viscosity of the asthenosphere given the initial melt fraction  $\bar{\Phi}$ . However, in the determination of the viscosity variations this initial melt fraction cancels out. The value of  $B_\eta$  is not well constrained. We choose  $B_\eta = 20$  (Mei et al., 2002). The melt dependent shear modulus is adopted from Mavko (1980) and Bierson and Nimmo (2016):

$$\mu(\theta, \phi) = \mu_{ast, \bar{\Phi}} \frac{1 + B_\mu \bar{\Phi}}{1 + B_\mu(\delta\Phi(\theta, \phi) + \bar{\Phi})}. \quad (3.13)$$

We adopt  $B_\mu = 67/15$  from Bierson and Nimmo (2016). In contrast to the viscosity distribution, the new lateral pattern  $\mu(\theta, \phi)$  depends on the initial average melt fraction  $\bar{\Phi}$ . As will be more clear in Section 3.3.1 the uncertainties in  $B_\eta$ ,  $B_\mu$  and  $\bar{\Phi}$  can also be characterised by varying the  $c$ -factor. Therefore, the investigation of the  $c$ -factor will receive the main attention.

### 3.2.5. FINITE ELEMENT MODEL

Due to the lateral changes of the viscosity and shear modulus, the tidal response of the visco-elastic models cannot be calculated using semi-analytical models (Sabadini et al., 2016). That is why a finite element model is used here. This model, originally developed by Hu et al. (2017), has been used to simulate the tidal dissipation for Io's homogeneously layered interior and has been benchmarked with semi-analytical models (Chapter 2).

Based on the interior structure and the tidal potential (Equation 3.1 the finite element model computes the spatial and temporal stress field in Io's interior. This deviatoric part of the stress field  $\sigma_D$  and the viscosity distribution are the crucial components to obtain the heat flux pattern  $Q_{prod}(\theta, \phi)$ , which is required to derive the shear modulus and viscosity distribution of Io's asthenosphere (Section 3.2.4). The volumetric tidal dissipation for a certain time step  $t$  and integration point  $i$  given by the grid of the finite element model is calculated by the following (Hanyk et al., 2005):

$$h_{i,t} = \frac{\Sigma_{D,i,t}}{2\eta(\theta_i, \phi_i)}, \quad (3.14)$$

where  $\eta(\theta_i, \phi_i)$  is the local viscosity value at the position of the integration point  $i$ , and

$$\Sigma_{D,i,t} = \sigma_{D,i,t} : \sigma_{D,i,t} \quad (3.15)$$

denotes an inner matrix product of the deviatoric stress tensor  $\sigma_{D,i,t}$  at the integration point  $i$ . In the following we refer to this value as the squared stress. Since the time scale for tidal heating and heat transfer are much larger than one orbital period, the volumetric tidal heat production is averaged over one orbital period to result in an average three-dimensional tidal dissipation pattern. The average volumetric tidal dissipation  $\bar{h}_{orbit}(\theta_i, \phi_i, r_i)$  is calculated for each integration point:

$$\bar{h}_{i,orbit} = \frac{1}{P_{orbit}} \int_{\tau}^{\tau+P_{orbit}} h_{i,t} dt, \quad (3.16)$$

where  $\tau$  is the time required for the visco-elastic model to adjust to the steady state. To be able to apply a spherical harmonic analysis to the results, the values of the tidal dissipation for each time step  $h_{i,t}$  and the averaged heat dissipation values  $\bar{h}_{i,orbit}$  at each integration point in the finite element model are interpolated to an equi-angular grid  $H_t(\theta, \phi, r, t)$  and  $\bar{H}_{orbit}(\theta, \phi, r)$ , respectively. When we project the volumetric dissipation in the interior  $\bar{H}_{orbit}(\theta, \phi, r)$  to Io's surface we get the produced heat flux pattern  $\bar{Q}_{prod}(\theta, \phi)$ .

### 3.2.6. FEEDBACK

The feedback between the tidal-heating-induced melt distribution and the melt-induced rheology variations affects the global and lateral properties of the interior. In this study, we only aim to investigate the effect of lateral variations of the tidal dissipation pattern and interior structure. We neglect the effect of changes in the total produced tidal dissipation rate, which has been previously investigated by [Fischer and Spohn \(1990\)](#) and [Husmann and Spohn \(2004\)](#). However, even though we define that the mean melt fractions remain the same over the course of time as for the initial interior model, small differences in the total of the tidally produced heat arise for different lateral variation of the rheological properties. This is because the melt fraction and the produced tidal dissipation are not linearly connected. We assume that the small amount of additional heat is removed from the system by a temporally more effective heat transport mechanism and that therefore the thermal budget of Io's mantle is not affected. That way we can keep the mean melt fraction as for the 1-dimensional reference model given in Table 3.1 for the feedback modelling. This procedure ensures, that the globally produced dissipation does not drift away.

Given Io's specific mantle heat capacity  $c_p = 1200 \text{ J K}^{-1} \text{ kg}^{-1}$  ([Tackley, 2001](#)), locations with strong volumetric tidal heating need several 10,000 years to heat up by 10 K in case no heat transport would be present. Thus, a change in the distribution of tidal dissipation does not immediately change the thermal state, melt fraction, and melt-dependent visco-elastic properties in the asthenosphere. In order to model the inertia of the system to adapt to the new heating pattern, we take into account both the former melt fraction and the change in the melt fraction due to the updated tidal

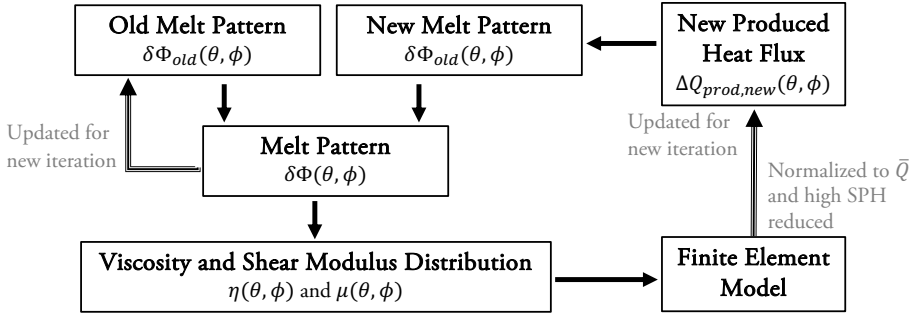


Figure 3.2: Flow chart of the feedback setup with takes into account the current thermal state and the updated tidal dissipation distribution. For the computation of the new melt fraction former melt fraction and the melt fraction resulting from the updated tidal dissipation distribution are averaged. Based on this melt fraction and the resulting lateral variations in the visco-elastic properties, i.e. the shear modulus and the viscosity the finite element model computes a new tidal dissipation pattern updated.

heating distribution and average both patterns. Based on the updated viscosity and shear modulus the new tidal heating pattern is computed. This approach mimics a continuous evolution of Io's thermal state but still allows for a quick evolution of the tidal dissipation patterns. Any overshooting of the solutions as a consequence of underestimating the inertia of the thermal system needs to be prevented since unrealistic sudden changes could otherwise lead to unnatural oscillations around an equilibrium solution or force Io's interior to run into a different state with different equilibrium, which would not be reached under realistic circumstances. A flow chart of the feedback is presented in Figure 3.2.

### 3.3. RESULTS AND DISCUSSION

We first look at the non-uniform distribution of rheological properties in the asthenosphere based on our presented patterns (Figure 3.1). In order to understand the complete tidal-dissipation-rheology feedback, effects of the lateral rheology structure on the dissipation pattern that already emerge in the first iteration, need to be investigated in detail. The stress pattern or, more precisely, the squared stress (Equation 3.15) as the output of the finite element model, is the most complex contribution of the distribution of tidal dissipation in Io's asthenosphere. It is therefore investigated first (Section 3.3.1). In a second step the viscosity pattern is included and the dissipation patterns resulting from non-uniform distribution of rheological properties are compared to the dissipation pattern of the initial model with homogeneous layers. Following that, we show for one set of selected initial conditions what happens when the feedback continues, i.e. when the updated dissipation pattern is continuously used as an input for a new lateral heterogeneous visco-elastic model.

### 3.3.1. NON-UNIFORM DISTRIBUTION OF RHEOLOGICAL PROPERTIES

In order to obtain the non-uniform distribution of the rheological properties we need the produced tidal heating patterns  $Q_{prod}$ . These initial patterns for a homogeneously layered interior are given by Equation 3.7 and Equation 3.8. In addition, we require the  $c$ -factor (Equation 3.9), which provides the link between heating and melt pattern. We use  $c = 0.02$ , mimicking a weak blurring by convection and a well-adjusted interior, and  $c = 0.01$  mimicking a strong blurring or a body that has just recently been tidally heated and whose interior is not yet fully adjusted to the non-uniform heating. With Equation 3.12 and Equation 3.13 we calculate the viscosity and the shear modulus distribution in Io's asthenosphere based on the melt fraction. We choose a fixed value of  $\bar{\Phi} = 0.1$  (corresponding to a mantle temperature of approx. 1485 K at a depth of 130 km below the surface) and  $B_\eta = 20$  as the standard values to describe the relationship between melt fraction and viscosity variation. As the strength of the viscosity variation is independent of the choice of  $\bar{\Phi}$  and the variations of the shear modulus are only marginally affected by the choice of  $\bar{\Phi}$ , different values of  $\bar{\Phi}$  are not explored.

We investigate eight models with laterally varying rheological structures. Two models are based on the Pattern D2-0 with different values of  $c$ , two models are based on the Pattern D2-30, and two models based on Pattern D4. In order to better understand the ongoing tidal dissipation mechanism in a laterally varying asthenosphere we also investigate two toy models. These two models do not represent a realistic interior model of Io. Their viscosity and shear modulus in the asthenosphere are spatially varying, but chosen such that a constant Maxwell time is enforced. The Maxwell time is defined as the fraction between viscosity and shear modulus and characterises the response of a visco-elastic material when given an instantaneous perturbation. For both constant-Maxwell-time models, i.e. D2-0-M and D4-M, the viscosity is computed based on the  $c$ -factor parameterization, however, the shear modulus distribution follows the viscosity variations, such that the Maxwell time of the asthenosphere does not vary spatially:

$$\tau_{ast}(\theta, \phi) = \frac{\eta(\theta, \phi)}{\mu(\theta, \phi)} = \tau_{ast,ref} = \frac{\eta_{ast}}{\mu_{ast}} \quad (3.17)$$

In addition to these eight models we also calculate a homogeneous asthenosphere model as reference (Model D0). The specific parameter choices and names of the models are presented in Table 3.2.

Figure 3.3 shows the corresponding melt fraction, viscosity and shear modulus distribution, and spatial variation of the Maxwell time for selected models. Note that the distributions of Model D2-30 and Model D2-30-c are not plotted here, as their resulting patterns are simply shifted by  $30^\circ$  compared to Model D2-0 and D2-0-c. Also the pattern of Model D4-M and D4-c can be easily derived from the patterns of Model D4, Model D2-0-c and Model D2-0-M. For Model D2-0 with  $c = 0.01$  the melt distribution corresponds to a peak-to-peak temperature difference of approximately 9 K (following [Hirschmann, 2000](#)). For Model D4 with  $c = 0.02$ , the resulting melt distribution corresponds to a peak-to-peak temperature difference of 27 K. Comparing with Figure 2.7a) and b) we find that a peak-to-peak temperature difference of 27 K is rather in the lower range of

Table 3.2: List of investigated models

Name	Pattern	$c$ -factor	Maxwell time $\tau_{ast}$
Model D0	-	-	constant
Model D2-0	D2-0	0.01	laterally varying
Model D2-0-c	D2-0	0.02	laterally varying
Model D2-0-M	D2-0	0.02	constant (forced)
Model D2-30	D2-30	0.01	laterally varying
Model D2-30-c	D2-30	0.02	laterally varying
Model D4	D4	0.01	laterally varying
Model D4-c	D4	0.02	laterally varying
Model D4-M	D4	0.02	constant (forced)

possible mantle temperature differences and corresponding to an asthenosphere with 30% convective heat transport and 70% magmatic heat transport. For all shown models significant variations in the viscosity distribution, shear modulus distribution and the Maxwell time of the material are present. Apart from the models with forced constant Maxwell time, the viscosity variations are stronger than the variations in the shear modulus. The stronger the variation in the melt fraction, i.e. the larger the  $c$ -factor, the stronger the spatial variations in the ratio of the viscosity and the shear modulus and therefore in the normalised Maxwell time. The variations of the Maxwell time indicate that large parts of Io's interior will respond differently to the tidal potential than a homogeneous interior. The influence of the parameter  $B_\eta$  on the viscosity and Maxwell time distribution is not explicitly shown here, but discussed in Section 3.3.3.

### 3.3.2. SQUARED STRESS PATTERN

Based on the heterogeneous asthenosphere structure caused by heterogeneous tidal heating, presented in Section 3.3.1, we compute the spatially and temporally varying stress field using the finite element model described in Section 3.2.5. As in Equation 3.15 the deviatoric components of the stress tensor are squared and the resulting values at the integration points interpolated to a equi-angular grid. We investigate the stress field in the upper asthenosphere, where the tidal dissipation, and therefore the influence of the stress field on the global distribution of tidal dissipation, is the strongest. Just as the tidal potential the periodic time-dependent squared stress pattern continuously moves eastwards around the body. For further analysis, however, the squared stress pattern is averaged over one orbital period, just as the volumetric tidal dissipation (Equation 3.16). As expected, the pattern for Model D0 has similar characteristics as Pattern D4 (Figure 3.1c). Just as Pattern D4 the squared stress pattern is mirror-symmetric with respect to three planes: the plane through the prime meridian, the equatorial plane and the plane perpendicular to these two planes. This geometry of symmetries results additionally in a rotational symmetry in longitudinal direction repeating at  $180^\circ$ . The differences between the reference squared stress pattern of the homogeneously layered model and the resulting squared stress pattern for the heterogeneous models are plotted in Figure 3.4b-i. Interestingly, the differences between the Model D0 and respective lateral varying models show asymmetry with respect to the prime meridian,

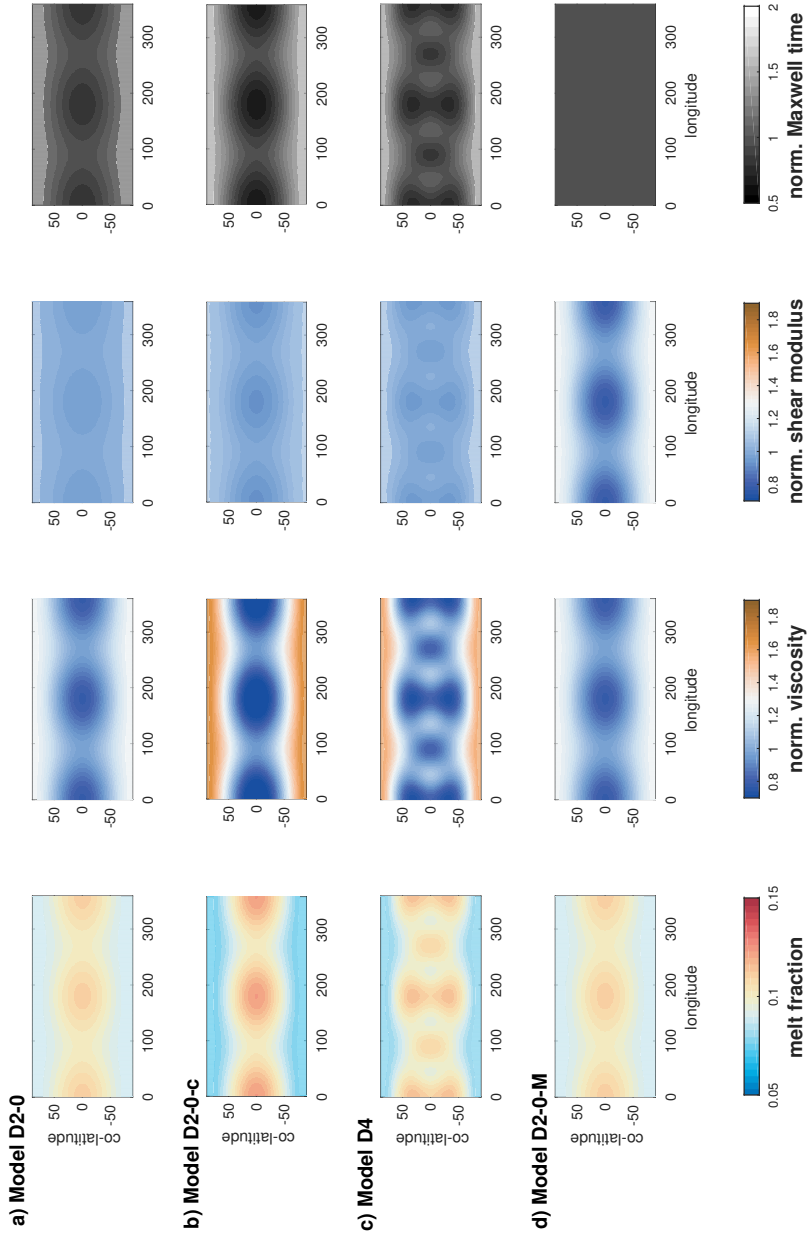


Figure 3.3: Distribution of melt fraction and rheological properties for Model D2-0 (a), Model D2-0-c (b), Model D4 (c) and Model D2-0-M (d). First column shows the spatial variation of the melt fraction around the average value of  $\phi = 0.1$ , both central columns show the variation of the viscosity and shear modulus normalised by their reference values (Table 3.1), and the fourth column shows variation in the Maxwell time normalized to the reference Maxwell time  $\tau_{asr}$ . For Model D2-0-M the spatial variation in the shear modulus is chosen to follow the variation in the viscosity, such that the Maxwell time does not vary spatially.

even though the initial non-uniform rheological distribution does not contain an asymmetry with respect to the prime meridian (Model D2-0, Model D2-0-c, Model D4, Model D4-c). The mirror symmetry at the equatorial plane and the rotational symmetry in longitudinal direction repeating at  $180^\circ$  remains. In general it can be stated that the stronger the lateral variations in the rheological properties, the stronger the amplitudes in the difference patterns. This behaviour shows for example in the resulting difference pattern of Model D2-0 and Model D2-0-c with stronger rheologic variations. The differences are approximately one order of magnitude smaller than the amplitudes in the squared stress field patterns. However, once introduced these asymmetries have the potential to grow due to the continuous feedback, as further investigated in Section 3.3.4.

In contrast to that, no asymmetric contributions emerge from the toy models, i.e. Model D2-0-M and Model D4-M (Figure 3.4f and i) with no spatial variations in the Maxwell time. Here, the differences between the reference squared stress pattern and the resulting squared stress pattern are large, however, symmetric towards the sub-Jovian meridian. Consequently, the asymmetry does not necessarily result from spatially varying rheological properties but from a spatial variation in Maxwell time (Figure 3.3).

The origin of the asymmetry arising in the squared stress pattern needs to be explained in detail. The only input that can cause this asymmetry with respect to the prime meridian is the rotation of the tidal bulge around the moon. Due to the visco-elastic properties of the material in the asthenosphere, the body responds to the tidal perturbation with a time delay. For a laterally uniform asthenosphere, the response of the body is delayed, but the amplitude of the deformation and arising stresses are still proportional to the tidal potential. If we integrate the absolute values of the stress states over one orbit the time delay cancels out. In other words, in the Fourier-transformed frequency domain the stress is proportional to the Fourier-transformed tidal potential (Beuthe, 2013). However, if the asthenosphere is not laterally uniform, and the Maxwell time of the material varies laterally, the time delay of the response varies laterally. As a consequence, the Fourier-transformed stress is not proportional to the tidal potential anymore as shown for Enceladus' ice shell of variable thickness (Beuthe, 2019). This leads to changes in the stress pattern in the heterogeneous layer compared to a homogeneous layer. Integrated over one orbit, these differences remain. The direction of the perturbation traveling around the body causes an asymmetry. For the toy models D2-M and D4-M in Figure 3.4 with constant Maxwell time, the time delay of the response is spatially constant, even though the rheology changes spatially. Although the resulting squared stress pattern is different to the squared stress pattern of a homogeneous asthenosphere, it contains the same three symmetries as Pattern D4. If Io's asthenosphere would be purely elastic and would only have a spatially varying shear modulus the response would be instantaneous and therefore also asymmetry would be induced.

### 3.3.3. DISTRIBUTION OF TIDAL DISSIPATION

We now look at the distribution of the produced tidal dissipation for the heterogeneous asthenosphere models. Specifically, we look at the produced tidal dissipation projected

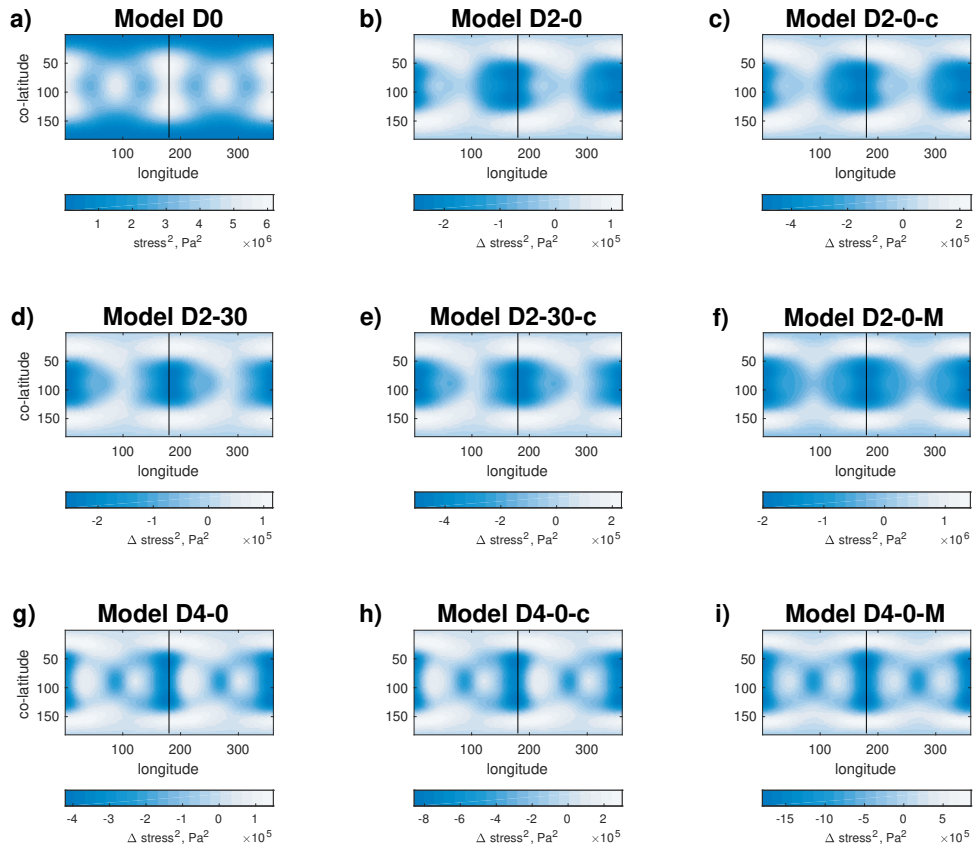


Figure 3.4: Averaged squared stress pattern for upper asthenosphere ( $R = 1.7649$  km): a) shows the stress pattern for the reference Model D0, b)-i) show differences between the reference, i.e. Model D0 show in a), and the stress patterns for heterogeneous models. Note that the color scale varies for sub-panels. Line at  $180^\circ$  longitude is plotted for visual reference.



onto Io's surface, i.e. the tidally produced heat flux, and compare these patterns to the heat flux pattern of the reference model (Model D0). Based on Equation 3.16, we compute the average tidal dissipation pattern using the averaged squared stress patterns (presented in Figure 3.4) and the viscosity distributions shown in Figure 3.3. Sub-panels b-i of Figure 3.5 show the differences to the dissipation pattern of the homogeneous model presented in Figure 3.5a. It can be seen that for low latitudes, close to the sub-Jovian and anti-Jovian point, that the regional amount of tidal dissipation is amplified for all models based on Pattern D2-0 and Pattern D2-30. For models based on Pattern D4, differences between the homogeneous model (Model D0) and non-uniform models show the typical Pattern D4 characteristics. As expected, the differences in the tidal dissipation increase with increasing  $c$ -factor. This becomes obvious when comparing the differences of Model D2-0 (Figure 3.5b) with Model D2-0-c (Figure 3.5c). The asymmetry arising in the squared stress pattern is present in the dissipation pattern, albeit its total influence on the pattern is reduced compared to the squared stress patterns. This is due to the fact that the viscosity distribution has a strong effect on the resulting dissipation pattern and is, in most cases, symmetric. If the viscosity structure is asymmetric (Model D2-30 and Model D20-30-c), an additional asymmetry is induced. The differences between the resulting dissipation patterns of Model D2-0-M and D4-M and the reference Model D0 (Figure 3.5f and i) do not show an asymmetry with respect to the prime meridian.

We investigate the extent of the shift of the resulting dissipation pattern with respect to the prime meridian. For the Models D2-0 and D2-0-c an eastward shift of the peaks in the dissipation pattern by 3-5 ° compared to the Pattern D2-0 can be detected. However, for Model D2-30 and Model D2-30-c, we find that the former peaks in the dissipation pattern, located 30° east of the sub-Jovian point and anti-Jovian point (Pattern D2-30), are shifted westwards. For the model with the weaker lateral variation (Model D2-30) the westward shift is stronger than for the Model with stronger variations (Model D2-30-c), while for the Model Model D2-0-c the eastward shift is stronger than for Model D2-0. This suggests that the strength of the offset depends on the strength of the lateral variations in the asthenosphere, with models with stronger lateral variations tending to a stronger offset in the tidal dissipation pattern. The models based on Pattern D4 show also a small eastward shift in the degree 2 components but also contain large degree 4 components with heating at the mid-latitudes, north and south of the sub-Jovian point.

In order to be able to make qualitative prediction regarding the increase and decrease in the amount of tidal dissipation, we look at the dissipating behaviour of an homogeneous asthenosphere with changing shear modulus and viscosity. Figure 3.6 shows the total dissipation (grey scale) of a homogeneous four-layer model of Io based on the semi-analytical approach of *Sabadini et al. (2016)*. Marked with the cross is our reference model (Table 3.1). The shear modulus and the viscosity of the asthenosphere are varied, while the remaining parameters remain constant. As can be seen, the total produced tidal dissipation is a function of the rheological properties of the asthenosphere. However, it does not show a linear behaviour. Given Equation 3.12 and 3.13, we plot how a change in melt fraction affects the shear modulus and viscosity given

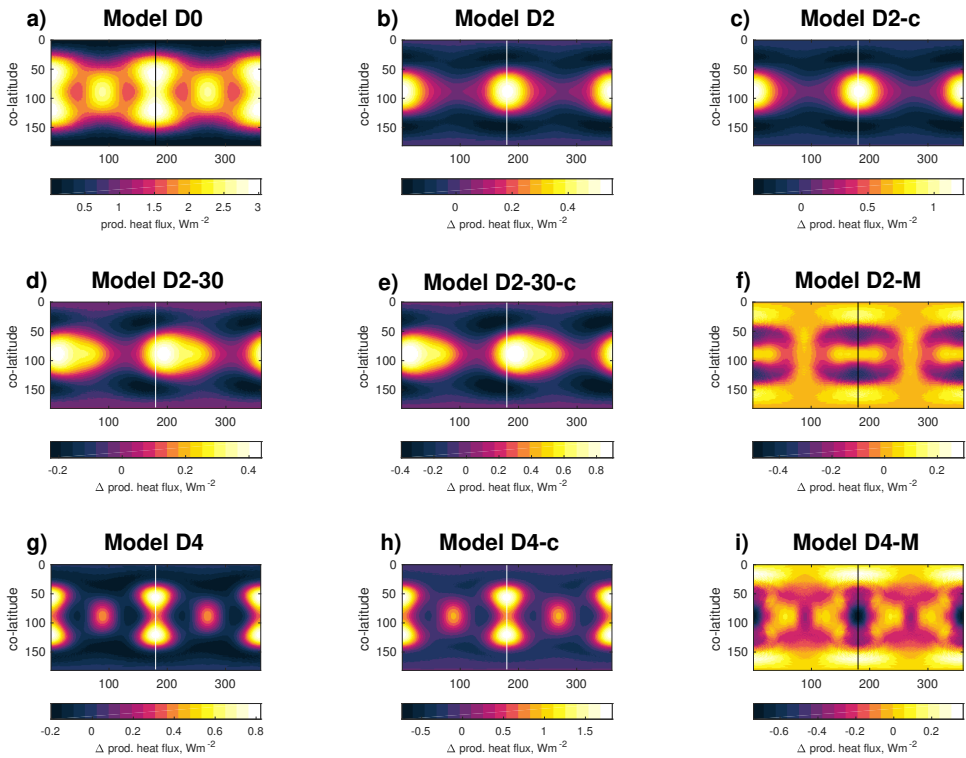


Figure 3.5: Produced heat flux pattern: a) shows the dissipation pattern for the reference Model D0, b)-i) show differences between the reference, i.e. Model D0 show in a), and the dissipation pattern resulting for heterogeneous models. Note that the color scale varies for sub-panels. Line at 180° longitude is plotted for visual reference.

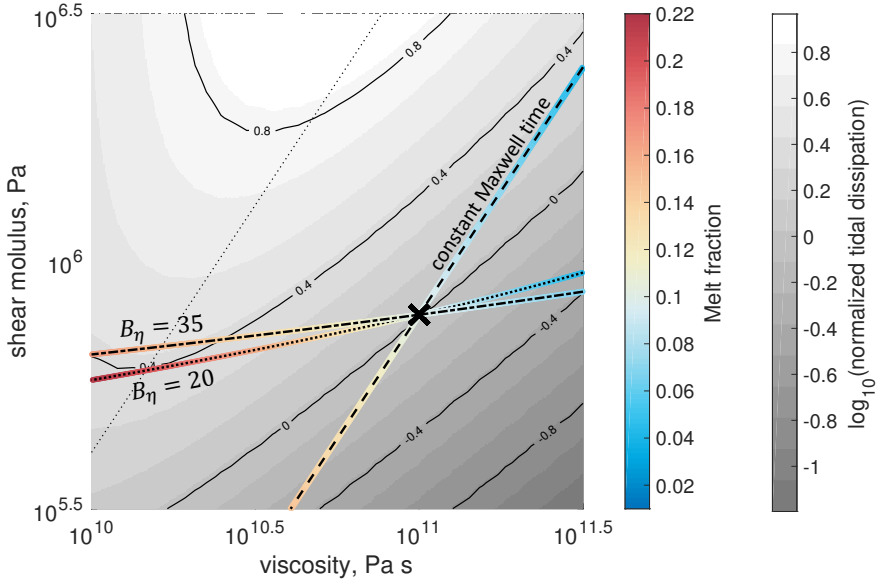


Figure 3.6: Parameter space spanned by the shear modulus and the viscosity around the rheological properties of the asthenosphere (indicated by the cross). Grey colour scale shows the amount of total produced dissipation for a homogeneous asthenosphere with given rheological parameters, normalised to the dissipation of the reference model. The dotted black line indicates the parameter combinations where the Maxwell time of the asthenosphere is equal to the tidal perturbation period of 42 hours. The rainbow-colored lines depict the change in viscosity and shear modulus with changing melt fraction based on Equation 3.12 and Equation 3.13 and different  $B_\eta$ . Lines are plotted for  $B_\eta = 20$ ,  $B_\eta = 35$  and the constant Maxwell time approach (Model 4-M).

the values for  $B_\eta$  and  $B_\mu$  of Table 3.1 (rainbow-coded line). Furthermore, we plot the function given a constant Maxwell approach used for Model D2-M and D4-M.

Disregarding the small asymmetries caused by the non-linear behaviour of the squared stress pattern, we find that the regional dissipative behaviour in the asthenosphere can be quantitatively predicted by the dissipative behaviour of homogeneous asthenosphere with the same shear modulus and viscosity as for a specific region. In general, regions with higher melt fractions than average result in areas with additional tidal dissipation. Regions with less melt than average result in less dissipation. However, Figure 3.6 also shows that this generalisation is broken once the melt fraction reaches a high level (17% for the here used reference model and  $B_\eta = 20$ ). For the resulting shear modulus and viscosities the amount of dissipation decreases.

In addition, it becomes obvious that unknown initial choices of our models influence the tidal heating pattern resulting from a heterogeneous asthenosphere:

- Different combinations of the reference viscosity and shear modulus of the asthenosphere (Table 3.1) are possible, while still in agreement with the total amount

of tidal dissipation. The choice of these initial parameters, however, changes the dissipative behaviour of the material with changing melt fraction.

- The computation of the stress field is based on Maxwell rheology. Different rheology models, such as the Andrade rheology, are suggested for planetary interiors (*Castillo-Rogez et al., 2011*). The Andrade rheology results in higher tidal dissipation values at higher viscosities (*Bierson and Nimmo, 2016; Renaud and Henning, 2018*). Using Io's mean heat flux as a constraint, this would allow for a higher reference viscosity. As a consequence, a lower mean melt fraction could be assumed. In this case also the dissipation behaviour of regions with higher and lower melt fraction as the average melt fraction would differ from the Maxwell rheology models.
- The values of  $B_\eta$  and  $B_\mu$ , quantifying the change of the viscosity and shear modulus as a function of melt fraction, are highly unknown. Even though various laboratory experiments have been accomplished (*Hirth and Kohlstedt, 1995; Mei et al., 2002*), the effect of melt on the visco-elastic material forced at Io's tidal perturbation cannot be exactly quantified. However, these values strongly influence the dissipative behaviour. As an example an additional line with  $B_\eta = 35$  is plotted to the line with  $B_\eta = 20$  in Figure 3.6. As can be seen, the lines are similar in their slopes, however, the line with  $B_\eta = 35$  is more sensitive to the change in melt fraction. This means that even small changes in the melt fraction have a significant effect on the amount of heat that is dissipated. For the function with  $B_\eta=35$  only a few percent change in melt fraction is necessary to cross the peak in the dissipation behaviour. Behind this point an increasing melt fraction would reduce the amount of tidal dissipation. This sensitivity can be parameterized with a stronger  $c$ -factor: Model D2-0- $c$  with  $c = 0.02$  and  $B_\eta=20$  results in very similar dissipation distribution as a model with  $c = 0.01$ , but  $B_\eta=35$  (not shown here).

We conclude that regardless of the choice of the initial parameters and rheology model the here described effects retain their validity, albeit with small quantitative differences. Even though good prediction of the updated tidal dissipation pattern can be made using Figure 3.6, the non-linear stress behaviour presented in Figure 3.4 cannot be easily assessed. Thus, for the exact computation of the tidal dissipation pattern of a non-uniform asthenosphere a numerical approach, such as finite element modelling, is indispensable.

#### 3.3.4. FEEDBACK

The results show that lateral variations in Io's rheological structure have an influence on the dissipation pattern, making the consideration of a dissipation-rheology feedback necessary. In particular, the induced asymmetry (Section 3.3.2) introduces an interesting characteristic, which needs to be investigated further. It is not clear whether a feedback would increase or suppress the asymmetry until an equilibrium is found, or if no equilibrium can be found with the offset continuously moving around the sphere.

For this feedback we only consider lateral variations. Furthermore, we assume

that the globally produced dissipation and the mean melt fraction in the asthenosphere do not change. This is reasonable under the assumption that an increase in the melt fraction due to a higher heat budget would increase the effectivity of the heat transport until the former equilibrium heat budget is reached (Moore, 2003).  $Q_{prod,new}(\theta, \phi)$  is therefore normalised to be in agreement with  $\bar{Q}_{prod}$ . We calculate the feedback for Pattern D2-0 with  $B_\eta = 20$  and  $c = 0.02$ . For the computation of the updated melt pattern in each iteration only degree 2 components are included. As for the initial Pattern D2-0, we assume that the blurring due to convection is wavelength-dependent and wavelengths shorter than for degree 2 are strongly reduced such that their influence on the updated tidal dissipation is negligible. As shown in Figure 3.2 we average over the old and the new melt fractions patterns since the new tidal dissipation pattern does not immediately determine the internal structure.

In order to obtain the distribution of rheological properties for the first iteration, we average between a uniform melt distribution and the melt fraction pattern arising for  $c = 0.02$  (D2-0-c). This is exactly the pattern of Model D2-0 with  $c = 0.01$ . For the computation of the new melt fraction the total amount of tidal dissipation pattern is normalised to be in agreement with the total amount of tidal dissipation  $\bar{Q}_{prod}$ . High spherical degrees components are removed, as shorter wavelength are stronger affected by the lateral heat transport due to mantle convection.

The resulting evolution of the dissipation pattern and melt fraction can be seen in Figure 3.7. From the figure it becomes apparent that the dissipation pattern changes. The peak in the melt fraction moves eastward, as already shown in Figure 3.5. In addition the variations in the melt fraction between equatorial and polar regions increase. After a few iterations, however, the solution converges. The resulting pattern shows a significant asymmetry towards the prime meridian in the peak in melt fraction. The dissipation pattern of the fourth iteration (not reduced in high degree spherical harmonics components) shows still a similar characteristic as Pattern D4 (Figure 3.1), however, the peaks near the equator, originally at  $270^\circ$  and  $90^\circ$ , are enhanced and the areas  $20^\circ$ - $50^\circ$  east of the prime meridian show a stronger tidal dissipation than west of the prime meridian. Reduced to degree components, the peak in the melt fraction can be found at  $15^\circ$  east of the prime-meridian.

This  $15^\circ$  shift is in agreement with the results obtained for Model D2-30 and Model D2-30-c in Section 3.3.3 with an initial  $30^\circ$  shift in the melt fraction. For these models the shift of the updated dissipation pattern is in western directions. The strength of the shift depends on the strength of the regional anomalies in the viscosity and shear modulus distribution, thus the  $c$ -factor. Furthermore, global and local runaway heating is prevented by two effects: 1) An increased amount of dissipation leads to an increase in melt which, in turn, leads to an increase in magmatic heat transport. At same stage, this prevents further heating up of the interior (Moore, 2001). This effect is implicitly included in the feedback modelling as we assume that the global tidal dissipation and average melt fraction remain constant; 2) in case tidal heating leads to an continuous increase of melt, the visco-elastic material eventually changes to a regime where less

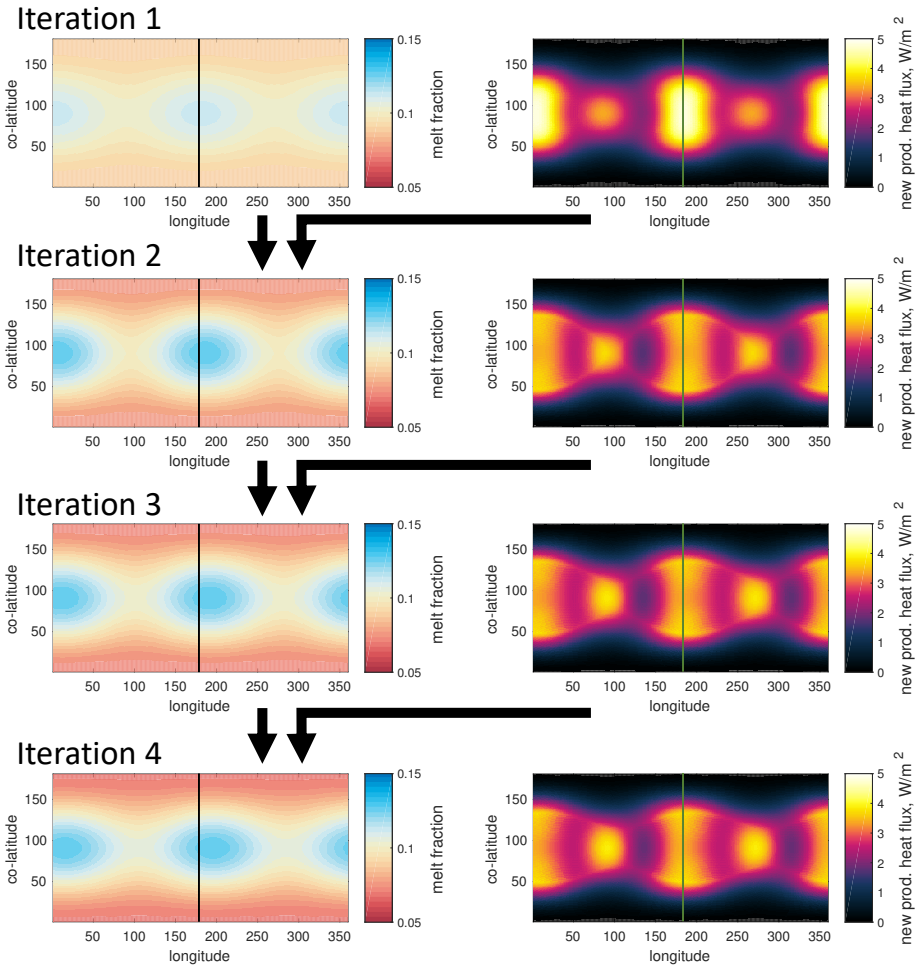


Figure 3.7: Feedback of the Model based on Pattern D2. Left column shows the melt fraction used as an input of the finite element model. Right column shows the tidal dissipation distribution resulting from the finite element model. This pattern is then transformed to a melt distribution (following Section 3.2) and averaged with the former melt fraction pattern to yield the new melt fraction distribution for the next iteration. Line added for visual reference.

heat is produced (Figure 3.6). This suggests that equilibrium solutions are likely, also for starting conditions not tested here. The offset of the peak in tidal heating depends on 1) the characteristics of the heat transport in Io's asthenosphere to weaken regional temperature anomalies caused by non-uniform tidal heating, 2) the dependency of the shear modulus and the viscosity on the melt fraction, i.e.  $B_\eta$  and  $B_\mu$ , 3) the initial structure of Io's interior.

This finding suggests that the offset shown in Io's volcanic activity pattern, peaking at  $30^\circ$  east of the prime meridian, could be caused by the described feedback caused by tidal dissipation in a visco-elastic asthenosphere and does not necessarily require tidal dissipation in a fluid magma ocean as suggested by *Tyler et al. (2015)*. In case future observations, such as the detection of librations (*Van Hoolst et al., 2020*), gravity and magnetic induction measurements, suggest that Io's asthenosphere behaves visco-elastic, the offset in the volcanic pattern can be used to find corresponding parameters (described above) that would result in a tidal heating distribution with the same offset.

### 3.4. CONCLUSION

Io's tidal heating is not uniformly distributed in the interior. As the heterogeneous nature of the tidally produced heat is likely not eliminated by vigorous mantle convection (Chapter 2), regional heterogeneities in Io's temperature field arise, leading to regional variations in the melt distribution. We investigated the feedback from these tidally-induced heterogeneities in the melt fraction on the tidal dissipation pattern itself. We assumed that tidal heating is purely happening in Io's asthenosphere, which we assume to be mainly solid and behaving visco-elastically. We only considered tidally-induced large-scale variations of the viscosity and shear modulus due to regional variations in the melt fraction. We did not consider local anomalies arising as a consequence of mantle convection and magmatic heat transport nor differences of the crustal thickness, as explored by *Běhouňková et al. (2010)*, *Han and Showman (2010)* and *Beuthe (2019)*.

The resulting tidal dissipation pattern is, in one part, determined by the squared stress pattern and, in the other part, determined by the lateral viscosity distribution. To compute the stress pattern we used a finite element model based on *Hu et al. (2017)* (benchmarked in 2), which can account for heterogeneous distribution of the viscosity and shear modulus. We find that the spatially varying visco-elastic properties induce an asymmetric contribution to the squared stress pattern when integrated over one orbital period. The stronger the lateral heat transport in the asthenosphere and the stronger the effect of partial melt on the rheological properties the more the resulting tidal dissipation pattern deviates from the standard tidal dissipation pattern. Changes in the tidal dissipation compared to the standard tidal dissipation pattern resulting from a homogeneous asthenosphere, can be approximated by the dissipative behaviour of a homogeneous asthenosphere with the same shear modulus and viscosity properties, as for the anomaly. Apart from this asymmetry, we found that in general an increase in the melt fraction causes an increase of the regional tidal dissipation in this area. The weaker the variations in the rheological properties, the more alike are the resulting tidal dissipation patterns to the standard dissipation pattern of the homogeneous

asthenosphere.

A continuous feedback between melt-dependent visco-elastic properties and tidal dissipation leads to new equilibrium tidal dissipation patterns and corresponding lateral variations of the melt fraction. These arising patterns contain an eastward shift of the location of the highest tidal dissipation. The stronger the remaining tidally-induced variations, the further away the offset is shifted from the sub-Jovian point.

The here presented models show that the tidally induced variations modify the tidal dissipation pattern and need therefore be taken into account. The arising differences show that for celestial bodies undergoing extreme tidal dissipation tidal heating, rheology and heat transport need to be considered as one coupled system. In addition, feedback between lateral variations in tidal heating and the viscosity and shear modulus in Io's asthenosphere produce an eastward offset in the peak of the tidal dissipation pattern. Therefore, we suggest that the observed offset in the volcanic intensity and density ([Davies et al., 2015](#); [Hamilton et al., 2013](#); [Kirchoff et al., 2011](#)) does not deliver a unique implication for a magma ocean with dissipation in the fluid medium ([Tyler et al., 2015](#)), but could potentially also be explained by a self-consistent feedback mechanism in the visco-elastic regime. An extended parameter study, testing the dependency of asthenospheric characteristics, such as heat transport and visco-elastic parameters, on the extent of the offset, could possibly be used to further constrain Io's interior.





# 4

## CAN A COMBINATION OF CONVECTIVE AND MAGMATIC HEAT TRANSPORT IN THE MANTLE EXPLAIN IO'S VOLCANIC PATTERN?

**T. STEINKE , D. VAN SLIEDREGT, K. VILELLA, W. VAN DER WAL,  
B. VERMEERSEN**

*Tidal dissipation makes Jupiter's moon Io the most volcanically active body in the Solar system. Most of the heat generated in the interior is lost through volcanic activity. In this study, we aim to answer the questions: Can convection and melt migration in the mantle explain the spatial characteristics of Io's observed volcanic pattern? And, if so, what constraints does this place on the viscosity and thickness of the convective layer? We examine three different spatial characteristics of Io's volcanic activity: i) The presence of global volcanism; ii) the presence of large-scale variations in Io's volcanic activity; and iii) the number of Io's volcanic systems. Our study relies on the assumptions that melt in the mantle controls Io's global volcanism, that the large-scale variations of Io's volcanic activity are caused by non-uniform tidal heating, and that the spatial density of volcanoes correlates with the spatial density of convective anomalies in the mantle. The results show that the observed small and large-scale characteristics of Io's volcanic pattern can be explained by sub-lithospheric anomalies influenced and caused by convective flow. Solutions that allow for active volcanism and Io's specific large-scale variations in volcanic activity range from a thick mantle of a high viscosity ( $10^{19}$  Pa s) to a thin asthenosphere of a low viscosity*

This chapter is published in the Journal of Geophysical Research: Planets [Steinke et al. \(2020b\)](#).

( $10^{12}$  Pa s). Provided that Io's volcanoes are induced by convective anomalies in the mantle, we find that more than 80% of Io's internal heat is transported by magmatic processes and that Io's upper mantle needs to be thicker than 50 km.

## 4.1. INTRODUCTION

Io's intensive volcanic activity and abundant volcanic surface features are signs of its intense heat loss and ongoing global resurfacing process driven by tidal dissipation. Most of Io's internally produced heat is brought to the surface by volcanic processes (Veeder *et al.*, 2012). The total number and spatial density variations of Io's volcanoes are likely controlled by sub-surface properties and mechanisms. This could help us to gain insights into interior processes and answer the crucial question whether or not a magma ocean is present beneath Io's crust.

4

Several studies investigated possible physical links between the locations of volcanic features and the interior of terrestrial planets and icy moons (e.g. Cañon-Tapia and Mendoza-Borunda, 2014; Cañon-Tapia, 2014; Crumpler, 1993; Crumpler and Revenaugh, 1997; Johnson and Richards, 2003; Smrekar and Sotin, 2012). In general, volcanism at the surface of planets and moons occurs when two conditions are fulfilled (Cañon-Tapia and Walker, 2004): (i) Molten and buoyant material is present, which is usually controlled by sub-lithospheric processes; and (ii) a weakness in the lithosphere is present, which allows buoyant material to rise.

If sub-lithospheric processes are assumed to control the locations of volcanoes, the volcanic pattern at the surface can be used to constrain the sub-lithospheric convective system, such as its thickness, viscosity, and heating rate. A large number of numerical and laboratory experiments of convective systems show that convection signatures, such as the spatial density and the geometry of thermal anomalies, depend on the Rayleigh number and aspect ratio of the system (e.g. Galsa and Lenkey, 2007; Parmentier and Sotin, 2000; Vilella *et al.*, 2018; Zhong, 2005; Zhou and Xia, 2010). If buoyant fluid is omnipresent below the crust, lithospheric anomalies, e.g. variations in crustal strength, are the controlling factors. In this case, volcanic chains or regions with elevated heat output are likely to form as a result of fault propagation. The propagation rate and azimuth of the emerging faults are controlled by the stress field in the rocky or icy crust due to tidal deformation, self-gravitation or other intrinsic sources. An example of this feature is Saturn's moon Enceladus (Crawford and Stevenson, 1985; Porco *et al.*, 2006; Yin and Pappalardo, 2015).

For Io, it is unknown whether sub-lithospheric or lithospheric anomalies control its volcanic pattern. Observations show that Io's volcanic activity is, at first order, globally distributed with a higher concentration of volcanoes in equatorial and mid-latitude regions (Davies *et al.*, 2015; Hamilton *et al.*, 2013; Kirchoff *et al.*, 2011; Veeder *et al.*, 2015). This large-scale pattern can be seen in both Io's heat output and the spatial density of volcanoes. Many studies attempted to link Io's volcanic activity to interior processes (e.g. Bierson and Nimmo, 2016; Ross *et al.*, 1990; Segatz *et al.*, 1988; Shahnas *et al.*, 2013; Tackley *et al.*, 2001). These studies suggest that the variations in

the volcanic activity at the surface are induced by heterogeneous tidal heating below Io's crust. Therefore, visco-elastic models or dynamic magma ocean models of Io's interior are generally evaluated based on the correlation between their resulting tidal heat production pattern and Io's observed volcanic activity pattern (e.g. [Hamilton et al., 2013](#); [Segatz et al., 1988](#); [Tyler et al., 2015](#)). However, Io's tidal heat production may be affected by thermal and chemical heterogeneities, which are neglected in spherically symmetric interior models. Thermal heterogeneities may even emerge self-consistently if the non-uniform nature of tidal dissipation is conserved in the temperature field of Io's dissipative layer (Chapter 2). Combined with the fact that heat loss mechanisms and dissipative processes in Io's interior are not fully understood yet ([de Kleer et al., 2019b](#); [Tyler et al., 2015](#)), this could be a reason for the low correlation between derived dissipation patterns and surface observations.

Statistical analysis of the spatial relation between adjacent surface features of volcanic origin reveals a clustered behaviour ([Hamilton et al., 2013](#)). This indicates that volcanic features may share the same anomaly on scales of several tens of kilometres. However, the statistical analysis of only active hot-spots, which represent the bulk of Io's heat output, shows uniform spreading ([Hamilton et al., 2013](#)). This uniform spreading can arise from 1) obliteration of older randomly spread volcanic features due to the appearance of new volcanoes ([Shoji and Hussmann, 2016](#)); 2) the competition of adjacent volcanic systems for ascending magma ([Hamilton et al., 2013](#)); or 3) evenly spread thermal anomalies in a convective layer below Io's lithosphere ([Schubert et al., 2001](#)). In any case, a uniform or random spreading implies that Io's largest volcano systems typically do not originate from the same anomaly. Global volcanic chains or bands of high heat output, such as present on Earth and Enceladus, do not seem to dominate Io's volcanic pattern ([Kirchoff et al., 2011](#)). The uniform spreading, in addition to Io's significant variations of volcanic activity, favours a sub-lithospheric control of Io's volcanic pattern. Previous studies have investigated Io's large-scale variations ([Bierson and Nimmo, 2016](#); [Hamilton et al., 2013](#); [Tackley, 2001](#)), Io's small-scale variations ([Shahnas et al., 2013](#); [Tackley et al., 2001](#)), and Io's global heat output ([Moore, 2003, 2001](#), e.g.) separately from each other. However, as all these characteristics are controlled by the same properties of the sub-lithospheric layer, a joint analysis of conditions that simultaneously allow for all these characteristics could provide powerful constraints on Io's interior.

The objective of this study is to test the hypothesis that convection and magmatic heat transport beneath Io's crust can explain the statistical spreading and the spatial density variations of Io's volcanic pattern. The novelty of our study is that three spatial characteristics of Io's volcanism are combined: 1) the presence of global volcanism, which requires the presence of magma; 2) the large-scale variations in the volcanic density of spherical harmonic degree  $\leq 4$ ; and 3) the small-scale spreading, i.e. the total number of Io's volcanoes. We allow Io's mantle to have vertically separated convective systems. For this study we assume that only the character of the upper convective system, here referred to as upper mantle, is linked to the volcanism at the surface. The aim of our analysis is to find properties of Io's upper mantle layer that can explain

these three characteristics of Io's volcanic pattern. Our analysis is based on three fundamental assumptions: 1) the presence of volcanism and, therefore, the presence of melt constrain the mantle temperature; 2) Io's large-scale volcanic activity variations are inherited from non-uniform tidal dissipation and the weakening of the heating pattern is caused by lateral convective flow; 3) the spatial frequency of thermal anomalies in the mantle control the global number of hot-spot features at the surface. These three characteristics are strongly sensitive to our main model parameters, the viscosity, the thickness of the upper mantle layer, and the fraction between convective and magmatic heat transport. Depending on the values of these parameters, the mantle layer could be referred to as a homogeneous mantle ranging from the core-mantle boundary to the base of the lithosphere, a partially molten low-viscosity asthenosphere, or a thin mushy magma ocean.

4

Although we assume that the sub-lithospheric layer is convective, this does not exclude that a significant amount of heat could be transported by advecting magma to the crust. Even if melt advection is the dominant mechanism to carry heat, thermal anomalies caused by the underlying convective dynamics are assumed to control the location of melt generation and accumulation, and therefore the location of Io's volcanoes. In contrast to previous studies, which correlate dissipation patterns to Io's observed volcanic activity pattern (e.g. [Hamilton et al., 2013](#); [Ross et al., 1990](#); [Tackley et al., 2001](#)), our approach is observation-driven and therefore independent of tidal dissipation models. To identify combinations of model parameters that can explain the small- and large-scale characteristics of Io's volcanic pattern, we use the thermal model developed in Chapter 2. This model was originally used to predict Io's mean mantle temperature and variations in Io's surface heat flux due to tidal dissipation and lateral heat flow of steady-state convection. Here, we use this model in an inverse manner by transferring it from the previously model-driven approach to an observation-driven approach. Furthermore, we use the scaling obtained by [Vilella et al. \(2018\)](#) to approximate the total amount of volcanic anomalies driven by convective dynamics in an internally heated system.

In Section 4.2, we discuss the volcanic observations used for our three-level analysis. The thermal model approximating the effect of the lateral heat flow as well as the scaling law approximating the average distance between volcanic features are introduced in Section 4.3. In Section 4.4, we present our results, i.e. the global, large-scale and small-scale characteristics of Io's convective mantle, as a function of our model parameters. In Section 4.5, we discuss the influence of model assumptions on our resulting parameter space as well as possible lithospheric effects on Io's volcanic pattern.

## 4.2. STATISTICAL ANALYSIS OF HOT-SPOT OBSERVATIONS

In this section, the input for our observation-driven approach is presented. We require two physical parameters that we derive from surface observations: 1) The strength of large-scale variations of Io's magmatic surface heat flux, which is used to quantify the amount of lateral heat flow due to convection; 2) the number of Io's volcanic anomalies, which will be compared to the number of thermal anomalies arising in the convective

system.

#### 4.2.1. SELECTION OF VOLCANIC DATA

Io's geologic surface features and infra-red emission have been observed by Voyager, Galileo, and New Horizons (e.g. [Davies et al., 2015](#); [Schenk et al., 2001](#); [Veeder et al., 2015](#); [Williams et al., 2011b](#)). Recent JIRAM observations on-board the JUNO mission ([Mura et al., 2019](#)) and continuous ground-based observations in the long wavelengths ([de Kleer and de Pater, 2016](#); [de Kleer et al., 2019](#)) provide complementary information on the characteristics and location of Io's hot-spots. Due to the diversity of these observations a large number of different data sets of volcanic features and hot-spots is available.

The strong temporal variations in volcanic activity and spatially-focused characteristic of volcanism in general makes the derivation of average properties over space and time challenging. First, it is unknown how the activities of recently active and inactive hot spots evolve over geological time scales. In addition, clustered volcanoes can result from a single or multiple volcanic system and the influence of intrusive volcanism on Io's heat flux pattern is not well constrained ([Veeder et al., 2015](#)). Finally, variations in the observed volcanic density could originate from a non-uniform coverage of observations ([de Kleer and de Pater, 2016](#); [Hamilton et al., 2013](#); [Mura et al., 2019](#)). In order to be able to quantify the influence of these uncertainties on our results, we set up and test two sets for Io's large-scale heat flux pattern, derived from different observations and filter options. For the number of Io's volcanic anomalies, we consider a minimum and a maximum value.

Our standard observation-based input contains the locations of recently active hot-spots discovered by Galileo, JUNO, and Earth-based observation given in [Davies et al. \(2015\)](#), [Mura et al. \(2019\)](#), and [de Kleer et al. \(2019\)](#). We refer to this collection of volcano locations as the standard hot-spot set. The combination of these data sets leads to multiple entries. Our objective is therefore to remove duplicates resulting from uncertainties in the derived locations, while keeping volcanoes of volcanic clusters. As a first step, duplicates in the combined data sets of [de Kleer et al. \(2019\)](#) and [Mura et al. \(2019\)](#) are removed. Then, the indicated uncertainty ranges in the localization of volcanic centres of the [de Kleer et al. \(2019\)](#) and [Mura et al. \(2019\)](#) data set are used to remove any potential overlap with the data set of [Davies et al. \(2015\)](#). The filtering process results in a set of 383 volcanic centres, which are, at first order, globally distributed. The full set of volcanic centres is visualised in Figure 4.1a. The included JUNO observation ([Mura et al., 2019](#)) reduces the observation bias of the previous observation sets towards lower latitudes ([de Kleer and de Pater, 2016](#)). However, it also introduces an additional observation bias towards Io's leading hemisphere. In order to quantify the effect of observation biases on our results, we do not include the JUNO observations by [Mura et al. \(2019\)](#) in our second set.

A second set is adopted from [Hamilton et al. \(2013\)](#). It contains recently active volcanoes as well as regions of former activity, i.e. patera floor units ([Williams et al.,](#)

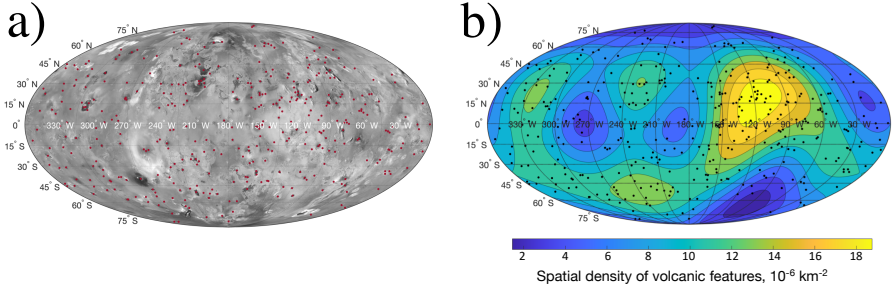


Figure 4.1: a) Location of volcanoes of our standard hot-spot set. Background shows mosaic of Io's surface (Williams et al., 2011a). b) Spherical harmonic analysis of the volcanic density distribution up to degree 4. Black spots indicate location of volcanoes.

4

2011b). In total, 173 hot-spots and 529 paterae are included (data set 1 and 2 in the supplementary material of Hamilton et al., 2013). With 96 detected overlapping features between the hot-spots and the paterae this results in 606 locations. This data set is visualized in 4.7 and is used to show the robustness of our large-scale analysis results presented in Section 4.4.2.

#### 4.2.2. SPHERICAL HARMONIC ANALYSIS OF THE VOLCANIC DENSITY

In this section, the volcanic data set is processed such that it can be used as an input for our geophysical model (Section 4.3). We use Io's spatial volcanic density of the previously introduced standard hot-spot set as a measure for Io's magmatic heat output. Note that we do not take eruption intensities into account. On the one hand, different instruments and physical models are used for the approximation of the eruption temperatures, and subsequent eruption intensities. This reduces the comparability between different data sets. On the other hand, taking only the intensities of one observation set might also not represent Io's mean heat output. However, observations of Io's active volcanoes reveal that the eruption frequency and intensity of Io's volcanoes are not uniform and that only a small number of active hot-spots, e.g. Loki Patera, contribute to the bulk of Io's recent total heat flow (de Kleer et al., 2019; Veeder et al., 2012). Qualitative differences between Io's volcanic density pattern and Io's volcanic intensity pattern, and consequences for our results, are discussed in Section 4.5.

We conduct a spherical harmonic analysis in order to examine the large-scale density distribution of Io's volcanoes. Our analysis is based on the technique used by Kirchoff et al. (2011). The normalized spherical harmonic coefficients of degree  $l$  and order  $m$  are expressed as follows (Johnson and Richards, 2003):

$$\left. \begin{matrix} C_{lm} \\ S_{lm} \end{matrix} \right\} = \frac{(-1)^m}{4\pi R_{Io}^2} \sqrt{\frac{(2 - \delta_{0m})(2l + m)(l - m)}{(l + m)!}} \sum_{n=1}^{N_{obs}} P_{lm}(\cos\theta_n) \begin{cases} \cos(m\phi_n) \\ \sin(m\phi_n) \end{cases}, \quad (4.1)$$

with  $C_{00} = N_{obs}/(4\pi R_{Io}^2)$ .  $N_{obs}$  is the total number of volcanic features of our standard hot-spot set,  $P_{lm}$  is the associated Legendre polynomial, and  $\theta_n$  and  $\phi_n$  are the co-

latitude and the longitude of each volcanic feature. The coefficients can then be used to reconstruct the volcanic density field as a function of the co-latitude  $\theta$  and the longitude  $\phi$  (Kirchoff *et al.*, 2011):

$$f_{obs}(\phi, \theta) = \sum_{l=0}^{L_{max}} \sum_{m=0}^l (-1)^m \sqrt{\frac{(2 - \delta_{0m})(2l + m)(l - m)}{(l + m)!}} P_{lm}(\cos \theta) (C_{lm} \cos(m\phi) + S_{lm} \sin(m\phi)). \quad (4.2)$$

We only consider spherical harmonics up to degree  $L_{max} = 4$ , because the tidal dissipation pattern of a radially symmetric interior structure only contains contributions  $\leq 4$  (Beuthe, 2013). We assume that variations of higher degrees do not originate from the non-uniform tidal heating. Therefore, they are not included in our inversely applied lateral heat flow scaling (Section 4.3.2). The resulting field  $f_{obs}$  is plotted in Figure 4.1b. The corresponding normalized spherical harmonic coefficients up to degree 4 are available in the data accompanying this paper (Steinke *et al.*, 2020c).

The peak of the volcanic density is located approximately 30 to 60 degrees east of the anti-sub-Jovian point as previously noted by Kirchoff *et al.* (2011) and Hamilton *et al.* (2013). Compared to the observation set adopted from Hamilton *et al.* (2013) the standard hot-spot set shows stronger contributions from non-symmetric coefficients, such as  $S_{10}$ . This is due to the included JUNO data set, which mainly contains observations from Io's leading hemisphere (Mura *et al.*, 2019). The resulting normalized coefficients are used as an input for our thermal model introduced in Section 4.3.2. A map of Io's volcanic density distribution up to degree 4 for the set from Hamilton *et al.* (2013) is presented in 4.7.

### 4.2.3. TOTAL NUMBER OF IO'S VOLCANIC ANOMALIES

In addition to the large-scale variations in the volcanic activity pattern, the total number of anomalies causing Io's volcanism is an important parameter. To determine an upper and lower limit for the number of Io's volcanic anomalies, we need to account for the underlying physical processes affecting the link between the available surface observables and the source of volcanism in Io's interior.

The clustering behaviour of volcanoes sharing one source of magma could lead to an overestimation of the total number of Io's volcanic anomalies. Therefore, we cannot simply take the number of volcanic features of our standard hot-spot set. Instead, following Davies *et al.* (2015), we use  $N_{min}=250$  to approximate the minimum number of Io's volcanic anomalies. Small variations in this approximation do not affect our results significantly (Section 4.4.3). Investigating Io's magmatic heat transport through the crust, Spencer *et al.* (2020a) show that magmatic intrusions are a crucial component of Io's crustal heat balance. Consequently, not all of Io's magma is delivered to the surface. This could lead to an underestimation of the number of magmatic systems at the base of the lithosphere. To approximate the maximum number of anomalies in the upper part of the mantle we use the number of features included in the Hamilton set (4.7) and assume that 80% of the magmatic systems do not reach the surface (Spencer *et al.*, 2020a). This results in  $N_{max}=3030$ . Altogether, we consider a conservative range



of 250 - 3030 for the number of Io's volcanic anomalies.

### 4.3. MODELLING THE CHARACTERISTICS OF IO'S CONVECTIVE LAYER

Following our framework, we assume that the melt distribution below Io's lithosphere and Io's surface volcanism are closely linked. We investigate three different mechanisms of the mantle dynamics that can influence the melt distribution below Io's lithosphere:

- Convection and magma transport regulate the mantle temperature, and therefore Io's melt fraction (Section 4.3.1).
- Convection controls how the non-uniformly tidally generated heat is transported laterally, and therefore the extent of Io's large-scale variations of the melt distribution (Section 4.3.2).
- Convection imposes regularly distributed cold downwellings and hot anomalies. The distance between these anomalies can be characterized by a specific wavelength whose value depends on the convective vigour. The resulting temperature variations lead to small-scale variations in the melt fraction, which are assumed to control the locations of Io's volcanic features (Section 4.3.3).

These characteristics of the convection pattern are dependent on parameters of Io's upper mantle, i.e. the mantle viscosity, the mantle thickness, and the fraction between convective heat transport and magmatic heat transport. These three parameters are unknown for Io and the resulting parameter space shall be constrained in three levels. In each level, a physical model is applied, which relates the parameter space of the upper mantle layer to one of the three spatial characteristics described above. Furthermore, parameter combinations resulting in incompatible conditions of the thermal system are eliminated in the first level analysis. This is due to the fact that the three parameters of Io's upper mantle given above, are not independent of each other, and in multiple ways connected to other properties of the thermal system. The aim of our three-level analysis is to progressively disregard all parts of the parameter space that are not able to explain Io's observed volcanic activity field. The fundamental relations, equations, and limitations of our three models are presented below.

#### 4.3.1. GLOBAL PRESENCE OF MAGMA

For the first level, we assume that Io's convective layer has no lateral variations. Mantle temperatures above the solidus must be widespread, allowing for a widespread presence of melt, melt migration and volcanism. This provides strong constraints on Io's interior. We assume that Io's interior is in thermal equilibrium (*Lainey et al., 2009*) meaning that all of the produced heat is transported to the surface. Thus,

$$\bar{Q}_{prod} = \bar{Q}_{out}, \quad (4.3)$$

where  $\bar{Q}_{out}$  is the mean heat flux lost to space and  $\bar{Q}_{prod}$  is the heat produced in Io's interior and transported to Io's surface. Furthermore, we assume that heat generated

by tidal dissipation within Io's interior is transported by melt advection, conduction and solid-state convection (e.g. [Elder, 2015](#), Chapter 2). Consequently, Io's heat output can be divided into a heat flux  $\bar{Q}_{cc}$  transferred by relatively slow mechanisms, i.e. conduction and solid-state convection, and a heat flux  $\bar{Q}_{mag}$  transported relatively fast, via buoyant molten rocks:

$$\bar{Q}_{prod} = \bar{Q}_{mag} + \bar{Q}_{cc} = \bar{Q}_{out}. \quad (4.4)$$

In the following, we refer to  $Q_{cc}$  and  $Q_{mag}$  as the convective and the magmatic heat flux, respectively. The ratio between the convective heat flux  $\bar{Q}_{cc}$  and the heat flux  $\bar{Q}_{out}$  is defined as in Chapter 2:

$$\bar{f}_{cc} = \frac{\bar{Q}_{cc}}{\bar{Q}_{out}}. \quad (4.5)$$

The determination of the heat flux fraction  $\bar{f}_{cc}$  requires the precise knowledge of the latent heat of the rising magma, the permeability of the mantle, and other parameters controlling the efficiency of magmatic heat transport ([Bierson and Nimmo, 2016](#); [Moore, 2001](#); [Spencer et al., 2020a](#)). As these parameters are challenging to obtain, we combine these parameters to one input parameter, namely  $\bar{f}_{cc}$ . Therefore, the above mentioned parameters are still implicitly included in our model. This approach has the crucial advantage to reduce the number of unconstrained parameters for our model. The value of  $\bar{f}_{cc}$  is unknown for Io and consequently one of the three parameters that we constrain in our parameter study.

If melt is only present in the upper part of Io's mantle, a large viscosity difference compared to the lower mantle emerges. We assume that the upper, low-viscosity layer of Io is convective (e.g. [Monnereau and Dubuffet, 2002](#); [Shahnas et al., 2013](#); [Tackley, 2001](#); [Tackley et al., 2001](#)), and that Io's total heat output is produced in this layer. Depending on the presence of melt, this layer could also represent Io's whole mantle. In accordance with previous studies (e.g. [Shahnas et al., 2013](#); [Tackley et al., 2001](#)), the influence of any deeper system is neglected. The thickness  $d$  and the viscosity  $\eta$  of the layer are unknown and form the remaining parameters. Any radial changes in the melt and temperature profile within the layer, which naturally arise in a system with magmatic and convective heat transport (e.g. [Moore, 2001](#); [Vilella and Kaminski, 2017](#)), are neglected. Other properties within this sub-lithospheric layer, such as the density  $\rho$ , the thermal expansivity  $\alpha_m$ , the conductivity  $k$  and the diffusivity  $\kappa$ , are kept constant throughout the convective system and given in Table 4.1.

The central links between the convective and magmatic heat transport are the melt fraction and the mantle temperature of the system. These properties are controlled by both the efficiency of the magmatic heat transport ([Moore, 2003, 2001](#)), and the efficiency of the convective heat transport. Note that even if magmatic segregation dominates the thermal state of the mantle (similar to [Bierson and Nimmo, 2016](#); [Moore, 2001](#); [Spencer et al., 2020a](#)), the given mantle conditions, such as the mantle viscosity and the temperature above the solidus temperature, still impose an additional amount of convective heat loss. In order to calculate the equilibrium mantle temperature of the system, we start with a global layer whose heat is partially removed by magmatic

heat flux  $\bar{Q}_{mag}$  and check whether a certain parameter combination of  $\eta$  and  $d$  can produce the remaining convective heat flux  $\bar{Q}_{cc} = \bar{f}_{cc}\bar{Q}_{out}$ , while maintaining a mantle temperature between solidus and liquidus. That way we obtain conditions for which Equation 4.4 is valid. The Rayleigh-Roberts number of the global layer, which defines the ratio between convection driving and prohibiting forces, is given by

$$\bar{Ra}_H = \frac{a_f g \rho_m \alpha_m \bar{f}_{cc} \bar{Q}_{out} d^4}{k_m \eta \kappa}, \quad (4.6)$$

where

$$a_f = \frac{1}{3} \left[ 1 + \frac{R_{con}}{R_{con} + d} + \left( \frac{R_{con}}{R_{con} + d} \right)^2 \right] \quad (4.7)$$

is the geometry factor accounting for spherical geometry (Deschamps et al., 2012), and  $R_{con}$  is the radial distance from the centre of Io to the bottom of the convective layer. We assume that melt does not interact with the convection pattern. The maximum temperature reached in the upper thermal boundary layer is a function of the three unknown parameters  $\eta$ ,  $\bar{f}_{cc}$  and  $d$ , and given in Chapter 2:

$$\bar{T}_m = \gamma_0 \left( a_f \bar{f}_{cc} \bar{Q}_{out} \right)^{\frac{3}{8}} \eta^{\frac{1}{8}}, \quad (4.8)$$

with

$$\gamma_0 = \sqrt{\frac{E_a}{5.8 R_{gas}}} \left( \frac{\kappa Ra_{H,crit}}{\rho_m g \alpha_m k^3} \right)^{\frac{1}{8}}. \quad (4.9)$$

Here,  $E_a$  is the activation energy,  $R_{gas}$  the gas constant and  $Ra_{H,crit}$  the critical Rayleigh-Roberts number.

Since we do not specify parameter values determining the efficiency of the magmatic heat transport, we obtain a solution volume in a three-dimensional parameter space instead of a single curve. The specific parameter combination  $\eta$ ,  $\bar{f}_{cc}$  and  $d$  at each point then defines these parameters, e.g. the melt flux, the melt segregation velocity, and the latent heat (Moore, 2003). However, constraints on these parameters imply limitations on the parameter space, which are discussed in Section 4.5.

$\bar{\Phi}$  is the global melt volume fraction, i.e. the porosity of the mantle, given by Hirschmann (2000)

$$\bar{\Phi} = \frac{\bar{T}_m - T_{sol}}{T_{liq} - T_{sol}}, \quad (4.10)$$

with the solidus temperature  $T_{sol}$  and the liquidus temperature  $T_{liq}$ . Minor non-linear effects due to latent heat consumption of the different components of the mantle are neglected. The viscosity  $\eta$  of the system is related to the melt volume fraction of the convective system (Mei et al., 2002):

$$\eta = \eta_0 \cdot \exp\left(-\alpha_\Phi \bar{\Phi}\right), \quad (4.11)$$

Table 4.1: Parameters of the convective layer (1) *Roberts (1967)*, (2) *Hirschmann (2000)*, (3) *Anderson et al. (2001)*, (4) *Mei et al. (2002)*, (5) *Lainey et al. (2009)*, (6) *Tackley (2001)*, (7) *Vilella et al. (2018)*.

Parameter	Variable	Value	Unit
Thermal conductivity	$k_m$	3	$\text{W m}^{-1} \text{K}^{-1}$
Acceleration of gravity	$g$	1.7	$\text{m s}^{-2}$
Thermal diffusivity	$\kappa$	$10^{-6}$	$\text{m}^2 \text{s}^{-1}$
Thermal expansivity	$\alpha_m$	$2 \cdot 10^{-5}$	$\text{K}^{-1}$
Critical Rayleigh-Roberts number <sup>(1)</sup>	$Ra_{H,crit}$	2772	-
Activation energy	$E_a$	$3 \cdot 10^5$	$\text{J mol}^{-1}$
Gas constant	$R_{gas}$	8.314	$\text{J K}^{-1} \text{mol}^{-1}$
Reference viscosity range	$\eta_0$	$10^{15} - 10^{23}$	$\text{Pa s}$
Mantle density	$\rho$	3244	$\text{kg m}^{-3}$
Liquidus temperature <sup>(2)</sup>	$T_{liq}$	1749	K
Solidus temperature <sup>(2)</sup>	$T_{sol}$	1359	K
Crustal thickness	$d_{crust}$	30	km
Radius Io <sup>(3)</sup>	$R_{Io}$	1821.6	km
Melt weakening factor <sup>(4)</sup>	$\alpha_\phi$	26	-
Mean heat flux <sup>(5)</sup>	$\overline{Q}_{out}$	2.3	$\text{W m}^{-2}$
Blurring coefficient <sup>(6)</sup>	$C_B$	2.869	-
Blurring exponent <sup>(6)</sup>	$\beta_B$	0.2105	-
Anomaly scaling coefficient <sup>(7)</sup>	$C_N$	0.0598	-
Anomaly scaling exponent <sup>(7)</sup>	$\beta_N$	0.25	-
Unknown parameter	Variable	Range	Unit
Viscosity convective layer	$\eta$	$10^{12} - 10^{20}$	$\text{Pa s}$
Thickness convective layer	$d$	20 – 1000	km
Heat flux fraction	$\overline{f}_{cc}$	0.005 – 0.99	-

where  $\alpha_\phi$  is the viscosity melt-weakening factor and  $\eta_0$  is the reference viscosity in a melt-free mantle. The temperature-dependence of the viscosity is neglected here, as we only consider melt-containing matrices. The unknown composition of Io's mantle leads to uncertainties in  $T_{sol}$ ,  $T_{liq}$ , and  $\eta_0$ . However, even a large range of  $\eta_0$  can provide strong limitations to the  $\eta$ - $\overline{f}_{cc}$ - $d$  parameter space as discussed in Section 4.4.1. The ranges of  $\eta_0$ ,  $T_{sol}$  and  $T_{liq}$  at 100 km depth used here are given in Table 4.1. We neglect any melting temperature reducing effect of sulphur or other volatiles as Io's high eruption temperatures indicate silicate volcanism (*McEwen et al., 1998*).

#### 4.3.2. LARGE-SCALE ANOMALIES

The aim of this second level analysis is to find additional parameter sets of  $\eta$ ,  $\overline{f}_{cc}$  and  $d$  that can be disregarded as they would not be able to explain large-scale variations of Io's observed volcanic activity. Therefore, we assume that Io's volcanic density variations are caused by lateral melt fraction variations in the convective layer, which in turn are caused by large-scale variations in the tidal heat production pattern. The model for analysing these large-scale variations in the volcanic density field is based on the

approach presented in Chapter 2. Our heat transport model is able to incorporate lateral differences in the heat production. In contrast to the model-driven approach in Chapter 2, the present model is used in a reverse manner such that it is suited for an observation-driven approach and independent of the underlying heating processes. Note that we do not consider radial differences in the heat production within the convective layer, but only consider the projection of the produced heat  $Q_{prod}(\theta, \phi)$  onto Io's surface. The projected heat is a function of longitude  $\phi$  and co-latitude  $\theta$ . Due to the lateral convective flow of heat (*Tackley, 2001*), the laterally varying patterns of  $Q_{prod}(\theta, \phi)$  and  $Q_{out}(\theta, \phi)$  are not identical. However, Equation 4.3 describing Io's global heat production and output remains valid. Heat transport by magma facilitates a more radial heat flow direction because the time scale of rising magma is much shorter than that of solid-state convection. Our model presumes that melt, and the heat carried by melt, are immediately removed from the convective system. Melt migration in lateral direction, such as investigated for Earth (*Keller et al., 2017; Sparks and Parmentier, 1991; Turner et al., 2017*), is assumed to not influence the large-scale pattern of the magmatic heat output. Even if melt is transported laterally over hundreds of kilometres to the nearest volcanic centre, the investigated heat flux pattern, with wavelengths of 2000 km and more, would be hardly affected.

A critical addition to the model introduced in Section 4.3.1 is that Equations 4.6, 4.8 and 4.10 are used independently for each column in the mantle defined by a latitude and longitude. As discussed in Chapter 2, we justify this regional approach with the good agreement between numerical results by *Laneville et al. (2013)* and the analytical approach used by *Vilella and Kaminski (2017)* (see further details in Section 4.1 of *Vilella and Kaminski, 2017*). In addition, we note that our results for the thermal anomalies (Section 4.4.3) indicate that the typical convection-length is significantly smaller than the wavelengths of the large-scale pattern considered here. Thus, the maximum temperature of the system (Equation 4.8), found in hot upwellings, can change regionally. Regional changes of the surface fraction between downwellings and hot upwellings are expected to remain small. Therefore, we argue that a regional application of the previous introduced scaling is reasonable.

As discussed in Section 4.2, we use the volcanic density fields to approximate Io's long-term heat output pattern  $Q_{mag}(\theta, \phi)$ . We assume that the melt volume fraction  $\Phi$  is proportional to the magmatic heat output  $Q_{mag}$ . This requires that the percentage of intrusive-to-extrusive volcanism is uniform, implying no large differences in crustal and magma properties. From the pattern of Io's observed volcanic activity we derive

$$\frac{f_{obs}(\theta, \phi)}{C_{00}} = \frac{Q_{mag}(\theta, \phi)}{Q_{mag}} = \frac{\Phi(\theta, \phi)}{\hat{\Phi}} = \xi(\theta, \phi), \quad (4.12)$$

where  $\hat{\Phi}$  is the mean melt volume fraction described by the integral over a sphere  $S$  of Io's radius  $R_{Io}$

$$\hat{\Phi} = \frac{1}{4\pi R_{Io}^2} \int_S \Phi(\theta, \phi) dS. \quad (4.13)$$

Note that the melt volume fraction arising from the temperature  $\overline{T}_m$  (Equation 4.10) does not result in the same value as the globally averaged melt volume fraction arising from the temperature field  $T_m(\theta, \phi)$ . Using Equation 4.12 and the co-latitude and longitude-dependent versions of Equations 4.8, 4.10 and 4.5 we obtain

$$Q_{cc,out}(\theta, \phi) = \left( \frac{T_{sol}(1 - \xi(\theta, \phi)) + \xi(\theta, \phi) \hat{T}_m}{a_f^{\frac{3}{8}} \eta^{\frac{1}{8}} \gamma_0} \right)^{\frac{8}{3}}. \quad (4.14)$$

In contrast to  $\overline{Q}_{cc,out}$ , the average resulting from the surface integral of  $T_m(\theta, \phi)$ , i.e.  $\hat{T}_m$ , is not equal to  $\overline{T}_m$  of a homogeneous layer. However, as the difference is small we take  $\overline{T}_m$  as a first estimate to start our iteration.  $Q_{cc,out}(\theta, \phi)$  is then iteratively obtained by re-computing  $\hat{T}_m$  with the location-dependent version of Equation 4.8 and forcing  $\overline{Q}_{cc,out}$  to remain constant for a given  $\overline{f}_{cc}$  (Equation 4.5).

$Q_{cc,out}(\theta, \phi)$  is affected by lateral flow, meaning that spatial peaks in the heat production pattern are smoothed. The strength of the blurring depends on the vigour of convection and can be simulated by applying a smoothing filter with filter weights

$$B(l) = C_B \overline{Ra}_H^{-\beta_B} \frac{R_{Io} \pi}{ld}, \quad (4.15)$$

which depends on the degree  $l$  of the spherical harmonic coefficient of the original signal, the thickness  $d$  of the convective layer, the radius of Io  $R_{Io}$ , and a set of numerical and analytically derived constants, i.e.  $C_B$  and  $\beta_B$  (Tackley, 2001) provided in Table 4.1. In case  $B(l)$  results in values larger than 1, it is forced to 1. To derive the heat production from the observed heat flux pattern, first,  $Q_{cc,out}(\theta, \phi)$  is decomposed in its spectral components  $C_{Q,nm}$  and  $S_{Q,nm}$  by

$$Q_{cc,out}(\theta, \phi) = \overline{f}_{cc} \overline{Q}_{out} + \sum_{l=1}^4 \sum_{m=0}^l P_{lm}(\cos\theta) (C_{Q,lm} \cos(m\phi) + S_{Q,lm} \sin(m\phi)). \quad (4.16)$$

To obtain  $Q_{cc,prod}(\theta, \phi)$  the filter is used reversely compared to 2. Consequently, it has an amplifying effect. Assumptions and caveats of this procedure are discussed below. The tidally produced heat flux pattern, which is transported by convection, is calculated by

$$Q_{cc,prod}(\theta, \phi) = \overline{f}_{cc} \overline{Q}_{out} + \sum_{l=1}^4 \frac{1}{B(l)} \sum_{m=0}^l P_{lm}(\cos\theta) (C_{Q,lm} \cos(m\phi) + S_{Q,lm} \sin(m\phi)). \quad (4.17)$$

The total heat production pattern projected to Io's surface is obtained by

$$Q_{prod}(\theta, \phi) = Q_{mag}(\theta, \phi) + Q_{cc,prod}(\theta, \phi). \quad (4.18)$$

The inverse application of the blurring is only valid under the assumption that the present-day volcanic distribution mirrors the underlying tidal heating. This implies that

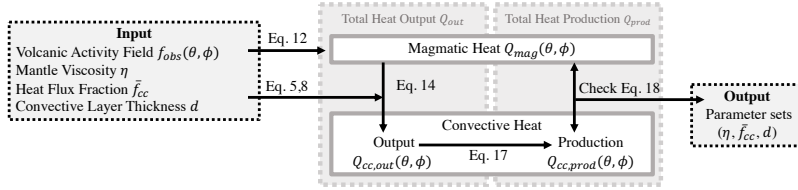


Figure 4.2: Flow chart of our observation-driven approach for large-scale anomalies. Input: the volcanic activity pattern and the parameters of the convective layer that shall be tested. Output: final parameter set in agreement with observations. The two central grey boxes show Io's heat flux output  $Q_{out}(\theta, \phi) = Q_{cc,out}(\theta, \phi) + Q_{mag}(\theta, \phi)$  and Io's heat production  $Q_{prod}(\theta, \phi) = Q_{cc,prod}(\theta, \phi) + Q_{mag}(\theta, \phi)$  projected to Io's surface. Arrows represent the direction of the respective equations.

## 4

the volcanic distribution is not a result of a random distribution or affected by additional interior or surface process other than lateral flow in convection cells with short wavelengths (see results in Section 4.4.3). The statistical significance of low-degree components of the volcanic density field (Kirchoff *et al.*, 2011) and the good agreement between volcanic density and heat flow maps (Davies *et al.*, 2015) for degree 2 indicate that Io's volcanic activity variations result from a physical process. We also include the less significant components of degree 1, degree 3, and degree 4. However, compared to degree 2, we find that these components play only a minor role in constraining our parameter space (not shown). Provided that the assumptions above are valid, the inverse application of the blurring of all significant spectral contributions of the pattern is a unique process. However, since inherently lost components of high degrees cannot be included, the inverted solutions are not complete. An extensive discussion on how uncertainties in the pattern representing Io's heat flux affect our final results can be found in Section 4.5.

The aim of this procedure is to identify parts of the  $\eta$ - $\bar{f}_{cc}$ - $d$  parameter space for which this calculation results in realistic values, i.e. positive values, for  $Q_{prod}(\theta, \phi)$  for all co-latitudes and longitudes, as the tidal heat production cannot be negative. In case of a turbulent convective system with high values for  $\bar{Ra}_H$  and large thickness  $d$ , the amplifying effect of the filter (Equation 4.17) results in negative values for  $Q_{cc,prod}(\theta, \phi)$  that cannot be compensated by  $Q_{mag}(\theta, \phi)$ . In other words: these types of systems cannot explain the observed large-scale variations in volcanic density as the lateral heat flow of the strongly turbulent system would suppress any large-scale temperature variations. Consequently, parts of the parameter space resulting in negative values in  $Q_{prod}(\theta, \phi)$  are disregarded. The procedure for the second level analysis is visualized in Figure 4.2.

### 4.3.3. NUMBER OF SMALL-SCALE ANOMALIES

For our third level analysis, we estimate the total number of Io's volcanoes from the spatial density of thermal anomalies in a purely internally heated convective system. This estimation is based on the critical assumption that the volcanic features at the surface are related to locations of melt focusing or melt generation below Io's lithosphere. Both processes are induced by small compositional or thermal anomalies. Convection

in the mantle with thermal up- and downwellings is a source of small-scale anomalies. The average distance between thermal anomalies of a system depends on the Rayleigh number, or the Rayleigh-Roberts number for an internally heated system, and can be analytically derived (*Schubert et al., 2001*) or approximated by a scaling law (e.g. *Parmentier and Sotin, 2000; Vilella et al., 2018; Zhong, 2005; Zhou and Xia, 2010*).

It may be most intuitive to relate Io's volcanoes to evenly spread hot upwellings. However, volumetric heated systems, such as for Io, are cooled by active downwellings. Upwellings in these systems are usually broad and non-buoyant (e.g. *Parmentier and Sotin, 2000*). However, small local temperature variations in the broad upwelling may lead to a significant difference in the melt fraction compared to cooler locations within the same upwelling. Thus, melt may be dominantly generated at the hottest points within these non-buoyant upwellings (see yellow surrounded features in Figure 4.7a and 4.7b). The melt rises through vents to the surface (*O'Reilly and Davies, 1981*) and volcanoes form just above these hot anomalies.

In the other possible case, melt is focused at downwellings. This requires buoyant melt that has been produced in upwelling regions to migrate laterally over large distances. Magma transport of several hundreds of kilometres has been reported and studied for plume-ridge systems on Earth (*Braun and Sohn, 2003*). In this study, the authors find that a solid pressure gradient of an uprising plume can facilitate a lateral melt migration over distances of more than 100 km. With typical hot-spot distances of 100 km – 400 km for Io, the lateral heat transport by magma does not affect the low spherical harmonic degrees of the heat flux pattern considered in the large-scale analysis (Section 4.3.2). Another potential link between surface volcanism and downwellings is delamination. Usually, downwellings lead to a thickening of the lithosphere. However, delamination of the lithosphere has been observed in numerical models of Io's asthenosphere (*Schools and Montesi, 2019*). Extreme basal heating reduces the lithosphere viscosity. As a result, the base of the lithosphere can more easily be dragged downwards, causing convective thinning of the lithosphere (*Spohn and Schubert, 1983*) and re-melting of the downwards dragged lithospheric material. The thinned lithosphere and the additional supply of lithospheric melt could facilitate Io's volcanism.

Based on high resolution numerical simulations, *Vilella et al. (2018)* derived a scaling to characterise the convection pattern of an internally heated layer. An automatic detection procedure of downwellings at mid-depth of the convective layer results in the following relationship

$$N_{d^2} = C_N \overline{Ra}_H^{\beta_N}, \quad (4.19)$$

where  $N_{d^2}$  is the dimensionless number of cold downwellings per unit area and  $C_N$  is a scaling factor. The exponent  $\beta_N$  is equal to 1/4 (Section 5.3 in *Vilella et al., 2018*). We convert  $N_{d^2}$  into the total number of downwellings:

$$N_{total} = N_{d^2} \frac{4\pi(R_{Io} - d_{crust} - d/2)^2}{d^2}, \quad (4.20)$$



where  $(R_{Io} - d_{crust} - d/2)$  is the distance from the centre of Io to the centre of the convective layer. This scaling was initially developed for downwellings. Since for Io's heated mantle the classical view of convective cells, in which every downwelling is associated with an upwelling, is not appropriate, it cannot be transferred for Io's broad upwelling regions. However, Figure 4.7a and 4.7b, show that the hottest locations within upwelling regions, correlate with the locations of downwellings. A numerical investigation, presented in 4.8, further shows that Equation 4.19 can be used to approximate the number of hot anomalies per unit area. As a consequence, Equation 4.19 is appropriate to approximate the number of volcanic anomalies, independently of whether these anomalies correlate with cold downwellings or hot anomalies within broad upwellings.

We use  $C_N$  for a rigid boundary condition (Table 4.1) and assume an uncertainty range of  $\pm 25\%$  in this coefficient, which we discuss in 4.8. Since the exponential nature of the viscosity and the term  $d^4$  in the Rayleigh-Roberts number dominate the resulting total number of volcanoes  $N_{total}$ , the influence of the uncertainty in  $C_N$  on the resulting parameter space is small (Section 4.4.3).

4

## 4.4. RESULTS

Here, we show how our initial parameter space is reduced by disregarding combinations of parameters that cannot explain the observed spatial characteristics of Io's volcanic activity field. This is done in three levels. Each level represents a different spatial characteristic as presented in Section 4.3. While for the first level, i.e. the calculation of Io's global mantle temperature, only Io-specific values given in Table 4.1 are required, the analysis of large-scale anomalies (second level) and small-scale anomalies (third level) requires Io's observed volcanic density distribution and the range of Io's volcanic centres presented in Section 4.2.

### 4.4.1. GLOBAL PRESENCE OF MAGMA

We use Equation 4.6 and 4.8 to calculate the mantle temperature and Rayleigh-Roberts number for our parameter space consisting of the viscosity  $\eta$ , the heat flux fraction  $\bar{f}_{cc}$ , and the thickness  $d$  of the convective layer (Table 4.1).

An overview of the three-dimensional parameter space with all remaining solutions is presented in Figure 4.3a. The domain forms a band from low viscosities and high heat flux fractions to high viscosities and low heat flux fractions (Figure 4.3b and c). Parameters for which the average melt volume fraction is not compatible with the viscosity  $\eta$  are disregarded (Equation 4.11). For this melt-viscosity constraint, we use a conservative approach with a wide range for the initial melt-free viscosity  $\eta_0$  (Table 4.1). Additionally, models resulting in mantle temperatures above the liquidus temperature or below the solidus temperature are disregarded. This is because we only consider solutions with a heat flux value  $1 > \bar{f}_{cc} > 0$ . Constraints on the  $\eta$ - $\bar{f}_{cc}$ -plane determining the thickness of the solution band (Figure 4.3b and c) result from these two restrictions. Note that at large  $d$ , small  $\eta$ , and large  $\bar{f}_{cc}$  the obtained Rayleigh-Roberts numbers are larger than  $10^{14}$  (Figure 4.3d). We cannot ensure that the scaling laws remain accurate at these extreme values. However, this part of the parameter space is disregarded due

to constraints resulting from the second and third level analysis (Section 4.4.2 and Section 4.4.3).

Apart from our three main model parameters  $\eta$ ,  $\bar{f}_{cc}$ , and  $d$ , uncertain properties of the convective system influence the mantle temperature and therefore the solution space. An important model uncertainty is the boundary condition between the convective layer and Io's lithosphere. In case a free-slip boundary instead of a rigid boundary is used, the critical Rayleigh-Roberts number decreases from  $Ra_{crit} = 2772$  to  $Ra_{crit} = 868$  (Vilella and Kaminski, 2017). In that case, the solution band in the  $\eta$ - $\bar{f}_{cc}$ -plane is shifted by approximately half an order of magnitude towards higher mantle viscosities. The same effect occurs if  $\gamma_0$  is reduced by 13% or if  $\bar{Q}_{out}$  is reduced by 30%. In addition, the liquidus and solidus temperatures of Io's mantle are uncertain. Changing these temperatures leads to a shift, thinning, or thickening of the valid parameter space in the  $\eta$ - $\bar{f}_{cc}$ -plane. In particular the parameter combinations with high  $\bar{f}_{cc}$  values are affected. For regimes in which heat is mainly extracted by melt ( $\bar{f}_{cc}$  close to 0), the temperature is not as strongly affected by the viscosity as for a convection-dominated regime (Figure 4.3b and c). However, compared to the full parameter range investigated here, the shift would remain small. This indicates that our results are not strongly affected by uncertainties in properties of Io's upper mantle.

#### 4.4.2. LARGE-SCALE ANOMALIES

For the large-scale analysis, we use the observation-driven approach presented in Section 4.3.2 and our standard hot-spot set presented in Section 4.2. Figure 4.4a shows the globally average mantle temperature  $\hat{T}_m$  for the parameter space that corresponds to Io's large-scale volcanic density variations. The cut at low viscosities ( $\eta < 10^{15}$  Pa s) and high heat flux fractions ( $\bar{f}_{cc} > 0.4$ ) is due to the fact that the lateral variations in Io's volcanic activity pattern cannot be explained by an extremely turbulent convective system. For such a system, the non-uniform tidal heating pattern is erased by the turbulent motion of the fluid. For the corresponding parameter combinations the amplifying filter (Equation 4.17) leads to negative values for  $Q_{prod}(\theta, \phi)$  (Equation 4.18). We conclude that thick and highly turbulent convective systems cannot explain Io's volcanic distribution.

Additional thinning in the  $\eta$ - $\bar{f}_{cc}$ -plane (Figure 4.4b and c) happens because locally the mantle temperature field exceeds or falls below the solidus-liquidus temperature range. In particular parameter combinations with large peak-to-peak temperature variations and high average mantle temperatures are affected by this constraint. Furthermore, parameter combinations with a small layer thickness  $d$ , small  $\bar{f}_{cc}$ , and low viscosity  $\eta$  result in a Rayleigh-Roberts number below the critical Rayleigh-Roberts number (Table 4.1). As convection would cease, this part of the parameter space is also disregarded.

The parameter space in agreement with the observations set adopted from Hamilton et al. (2013) is plotted in 4.7. Both observation sets result in similar solutions. This indicates that the influence of data set choices, such as the filtering of volcano locations

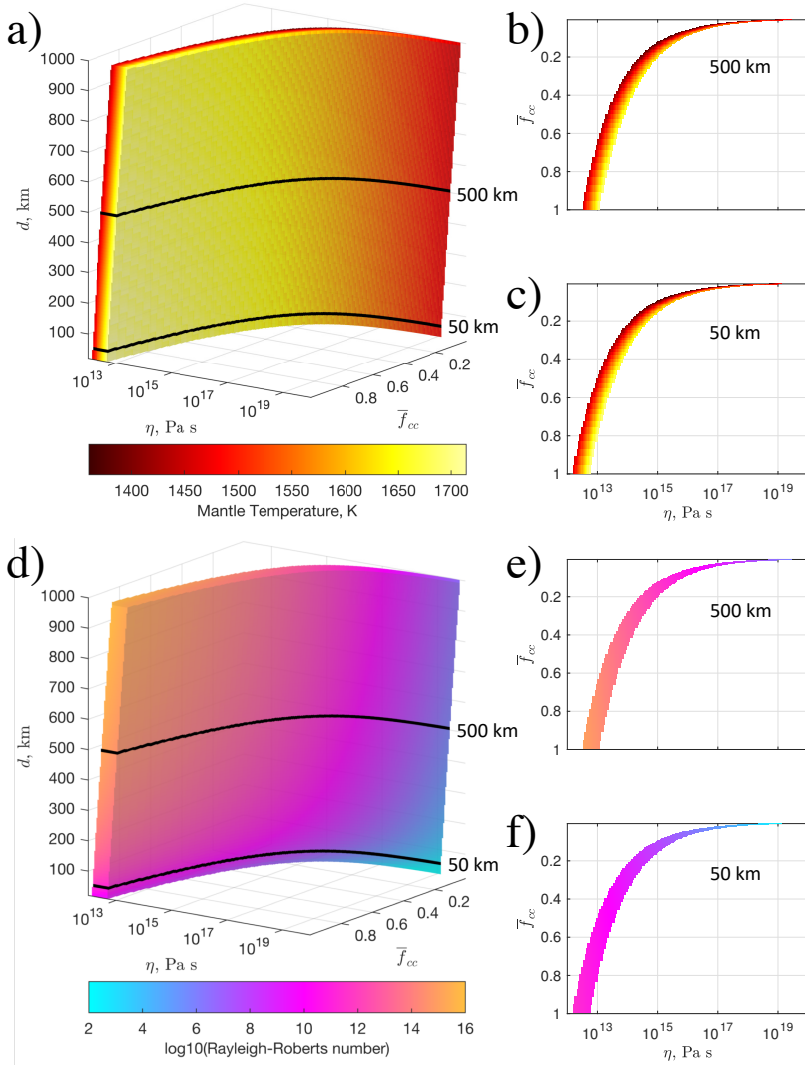


Figure 4.3: Overview of solutions in a three-dimensional parameter space spanned by the viscosity  $\eta$ , the heat transport fraction  $\bar{f}_{cc}$ , and the thickness  $d$ . a) shows the mantle temperature ranging from the solidus temperature to the liquidus temperature. Black lines indicate  $\eta$ - $\bar{f}_{cc}$ -plane at 500 km and 50 km shown in the two-dimensional parameter space in b) and c), respectively. d) shows the three-dimensional parameter space for the Rayleigh-Roberts number, e) and f) show the two-dimensional parameter space for  $d = 500$  km and for  $d = 50$  km, respectively.

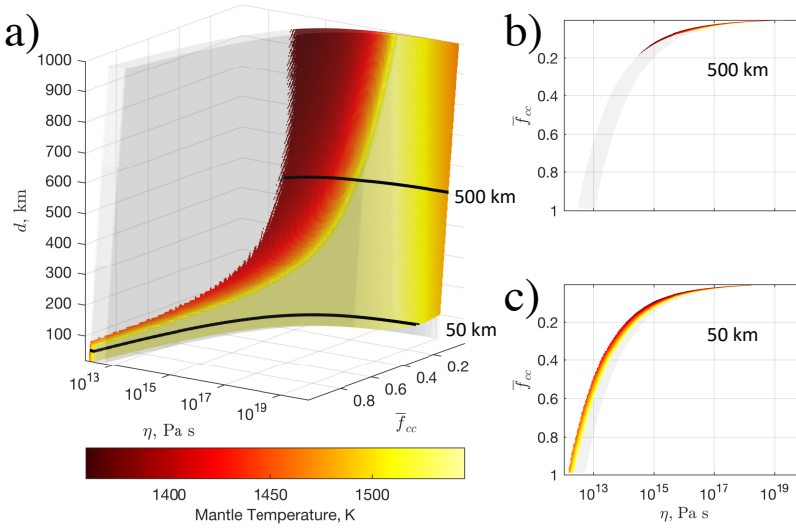


Figure 4.4: Overview of solutions with constraints from the observed large-scale variations. a) shows the average mantle temperature  $\hat{T}_m$  in a three-dimensional parameter space spanned by the viscosity  $\eta$ , the heat flux fraction  $\bar{f}_{cc}$ , and the thickness  $d$ . b) and c) show the mantle temperature in the two-dimensional parameter space for  $d = 500$  km and  $d = 50$  km, respectively. Transparent gray areas display solution space of Section 4.4.1.

and the inclusion of JUNO observations (Mura *et al.*, 2019), is small.

#### 4.4.3. NUMBER OF SMALL-SCALE ANOMALIES

Finally, we focus on the number of convection-driven thermal anomalies, which we assume to correlate with Io's volcanic features (Section 4.3.3). In Figure 4.5a-c, we present the numbers of thermal anomalies for the three-dimensional parameter space remaining from Section 4.4.2. Note that for models with approximately more than  $10^5$  thermal anomalies, a correlation between thermal anomalies at the base of the lithosphere and Io's volcanic surface features is not provided. Io's volcanoes could be located so close to each other that their magma chambers would form a continuous magma ocean. In this case, the volcano distribution is most likely driven by lithospheric anomalies. As this would violate our fundamental assumption that the volcanoes are correlated with thermal anomalies in the upper mantle, the third level analysis cannot be applied to this part of the parameter space.

We take the range of 250 to 3030 volcanic centres derived for Io in Section 4.2 and add a  $\pm 25\%$  range to account for the uncertainty on the scaling discussed in 4.8. We disregard all parameter combinations with smaller or larger values. The remaining parameter space is presented in Figure 4.5d-g. It can be seen that Io's range of volcanic centres can only be explained by a mantle thickness  $d > 50$  km, high mantle viscosities, and a magma-dominated heat transport ( $\bar{f}_{cc} < 0.20$ ). Solutions with a thickness below

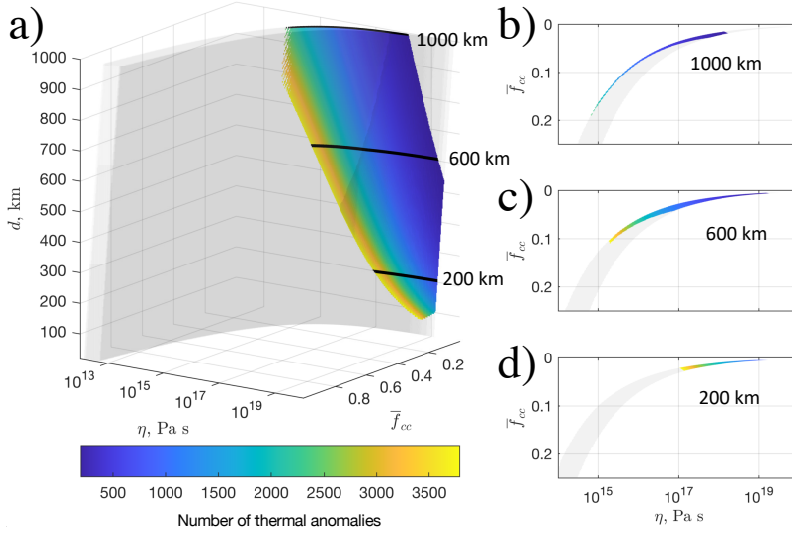


Figure 4.5: Number of thermal anomalies. a) shows the three-dimensional parameter space obtained in Section 4.4.2, b) and c) show the two-dimensional parameter space for  $d = 500$  km and  $d = 50$  km, respectively, with the same colour scale as for panel a). d)–g) show the number of thermal anomalies for the remaining parameter space taking into account a range of Io’s total number of volcanoes of  $250\text{--}3030 \pm 25\%$  range. d) shows the three-dimensional parameter space, and e), f) and g) show the two-dimensional parameter space for  $d = 1000$  km,  $d = 600$  km, and  $d = 200$  km, respectively, with the same colour scale as for panel d). Note that panels e)–g) have different axes than panels a)–d). Transparent gray areas display the solution space of Section 4.4.1.

50 km, either result in a Raleigh-Robert number below the critical Rayleigh-Roberts number, or the scaling results in more than 3787 anomalies. A limit caused by too few volcanoes arises as well for models with extremely low heat flux fractions and thick convective layers. A large part of the remaining parameter space results in mantle temperatures just above the solidus temperature (compare Figure 4.4a and Figure 4.5d). The high uncertainties on Io’s crustal thickness hardly affect our results. A crustal thickness of 60 km instead of 30 km changes the number of thermal anomalies by less than 5% (Equation 4.20).

## 4.5. DISCUSSION

Our results place strong constraints on Io’s upper mantle. However, several assumptions and simplifications have been made that require further justification.

The constraints provided by the second level analysis (large-scale analysis) on the parameter space are controlled by the ratio between the largest amplitudes of Io’s magmatic heat flux variations  $Q_{mag}(\theta, \phi)$  and Io’s mean heat output  $Q_{out}$ . However, this ratio is affected by uncertainties. Observations and models indicate a significant amount of background heat flow, i.e. heat originating from unaccounted sources

(Spencer *et al.*, 2020a; Veeder *et al.*, 2015). The amount and distribution of this background heat flow could alter the ratio between the largest amplitudes of  $Q_{mag}(\theta, \phi)$  and  $\bar{Q}_{out}$  and therefore the constraints on our three-dimensional parameter space. Accounting for an additional homogeneous background heat flux would allow for higher Rayleigh-Roberts numbers and larger layer thicknesses. An additional uncertainty arises by how the available volcanic observations are used to derive  $Q_{mag}(\theta, \phi)$ . We use Io's volcanic density pattern presented in Section 4.2.2 to characterise the variations in the magmatic heat output. However, Io's volcanoes show a large variation in their eruption intensities and frequencies, which we do not take into account. In order to estimate the effect of this simplification on our results, we perform an additional spherical harmonic analysis using the data set presented in Davies *et al.* (2015) and we weight the volcano locations with their eruption power following the weighting approach by Kirchoff *et al.* (2011). This leads to an even stronger degree 2 component than for the volcanic density pattern resulting from the Hamilton set presented in 4.7 and therefore would lead to an even stronger constraint on the parameter space (not shown here). The evenly spread volcanic density pattern can therefore be considered as a conservative choice. As the volcanic density patterns of the standard hot-spot and the Hamilton set almost result in the same parameter space solution (Section 4.4.2 and 4.7), the effects of the above described uncertainties on our conclusions should be small.

Our results suggest that a significant part of Io's produced heat is transported by advecting magma. However, since Io's strongly heated mantle can maintain a sufficiently high Rayleigh-Roberts number to allow for convection, this result is not in contradiction with our hypothesis that the volcanoes are linked to the convection pattern. A magma-dominated heat transport for Io is in agreement with results by Moore (2001), Bierson and Nimmo (2016), and Spencer *et al.* (2020a). However, two additional limitations on our parameter space, which have not been discussed before, need to be placed: 1) Potentially unrealistic melt segregation velocities (Moore, 2003) arise if the resulting melt fraction is very low, but the magmatic heat transport is extremely large (small  $f_{cc}$ ), or if the resulting melt fraction is high, but the magmatic heat transport is small ( $f_{cc}$  close to 1). This would lead to a further thinning of the parameter space in the  $\eta$ - $f_{cc}$ -plane. 2) At melt volume fractions above 30%-40%, fluid melt pockets enclose the solid particles (Moore, 2001). In this case, Io's upper mantle needs to be considered as a purely convective magma ocean with a very low viscosity. This is not in agreement with a partially magmatic and partially solid-state convective heat transport. All parameter combinations with melt volume fraction above 50% are disregarded due to other constraints (Section 4.4.2). Eliminating solutions with melt volume fraction higher than 40% would further thin the solution space in the  $\eta$ - $f_{cc}$ -plane. However, since in both cases the critical thresholds are highly uncertain and would affect only a small part of our final parameter space, and therefore not our conclusions, we do not apply these additional limitations to Figure 4.4.

Although our coupled model design does not violate fundamental thermal concepts within the given boundaries discussed above, the used scalings contain simplifications. Inaccuracies could arise as a result of strong interactions between melt and convective

flow. Heat transport in a partially molten and convecting system has not received accurate quantitative treatment in the literature (see further discussion in [Breuer and Moore, 2015](#)). For example, magmatic emplacement and melt focusing were not initially included in our used scaling laws ([Tackley, 2001](#); [Vilella and Kaminski, 2017](#); [Vilella et al., 2018](#)). These interactions between solid and liquid phases in Io's tidally deformed interior could be driving mechanisms of Io's heat production and heat transport. Extensive lateral heat transport and interactions between tidal heating and rheology in mantle upwellings, shallow magma chambers, or decompacting boundary layers may explain Io's localized heat output anomalies such as Loki Patera. Assuming that these interactions only affect regional scales, we expect the effects on our solution space to be small. Nevertheless, it may be interesting to investigate the detailed effects of two-phase flow on Io's heat transport and heat production in relation to Io's focused heat output. This requires additional theoretical developments and is therefore beyond the scope of this work.

4

We find that the observed number of Io's volcanoes is orders of magnitudes smaller than the number of thermal anomalies resulting from a shallow and turbulent convective magma ocean with a low viscosity (Figure 4.5). Based on our hypothesis that Io's volcanic distribution is controlled by sub-lithospheric dynamics, our results do not favour the presence of a turbulent convective magma ocean. Instead, our results favour a partially molten layer, with the majority of parameter combinations resulting in low to medium melt volume fractions. In these regimes, active downwellings and delamination (e.g. [Schools and Montesi, 2019](#); [Vilella and Kaminski, 2017](#)) could pull lower parts of Io's lithosphere into Io's mantle. This could lead to a continuous recycling of the lithosphere material, required to explain Io's observed eruption temperatures ([Keszthelyi et al., 2007](#); [McEwen et al., 1998](#)). Other reasons for Io's observed volcanic density, which are not based on the assumption that today's volcanic activity is controlled by Io's current convection pattern and do not preclude a magma ocean ([Keszthelyi et al., 1999](#)), need to be considered. For example, locations of the volcanoes could be a result of ancient impacts. Volcanoes could have formed in an earlier evolutionary stage and remained, while the interior kept evolving. However, the continuous and wide-spread resurfacing and observed changes in the volcanic activity in location and time ([Geissler et al., 2004](#)) makes the theory of frozen-in volcanoes unlikely. Another cause for Io's volcanic distribution could be crustal stresses that induce crustal weaknesses. Long faults accompanied by volcanic chains of global scale, which could indicate fault propagation due to tidal stresses, have not been observed. However, weaknesses in the crust due to thermal stresses, arising as a consequence of Io's continuous resurfacing, have been suggested ([Kirchoff and McKinnon, 2009](#); [Kirchoff et al., 2020](#)). These stresses cause the elevation of Io's high mountains and may also cause volcanism. This mechanism would lead to continuous change of volcano locations, in agreement with [Geissler et al. \(2004\)](#). In the case magma forms evenly in the regions of diffuse upwellings, or the distance between adjacent thermal anomalies is sufficiently small for the formation of a continuous magma reservoir, competition for magma could also explain the uniform spreading of Io's hot-spots ([Hamilton et al., 2013](#)). In order to make definitive conclusions on Io's interior, detailed modelling aiming to answer how magma can rise through Io's thick

crust is essential. Stronger constraints on crustal properties and conditions at the base of the crust that invoke heat-piping could potentially rule out some of the possible theories for Io's volcanic activity pattern.

## 4.6. CONCLUSION

Io is covered by a large number of active hot-spots and volcanic features (Figure 4.1). We investigated whether Io's volcanoes can be explained by sub-lithospheric convection processes below the lithosphere. Furthermore, we tested what constraints on the viscosity, the thickness, and the fraction between convective and total heat transport of Io's uppermost convective layer can be placed. This study is motivated by the observed uniform distribution of active hot-spots (*Hamilton et al., 2013*), which fits the characteristics of uniformly distributed thermal anomalies in a convective system. Furthermore, global volcanic chains, which would indicate a strong relationship between volcanic activity and tectonics, have not been observed.

One key difference compared to previous studies is the observation-driven approach. In contrast to tidal dissipation modelling studies (e.g. *Hamilton et al., 2013*; *Ross et al., 1990*; *Segatz et al., 1988*; *Tyler et al., 2015*), our analysis is independent of the underlying tidal dissipation mechanism and distribution. The basis for our analysis is a set composed of the location of 383 recently active hot-spots detected by satellite-based and Earth-based observations (*Davies et al., 2015*; *de Kleer et al., 2019*; *Mura et al., 2019*). Another key difference of this study is that we investigated three different spatial characteristics simultaneously. These characteristics of Io's surface are assumed to be linked to corresponding spatial characteristics of convective flow in Io's interior. The three investigated characteristics act at different spatial wavelengths and are 1) the temperature of the upper mantle allowing for widespread volcanism; 2) the large-scale (spherical harmonic degree  $\leq 4$ ) temperature variations originating from non-uniform tidal heating; and 3) small-scale features arising from thermal anomalies in the upper mantle. Using steady state scaling laws based on the work presented in Chapter 2 and *Vilella et al. (2018)*, we quantified these three characteristics of convection processes as a function of the above given parameters of the convective layer. This allowed us to step-wise confine the parameter space in agreement with surface observations. Importantly, the three analysis levels are independent from each other, i.e. uncertainties and assumptions on one particular level do not affect the constraints on the parameter space given by other levels.

Our results show that, due to constraints from the mantle temperature and the relationship between temperature, melt, and viscosity, strong constraints can be placed on the three-dimensional parameter space. A thick and turbulent convective system with a low viscosity would erase any large-scale lateral temperature and melt variations in the interior. This is not in agreement with the low-degree variations in Io's volcanic activity pattern. Consequently, parameter combinations resulting in a high Rayleigh-Roberts number are disregarded (Figure 4.3a). If the total number of volcanic anomalies is related to the spatial density of downwellings or hot anomalies in Io's upper convective layer, additional constraints arise that rule out a fluid-phase dominated magma ocean. Based on observations and accounting for intrusive volcanism and



clustered volcanoes, we approximated Io's total number of volcanoes to be between 250 and 3030. This range of volcanic features can be obtained by a convective layer with a magma-dominated heat transport (>80%), a mantle viscosity between  $10^{15}$  Pa s and  $10^{19}$  Pa s, and a thickness  $\geq 50$  km.

We conclude that the global, large, and small-scale characteristic of Io's volcanic pattern can be explained by sub-lithospheric convection-driven anomalies in a system with convective and magmatic heat transport. We showed that our results are robust against parameter uncertainties and variations in the observation input (Section 4.4.1 and 4.7). While this suggests that our working hypothesis is consistent with observations, it is important to keep in mind that other processes of lithospheric origin may also explain Io's distinct volcanic distribution (Section 4.5). More advanced numerical models studying the interactions between Io's asthenosphere, lithosphere, and crust, incorporating solid and liquid flow, are needed. Furthermore, observing Io's topography and gravity field with an Io-dedicated mission as well as other observation strategies identified by *de Kleer et al. (2019b)* would allow us to conclude with certainty whether the volcanic distribution is driven by lithospheric or sub-lithospheric anomalies.

4

#### 4.7. APPENDIX-A: ALTERNATIVE OBSERVATION SET

To show that the obtained constraints on Io's interior are not purely a consequence of our chosen standard observation set, we here introduce a second observation set, which is adopted from *Hamilton et al. (2013)*. It contains 173 active volcanoes as well as 529 volcanic features of former volcanic activity (Data set 1 and 2 in the supplementary material of *Hamilton et al., 2013*). The 702 features are further reduced to 606, due to multiple entries. The locations of these features are presented in Figure 4.6a. All normalized spherical harmonic coefficients up to degree 4, resulting from the analysis presented in Section 4.2.2 are available under *Steinke et al. (2020c)*. The adopted set also shows a peak in the volcanic density located east of the anti-sub-Jovian point. Compared to our standard hot-spot set the set from Hamilton shows a stronger  $C_{22}$  coefficient. The resulting parameter sets constrained by the large-scale variations of the Hamilton set (corresponding to Figure 4.4) are shown in Figure 4.6c, d, and e. For both observation sets, parameter combinations that result in high Rayleigh-Roberts numbers, leading to negative values for  $Q_{prod}(\theta, \phi)$  (Equation 4.18), are cut off.

#### 4.8. APPENDIX-B: SCALING FOR THE NUMBER OF VOLCANOES

In this paragraph, we use the numerical simulations and counting method developed in *Vilella et al. (2018)* to provide constraints on the number of hottest locations within upwelling regions per unit area ( $N_{d^2}$ ). Typical convection patterns (horizontal plane just below the thermal boundary) obtained for systems with a Rayleigh-Roberts number of  $10^6$  and  $10^9$  are presented in Figure 4.7a and 4.7b, respectively. As hot anomalies (indicated in yellow) are less distinct than cold downwellings (blue), the measure of  $N_{d^2}$  is highly sensitive to the detection criteria, causing a large uncertainty on the parameterization of hot anomalies. To account for these uncertainties, we determine  $N_{d^2}$  for various values of the detection criteria and report these variations in Figure 4.7c. Vari-

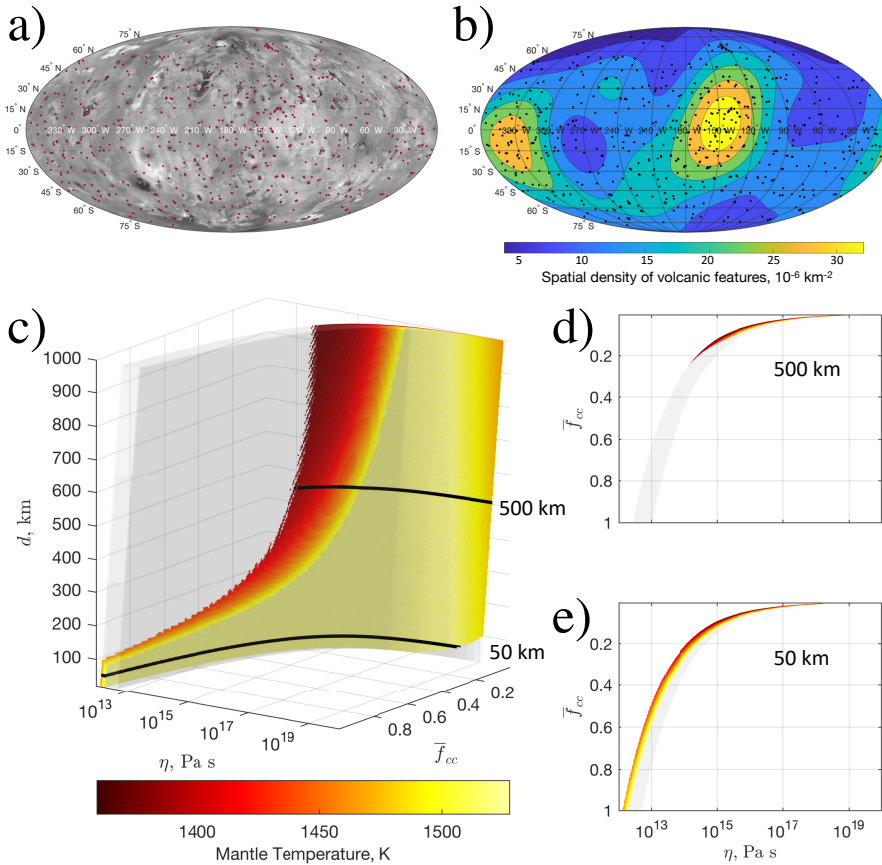


Figure 4.6: a) Location of volcanoes of the Hamilton set (*Hamilton et al., 2013*). Background shows mosaic of Io’s surface (*Williams et al., 2011a*). b) Spherical harmonic analysis of the volcanic density distribution up to degree 4. Black spots indicate location of volcanoes. Overview of solutions with included constraints due to the observed large-scale variations of the Hamilton set is shown in c)-e). c) shows the average mantle temperature in a three-dimensional parameter space spanned by the viscosity  $\eta$ , the heat flux fraction  $\bar{f}_{cc}$ , and the thickness  $d$ , d) and e) show the mantle temperature in the two-dimensional parameter space for  $d = 500$  km and  $d = 50$  km, respectively. Transparent gray areas display solution space of Section 4.4.1.

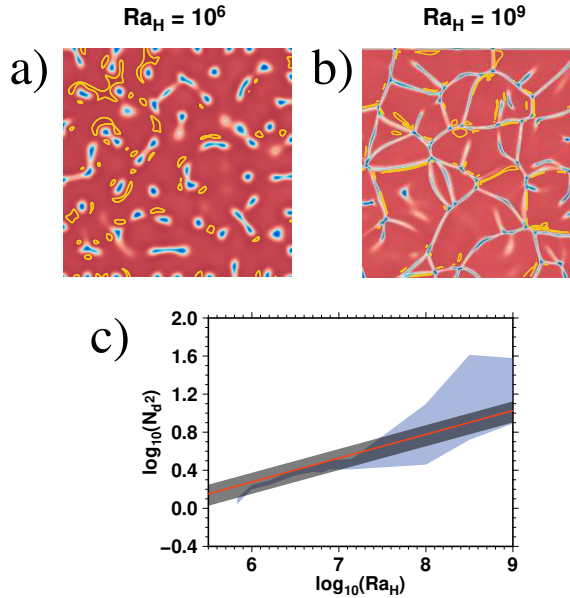


Figure 4.7: Temperature fields in a plane located just below the thermal boundary layer for a) a Rayleigh-Roberts number ( $Ra_H$ ) of  $10^6$  and b)  $10^9$ . Note that the dimension of the horizontal plane is different for  $Ra_H = 10^6$  (6:6) and  $Ra_H = 10^9$  (2:2). Blue and red colours correspond to material that is colder and hotter than the local horizontal average, respectively. The colour scale is not the same in the two panels and was chosen to increase the visibility of the convective structures. Yellow contours illustrate the hot thermal anomalies that have been determined using the detection procedure described in [Vilella et al. \(2018\)](#). The change of the number of thermal anomalies per unit area ( $N_{d^2}$ ) with the Rayleigh-Roberts number is reported in c). The blue shaded area corresponds to the number of hot thermal anomalies. The uncertainties due to the counting method are shown by the vertical extent of this area. The solid red curve is the scaling law for the number of cold anomalies proposed by [Vilella et al. \(2018\)](#), while the grey shaded area illustrates a 25% error on this count.

ations of  $N_{d^2}$  are modest for low  $Ra_H$  but increase with  $Ra_H$  as the complexity of the convective flow increases (see [Vilella et al., 2018](#), for more details). Interestingly, we find that the number of the hottest points within broad upwellings and the number of cold downwellings are somewhat equivalent (Figure 4.7c). This could be seen in connection to the observation that the location of the hot anomalies are spatially correlated to the location of cold downwellings (Figure 4.7a and 4.7b). The only notable difference is the underestimation of  $N_{d^2}$  for large  $Ra_H$ . However, in Section 4.4.3, the constraint on the number of volcanoes is used to exclude models with too many volcanoes. As such, this underestimation is not an issue as it implies more conservative results. We can therefore safely use Equation 4.19 to characterize the number of hottest points within upwelling regions per unit area.

# 5

## CONCLUSION AND OUTLOOK

The overarching goal of this thesis was to improve the understanding of the interconnection between Io's volcanic activity and interior dynamics. In this chapter, the main conclusions are presented together with recommendations for follow-up research. Section 5.1 provides answers to the research questions posed in the beginning of this dissertation, whereas in Section 5.2 the main findings of this dissertation are critically assessed and set in context to previous studies. Recommendations for future modelling work in order to assess open and arising questions are offered in Section 5.3. Finally, an outlook on future Io observations is provided in Section 5.4.

### 5.1. ANSWERS TO RESEARCH QUESTIONS

This section comprises and connects all results presented in Chapters 2, 3 and 4 focusing on the research questions stated in Section 1.5.

RS 1: *What mantle properties and processes influence the strength of the lateral variations induced by non-uniform tidal heating?*

Io's tidal dissipation is non-uniformly distributed. Previous studies suggested a correlation between Io's non-uniform tidal dissipation and the heat output at the surface (Section 1.4.4). However, these studies did not quantitatively describe the strength of this correlation based on the underlying physical processes influencing this correlation. In addition, only spatial variations of the heat output at the surface were considered, whereas lateral heterogeneities in the interior state and structure causing these spatial variations at the surface were not further investigated. In Chapter 2 of this dissertation a consistent model of Io's mantle that links heating and heat transport was developed in order to identify the parameters that influence to what extent long-wavelength heterogeneities in the mantle and on Io's surface are related to the non-uniformly distributed heat production. The developed model combines mantle convection, melt migration and non-uniform heating. We found that four interior properties determine to what extent the tidal heating pattern becomes visible on Io's surface: 1) The initial heating pattern itself: If two layers contribute to the bulk of Io's tidally produced heat, the pattern of

the projected heat flux is more laterally uniform. Lateral variations in the intensity of Io's volcanic activity are therefore less likely to be detectable. 2) The heat transport mechanism: The higher the convective contribution to the total heat transport in the mantle, the smaller the tidally-induced variations that remain. 3) The thickness of the convective layer: The thicker the layer, the stronger the lateral heat transport in the mantle and the smaller the remaining variation. 4) The viscosity of the upper convective layer: The lower the viscosity, the higher the vigour of convection and the stronger the lateral blurring of the non-uniform heating. The consistent implementation of all relevant heat transport processes in Io's mantle and crust shows that, besides the already considered spatial variations in the surface heat flux and volcanic activity, also the temperature and melt fraction in the mantle and the lid thickness may vary laterally due to non-uniform tidal heating.

RS 2: *To what extent does the non-uniform heating influence the lateral temperature distribution in the mantle and the volcanic heat output at the surface?*

With our model-driven analysis presented in Chapter 2, we found a wide range of possible peak-to-peak temperature anomalies originating from non-uniform tidal dissipation. The results range from no significant variations (less than 1 K) for a thick, purely convecting mantle, to 190 K for a thin asthenosphere, separated from the deeper mantle and with dominating magmatic heat transport. Consequently, the absence of distinct long-wavelength variations in the heat output does not necessarily indicate a magma ocean with strong lateral heat transport (Section 1.4.1) but could also be explained by a solid, strongly convecting mantle with tidal heating in the asthenosphere and in the deep mantle. Our observation-driven analysis of Io's volcano distribution presented in Chapter 4, however, reveals considerable strong spatial long-wavelength variations in Io's volcanic activity. These observations suggest that these long-wavelength variations are also likely present in Io's interior and could show as variations in the mantle temperature, melt fraction, and lid thickness. The assumption of a well-mixed interior is therefore likely violated. Combining our modelling results and observations suggests that tidal heating, heat transport, and the interior structure of Io cannot be considered separately. Io's interior needs to be understood and modelled as a non-spherically symmetric system. This motivates three-dimensional modelling approaches for the computation of Io's tidal dissipation pattern and thermal heat transport.

RS 3: *What is the influence of the tidally-induced lateral variations in the rheological properties on the tidal heating pattern?*

Previous studies that computed Io's tidal dissipation pattern treated the interior structure as spherically symmetric and neglect lateral variations that are induced by tidal dissipation (see conclusion to RS 2). We solved this inconsistency by developing a numerical model based on finite elements that couples tidal dissipation, heat transport, and visco-elastic properties of Io's interior. The results presented in Chapter 3 show that tidally-induced lateral variations in the rheological structure cause a change in the amount of regionally produced tidal dissipation in Io's asthenosphere. Regions with higher than average melt fractions lead to a regional increase of tidal heating compared to a homogeneous model. For regions with melt fractions below the average melt fraction, the regionally dissipated heat is reduced. In addition to this effect, tidally-induced

lateral variations in the rheological properties induce a small asymmetry of the tidal dissipation pattern with respect to the prime meridian, which is not present for homogeneous layered interior structures. This break in symmetry is caused by the spatial variation in the time delay in the tidal response of the asthenosphere due to spatially varying visco-elastic properties and the revolution of the tidal bulge around the body.

RS 4: *How does this dissipation-rheology feedback influence Io's volcanic pattern?*

As the induced asymmetry of the tidal dissipation pattern (see conclusion to RS 3), in turn, affects the distribution of visco-elastic properties in the asthenosphere, a feedback between the tidally produced heat pattern and the heat-dependent rheologic properties needs to be explored. This was done in the second part of Chapter 3. While the induced asymmetry in the tidal dissipation pattern for a symmetric lateral varying melt distribution is small, the offset increases as the feedback proceeds. The peaks in the tidal dissipation pattern, originally at the sub- and anti-Jovian points for a homogeneous asthenosphere, shift eastwards. Eventually, the effect of mantle convection, which weakens lateral variations in the mantle, and the effect of tidal dissipation in a heterogeneous asthenosphere, which induces the eastward offset anomaly, balance each other, until an equilibrium pattern evolves. The peaks in the modelled tidal heating pattern can be found 15° eastward of the sub-Jovian and anti-Jovian points. Earth and satellite-based observations show that the areas with the highest volcanic activity can be found east of the sub-Jovian and anti-Jovian points. So far, the only possible explanation for this observation was tidal dissipation in a magma ocean (Tyler *et al.*, 2015). However, due to a strong lateral heat flow in a fully fluid magma ocean, the offset in the tidal dissipation pattern in the interior is unlikely to show in the volcanic pattern at the surface. Therefore, the here investigated mechanism is, to date, the only mechanism that can explain both the eastward offset in the dissipation pattern and the visibility of the arising offset in the observed volcanic pattern.

RS 5: *Can the small and large-scale characteristics of Io's volcanic activity pattern be explained by a partially convective and partially magmatic heat transport?*

Whereas tidal dissipation likely introduces long-wavelength variations of spherical harmonic degree 2 and 4 in Io's mantle, convection and magmatic heat transport are known to cause small-scale heterogeneities, for example up- and downwellings (Figure 1.6). Like for tidal dissipation, these heterogeneities could show in the characteristics of Io's volcanic distribution. In this case the heat transport and tidal dissipation regimes (Section 1.4.2 and Section 1.4.3) could explain both the observed small-scale characteristics and long-wavelength variations in the volcanic pattern. Whereas previous studies investigated both characteristics separately, our study in Chapter 4 combines both. We assumed that 1) melt in the mantle controls Io's global volcanism; 2) the spatial large-scale variations of Io's volcanic density are caused by non-uniform tidal heating in the interior; and 3) the spatial density of volcanoes correlates with the spatial density of convective anomalies in the mantle. Using a scaling-based analysis (Chapter 4) we found that a partially convective and partially magmatic heat transport in Io's upper mantle can produce the observed small- and large-scale characteristics of the volcanic pattern.

RS 6: *What constraints do the characteristics of the volcanic activity pattern place on Io's upper mantle?*

Given the assumptions and the scaling-based analysis stated above in RS 5, we investigated a three-dimensional parameter space spanned by the viscosity and the thickness of the upper mantle layer and the fraction between convective and total heat transport. Parameter combinations that result in spatial features correlating with Io's observed global and large-scale surface characteristics range from a thick mantle of high viscosity ( $10^{19}$  Pa s) to a thin asthenosphere of low viscosity ( $10^{12}$  Pa s). We further reduced the parameter space by removing solutions whose resulting spatial density of convective anomalies in the mantle does not match the spatial density of Io's volcanoes. For this additional condition, we found that more than 80% of Io's internal heat is transported by magmatic processes and that the upper convective layer of Io's mantle needs to be thicker than 50 km.

## 5.2. CONCLUSIONS

The research presented in this dissertation shows that Io's interior needs to be considered as one coupled system. We showed that taking into account interacting processes, in particular the connection between tidal heating and rheology, leads to feedbacks that have not been explored previously. The distribution of Io's volcanoes on global, large, and small spatial scales provides valuable insights into the tidal heating process and heat transport below Io's crust. The main conclusions of this thesis are:

- Solid state convection and magmatic heat transport co-exist in Io's mantle, with likely dominating magmatic heat transport.
- Tidal dissipation in Io's interior can induce lateral variations of the physical properties of the asthenosphere.
- The feedback between tidal dissipation in the visco-elastic asthenosphere and the temperature-dependent rheology can explain the eastward offset, which is observed in Io's volcanic activity pattern.

On the one hand, the work accomplished in this thesis shows that improvements in the understanding of Io's interior do not necessarily require new observations, since physical links between different mechanisms in Io's interior have not been fully explored, yet. On the other hand, our research pointed out many unknown but crucial quantities, which could not be constrained but significantly affect the strength and manners of processes in Io's interior. Therefore, neither of these two aspects should be disregarded.

The research presented in this dissertation should be considered as a collection of novel conceptual studies investigating Io's interior. We made use of simplistic scaling laws capable to explore general relations rather than computationally expensive models with a large number of uncertain parameters. For this reason, this thesis can be considered as the initial step towards more sophisticated models investigating feedbacks in Io's interior and their link to Io's volcanism showing at the surface. In the following, we critically assess the main findings of this dissertation.

Io's mantle layer is commonly modelled as either a solid convective mantle, adapting models of terrestrial planets, or as a fluid magma ocean, adapting models of fluid

water oceans of icy moons. However, neither of these two classifications likely accurately describes Io's partially fluid, partially solid interior. In fact, using one or the other end-member model could lead to wrong conclusions. In Chapter 2, we developed a simple 1D thermal model that allows for a co-existence of solid-state mantle convection and magmatic heat transport. Unlike the thermal models of the end-members above, our models allow for a thermal equilibrium between tidal dissipation and heat loss given a partially molten mantle. Our thermal model (Chapter 2 and Chapter 4) couples both processes through the presence of melt. However, the model treats the melt fraction and the efficiency of the magmatic heat transport as independent variables, whereas in reality, these parameters are strongly connected. Furthermore, the model does not account for interactions between up- and downwellings and magma advection, since these interactions have not been quantitatively studied in the literature so far. Given our conceptual analysis of Io's interior and widely explored parameter space, uncertainties in the used scaling law caused by unknown mechanisms are unlikely to significantly affect our main conclusions. Instead, these model additions can be seen as a possibility to further constrain the parameter space obtained in Chapter 4. An extensive discussion of required theoretical research and laboratory experiments to quantify the effect of these interactions on the interior heat transport is given in Section 5.3.1.

Like our thermal model, also our tidal dissipation model (Chapter 2 and Chapter 3) does not incorporate all effects of a partially fluid, partially solid medium. For the computation of the amount and distribution of tidal dissipation we used the Maxwell rheology, which originally assumes a solid mantle. For the tidal dissipation computations in Chapter 2 and Chapter 3 we chose the interior visco-elastic properties such that that Io's observed total heat output is matched. For our approach, the viscosity used for the visco-elastic systems is not the same as the viscosity defining the vigour of mantle convection. For this reason we treated these viscosities separately. The parameters and effects studied in Chapter 2 and Chapter 3, such as the effect of small melt variations on the amount and distribution of tidal dissipation, are not significantly affected by the use of the Maxwell rheology versus advanced models, such as the Burger and Andrade rheologies. However, scaling laboratory experiment, such as the effect of melt on the visco-elasticity, to a system the size of Io can lead to inaccuracies in the investigated parameters. Recommendations on how already accomplished and future advances in dissipation model of mixed phases can improve our tidal dissipation modelling are discussed in Section 5.3.2.

Our results show that self-consistent modelling of Io's interior introduces new effects that need to be further explored. Tidal dissipation induces lateral variations in the asthenosphere that need to be taken into account when modelling Io's interior. In Chapter 3, we were able to show that including even small tidally-induced lateral variations leads to significant differences in the tidal dissipation pattern over time, which have not been identified before. The continuous feedback results in an asymmetry in the tidal dissipation pattern and therefore shows promise to explain the observed asymmetry of Io's volcanic pattern (Chapter 3). Uncertain parameters, whose effect on the feedback needs further investigation and other model improvements are dis-



cussed in Section 5.3.3. Furthermore, the newly discovered effect could have important implications for tidally heated exoplanets whose thermal fingerprints, and potentially volcanic activity pattern, might be observed in the future.

The distribution of Io's volcanoes on global, large, and small spatial scales provides valuable insights into the tidal heating process and heat transport below Io's crust. Besides the investigated correlation between long-wavelength variations in the volcanic activity and tidal dissipation patterns, the spatial neighborhoods of Io's volcanoes has potentially been underrated in previous studies. The fundamental unknown in this respect is whether Io's volcanoes are caused by sub-lithospheric or lithospheric anomalies. Our results presented in Chapter 4 are based on the hypothesis that Io's volcanoes are correlated with up- and downwellings in the mantle, which implies that Io's volcanoes are caused by sub-lithospheric anomalies. This hypothesis needs to be tested, which requires models that simulate volcanic systems and their origin at the intersection between mantle and crust (Section 5.3.4). The questions how Loki Patera and the other most powerful volcanoes are capable to maintain their high and continuous heat output over several decades or longer is of major importance to understand Io's global heat transport. Suggestions for open questions that need to be answered to understand the effect of these local processes for Io are provided in Section 5.3.4.

### 5.3. RECOMMENDATIONS FOR FUTURE WORK

From the results and conclusions stated above, open issues came to light, which lead to the following suggestions for further model-based investigations.

#### 5.3.1. HEAT TRANSPORT IN A SOLID-LIQUID MEDIUM

The results of Chapter 2 and 3 show that Io's heat transport in the mantle is likely driven by both magmatic and convection processes. However, the efficiency of magma transport through a porous matrix for a given melt fraction is not well constrained. To allow stronger constraints to our parameter space explored in Chapter 4, as well as other one-dimensional models (*Bierson and Nimmo, 2016; Elder, 2015; Moore, 2001; Spencer et al., 2020a,b, 2021*) laboratory experiments and detailed models of fluid behaviour in a porous matrix are required. A joint modelling and laboratory approach could result in a better understanding of how the permeability of the matrix changes as a function of the melt fraction and how the grain size and packing influences these parameters. First advances have been made (*Katz, 2008; Lichtenberg et al., 2019*), however specific Io conditions, such as the low pressure and higher melt fraction, need to be studied. In addition to constraints on the magmatic heat transport parameterization, interactions between mantle convection and magma transport have not received accurate quantitative treatment so far. One-dimension models only assume the co-existence of both mechanisms (*Elder, 2015*, and Chapter 2 of this thesis). We know from Earth that melt is focused at specific locations, for example at mid-ocean ridges, and that these locations commonly correlate with the convection pattern in the mantle (*Spiegelman and McKenzie, 1987*). Also how melt is extracted and migrates laterally is connected to the underlying convection motion as studied for Earth (*Braun and Sohn, 2003; Spiegelman,*

1993). Therefore, these interactions may significantly influence the efficiency and spatial characteristics of the heat transport processes in Io's mantle. This requires advanced 2D or 3D numerical models with high spatial and temporal resolution that can simultaneously and consistently incorporate melt migration and convection (e.g. *Dannberg and Heister, 2016; Dannberg et al., 2019; Moore and Webb, 2013*). With the help of these models it might be possible to improve constraints such as the vigour of convection in Io's mantle and the exact fraction between magmatic and convective heat transport in the mantle and in the crust. Model improvements regarding high-resolution 2D and 3D modelling in order to explain Io's local surface features, which cannot be simulated with global models, are discussed in Section 5.3.4.

### 5.3.2. TIDAL DISSIPATION IN A SOLID-LIQUID MEDIUM

Strong interactions between the solid and the liquid phase not only control the heat transport in Io's mantle but also influence Io's tidal dissipation. So far, only dissipation in both end-members, i.e. a solid visco-elastic mantle (e.g. *Bierson and Nimmo, 2016; Segatz et al., 1988*, and this thesis) and a global magma ocean (*Tyler et al., 2015*), are explored. However, pumping fluid magma through the porous solid rock matrix could result in significant heat production (*Vance et al., 2007*). Poroviscoelastic models couple the porous solid and interstitial fluid deformation and thus take this heating mechanism into account. Poroviscoelastic models have been applied to the porous core of Enceladus (*Liao et al., 2020*), but they have not been applied to Io. In contrast to the rock-water medium in Enceladus' porous core, the two phases in Io's mantle, i.e. solid and fluid rock, are only defined by a small difference in their melting temperature. For this reason tidal dissipation and the porous behaviour are strongly coupled. In addition, an analysis of how the tidally induced flows influence the geometry and therefore friction properties of the two-phase medium is required.

### 5.3.3. FEEDBACK BETWEEN INTERIOR STATE, HEAT TRANSPORT AND TIDAL HEAT GENERATION

To increase the validity of the conclusions that can be drawn based on Io's volcanic activity pattern we suggest to implement a more consistent thermal evolution model. Furthermore, we propose to 1) include radial and lateral varying structural differences, such as tidally-induced variations of the crustal thicknesses, 2) vary the strength of convection and the reference visco-elastic properties, and 3) include small heterogeneities, as random perturbations in the initial models. In addition, model advances discussed in Section 5.3.1 and Section 5.3.2, such as tidal dissipation in a two-phase medium, can be included in the feedback modelling.

The investigated feedback (Chapter 3) may also be applied to tidally heated exoplanets. *Demory et al. (2016)* detected longitudinal variations in the thermal signal of the exoplanet 55 Cancri e, which motivates this type of investigation. A simple feedback model as applied in Chapter 3, with none of the above discussed additions, would be sufficient for such a parameter study. A thinner asthenosphere, caused by a steeper pressure gradient with depth of a larger planet, may lead to a stronger tidal heating pattern, and potentially stronger offset of the evolving heating pattern. This

would make the presence of tidally induced heterogeneities and the presence of a tidal-dissipation-rheology feedback for a large exoplanet even more likely than for Io.

### 5.3.4. FROM GLOBAL TO LOCAL SCALES

Mechanisms that could explain Io's volcanic system, with Loki Patera as the largest end-member, need to be investigated including structural and chemical aspects, such as the rising of magma through dikes and the effect of melting temperature reducing elements. Due to the large number of unknowns it is not feasible to investigate a whole volcanic system in detail including all possible mechanisms and structures. Consequently, the model parameters need to be reduced and the focus needs to be placed on individual processes:

- How is magma formed and how does the melt work its way through the crust to the surface?
- Is the emergence of magma reservoirs and melt focusing areas controlled by the convection pattern in the mantle? Do these areas relate to downwelling or to the hottest locations within broad upwellings (see Section 4.5)?
- Are stresses in the crust and Io's large mountains also influenced by sublithospheric anomalies, for example convective thinning by active downwellings (*Spohn and Schubert, 1983*), which further invoke the rising of magma through the crust?
- What role does a regional tidal-dissipation-rheology feedback, such as investigated for long-wavelengths variations on global scale in Chapter 3, play for small-scale processes?
- Are Io's volcanoes controlled by different chemical processes?

In order to answer these open questions it is required to model Io's crust and upper mantle in more detail using 3D or 2D models with high-resolution. Advances in modelling heat piping in 2D have been achieved recently (e.g. *Elder, 2015; Schools and Montesi, 2019*), however, these models do not include chemical processes. As the eruption style correlates very well with the chemical composition of the erupted material (*Davies, 1996, 2007; Davies et al., 2000*), it is essential to incorporate chemical aspects into models of Io's crust and mantle, such that above listed possibilities of interior processes can be distinguished or even ruled out based on Io's observed volcanic properties (*Davies et al., 2010; Spencer et al., 2020b*). As volcanoes on Io show very different characteristics, one interior process would likely not fit all volcanic systems. It is therefore necessary to improve the categorisation of Io's volcanoes, form different classes of volcanoes based on observations, and adapt regional models of Io's upper mantle and crust such that they fit the identified group of volcanic systems.

## 5.4. OUTLOOK

Future Io observations are indispensable to place constraints on Io's interior and proceed in Io-related research. Earth-ground-based and Earth-orbit-based observations of

Io, such as the Atacama Large (sub) Millimeter Array (ALMA) allow for the determination of the SO<sub>2</sub>, SO, NaCl, and KCl flux, and therefore provide better constraints on Io's volcanic chemistry (*de Pater et al., 2020*). The James Webb telescope (*NASA/GSFC, 2021*) will also help to characterize Io's atmosphere, surface characteristics and position of volcanic centers with its near and mid infrared instruments. However, neither the models presented in this thesis, nor the above suggested model advances, nor future Earth-(orbit)-based Io observation will likely not be sufficient to provide a clear and unequivocal proof for the existence or non-existence of a magma ocean. A satellite mission (clipper or orbiters) dedicated to exploration of Io is therefore superior to the above named efforts. Of particular value to confirm or reject the magma ocean hypothesis are geodetic and geophysical measurements, which require multiple spacecraft flybys. Four specific observations are suggested:

- Static and temporal changes of the gravity field and topography: The body's response to the external tidal potential differs significantly in case the upper crust is decoupled from the deeper interior by a fluid layer. This behaviour is typically parameterized by the tidal Love numbers  $k_2$  and  $h_2$ . For models consistent with Io's total heat production, the response in the gravity field is five times greater if Io has a liquid magma ocean instead of a predominantly solid mantle. The real part of  $k_2$  is approximated to be 0.09 for a visco-elastic, partially-molten mantle and close to 0.5 for a magma ocean (*Bierson and Nimmo, 2016*). This significant difference is expected to be detectable by a Io-dedicated space mission.
- Observations of Io's forced libration amplitude: Librations would provide an independent proof to predict whether or not the crust is detached from a deeper mantle. Libration amplitudes greater than 0.5 km are expected for a thick crust that is detached from the deeper mantle (*Van Hoolst et al., 2020*).
- Magnetic field induction: The implications of the currently available magnetic field observations from Galileo are highly debated (*Blöcker et al., 2018; Khurana et al., 2011*) as it is not certain if variations of the magmatic field are due to magnetic induction of the magma ocean or variations in Jupiter's magnetic field. Additional magnetic field observations may allow to verify or invalidate the significance of the induction signal versus a random signal and therefore provide stronger conclusions.
- Passive radar: This method is similar to a ground-penetrating radar, however, using Jupiter's radio emissions and correlating the received signal with the signal back-scattered from Io does not require an active radar source of the instrument. With this method a potential liquid layer beneath Io's crust can be detected (*Peters et al., 2020*).

Besides these geophysical observation techniques, space-based exploration also provides various complementary observations such as a particle detector, and thermal cameras, which allow for an improved determination of eruption temperatures and eruption characteristics providing stronger compositional constraints on the magma origin.

The JUNO spacecraft studying the interior and origins of Jupiter already took images of Io's volcanic activity (*Mura et al., 2019*). During the extended mission JUNO will continuously encircle Jupiter with flybys for Io planned for Dec. 30, 2023, and Feb. 3, 2024. During these flybys magnetic field and visual observations shall take place (*NASA/JPL, 2021*). The Europa clipper (National Aeronautics and Space Administration) and JUICE (European Space Agency), both focusing on the icy satellites of the Jovian system, are not dedicated to Io. Near flybys, even during the extended mission scenarios, are unlikely. Io-dedicated missions would allow more precise geophysical measurements. The IVO (Io Volcano Investigator) mission has been proposed (*University of Arizona, 2021*) to carry out Io-dedicated experiments. Unfortunately, in 2021 the mission was not selected to be investigated further. But with an increasing interest in Earth's early evolution and tidally-heated exoplanets a future Io-dedicated missions will be just a matter of time.

# REFERENCES

- Anderson, J. D., R. A. Jacobson, E. L. Lau, W. B. Moore, and G. Schubert (2001), Io's gravity field and interior structure, *Journal of Geophysical Research: Planets*, 106(E12), 32,963–32,969.
- Běhouňková, M., G. Tobie, G. Choblet, and O. Čadek (2010), Coupling mantle convection and tidal dissipation: Applications to Enceladus and Earth-like planets, *Journal of Geophysical Research: Planets*, 115, E09,011.
- Běhouňková, M., G. Tobie, G. Choblet, and O. Čadek (2011), Tidally induced thermal run-aways on extrasolar Earths: impact on habitability, *The Astrophysical Journal*, 728(2), 89–95.
- Berckhemer, H., W. Kampfmann, E. Aulbach, and H. Schmeling (1982a), Shear modulus and  $q$  of forsterite and dunite near partial melting from forced-oscillation experiments, *Physics of the Earth and Planetary Interiors*, 29(1), 30–41.
- Berckhemer, H., W. Kampfmann, E. Aulbach, and H. Schmeling (1982b), Shear modulus and  $Q$  of forsterite and dunite near partial melting from forced-oscillation experiments, *Physics of the Earth and Planetary Interiors*, 29(1), 30 – 41, special Issue Properties of Materials at High Pressures and High Temperatures.
- Beuthe, M. (2013), Spatial patterns of tidal heating, *Icarus*, 223(1), 308–329.
- Beuthe, M. (2019), Enceladus's crust as a non-uniform thin shell: II tidal dissipation, *Icarus*, 332, 66–91.
- Bierson, C., and F. Nimmo (2016), A test for Io's magma ocean: Modeling tidal dissipation with a partially molten mantle, *Journal of Geophysical Research: Planets*, 121(11), 2211–2224.
- Bierson, C. J., and F. Nimmo (2020), Explaining the Galilean satellites' density gradient by hydrodynamic escape, *The Astrophysical Journal*, 897(2), L43.
- Bierson, C. J., and G. Steinbrügge (2021), Tidal heating did not dry out Io and Europa, *The Planetary Science Journal*, 2(3), 89.
- Bills, B. G. (2005), Free and forced obliquities of the Galilean satellites of Jupiter, *Icarus*, 175(1), 233–247.
- Blöcker, A., J. Saur, L. Roth, and D. F. Strobel (2018), MHD modeling of the plasma interaction with Io's asymmetric atmosphere, *Journal of Geophysical Research: Space Physics*, 123(11), 9286–9311.

- Braun, M. G., and R. A. Sohn (2003), Melt migration in plume–ridge systems, *Earth and Planetary Science Letters*, 213(3), 417 – 430.
- Breuer, D., and B. Moore (2015), Dynamics and thermal history of the terrestrial planets, the Moon, and Io.
- Cañon-Tapia, E., and R. Mendoza-Borunda (2014), Insights into the dynamics of planetary interiors obtained through the study of global distribution of volcanoes I: Empirical calibration on Earth, *Journal of Volcanology and Geothermal Research*, 281, 53–69.
- Cañon-Tapia, E., and G. P. Walker (2004), Global aspects of volcanism: the perspectives of “plate tectonics” and “volcanic systems”, *Earth-Science Reviews*, 66(1-2), 163–182.
- Cantrall, C., K. de Kleer, I. de Pater, D. A. Williams, A. G. Davies, and D. Nelson (2018), Variability and geologic associations of volcanic activity on Io in 2001–2016, *Icarus*, 312, 267–294.
- Canup, R. M., and W. R. Ward (2002), Formation of the Galilean Satellites: Conditions of Accretion, *The Astronomical Journal*, 124(6), 3404–3423.
- Canup, R. M., and W. R. Ward (2009), Origin of Europa and the Galilean satellites, *Europa*, pp. 59–83.
- Carlson, R., P. Weissman, W. Smythe, J. Mahoney, et al. (1992), Near-infrared mapping spectrometer experiment on Galileo, *Space Science Reviews*, 60(1-4), 457–502.
- Carr, M., H. Masursky, R. Strom, and R. Terrile (1979), Volcanic features of Io, *Nature*, 280(5725), 729–733.
- Carr, M. H. (1986), Silicate volcanism on Io, *Journal of Geophysical Research: Solid Earth*, 91(B3), 3521–3532.
- Carr, M. H., A. S. McEwen, K. A. Howard, F. C. Chuang, P. Thomas, P. Schuster, J. Oberst, G. Neukum, G. Schubert, and Galileo-Imaging-Team (1998), Mountains and calderas on Io: Possible implications for lithosphere structure and magma generation, *Icarus*, 135(1), 146–165.
- Castillo-Rogez, J. C., M. Efroimsky, and V. Lainey (2011), The tidal history of Iapetus: Spin dynamics in the light of a refined dissipation model, *Journal of Geophysical Research: Planets*, 116, E09,008.
- Cañon-Tapia, E. (2014), Insights into the dynamics of planetary interiors obtained through the study of global distribution of volcanoes II: Tectonic implications from Venus, *Journal of Volcanology and Geothermal Research*, 281, 70 – 84.
- Crawford, G. D., and D. J. Stevenson (1985), Gas-driven water volcanism and resurfacing on Europa, *Lunar and Planetary Science Conference*, 16, 148–149.
- Crumpler, L. (1993), Comparison of the distribution of large magmatic centers on Earth, Venus, and Mars, *Lunar and Planetary Science Conference*, 24.

- Crumpler, L., and J. Revenaugh (1997), Hot spots on Earth, Venus, and Mars: Spherical harmonic spectra, *Proc. Lunar Planet. Sci. 27th*, pp. 275–276.
- Dannberg, J., and T. Heister (2016), Compressible magma/mantle dynamics: 3-D, adaptive simulations in ASPECT, *Geophysical Journal International*, 207(3), 1343–1366.
- Dannberg, J., R. Gassmüller, R. Grove, and T. Heister (2019), A new formulation for coupled magma/mantle dynamics, *Geophysical Journal International*, 219(1), 94–107.
- Davies, A., R. Davies, G. Veeder, K. de Kleer, I. de Pater, D. Matson, T. Johnson, and L. Wilson (2018), Discovery of a powerful, transient, explosive thermal event at Marduk Fluctus, Io, in Galileo NIMS data, *Geophysical Research Letters*, 45(7), 2926–2933.
- Davies, A. G. (1996), Io's volcanism: Thermo-physical models of silicate lava compared with observations of thermal emission, *Icarus*, 124(1), 45–61.
- Davies, A. G. (2001), Volcanism on Io: The view from Galileo, *Astronomy & Geophysics*, 42(2), 2.10–2.15.
- Davies, A. G. (2007), *Volcanism on Io*, vol. 7, Cambridge University Press.
- Davies, A. G., R. Lopes-Gautier, W. D. Smythe, and R. W. Carlson (2000), Silicate cooling model fits to Galileo NIMS data of volcanism on Io, *Icarus*, 148(1), 211–225.
- Davies, A. G., L. P. Keszthelyi, D. A. Williams, C. B. Phillips, A. S. McEwen, R. M. C. Lopes, W. D. Smythe, L. W. Kamp, L. A. Soderblom, and R. W. Carlson (2001), Thermal signature, eruption style, and eruption evolution at Pele and Pillan on Io, *Journal of Geophysical Research: Planets*, 106(E12), 33,079–33,103.
- Davies, A. G., L. P. Keszthelyi, and A. J. Harris (2010), The thermal signature of volcanic eruptions on Io and Earth, *Journal of Volcanology and Geothermal Research*, 194(4), 75–99.
- Davies, A. G., G. J. Veeder, D. L. Matson, and T. V. Johnson (2015), Map of Io's volcanic heat flow, *Icarus*, 262, 67–78.
- de Kleer, K., and I. de Pater (2016), Spatial distribution of Io's volcanic activity from near-IR adaptive optics observations on 100 nights in 2013–2015, *Icarus*, 280, 405–414.
- de Kleer, K., M. Skrutskie, J. Leisenring, A. Davies, A. Conrad, I. De Pater, A. Resnick, V. Bailey, D. Defrere, P. Hinz, et al. (2017), Multi-phase volcanic resurfacing at Loki Patera on Io, *Nature*, 545(7653), 199–202.
- de Kleer, K., I. de Pater, E. M. Molter, E. Banks, A. G. Davies, C. Alvarez, R. Campbell, J. Aycock, J. Pelletier, and T. Stickel (2019), Io's volcanic activity from time domain adaptive optics observations: 2013–2018, *The Astronomical Journal*, 158(1), 29.
- de Kleer, K., F. Nimmo, and E. Kite (2019a), Variability in Io's volcanism on timescales of periodic orbital changes, *Geophysical Research Letters*, 46(12), 6327–6332.



- de Kleer, K., A. McEwen, C. Bierson, A. Davies, D. DellaGiustina, A. Ermakov, J. Fuller, C. Hamilton, and C. Harris (2019b), Tidal Heating: Lessons from Io and the Jovian System, *Report from the KISS Workshop*.
- de Pater, I., A. G. Davies, A. McGregor, C. Trujillo, M. Ádámkóvics, G. J. Veeder, D. L. Matson, and G. Leone (2014), Global near-IR maps from Gemini-N and Keck in 2010, with a special focus on Janus Patera and Kanehekili Fluctus, *Icarus*, 242, 379–395.
- de Pater, I., C. Laver, A. G. Davies, K. de Kleer, D. A. Williams, R. R. Howell, J. A. Rathbun, and J. R. Spencer (2016), Io: Eruptions at Pillan, and the time evolution of Pele and Pillan from 1996 to 2015, *Icarus*, 264, 198–212.
- de Pater, I., K. de Kleer, A. G. Davies, and M. Ádámkóvics (2017), Three decades of Loki Patera observations, *Icarus*, 297, 265–281.
- de Pater, I., S. Luszcz-Cook, P. Rojo, E. Redwing, K. de Kleer, and A. Moullet (2020), ALMA observations of Io going into and coming out of eclipse, *The Planetary Science Journal*, 1(3), 60.
- de Pater, I., J. T. Keane, K. de Kleer, and A. G. Davies (2021), A 2020 observational perspective of Io, *Annual Review of Earth and Planetary Sciences*, 49.
- Demory, B.-O., M. Gillon, J. De Wit, N. Madhusudhan, E. Bolmont, K. Heng, T. Kataria, N. Lewis, R. Hu, J. Krick, et al. (2016), A map of the large day–night temperature gradient of a super-Earth exoplanet, *Nature*, 532(7598), 207–209.
- Deschamps, F., C. Yao, P. J. Tackley, and C. Sanchez-Valle (2012), High Rayleigh number thermal convection in volumetrically heated spherical shells, *Journal of Geophysical Research: Planets*, 117(E9).
- Dobos, V., R. Heller, and E. L. Turner (2017), The effect of multiple heat sources on exomoon habitable zones, *Astronomy & Astrophysics*, 601, A91.
- Efroimsky, M. (2012), Tidal dissipation compared to seismic dissipation: In small bodies, Earths, and super-Earths, *The Astrophysical Journal*, 746(2), 150–169.
- Elder, C. M. (2015), The effects of melt on impact craters on icy satellites and on the dynamics of Io's interior, dissertation, *The University of Arizona*.
- Fischer, H.-J., and T. Spohn (1990), Thermal-orbital histories of viscoelastic models of Io (J1), *Icarus*, 83(1), 39–65.
- Frouard, J., and M. Efroimsky (2017), Tides in a body librating about a spin–orbit resonance: Generalisation of the Darwin–Kaula theory, *Celestial Mechanics and Dynamical Astronomy*, 129(1-2), 177–214.
- Galsa, A., and L. Lenkey (2007), Quantitative investigation of physical properties of mantle plumes in three-dimensional numerical models, *Physics of Fluids*, 19(11), 116,601.
- Geissler, P., A. McEwen, C. Phillips, L. Keszthelyi, and J. Spencer (2004), Surface changes on Io during the Galileo mission, *Icarus*, 169(1), 29–64.

- Grasset, O., and E. Parmentier (1998), Thermal convection in a volumetrically heated, infinite Prandtl number fluid with strongly temperature-dependent viscosity: Implications for planetary thermal evolution, *Journal of Geophysical Research: Solid Earth*, 103(B8), 18,171–18,181.
- Greenberg, R. (1981), Tidal evolution of the Galilean satellites: A linearized theory, *Icarus*, 46(3), 415–423.
- Hamilton, C. W., C. D. Beggan, S. Still, M. Beuthe, R. M. Lopes, D. A. Williams, J. Radebaugh, and W. Wright (2013), Spatial distribution of volcanoes on Io: Implications for tidal heating and magma ascent, *Earth and Planetary Science Letters*, 361, 272–286.
- Han, L., and A. P. Showman (2010), Coupled convection and tidal dissipation in Europa's ice shell, *Icarus*, 207(2), 834–844.
- Hanyk, L., C. Matyska, and D. A. Yuen (2005), Short time-scale heating of the Earth's mantle by ice-sheet dynamics, *Earth, Planets and Space*, 57(9), 895–902.
- Hay, H. C. F. C., A. Trinh, and I. Matsuyama (2020), Powering the Galilean satellites with moon-moon tides, *Geophysical Research Letters*, 47(15), e2020GL088,317.
- Hirschmann, M. M. (2000), Mantle solidus: Experimental constraints and the effects of peridotite composition, *Geochemistry, Geophysics, Geosystems*, 1, 2000GC000,070.
- Hirth, G., and D. L. Kohlstedt (1995), Experimental constraints on the dynamics of the partially molten upper mantle: Deformation in the diffusion creep regime, *Journal of Geophysical Research: Solid Earth*, 100(B2), 1981–2001.
- Hu, H., W. Wal, and L. Vermeersen (2017), A numerical method for reorientation of rotating tidally deformed viscoelastic bodies, *Journal of Geophysical Research: Planets*, 122(1), 228–248.
- Huang, S.-S. (1959), Occurrence of life in the universe, *American Scientist*, 47(3), 397–402.
- Hussmann, H., and T. Spohn (2004), Thermal-orbital evolution of Io and Europa, *Icarus*, 171(2), 391–410.
- Jackson, B., R. Barnes, and R. Greenberg (2008), Tidal heating of terrestrial extrasolar planets and implications for their habitability, *Monthly Notices of the Royal Astronomical Society*, 391(1), 237–245.
- Jackson, I. (1993), Dynamic compliance from torsional creep and forced oscillation tests: An experimental demonstration of linear viscoelasticity, *Geophysical Research Letters*, 20(19), 2115–2118.
- Jara-Oru e, H. M., and B. L. Vermeersen (2011), Effects of low-viscous layers and a non-zero obliquity on surface stresses induced by diurnal tides and non-synchronous rotation: The case of Europa, *Icarus*, 215(1), 417–438.

- Johnson, C. L., and M. A. Richards (2003), A conceptual model for the relationship between coronae and large-scale mantle dynamics on Venus, *Journal of Geophysical Research: Planets*, 108(E6).
- Karato, S.-i. (2008), Deformation of Earth materials, *An Introduction to the Rheology of Solid Earth*, 463.
- Katz, R. F. (2008), Magma Dynamics with the enthalpy method: Benchmark solutions and magmatic focusing at mid-ocean ridges, *Journal of Petrology*, 49(12), 2099–2121.
- Katz, R. F., M. Spiegelman, and C. H. Langmuir (2003), A new parameterization of hydrous mantle melting, *Geochemistry, Geophysics, Geosystems*, 4, 1–19.
- Kaula, W. M. (1964), Tidal dissipation by solid friction and the resulting orbital evolution, *Reviews of Geophysics*, 2(4), 661–685.
- Keller, T., R. F. Katz, and M. M. Hirschmann (2017), Volatiles beneath mid-ocean ridges: Deep melting, channelised transport, focusing, and metasomatism, *Earth and Planetary Science Letters*, 464, 55–68.
- Keszthelyi, L., and A. McEwen (1997), Magmatic differentiation of Io, *Icarus*, 130(2), 437–448.
- Keszthelyi, L., A. McEwen, and G. Taylor (1999), Revisiting the hypothesis of a mushy global magma ocean in Io, *Icarus*, 141(2), 415–419.
- Keszthelyi, L., W. Jaeger, M. Milazzo, J. Radebaugh, A. G. Davies, and K. L. Mitchell (2007), New estimates for Io eruption temperatures: Implications for the interior, *Icarus*, 192(2), 491–502.
- Khurana, K. K., X. Jia, M. G. Kivelson, F. Nimmo, G. Schubert, and C. T. Russell (2011), Evidence of a global magma ocean in Io's interior, *Science*, 332(6034), 1186–1189.
- Kirchoff, M. R., and W. B. McKinnon (2009), Formation of mountains on Io: Variable volcanism and thermal stresses, *Icarus*, 201(2), 598–614.
- Kirchoff, M. R., W. B. McKinnon, and P. M. Schenk (2011), Global distribution of volcanic centers and mountains on Io: Control by asthenospheric heating and implications for mountain formation, *Earth and Planetary Science Letters*, 301(1-2), 22–30.
- Kirchoff, M. R., W. B. McKinnon, and M. T. Bland (2020), Effects of faulting on crustal stresses during mountain formation on Io, *Icarus*, 335, 113,326.
- Kumar, S. (1980), A model of the SO<sub>2</sub> atmosphere and ionosphere of Io, *Geophysical Research Letters*, 7(1), 9–12.
- Kuramoto, K., and T. Matsui (1994), Formation of a hot proto-atmosphere on the accreting giant icy satellite: Implications for the origin and evolution of Titan, Ganymede, and Callisto, *Journal of Geophysical Research: Planets*, 99(E10), 21,183–21,200.

- Lainey, V., J.-E. Arlot, Ö. Karatekin, and T. Van Hoolst (2009), Strong tidal dissipation in Io and Jupiter from astrometric observations, *Nature*, 459(7249), 957–959.
- Laneuville, M., M. Wieczorek, D. Breuer, and N. Tosi (2013), Asymmetric thermal evolution of the Moon, *Journal of Geophysical Research: Planets*, 118(7), 1435–1452.
- Langseth, M. G., S. J. Keihm, and K. Peters (1976), Revised lunar heat-flow values, *Lunar and Planetary Science Conference Proceedings*, 7, 3143–3171.
- Lellouch, E., M. A. McGrath, and K. L. Jessup (2007), Io's atmosphere, in *Io After Galileo*, pp. 231–264, Springer.
- Leone, G., L. Wilson, and A. G. Davies (2011), The geothermal gradient of Io: Consequences for lithosphere structure and volcanic eruptive activity, *Icarus*, 211(1), 623–635.
- Liao, Y., F. Nimmo, and J. A. Neufeld (2020), Heat production and tidally driven fluid flow in the permeable core of Enceladus, *Journal of Geophysical Research: Planets*, 125(9), e2019JE006,209.
- Lichtenberg, T., T. Keller, R. F. Katz, G. J. Golabek, and T. V. Gerya (2019), Magma ascent in planetesimals: Control by grain size, *Earth and Planetary Science Letters*, 507, 154–165.
- Limare, A., K. Vilella, E. Di Giuseppe, C. Farnetani, E. Kaminski, E. Surducan, V. Surducan, C. Neamtu, L. Fourel, and C. Jaupart (2015), Microwave-heating laboratory experiments for planetary mantle convection, *Journal of Fluid Mechanics*, 777, 50–67.
- Lissauer, J. J., and I. De Pater (2013), *Fundamental planetary science: physics, chemistry and habitability*, Cambridge University Press.
- Lopes, R. M. C., and D. A. Williams (2005), Io after Galileo, *Reports on Progress in Physics*, 68(2), 303–340.
- Lunine, J. I., and D. J. Stevenson (1982), Formation of the Galilean satellites in a gaseous nebula, *Icarus*, 52(1), 14 – 39.
- Makarov, V. V., and M. Efroimsky (2014), Tidal dissipation in a homogeneous spherical body. II. Three examples: Mercury, Io, and Kepler-10 b, *The Astrophysical Journal*, 795(1), 7–16.
- Mavko, G. M. (1980), Velocity and attenuation in partially molten rocks, *Journal of Geophysical Research: Solid Earth*, 85(B10), 5173–5189.
- McEwen, A. S., L. Keszthelyi, J. R. Spencer, G. Schubert, D. L. Matson, R. Lopes-Gautier, K. P. Klaasen, T. V. Johnson, J. W. Head, P. Geissler, S. Fagents, A. G. Davies, M. H. Carr, H. H. Breneman, and M. J. S. Belton (1998), High-temperature silicate volcanism on Jupiter's moon Io, *Science*, 281(5373), 87–90.

- McEwen, A. S., M. J. S. Belton, H. H. Breneman, S. A. Fagents, P. Geissler, R. Greeley, J. W. Head, G. Hoppa, W. L. Jaeger, T. V. Johnson, L. Keszthelyi, K. P. Klaasen, R. Lopes-Gautier, K. P. Magee, M. P. Milazzo, J. M. Moore, R. T. Pappalardo, C. B. Phillips, J. Radebaugh, G. Schubert, P. Schuster, D. P. Simonelli, R. Sullivan, P. C. Thomas, E. P. Turtle, and D. A. Williams (2000), Galileo at Io: Results from high-resolution imaging, *Science*, 288(5469), 1193–1198.
- McEwen, A. S., L. P. Keszthelyi, R. Lopes, P. M. Schenk, and J. R. Spencer (2004), The lithosphere and surface of Io, *Jupiter: The Planet, Satellites and Magnetosphere*, pp. 307–328.
- Mei, S., W. Bai, T. Hiraga, and D. L. Kohlstedt (2002), Influence of melt on the creep behavior of olivine–basalt aggregates under hydrous conditions, *Earth and Planetary Science Letters*, 201(3-4), 491–507.
- Monnereau, M., and F. Dubuffet (2002), Is Io’s mantle really molten?, *Icarus*, 158(2), 450–459.
- Moore, W. (2003), Tidal heating and convection in Io, *Journal of Geophysical Research: Planets*, 108(E8), 1–6.
- Moore, W. B. (2001), The thermal state of Io, *Icarus*, 154(2), 548–550.
- Moore, W. B., and A. A. G. Webb (2013), Heat-pipe Earth, *Nature*, 501(7468), 501–505.
- Moore, W. B., G. Schubert, J. D. Anderson, and J. R. Spencer (2007), The interior of Io, in *Io After Galileo*, pp. 89–108, Springer.
- Morabito, L., S. Synnott, P. Kupferman, and S. A. Collins (1979), Discovery of currently active extraterrestrial volcanism, *Science*, 204(4396), 972–972.
- Mosqueira, I., P. Estrada, and D. Turrini (2010), Planetesimals and satellitesimals: formation of the satellite systems, *Space science reviews*, 153(1-4), 431–446.
- Mura, A., A. Adriani, F. Tosi, R. Lopes, G. Sindoni, G. Filacchione, D. Williams, A. Davies, C. Plainaki, and S. Bolton (2019), Infrared observations of Io from Juno, *Icarus*, p. 113607.
- Murray, C. D., and S. F. Dermott (1999), *Solar system dynamics*, Cambridge university press.
- NASA/GSFC (2021), James Webb Space Telescope, <https://www.jwst.nasa.gov>, Accessed: 2021-03-09.
- NASA/JPL (2021), JUNO extended mission, <https://www.nasa.gov/feature/jpl/nasa-s-juno-mission-expands-into-the-future>, Accessed: 2021-02-28.
- Nosonovsky, M. (2007), Model for solid-liquid and solid-solid friction of rough surfaces with adhesion hysteresis, *The Journal of Chemical Physics*, 126(22), 224,701.

- Oberg, N., I. Kamp, S. Cazaux, and C. Rab (2020), Photoevaporation of the Jovian circum-planetary disk i. explaining the orbit of callisto and the lack of outer regular satellites, *A&A*, 638, A135.
- Ojakangas, G. W., and D. Stevenson (1986), Episodic volcanism of tidally heated satellites with application to Io, *Icarus*, 66(2), 341–358.
- Ojakangas, G. W., and D. J. Stevenson (1989), Thermal state of an ice shell on Europa, *Icarus*, 81(2), 220–241.
- O’Reilly, T. C., and G. F. Davies (1981), Magma transport of heat on Io: A mechanism allowing a thick lithosphere, *Geophysical Research Letters*, 8(4), 313–316.
- Parmentier, E., and C. Sotin (2000), Three-dimensional numerical experiments on thermal convection in a very viscous fluid: Implications for the dynamics of a thermal boundary layer at high Rayleigh number, *Physics of Fluids*, 12(3), 609–617.
- Parmentier, E., C. Sotin, and B. Travis (1994), Turbulent 3-D thermal convection in an infinite Prandtl number, volumetrically heated fluid: Implications for mantle dynamics, *Geophysical Journal International*, 116(2), 241–251.
- Peale, S. (1976), Orbital resonances in the Solar system, *Annual review of astronomy and astrophysics*, 14(1), 215–246.
- Peale, S. J., P. Cassen, and R. T. Reynolds (1979), Melting of Io by tidal dissipation, *Science*, 203(4383), 892–894.
- Peters, S., D. Schroeder, A. Romero-Wolf, and G. Steinbrügge (2020), Passive radar investigations of Io using Jupiter’s radio emissions, in *Lunar and Planetary Science Conference*, 2326, p. 2993.
- Phillips, C. B., A. S. McEwen, L. P. Keszthelyi, P. E. Geissler, D. P. Simonelli, M. Malazzo, and Galileo-Imaging-Team (2000), Volcanic resurfacing rates and styles on Io, in *AAS/Division for Planetary Sciences Meeting Abstracts #32*, *AAS/Division for Planetary Sciences Meeting Abstracts*, vol. 32, p. 29.05.
- Porco, C. C., P. Helfenstein, P. Thomas, A. Ingersoll, J. Wisdom, R. West, G. Neukum, T. Denk, R. Wagner, T. Roatsch, et al. (2006), Cassini observes the active south pole of Enceladus, *Science*, 311(5766), 1393–1401.
- Renaud, J. P., and W. G. Henning (2018), Increased tidal dissipation using advanced rheological models: Implications for Io and tidally active exoplanets, *The Astrophysical Journal*, 857(2), 98.
- Roberts, J. H., and F. Nimmo (2008), Tidal heating and the long-term stability of a subsurface ocean on Enceladus, *Icarus*, 194(2), 675–689.
- Roberts, P. (1967), Convection in horizontal layers with internal heat generation, *Journal of Fluid Mechanics*, 30(1), 33–49.

- Ross, M., and G. Schubert (1985), Tidally forced viscous heating in a partially molten Io, *Icarus*, 64(3), 391 – 400.
- Ross, M., and G. Schubert (1986), Tidal dissipation in a viscoelastic planet, *Journal of Geophysical Research: Solid Earth*, 91(B4), 447–452.
- Ross, M., G. Schubert, T. Spohn, and R. Gaskell (1990), Internal structure of Io and the global distribution of its topography, *Icarus*, 85(2), 309–325.
- Roth, L., J. Saur, K. D. Retherford, A. Blöcker, D. F. Strobel, and P. D. Feldman (2017), Constraints on Io's interior from auroral spot oscillations, *Journal of Geophysical Research: Space Physics*, 122(2), 1903–1927.
- Roth, L., J. Boissier, A. Moullet, Á. Sánchez-Monge, K. de Kleer, M. Yoneda, R. Hikida, H. Kita, F. Tsuchiya, A. Blöcker, et al. (2020), An attempt to detect transient changes in Io's SO<sub>2</sub> and NaCl atmosphere, *Icarus*, p. 113925.
- Rovira-Navarro, M., W. van der Wal, T. Steinke, and D. Dirx (2021), Tidally heated exomoons around gas giants, *The Planetary Science Journal*, 2(3), 119.
- Russell, E., F. Brown, R. Chandos, W. Fincher, L. Kubel, A. Lacis, and L. Travis (1992), Galileo photopolarimeter/radiometer experiment, *Space science reviews*, 60(1-4), 531–563.
- Sabadini, R., B. Vermeersen, and G. Cambiotti (2016), Rotational dynamics of viscoelastic planets: Linear theory, in *Global Dynamics of the Earth: Applications of Viscoelastic Relaxation Theory to Solid-Earth and Planetary Geophysics*, pp. 87–148, Springer.
- Sagan, C., and S. F. Dermott (1982), The tide in the seas of Titan, *Nature*, 300(5894), 731–733.
- Saur, J., F. M. Neubauer, D. F. Strobel, and M. E. Summers (1999), Three-dimensional plasma simulation of Io's interaction with the Io plasma torus: Asymmetric plasma flow, *Journal of Geophysical Research: Space Physics*, 104(A11), 25,105–25,126.
- Schenk, P., H. Hargitai, R. Wilson, A. McEwen, and P. Thomas (2001), The mountains of Io: Global and geological perspectives from Voyager and Galileo, *Journal of Geophysical Research: Planets*, 106(E12), 33,201–33,222.
- Schools, J., and L. Montesi (2019), Modeling melt migration in the lithosphere and asthenosphere of Io, with Applications to heat pipe evolution and cyclical volcanism, *AGU Fall Meeting, 2019*, P51A–06.
- Schubert, G. (1979), Subsolidus convection in the mantles of terrestrial planets, *Annual Review of Earth and Planetary Sciences*, 7(1), 289–342.
- Schubert, G., D. Stevenson, and K. Ellsworth (1981), Internal structures of the Galilean satellites, *Icarus*, 47(1), 46–59.
- Schubert, G., D. L. Turcotte, and P. Olson (2001), *Mantle Convection in the Earth and Planets*, Cambridge University Press.

- Schubert, G., J. Anderson, T. Spohn, and W. McKinnon (2004), Interior composition, structure and dynamics of the Galilean satellites, *Jupiter: The planet, satellites and magnetosphere, 1*, 281–306.
- Segatz, M., T. Spohn, M. Ross, and G. Schubert (1988), Tidal dissipation, surface heat flow, and figure of viscoelastic models of Io, *Icarus*, 75(2), 187–206.
- Shahnas, M., R. Pysklywec, and W. Peltier (2013), Layered convection in Io: Implications for short-wavelength surface topography and heat flow, *Icarus*, 225(1), 15–27.
- Shoji, D., and H. Hussmann (2016), A stochastic basis to the spatially uniform distribution of randomly generated Ionian paterae, *Journal of Geophysical Research: Planets*, 121(10), 2055–2062.
- Smith, B., E. Shoemaker, S. Kieffer, and A. Cook (1979a), The role of SO<sub>2</sub> in volcanism on io, *Nature*, 280(5725), 738–743.
- Smith, B. A., L. A. Soderblom, R. Beebe, J. Boyce, G. Briggs, M. Carr, S. A. Collins, A. F. Cook, G. E. Danielson, M. E. Davies, et al. (1979b), The Galilean satellites and Jupiter: Voyager 2 imaging results, *Science*, 206(4421), 927–950.
- Smrekar, S. E., and C. Sotin (2012), Constraints on mantle plumes on Venus: Implications for volatile history, *Icarus*, 217(2), 510 – 523.
- Soderblom, L. A. (1980), The Galilean moons of Jupiter, *Scientific American*, 242(1), 88–101.
- Sohl, F., T. Spohn, D. Breuer, and K. Nagel (2002), Implications from Galileo observations on the interior structure and chemistry of the Galilean satellites, *Icarus*, 157(1), 104–119.
- Sparks, D. W., and E. Parmentier (1991), Melt extraction from the mantle beneath spreading centers, *Earth and Planetary Science Letters*, 105(4), 368 – 377.
- Spencer, D. C., R. F. Katz, and I. Hewitt (2020a), Magmatic intrusions control Io’s crustal thickness, *Journal of Geophysical Research: Planets*, 125(6), e2020JE006,443.
- Spencer, D. C., R. F. Katz, I. J. Hewitt, D. A. May, and L. P. Keszthelyi (2020b), Compositional layering in Io driven by magmatic segregation and volcanism, *Journal of Geophysical Research: Planets*, 125(9), e2020JE006,604.
- Spencer, D. C., R. F. Katz, and I. J. Hewitt (2021), Tidal controls on the lithospheric thickness and topography of Io from magmatic segregation and volcanism modelling, *Icarus*, 359, 114,352.
- Spiegelman, M. (1993), Physics of melt extraction: Theory, implications and applications, *Philosophical Transactions of the Royal Society of London. Series A: Physical and Engineering Sciences*, 342(1663), 23–41.
- Spiegelman, M., and D. McKenzie (1987), Simple 2-D models for melt extraction at mid-ocean ridges and island arcs, *Earth and Planetary Science Letters*, 83(1-4), 137–152.



- Spohn, T. (1991), Mantle differentiation and thermal evolution of Mars, Mercury, and Venus, *Icarus*, 90(2), 222–236.
- Spohn, T. (1997), Tides of Io, in *Tidal Phenomena*, pp. 345–377, Springer.
- Spohn, T., and G. Schubert (1983), Convective thinning of the lithosphere: A mechanism for rifting and mid-plate volcanism on Earth, Venus, and Mars, in *Processes of Continental Rifting, Developments in Geotectonics*, vol. 19, edited by P. Morgan and B. Baker, pp. 67 – 90, Elsevier.
- Steinke, T., H. Hu, D. Höning, W. van der Wal, and B. Vermeersen (2020a), Tidally induced lateral variations of Io's interior, *Icarus*, 335, 113,299.
- Steinke, T., D. van Sliedregt, K. Vilella, W. van der Wal, and B. Vermeersen (2020b), Can a combination of convective and magmatic heat transport in the mantle explain Io's volcanic pattern?, *Journal of Geophysical Research: Planets*, 125(12), e2020JE006,521.
- Steinke, T., D. van Sliedrecht, K. Vilella, W. van der Wal, and B. Vermeersen (2020c), Data accompanying the paper: Can a combination of convective and magmatic heat transport in the mantle explain Io's volcanic pattern?, doi:10.5281/zenodo.3976806.
- Stevenson, D. J. (2003), Styles of mantle convection and their influence on planetary evolution, *Comptes Rendus Geoscience*, 335(1), 99 – 111.
- Stevenson, D. J., and S. C. McNamara (1988), Background heatflow on hotspot planets: Io and Venus, *Geophysical Research Letters*, 15(13), 1455–1458.
- Tabor, D. (1992), Friction as a dissipative process, in *Fundamentals of friction: macroscopic and microscopic processes*, pp. 3–24, Springer.
- Tackley, P. J. (2001), Convection in Io's asthenosphere: Redistribution of nonuniform tidal heating by mean flows, *Journal of Geophysical Research: Planets*, 106(E12), 32,971–32,981.
- Tackley, P. J., G. Schubert, G. A. Glatzmaier, P. Schenk, J. T. Ratcliff, and J.-P. Matas (2001), Three-dimensional simulations of mantle convection in Io, *Icarus*, 149(1), 79–93.
- Thomas, P., M. Davies, T. Colvin, J. Oberst, P. Schuster, G. Neukum, M. Carr, A. McEwen, G. Schubert, M. Belton, et al. (1998), The shape of Io from Galileo limb measurements, *Icarus*, 135(1), 175–180.
- Tobie, G., A. Mocquet, and C. Sotin (2005), Tidal dissipation within large icy satellites: Applications to Europa and Titan, *Icarus*, 177(2), 534–549.
- Tosi, N., M. Godolt, B. Stracke, T. Ruedas, J. L. Grenfell, D. Höning, A. Nikolaou, A.-C. Plesa, D. Breuer, and T. Spohn (2017), The habitability of a stagnant-lid Earth, *Astronomy & Astrophysics*, 605, A71.
- Tsang, C. C., J. A. Rathbun, J. R. Spencer, B. E. Hesman, and O. Abramov (2014), Io's hot spots in the near-infrared detected by LEISA during the New Horizons flyby, *Journal of Geophysical Research: Planets*, 119(10), 2222–2238.

- Tsang, C. C. C., J. R. Spencer, E. Lellouch, M. A. Lopez-Valverde, and M. J. Richter (2016), The collapse of io's primary atmosphere in jupiter eclipse, *Journal of Geophysical Research: Planets*, 121(8), 1400–1410.
- Turcotte, D. L., and G. Schubert (2002), *Geodynamics*, Cambridge university press.
- Turner, A. J., R. F. Katz, M. D. Behn, and T. Keller (2017), Magmatic focusing to mid-ocean ridges: the role of grain-size variability and non-Newtonian viscosity, *Geochemistry, Geophysics, Geosystems*, 18(12), 4342–4355.
- Turtle, E. P., W. L. Jaeger, and P. M. Schenk (2007), Ionian mountains and tectonics: Insights into what lies beneath Io's lofty peaks, in *Io After Galileo*, pp. 109–131, Springer.
- Tyler, R. H. (2009), Ocean tides heat Enceladus, *Geophysical Research Letters*, 36(15).
- Tyler, R. H., W. G. Henning, and C. W. Hamilton (2015), Tidal heating in a magma ocean within Jupiter's moon Io, *The Astrophysical Journal Supplement Series*, 218(2), 22.
- University of Arizona (2021), IVO: Io Volcano Observer- Follow the heat, <https://ivo.lpl.arizona.edu>, Accessed: 2021-02-28.
- Van Hoolst, T., R.-M. Baland, and A. Trinh (2013), On the librations and tides of large icy satellites, *Icarus*, 226(1), 299–315.
- Van Hoolst, T., R.-M. Baland, A. Trinh, M. Yseboodt, and F. Nimmo (2020), The librations, tides, and interior structure of Io, *Journal of Geophysical Research: Planets*, 125(8), e2020JE006473.
- van Sliedregt, D. (2020), Volcanism on Io: A Comparison between the volcanic distribution and tidal stress, Master thesis, *AE, Delft University of Technology*.
- Vance, S., J. Harnmeijer, J. Kimura, H. Hussmann, B. DeMartin, and J. M. Brown (2007), Hydrothermal systems in small ocean planets, *Astrobiology*, 7(6), 987–1005.
- Veeder, G. J., D. L. Matson, T. V. Johnson, D. L. Blaney, and J. D. Goguen (1994), Io's heat flow from infrared radiometry: 1983–1993, *Journal of Geophysical Research: Planets*, 99(E8), 17,095–17,162.
- Veeder, G. J., A. G. Davies, D. L. Matson, T. V. Johnson, D. A. Williams, and J. Radebaugh (2012), Io: Volcanic thermal sources and global heat flow, *Icarus*, 219(2), 701–722.
- Veeder, G. J., A. G. Davies, D. L. Matson, T. V. Johnson, D. A. Williams, and J. Radebaugh (2015), Io: Heat flow from small volcanic features, *Icarus*, 245, 379–410.
- Vilella, K., and E. Kaminski (2017), Fully determined scaling laws for volumetrically heated convective systems, a tool for assessing habitability of exoplanets, *Physics of the Earth and Planetary Interiors*, 266, 18–28.
- Vilella, K., A. Limare, C. Jaupart, C. G. Farnetani, L. Fourel, and E. Kaminski (2018), Fundamentals of laminar free convection in internally heated fluids at values of the Rayleigh–Roberts number up to  $10^9$ , *Journal of Fluid Mechanics*, 846, 966–998.

- Wienbruch, U., and T. Spohn (1995), A self sustained magnetic field on Io?, *Planetary and Space Science*, 43(9), 1045–1057.
- Williams, D. A., L. P. Keszthelyi, D. A. Crown, J. A. Yff, W. L. Jaeger, P. M. Schenk, P. E. Geissler, and T. L. Becker (2011a), *Geologic map of Io*, US Department of the Interior, US Geological Survey.
- Williams, D. A., L. P. Keszthelyi, D. A. Crown, J. A. Yff, W. L. Jaeger, P. M. Schenk, P. E. Geissler, and T. L. Becker (2011b), Volcanism on Io: New insights from global geologic mapping, *Icarus*, 214(1), 91–112.
- Wilson, J. K., M. Mendillo, J. Baumgardner, N. M. Schneider, J. T. Trauger, and B. Flynn (2002), The dual sources of Io's sodium clouds, *Icarus*, 157(2), 476–489.
- Wu, P. (2004), Using commercial finite element packages for the study of earth deformations, sea levels and the state of stress, *Geophysical Journal International*, 158(2), 401–408.
- Yin, A., and R. T. Pappalardo (2015), Gravitational spreading, bookshelf faulting, and tectonic evolution of the South Polar Terrain of Saturn's moon Enceladus, *Icarus*, 260, 409–439.
- Yoder, C. F. (1979), How tidal heating in Io drives the Galilean orbital resonance locks, *Nature*, 279(5716), 767–770.
- Yoder, C. F., and S. J. Peale (1981), The tides of Io, *Icarus*, 47(1), 1–35.
- Zhong, S. (2005), Dynamics of thermal plumes in three-dimensional isoviscous thermal convection, *Geophysical Journal International*, 162(1), 289–300.
- Zhou, Q., and K.-Q. Xia (2010), Physical and geometrical properties of thermal plumes in turbulent Rayleigh–Bénard convection, *New Journal of Physics*, 12(7), 075,006.

# ACKNOWLEDGEMENTS

In a way, the solar system is a huge laboratory. It is filled with a lot of empty space and a large number of different samples just waiting to be explored. Io is one such sample. While the outward appearance already looks stunning to a layman, in my opinion, the ultimate beauty of Io lies in the physics that makes Io look the way it does - "all yellow". Diving into Io's interior and putting pieces of known physical principles together to form something new, has been a blast with exiting findings but also hard work and setbacks. I remember my first conference, where I, full of excitement and naivety, found myself confronted with two kind of people - 1) "Io? Never heard of it. Does it have a water ocean that could bear life? No? Oh, too bad!" and 2) "Oh, nice idea! We tried this already, but our models fail to explain the observations. So we stopped working on Io. It is too challenging!". This crash with reality led to my first meltdown (of many) and yet to the actual start of my doctoral studies. Fortunately, I found myself surrounded by a supportive environment and with experts (and future experts) at my side. All these people brought me to where I am today, writing these last lines of my PhD thesis - with so many important things still left to say...

First of all, thank you Bert, for bringing this nice piece of research to life. Thanks for your support and trust in my skills and ideas, while, at the same time, you were always ready to challenge them with interesting questions. Sometimes, these questions felt out-of-context to me at first. However, back at my desk, they helped me to view the problems from a wider perspective and stimulated many new out-of-the-box ideas, which significantly contributed to this thesis. Imke, it was a pleasure to have you on this. Combining the modelling expertise at TU Delft with your Io-observation expertise was more challenging in practice than on paper. Even though only small parts of our extensive exchange on our views on Io made it into workable content, I have learned a lot from you during this process. Changing the perspective was refreshing, motivating, and in the end worthwhile. Thanks a lot for your hospitality in Berkeley. These weeks mark one of the highlights of my PhD studies. Dear Wouter, it was great fun working with you. As my daily supervisor you have been through quite an amount of ups and downs with me. I am very grateful for all your support. I could always count on you (even if this, at times, meant long nights for you, or that you had to advocate for my interests towards other parties). You always seemed to have a good sense of what I needed in the moment, even if it was just a little extra time for small talk on Skype during the lockdowns.

This dissertation would not have been possible without the help and support of numerous external collaborators, co-authors and contacts: Thank you! Kenny Vilella for your insight into volumetric-heated convection and your endless support with my second paper; Mikael Beuthe for trusting my initial results (Chapter 3) more than I

did; Ashley Davies for your contagious enthusiasm, the amazing day at JPL and much more; Katherine de Kleer for hosting me at Caltech and for many insightful discussions on Io; Dan Spencer and Richard Katz for insightful discussions on Io's magmatic heat transport; and many, many more brilliant people, who provided critical remarks and inspiring ideas that have advanced my research and the quality of my thesis: Marie Běhounková, Isamu Matsuyama, Francis Nimmo, Catherine Elder, Tim Van Hoolst, Carver Bierson, Mathilde Kervazo, Gregor Steinbrügge, Tilman Spohn, James Tuttle Keane, Nicola Tosi, Wim Spakman, and Walter Kiefer. Furthermore, I would like to thank my TU Delft colleagues and students: Hermes for being my first guide into the topic; Haiyang for all the modelling work in ABAQUS that I could step into; Marc for in-depth discussions on tidal dissipation mechanisms and critical feedback on my draft thesis; and Bas, for being my partner in crime to conquer ABAQUS. Special gratitude goes to Duncan for analysing the statistical properties of Io's volcanoes in his Master thesis, Mark Bemelmans for helping me to validate the finite element models, and Wiereen Parag for providing me a quick start into the project based on his Master thesis. Also, thanks to the committee members of my PhD defence for accepting the invitation and being part in this very last step towards my degree.

Unfortunately, a PhD cannot be achieved by simply talking about science. The inspiring, international environment at TU Delft made all the hard work feel more fun. Thanks to my fellow PhDs and PostDocs: Jesse, Tim, Svenja, Jacco, Mao, Yuxin, Gourav, Tati, Kartik, Günther, Nick, Dora, Marcel, Thomas, Loic, Elisabetta and the ones already mentioned. I especially enjoyed the many lunch and Space Bar conversations, which have broadened my view of the world, and all the fun and quality moments aside of work. You made this PhD time a prime experience. The same holds for the staff members on the 9th floor: Dominic, Bart, Jose, Wim, Eelco, Pieter, Daphne, Ejo, Stephanie, Ron, Vidhya, Kevin, Bernard, Jeannette, and all others. Special thanks to my "office husband" Bas. You have been most crucial in the last years. Thanks for your help, your support in overcoming my regular Berlin blues in my first year, and your friendship. Thank you, Marc Naeije, for taking good care of our "Greek mathematicians and astronomers" that had to deal with my extensive finite element runs. To Relly, the warm soul of our department, thank you for all your support from my first steps as a PhD student to my last ones towards my defence. Also, I would like to thank the fellows from the PepSci network - Claudia, Bram, Nina, Kaustubh, Jurrian, Vincent, Katya and many more for all the great vibrant meetings across the Netherlands.

My sincere thanks go to all those who encouraged me on my long way, trusted in my strengths and provided support and guidance. Here I would like to mention my professors, lecturers and fellow students in Karlsruhe. Thank you for the wonderful tour around the world of nature, mathematics and technology. To my previous colleagues at the German Aerospace Center in Berlin - Frank, Hauke, Alex, Doris, Martin, Lena, Ina, Tina, and Jürgen Oberst - Thank you for your continuous interest in what and how I am doing. After some wonderful years in the field of planetary science I decided to move back to planet Earth, since, after all, I did not discover a Planet B. From asthenosphere to atmosphere does not seem far, letter-wise, but it is quite a different, yet exciting world,

that I keep discovering day by day. Thanks to my new colleagues at TNO in Utrecht for supporting and trusting me in this.

Yue, Ole and Dave, thanks for lighting up my lockdown evenings with fireworks and amazing adventures to Planet 9. I hope to see you more in person again. Thank you, Heike and Frank, for keeping me grounded and hosting Dennis and me, longer than usual, when we were in desperate need to escape our flat in Leiden during the pandemic.

Last but not least, the most important people in this, my roots and my anchor. I have been blessed with a family that has always given me a firm foundation and a loving environment to grow. Even though this success was ever a matter of course (and only you know what I mean by that), it is rooted in this strong foundation. Thanks for all the encouragement, support and trust. Dear Dennis, this thesis would have not been finished without you. Thanks for unconditional support, endless proofreading, discussions on the topic, and for keeping up with me throughout a pandemic. But most of all, thanks for your friendship, open arms and happiness you bring to my life.

Leiden, November 2021

*Teresa Steinke*



# CURRICULUM VITAE

## **Teresa STEINKE**

July 4, 1990	Born in Dresden, Germany
2000-2009	Ernst-Sigle-Gymnasium, Kornwestheim, Germany
2006-2007	Horowhenua College, Levin, New Zealand
2009-2012	Bachelor of Science in Geophysics Karlsruhe Institute of Technology, Karlsruhe, Germany
2012-2015	Master of Science in Geophysics Karlsruhe Institute of Technology, Karlsruhe, Germany
2013-2015	Master of Science in Geodesy and Geoinformatics Karlsruhe Institute of Technology, Karlsruhe, Germany
2016-2021	PhD candidate - Astrodynamics and Space Missions Delft University of Technology, Delft, The Netherlands
2021-present	Scientist - Climate, Air and Sustainability TNO, Utrecht, The Netherlands





# PUBLICATIONS

## JOURNAL PUBLICATIONS

- Rovira-Navarro, M., van der Wal, W., **Steinke, T.**, and Dirkx, D. (2021). Tidally heated exomoons around gas giants. *The Planetary Science Journal*, 2(3), 119.
- **Steinke, T.**, van Sliedregt, D., Vilella, K., Van der Wal, W., and Vermeersen, B. (2020). Can a combination of convective and magmatic heat transport in the mantle explain Io's volcanic pattern?. *Journal of Geophysical Research: Planets*, 125(12), e2020JE006521.
- **Steinke, T.**, Hu, H., Höning, D., Van der Wal, W., and Vermeersen, B. (2020). Tidally induced lateral variations of Io's interior. *Icarus*, 335, 113,299.
- Steinbrügge, G., **Steinke, T.**, Thor, R., Stark, A., and Hussmann, H. (2019). Measuring Ganymede's librations with laser altimetry. *Geosciences*, 9(7), 320.
- Steinbrügge, G., Padovan, S., Hussmann, H., **Steinke, T.**, Stark, A., and Oberst, J. (2018). Viscoelastic tides of Mercury and the determination of its inner core size. *Journal of Geophysical Research: Planets*, 123(10), 2760-2772.

## SELECTED CONFERENCE CONTRIBUTIONS

- **Steinke, T.**, van Sliedregt, D., Vilella, K., van der Wal, W., and Vermeersen, B. (2020). Constraints on Io's interior by combining small-and large-scale characteristics of the volcanic pattern. *European Planetary Science Congress*, pp. EPSC2020-859.
- **Steinke, T.**, van der Wal, W., and Vermeersen, B. L. (2019). Modelling the Feedback of Io's tidally induced heterogeneous interior on tidal dissipation. *AGU Fall Meeting*, Vol. 2019, pp. P51A-07.
- **Steinke, T.**, Hu, H., van der Wal, W., and Vermeersen, B. L. (2018). Heterogeneous effects of non-uniform tidal heating on Io's interior. *AGU Fall Meeting*, Vol. 2018, pp. P51E-2928.
- **Steinke, T.**, van der Wal, W., and Vermeersen, B. (2018). Feedback between tidal dissipation and temperature-dependent mantle viscosity: Implications for Jupiter's moon Io. *EGU General Assembly Conference*, p. 17310.

- **Steinke, T.**, van der Wal, W., Hu, H., and Vermeersen, B. (2017). Tidal Dissipation within the Jupiter Moon Io - A numerical approach. *EGU General Assembly Conference*, p. 9341.
- **Steinke, T.**, Stark, A., Steinbrügge, G., Hussmann, H., and Oberst, J. (2015). Estimation of Ganymede's topography, rotation and tidal deformation – A study of synthetic Ganymede Laser Altimeter observations. *European Planetary Science Congress*, Vol. 10.
- **Steinke, T.**, Sohl, F., Hussmann, H., Knapmeyer, M., and Wagner, F. W. (2013). Interior structure and tidal response of Mercury. *EGU General Assembly Conference*, pp. EGU2013-7006.